PRE-INTEGRATED NON-EQUILIBRIUM COMBUSTION-RESPONSE MAPPING FOR INTERNAL COMBUSTION ENGINE EMISSIONS

A Thesis for the Degree of Doctor of Philosophy (PhD)

Submitted to the Faculty of Engineering

University of Glasgow

by

Mr Nguyen Thai Chung
MEng (Vietnam)
B Business Administration (Vietnam)
B Language Teaching (Vietnam)
BEng (Vietnam)

Department of Mechanical Engineering
October 2004

Table of Contents

List of Tables

List of Figures

Abstract

This study establishes a novel method to predict emissions in internal combustion (IC) engines. The method couples a multi-dimensional engine modeling program with pre-integrated non-equilibrium chemical kinetic reaction results. Prior to engine simulation, detailed chemical kinetic reactions of air/fuel mixtures at different temperatures, pressures, and compositions, which possibly occur in the IC engine, are calculated using SENKIN, a subprogram in CHEMKIN-II computer package [1]. The reaction results are decoupled from their chemical eigenvalue (order of about 10^{-10} s) then integrated and saved in physical timescale (order of about 10^{-5} s) in a database file. In the database, reaction results of different initial conditions (temperature, pressure, and composition) are stored in different zones; the zones are indexed using their respective reaction conditions.

In the modeling process, fluid and thermal dynamics, movement of piston and valves, and spray droplets interaction are simulated by KIVA-3V [2] using the finite-volume technique. During combustion of the air/fuel mixture, instead of calculating directly the non-equilibrium chemical reactions, reaction results are obtained from the database file. KIVA-3V sends a request, with inputs of temperature, pressure, composition, and reaction time of combustible mixture to an interpolating subroutine. This interpolating subroutine uses these reaction conditions as indices to lookup the requested results in the database file, then returns temperature, heat release, and species concentrations after reaction to the main program.

The approach avoids direct time consuming calculation of detailed chemical reactions as well as the errors introduced by coupling the physical and chemical processes,

which have different eigenvalues. The required computational effort is shortened. Emissions are predicted accurately since reaction of air/fuel mixture is calculated using the detailed kinetics mechanism. The database file for each fuel must be generated once, and can be used for any application which requires chemical reactions of this fuel.

The approach is applied to model a Caterpillar 3401 direct injection (DI) compression ignition (CI) Diesel engine, a Rover K4 methane-fuelled spark ignition (SI) engine, a Ricardo E6 co-operative fuel research (CFR) SI gasoline engine, and a Toledo 1500 four-stroke SI gasoline engine. Predicted results agree well with the experimental data.

Acknowledgements

I would like to thank Professor Theodosios P. Korakianitis, my supervisor, for his many suggestions and constant support during this research. I am also thankful to Dr Shi Yubing for sharing with me his knowledge of fluid dynamics and providing many useful references.

I am grateful to my father Nguyen Dinh, my mother Nguyen Thi Nen, my wife Vu Thi Kim Lien, and my son Nguyen Vu Hoang Long for their love and encouragement and for the happiness they bring to, and the difficulties they share with me.

I should also mention that my study was sponsored by the Vietnamese government. Special thanks also to Professor Nguyen Vinh Phat, Mr Bui Van Luu who had changed my life to academic direction, Professor Le Viet Luong, Professor Bui Hai, Professor Nguyen Sy Mao who have a big influence on my research direction.

Finally, I wish to thank the following: Mr George Silvie, Mr Ian Russell, and Mr Ian Peden (for their work in the experimental setup).

Glasgow, Scotland July 28, 2004

Nomenclature

$\mathbf{A}$	cell surface projection area (appendix B)
A	pre-exponential (equation 3.1.22)
A_0, A_1, A_2, A_3	constants (chapter 5)
a	crank shaft radius (equations 4.1.2, 4.1.3)
a_i	polynomial coefficients
B	cylinder diameter (equation 4.1.2),
	breakup transition probability function (appendix A)
$\mathbf{b}$, b	grid velocity and its components (equation 6.3.3),
b	collision impact parameter (appendix A)
C_{EBU}	constant (equation 4.2.7)
C_D	drag coefficient (appendix A)
c	constant
c_0	constant (equation 5.1.5)
c_1, c_2	constants (equation 4.1.1)
c_3, c_4	constants (chapter 5)
c_l	specific heat of liquid fuel (equation 3.1.16)
c_p	specific heat at constant pressure
c_{ps}	constant (appendix A)
c_s	constant (equations 3.1.7, 5.1.4)
c_v	specific heat at constant volume

c_{ϵ_1}, c_{ϵ_2}	constants (equations 3.1.7, 5.1.4)
c_{ϵ_3}	constant (equation 5.1.4)
D	diffusion coefficient
E	activation energy
e	specific energy (equation 3.1.22)
$\mathbf{F}$	droplet acceleration (appendix A)
$\mathbf{F}'$	rate of change of velocity
f	probability density function
f'	discrete distribution of probability density function
G	arbitrary variable
G	Gaussian distribution
$\mathbf{g}$	gravitational acceleration
g	turbulent quantity (appendix B)
$g(r)$	χ-square distribution (appendix B)
H	enthalpy
h	specific enthalpy
$\bar{\mathbf{I}}$	unit tensor
$\mathbf{J}$	heat flux vector (equation 3.1.8)
J_w	heat flux normal to wall
K_c, K_p	equilibrium constants
$\mathbf{k}$	unit tangential to wall
k	turbulence kinetic energy
k_b,k_f	reaction coefficients
L	latent heat, turbulent length scale (appendix B)
l	accuracy governing input constant (section 6.3.2),
l_o	connecting rod length
M	mass
M'	vertex mass
N_c	number of species in reaction

N_{pc}	number of particle
N_r	number of reaction
N_z	number of zone (section 6.2)
NS	number of subcycle in phase C
Nu	Nusselt number
$\mathbf{n}$	normal unit vector
$\mathbf{O}$	increasing rate of momentum
Pr	Prandtl number
p	pressure
Q	source terms
q	heat source
R	rate of change of spray droplet radius
R_0	universal gas constant
r	radius of spray droplet
r_{32}	Sauter mean radius
Re	Reynolds number
S	entropy
s	distance between crankshaft axis and piston pin axis
Sc	Schmidt number
Sh	Sherwood number
T	temperature (K)
t	time
x	cell average dimension
$\mathbf{x}$	position vector
X	molar concentration
$\mathbf{u}$	gas velocity vector
$\mathbf{u}'$	gas turbulence velocity vector
$u,\ v,\ w$	components of velocity

u^*	shear speed
V	volume
$\mathbf{v}$	velocity vector of spray droplet
v	specific volume (section 5.2.2)
W	molecular weight
$\dot{W}$	source term
We	Weber number
Y	mass fraction
y	distortion from sphericity of spray droplet
$\dot{y}$	rate of change of distortion
y_a	distance from wall (chapter 5)

Greek

α	dimensionless quantity (equation 5.1.1), face of computational cell, surface-tension (appendix A)
β	temperature exponent (equation 3.1.22), face of momentum cell
Γ	third-body molecule
γ	ratio of radii of 2 collision droplets (appendix A)
δ	Dirac delta function (equation 3.1.2)
ζ	Reynolds number near the cylinder wall
ϵ	dissipation rate
θ	crank angle
θ_0	crank angle at the start of combustion
θ	liquid volume fraction
ι	specific internal energy
κ	thermal conductivity
λ	second viscosity coefficient
μ	first viscosity coefficient

ν'	Stoichiometric coefficient on reactant side
ν''	Stoichiometric coefficient on product side
ν_T	turbulent exchange coefficient (equation 4.2.6)
$\bar{\Pi}$	stress tensor
ρ	density
ρ_l'	liquid macroscopic density
$\dot{\rho}$	density change rate
$\bar{\sigma}$	viscous stress tensor
σ	collision transition probability function (appendix A)
τ	component of stress tensor
Φ	implicitness parameter
ϕ	equivalence ratio
χ	chemical species
Ω	arbitrary element
$\dot{\omega}$	production rate

Superscripts

0	standard state
$'$	reactant side
$''$	product side
$'$	time averaging (section 4.2)
$''$	Farve averaging (section 4.2)
c	chemical
B	phase B
G	Lagrangian phase
i	zone index (chapter 6)
n	step index
p	predicted
s	spray
T	transpose sign

t	intermediate step
v	subcycle index in convection calculation in phase C (appendix B)

Subscripts

0	reference point
1	species 1 (fuel)
1	droplet number 1 (appendix A)
2	droplet number 2 (appendix A)
a,b,c,d	vertices of a cell face (appendix A)
a	acceleration
b	backward
bu	breakup
c	chemical
clr	clearance (equation 4.1.2)
cr	Courant condition
cri	critical
cv	convection
coll	collision
d	droplet
dif	diffusion
f	forward
G	arbitrary variable
gr	growth term
(i,j,k)	Cartesian coordinates
j	zone index (section 6.2.3)
k	to turbulent kinetic energy
l	liquid
la	laminar
p	pressure

pc	partilce
ph	physical
m	species m
r	reaction r^{th}
rd	distortion
$turb$	turbulent
w	wall
ϵ	turbulent kinetic energy dissipation rate

Abbreviations and acronyms

ABDC	after bottom dead center
AFR	air/fuel ratio
ATDC	after top dead center
BBDC	before bottom dead center
BTDC	before top dead center
CA	crank angle
CARS	coherent anti-Stokes Raman scattering
CFD	computational fluid dynamics
CFR	fuel co-operative research
CI	compression ignition
CMC	conditional moment closure
DI	direct injection
DNS	direct numerical simulation
EBM	eddy breakup model
EDC	eddy dissipation concept
EPS	dissipation of turbulence kinetic energy
FBN	fuel-bound nitrogen
FID	flame ionization detector
HC	unburned hydrocarbon
IC	internal combustion
ICCD	intensified charge coupled device

IEM	interaction-by-exchange-with-the-mean
LES	large eddy simulation
LEM	linear eddy model
LIM	local integral moment
LRS	laser Raman scattering
NDIR	nondispersive infrared
PC	personal computer
PDF	probability density function
PGS	pressure gradient scaling
QSOU	quasi second order upwin
RANS	Reynolds-averaged Navier-Stokes
SI	spark ignition
SRS	spontaneous Rayleigh scattering
TKE	turbulence kinetic energy
Other symbols	
bold face	a vector
bold face with	
dot	temporal derivative
HC	unburned hydrocarbon
NH_i (i=1, 2, 3)	nitrogen hydrates (reactions 2.2.8)
over-bar ($\bar{}$)	a tensor
over-check ($\check{}$)	normalized value
over-line ($\overline{abcd}$)	time averaging
over-tilde ($\tilde{}$)	Favre averaging
RH	hydrocarbon molecular (reactions 2.2.8)
Δh_f^0	heat of formation at the standard state
$\Delta\theta_{bn}$	duration of combustion (equation 4.1.1)
∇	difference operator

Chapter 1

Introduction

1.1 Effects of emissions on humans and the environment

Emissions are a big concern to scientists because of their severe effects on human health and the environment. There is a link between emissions and poor visibility, eye and throat irritation, respiratory complication, and a variety of health hazards. Many authors [3] have shown that carbon monoxide (CO) is a poisonous gas that deprives body tissues of necessary oxygen. It is proven that nitrogen dioxide (NO_2) is a lung irritant which causes bronchitis, pneumonia, and increases susceptibility to respiratory infections. Sulfur dioxide (SO_2) affects breathing, and may aggravate existing respiratory and cardiovascular disorder. SO_2 can cause visibility impairment. Particulate mater, specially with diameter smaller than 10 μm (PM_{10}), impairs visibility, and decreases efficiency of the immune system as the body is unable to engage micro-particulates with usual methods of filtration. Ozone (O_3) can cause damage of lung tissue and reduces lung function.

Many studies [4, 5, 6] have proven that nitrogen oxides and sulphur oxides are the main contributors to forest deterioration. Nitrogen monoxide (NO) is a free radical

which may react with metal atoms such as iron and copper, and this inhibits plant growth. Nitrogen oxides (NO_x) and sulphur oxides are diluted in rain water to become "acid rain". The long term deposition of the protons in these acids has the effect of increasing soil acidity. This leaches away essential nutrients such as calcium and potassium, thus reducing soil fertility. Yellowing of leaves or needles due to losses of magnesium and manganese is accelerated by acidic deposition.

Emissions have similar effects on buildings and monuments. NO_2 is a precursor to O_3 via reaction with oxygen. Carbon dioxide (CO_2) molecules are transparent to short-wave solar radiation, but absorb long-wave (heat wave) radiation. The earth warms up from the absorption of sunlight then radiates the energy as heat. The CO_2 in the earth's atmosphere in turn absorbs some of the heat energy and re-radiates part of the trapped energy back to earth. The result is an increase in the earth's temperature and a change in climate, resulting in the so-called "greenhouse effect" [7].

1.2 Legislation on emissions of internal combustion engines

In the early 1950s it was pointed out that the biggest source of emissions are internal combustion (IC) engines, which are widely used in common life, from electricity power stations, airplanes, automobile vehicles, etc. (IC engines can be classified in many types, such as gas turbines, reciprocating engines, etc. Within this work the term IC engine refers to internal combustion reciprocating engines). Due to the serious effects of emissions on human and the environment, emissions of IC engines are limited by legislations, especially on automobile vehicles. In the 1970s, legislation was introduced

Legislation / Year [g/kWh]	CO	HC	NO_x	PM
Euro 0 / 1988	11.2	2.4	14.4	
Euro 1 / 1992	4.5	1.1	8.0	0.36
Euro 2 / 1995	4.0	1.1	7.0	0.15
Euro 3 / 2000	2.1	0.66	5.0	0.10
Euro 4 / 2005	1.5	0.46	3.5	0.02
Euro 5 / 2008	1.5	0.46	2.0	0.02

Table 1.1: European legislation on emissions from vehicles powered by gasoline engine (from [8])

U.S.A. legislation [g/mile]	CO	HC	NO_x	PM
Light duty vehicles	90	15	6.2	
Tier 1, 1994-6	3.4	0.25	0.4	0.08
Tier 2, 2004	1.7	1.25	0.2	
Low emissions vehicles	7.0	0.3	2.0	
Ultra low emissions vehicles	3.5	0.18	1.0	

Table 1.2: U.S.A. legislation on emissions from vehicles powered by gasoline engine (from [9])

in various countries, to control the exhaust pollutant emissions from both diesel- and gasoline-power vehicles. Since then, the legislation has been progressively tightening in Europe. For instance, the NO_x emissions legislation introduced in the year 2000 in Europe for a medium-size vehicle (EEC, stage III) limits NO_x emissions to about one-third of its level in the year 1988 [8, 9, 10]. The legislation on emissions from gasoline-power vehicles in Europe is shown in table 1.1.

Similar trends are found in Japan and the U.S.A.. The Environmental Protection Agency (EPA) recently announced very stringent emission standards to come in effect from 2007 [10]. The U.S.A. legislation on emissions from gasoline-power vehicles is illustrated in table 1.2.

The strict legislation on emissions in IC engines makes engine design a harder task. The legislation requires IC engines to operate cleaner, while still under high

efficiency and high power output.

1.3 Progress in modeling engine operation and its emissions

Modeling the operation of IC engines and predicting emissions to produce better designs for cleaner engines is a difficult mission for researchers. This involves simulation of complex processes: evaporation of liquid fuel to gaseous-phase, fluid dynamics, and chemical reaction of air/fuel mixture. These processes occur in the turbulent environment of IC engine combustion chambers. The most difficult task in the simulation is to couple properly the physical and chemical processes, which occur in very different timescales. Over the years many approaches have been developed to resolve this difficult task.

The zero-dimensional approach consists of empirical equation models ([11, 12, 13]), single-zone models ([14]), and multi-zone models ([15]). In this approach, the operation of IC engines is modelled without accounting for the effects of engine geometry. The complex processes in the cylinder chamber are described using empirical equations. The empirical equation method is normally used only for parametric studies. The single-zone models overpredict peak pressure and NO_x, underpredict burning duration, and are unable to predict HC and CO [16]. In the multi-zone model, predicted CO_2 is 60% of the experimental data, predicted CO is 80%, and it still fails to predict NO_x emissions [15].

Senecal et al. [17] and Uludogan et al. [18] found that detailed chemical kinetics can be used to predict accurately chemical reactions, and that multi-dimensional modeling of physical processes IC engines gives good results. A promising approach

for engine modeling and emissions prediction is to couple multi-dimensional fluid dynamics simulation with detailed chemical kinetics reaction. However, coupling directly the physical and chemical processes results in a stiff system of equations and causes errors due to the difference in eigenvalues. Several researchers have tried to couple two programs to predict emissions in IC engines [12]. It is feasible to calculate a simple engine geometry with a light fuel (such as methane) with few species and reactions. It is computationally intensive to calculate emissions for heavy fuel combustion, which involves hundreds of species and thousands of reactions in a fine grid geometry.

1.4 Purpose, method and structure of this work

In this study, a pre-integrated non-equilibrium combustion response mapping method is developed for prediction of emissions of IC engines. The method is to couple a detailed chemical kinetic model with a multi-dimensional fluid dynamics model. Prior to the engine modeling, detailed chemical kinetic reactions are pre-calculated for a variety of initial reaction conditions (temperature, pressure, and species concentrations at the beginning of reaction), and results (species production rates, and rates of increase of temperature and pressure) are stored in a database file in physical timescale (timescale for calculation of the physical processes, order of about 10^{-5} s). Once the database has been created, an engine model is used to calculate the physical processes of the engine. During combustion, instead of calculating directly the chemical reactions, detailed reaction results are obtained from the database file.

In our application KIVA-3V [2] is used to model operation of engine processes except the chemical reactions during the combustion process. SENKIN, a subprogram

in CHEMKIN-II [1] package, is used for detailed chemical kinetics calculation of air/fuel mixture. The pre-integrated approach is validated on three types of IC engine: diesel, gasoline, and methane-fuelled engines. Calculated results are compared to experimental data obtained form a Caterpillar 3401 four-stroke compression ignition (CI) diesel engine, a Cooperative Fuel Research (CFR) spark ignition (SI) engine, a Rover K4 four-stroke gas-fuelled SI engine, and a Toledo 1500 four-stroke SI gasoline engine.

The dissertation consists of 10 chapters. Chapter 1 is an introduction of the hazards and the urgent need to reduce emissions in IC engines; and describes the direction of approach to predict emissions. An overview of IC engine operation and emissions formation mechanisms are presented in chapter 2. The governing equations of the problem are introduced in chapter 3. Chapter 4 reviews the approaches proposed by previous authors to solve the problem. Chapter 5 describes the modeling programs used in approach. Chapter 6 discusses in detail the "Pre-integrated non-equilibrium combustion response mapping technique for internal combustion engines". Experiments and sample calculations are described in chapter 7. Results and discussions are presented in chapter 8. Conclusions and recommendations are in chapters 9 and 10 respectively.

Chapter 2

Internal combustion engines and emissions

This chapter gives an overview of IC engines and their operating principles. The formation mechanisms of emissions of IC engines are presented. General factors affecting the formation of emissions are also described.

2.1 Internal combustion engine

In IC engines, chemical energy is converted into mechanical power by burning fuel inside the combustion chamber. High temperature and pressure resulting from the chemical reaction of air/fuel mixture in the cylinder forces the piston to move, and mechanical power is transmitted to the crankshaft via the connecting mechanism. There are many different types of IC engines. According to the method of ignition for the mixture of air/fuel, IC engines can be classified as: spark ignition (SI) engines, where air/fuel mixture is ignited by a spark plug; and compression ignition (CI) engines, where temperature and pressure in the cylinder are high enough to cause spontaneous ignition of air/fuel mixture. The CI engine is also referred to as the diesel or oil engine.

2.1.1 Spark ignition engine

In many current SI engine designs air and fuel are mixed in the intake system before entering the engine cylinder. The air/fuel ratio (AFR) of the mixture is around stoichiometric. In the typical arrangement of SI engines air/fuel mixture is inducted, then trapped into the combustion chamber via the valve system. The mixture then is compressed, and temperature and pressure in the combustion chamber increase. Most of the fuel is in the vapour state, and mixed well with air before the spark plug is initiated. The mixture inside the cylinder is ignited at a desired crank angle by the spark plug. Following ignition, a turbulent flame develops and propagates through the volume within the cylinder until most of the fuel oxidizes while the flame reaches the combustion chamber walls, then extinguishes. The power output of SI engines is controlled by varying the inlet pressure via the throttle valve, the amount of air/fuel mixture supplied to the engine using the computer control system, and the ignition crank angle [19]. A typical operating arrangement of a four-stroke SI engine is sketched in figure 2.1.

2.1.2 Compression ignition engine

In CI engines, only air is inducted and compressed in the cylinder during the intake and compression processes. The air flow at a given engine speed is essentially unchanged. Fuel is injected through small orifices or nozzles into the combustion chamber toward the end of the compression stroke, just before the desired start of combustion. The injected fuel is mixed with the trapped, compressed, high pressure, hot air. A heterogeneous mixture is formed within the combustion chamber, with a wide range of air/fuel ratios. During the compression process, when the pressure

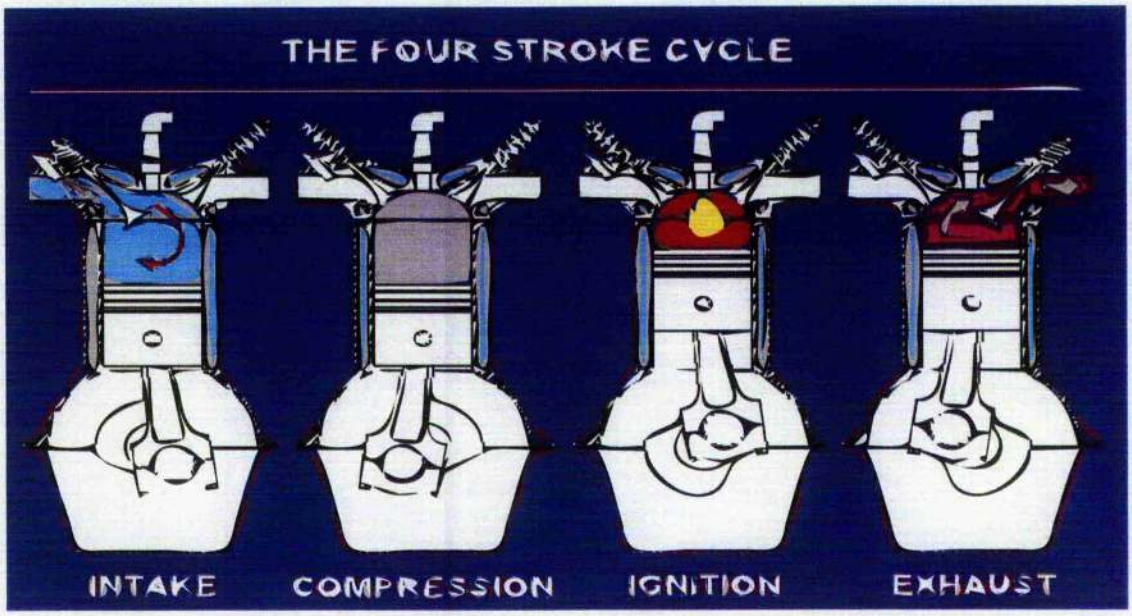

Figure 2.1: Illustration of the processes of four-stroke SI engines

and temperature of the mixture rise above the level required for spontaneous ignition of the diesel fuel, a portion of the already-mixed air and fuel ignites (after a short delay period) in one or more locations inside the combustion chamber. The ignition points are usually located where the mixture has attained, approximately, stoichiometric ratio. The location and the timing of ignition points are not controllable. The combustion process in CI engines mainly depends on the fuel evaporation rate, its mixing with the surrounding air, and the rate of combustion of the premixed fuel and air after ignition. Once combustion starts, the evaporation rate and the mixing process are accelerated due to the increasing pressure in the cylinder. Since diesel fuel does not autoignite and fuel injection in CI engines begins before combustion starts, there is no knock limit as in SI engines. In SI engines there is a knock limit resulting

from spontaneous ignition of the premixed fuel and air in the end-gas. Usually, the power output and load control of CI engines are achieved by varying the amount of fuel injected per cycle, and the engine can be operated un-throttled [20].

2.2 Formation of emissions in internal combustion engines

Combustion of air/fuel mixture in the combustion chamber is not complete. During the combustion process, a large variety of diverse reaction products are formed. Knowledge about the formation mechanism of emissions is still not complete; but it is usually assumed that various parts of combustion occur as in the following.

2.2.1 Formation of NO

There are four main routes of formation of NO_x. They are the thermal route, the prompt route, the nitrous oxide (N_2O) route, and the fuel-bound nitrogen route.

Thermal NO

The thermal or Zeldovich-NO was postulated by Zeldovich [21]. The mechanism of formation of thermal NO based on the elementary reactions:

$$O + N_2 \longrightarrow NO + N \tag{2.2.1}$$

$$O_2 + N \longrightarrow NO + O \tag{2.2.2}$$

$$N + OH \rightarrow NO + H. \tag{2.2.3}$$

Reaction (2.2.1) has very high activation energy due to the strong triple bond in the N_2 molecule. This reaction is sufficiently fast only at high temperatures, so that temperature is the rate-limiting step of the thermal NO formation. The thermal

mechanism is highly dependent on temperature, linearly dependent on oxygen atom concentration, and independent of the fuel type. NO can be formed in both the flame front and post-flame gases. Because burned gas produced early in the combustion process is compressed to higher temperature than normal temperatures reached immediately after combustion, NO formation in the post-flame gases always dominates any flame-front produced NO [22]. This is further enhanced by the large burned gas region and large residence time of burned gas.

Prompt NO

The prompt or Fenimore mechanism was postulated by Fenimore [23]. NO results from the radical CH which is generated through a complex reaction scheme. The CH is formed as an intermediate radical at the flame front only, reacts with the nitrogen of the air forming hydrocyanic acid (HCN), which then reacts further to form the NO. This mechanism is weakly dependent on temperature and accounts for only a relatively small proportion of NO emissions in fuel lean combustion. The formation of NO via Fenimore mechanism can be expressed as:

$$CH + N_2 \longrightarrow HCN + N. \tag{2.2.4}$$

Many authors have observed that in the vicinity of the flame zone NO formation rates are considerably larger than in the post-flame zone. Numerical modeling showed that if the reactions leading to NO formation are decoupled from those of combustion processes (thermal-NO), calculations of NO formation rate yield lower values than those experimentally observed. Also the amount of NO formed near the flame is higher as the air/fuel ratio decreases [24], being a maximum in the fuel-rich region and dropping off sharply at an equivalence ratio of 1.4. Such discrepancies become still larger

in combustion of fuel-rich hydrocarbon mixtures. This anomalous concentration of NO is said to be due to a different route from the thermal-NO. Such rapidly-formed NO (produced before thermal-NO, and thus always within a given residence time) is called "prompt-NO".

Various concepts have been proposed to explain the rapid formation of these anomalous quantities of NO. Some authors [25] postulate that in fuel lean and near-stoichiometric flames, they are caused by an overshoot of radical concentrations (O, OH) above the equilibrium values, which in turn has the effect of enhancing thermal-NO. A simple approach to the radical species involved is given by the pool of radicals formed in the following set of reactions, which are locally in equilibrium:

$$\begin{aligned} O + H_2 &\longrightarrow OH + H \\ H + O_2 &\longrightarrow OH + O \\ H_2 + OH &\longrightarrow H + H_2O, \end{aligned} \tag{2.2.5}$$

O and OH radicals would thereafter enter the mechanism of thermal-NO formation. Accurate values of the temperature and radical concentrations used in calculations of the thermal-NO mechanism yielded results that were closer to experimental values [26]. It has been suggested that N_2O plays an important role in the low temperature ($\leq 1,225^oC$) combustion of lean CO-air mixtures, as radical concentration overshoots cannot explain the increase of NO formation. The following mechanism was proposed by Wolfrum [27]:

$$\begin{aligned} N_2 + O + \Gamma &\longrightarrow N_2O + \Gamma \\ N_2O + H &\longrightarrow N_2 + OH, \end{aligned} \tag{2.2.6}$$

where Γ is a third-body molecule.

However, kinetic modeling demonstrates that N_2O does not play a significant role in formation of NO at high temperatures. Although O and OH were found to be high in fuel-rich mixtures, they do not account for the large formation of NO. A more plausible explanation is provided by reactions involving hydrocarbon fractions and atmospheric nitrogen as the source of nitrogen-containing radicals, which are eventually oxidized to form NO. The following reactions for a hydrocarbon species RH have been proposed by several authors [24, 28]:

$$\begin{aligned}
\text{Fuel, RH} &\longrightarrow \text{CH}, \text{C}_2 \\
\text{C} + \text{N}_2 &\longrightarrow \text{CN} + \text{N} \\
\text{C}_2 + \text{N}_2 &\longrightarrow 2\text{CN} \\
\text{CH} + \text{N}_2 &\longrightarrow \text{CN} + \text{HN} \\
\text{CH} + \text{N}_2 &\longrightarrow \text{CNH} + \text{N} \\
\text{CH}_2 + \text{N}_2 &\longrightarrow \text{HCN} + \text{N} \\
\text{C}_2\text{H} + \text{N}_2 &\longrightarrow \text{HCN} + \text{CN} \\
\text{HCN} + \text{oxidant} &\longrightarrow \text{NH}_i.
\end{aligned} \tag{2.2.7}$$

In a further stage, nitrogen hydrates species (NH_i, i=1, 2, 3) yield NO by:

$$\begin{aligned}
\text{NH} + \text{H} &\longrightarrow \text{N} + \text{H}_2 \\
\text{N} + \text{O}_2 &\longrightarrow \text{NO} + \text{O} \\
\text{N} + \text{OH} &\longrightarrow \text{NO} + \text{H}.
\end{aligned} \tag{2.2.8}$$

NO generated via nitrous oxide

The nitrous oxide N_2O mechanism is analogous to the thermal mechanism in that oxygen atom O reacts with nitrogen molecule. However, with the presence of a third

molecule Γ, N_2O is created in third-body reaction:

$$N_2 + O + \Gamma \longrightarrow N_2O + \Gamma. \tag{2.2.9}$$

This third-body reaction has low activation energy so that it can occur in low temperature conditions. The N_2O may subsequently react with O atoms to form NO as:

$$N_2O + O \longrightarrow NO + NO.$$

This reaction is usually insignificant contributor to the total NO. However, at high pressures NO generated via N_2O is promoted because of the third-body reaction.

Conversion of fuel nitrogen into NO

The nitrogen-containing compounds in the fuel evaporate during the gasification process and lead to NO formation in the gas phase. Because of the low nitrogen-containing compounds percentage in the fuel, the conversion of fuel-bound nitrogen does not contribute much NO in IC engine applications [22].

2.2.2 Formation of CO

CO emissions are the result of incomplete combustion of fuel. This can be caused by too short residence time, lack of available oxygen, too low combustion temperature, etc. There are two mechanisms of CO formation. The first one occurs in lean air/fuel mixture; the other case occurs in fuel-rich zones. In the first case, the lean mixture is not able to sustain the propagation of the flame. Concentration of CO generated by this mechanism depends on the equivalence ratio of the mixture and on temperature [29]. In the fuel-rich case, there is insufficient O_2 to oxidize all the C into CO_2, and

as a results some CO is generated instead:

$$\begin{aligned} C &+ \frac{1}{2}O_2 \longrightarrow CO \\ C &+ O_2 \longrightarrow CO_2 \\ C &+ CO_2 \longrightarrow 2CO \\ C &+ H_2O \longrightarrow CO + H_2. \end{aligned}$$

2.2.3 Formation of HC

Unburned hydrocarbon (HC) emissions are the result of incomplete combustion of fuel. They contribute to smog formation and several types of unburned hydrocarbons are toxic air contaminants, including benzene and formaldehyde. HC are also responsible for exhaust odors. In general, unburned hydrocarbons are a consequence of local flame extinction. There are two effects: flame extinction by strain; and flame extinction at walls and in gaps. In the first case, if the strain rate is too high, the flame is "blown out", the temperature drops because the convective-diffusive heat removal rate is increasing, while at the same time the rate of heat generation is decreasing due to decreasing reaction rate and to the reduced residence time in the flame zone. Flame extinction at the walls and in the gaps are caused by interaction of the flame with the cooler walls of the engine. The reasons for extinction are heat transfer (cooling of reaction zone), as well as the removal of reactive intermediates by surface reactions. The flame front can not be sustained near cold walls. The quenching distance is of the order of the flame thickness.

Production rates of emissions are calculated for each elementary reaction using the Arrhenius relation prescribed by equation 3.1.21. Many reaction mechanisms and

reaction coefficients have been developed, including detailed reaction mechanisms, and simplified (reduced) mechanisms. Details of the governing equation for emissions calculations are presented in section 3.1.1.

Chapter 3

Governing equations and their solution

This chapter presents the governing equations for reactive flows in IC engines.

3.1 Governing equations for modeling IC engines

The governing equations in IC engines are the compressible Navier-Stokes equations including source terms due to fuel injection and chemical reaction of air/fuel mixture. In addition to the equation of conservation of total mass, the equations of conservation of mass of species are included in the equation system.

Conservation of mass:

$$\frac{\partial \rho}{\partial t} + \nabla \cdot (\rho \mathbf{u}) = \dot{\rho}^s, \tag{3.1.1}$$

where ρ is the total mass density, $\mathbf{u}$ is the fluid velocity vector, $\dot{\rho}^s$ is the mass source term due to fuel spray.

Conservation of mass of species m:

$$\frac{\partial \rho_m}{\partial t} + \nabla \cdot (\rho_m \mathbf{u}) = \nabla \cdot [\rho D \nabla (\frac{\rho_m}{\rho})] + \dot{\rho}^c_m + \dot{\rho}^s \delta_{m1}, \tag{3.1.2}$$

where ρ_m is the mass density of species m, D is the Fick's Law single diffusion coefficient, $\dot{\rho}_m^c$ is the mass source term due to chemistry, δ_{m1} is the Dirac delta function (species 1 is the species of which the fuel spray droplets are composed of).

Mass consistency:

$$\sum_{m-1}^{N_c} \frac{\rho_m}{\rho} = 1, \tag{3.1.3}$$

where N_c is the number of chemical species in the fluid.

Conservation of momentum:

$$\frac{\partial(\rho \mathbf{u})}{\partial t} + \nabla \cdot (\rho \mathbf{u}\mathbf{u}) = -\nabla p - \nabla(2/3\rho k) + \nabla \cdot \bar{\sigma} + \mathbf{O}^s + \rho \mathbf{g}, \tag{3.1.4}$$

where p is the fluid pressure, k is turbulent kinetic energy, $\bar{\sigma}$ is the Newtonian viscous stress tensor, $\mathbf{O}^s$ is the rate of momentum gain per unit volume due to the spray, and $\mathbf{g}$ is vector of acceleration due to gravity.

Conservation of energy:

$$\frac{\partial(\rho \iota)}{\partial t} + \nabla \cdot (\rho \mathbf{u} \iota) = -p \nabla \cdot \mathbf{u} - \nabla \cdot \mathbf{J} + \dot{Q}^s + \rho\epsilon + \dot{Q}^c, \tag{3.1.5}$$

where ι is the specific internal energy (exclusive of chemical energy), $\dot{Q}^s$ is the energy source term due to spray interaction, ϵ is dissipation rate of turbulent kinetic energy, $\dot{Q}^c$ is the energy source term due to chemical heat release.

Turbulent kinetic energy:

$$\frac{\partial(\rho k)}{\partial t} + \nabla \cdot (\rho \mathbf{u} k) = \bar{\sigma} : \nabla \mathbf{u} + \nabla \cdot [(\frac{\mu}{Pr_k}) \nabla k] - \rho\epsilon + \dot{W}^s, \tag{3.1.6}$$

where $\dot{W}^s$ is the source term due to turbulent eddies dispersing the spray droplets.

Turbulent kinetic energy dissipation:

$$\frac{\partial(\rho \epsilon)}{\partial l} + \nabla \cdot (\rho \mathbf{u} \epsilon) = \nabla \cdot [(\frac{\mu}{Pr_\epsilon}) \nabla \epsilon] + \frac{\epsilon}{k} [c_{\epsilon_1} \boldsymbol{\sigma} : \nabla \mathbf{u} - c_{\epsilon_2} \rho\epsilon + c_s \dot{W}^s]. \tag{3.1.7}$$

Heat flux:

$$\mathbf{J} = -\kappa\nabla T - \rho D \sum_m h_m \nabla(\rho_m/\rho). \tag{3.1.8}$$

Equations of state:

$$p = R_0 T \sum_m (\rho_m/W_m) \tag{3.1.9}$$

$$\iota(T) = \sum_m (\rho_m/\rho)\iota_m(T) \tag{3.1.10}$$

$$c_p(T) = \sum_m (\rho_m/\rho)c_{p,m}(T) \tag{3.1.11}$$

$$h_m(T) = \iota_m(T) + R_0 T/W_m, \tag{3.1.12}$$

where T is the fluid temperature, h_m is the specific enthalpy of the species m, R_0 is the universal gas constant, W_m is the molecular weight of species m, $c_{p,m}(T)$ is the specific heat at constant pressure of species m, and $h_m(T)$ is the specific enthalpy of species m.

The Newtonian viscous stress tensor $\bar{\sigma}$ is:

$$\bar{\sigma} = \mu[\nabla\mathbf{u} + (\nabla\mathbf{u})^{\mathrm{T}}] + \lambda\nabla\cdot\mathbf{u}\bar{\mathbf{I}}, \tag{3.1.13}$$

where μ and λ are first and second viscosity coefficients, $\bar{\mathbf{I}}$ is the unit tensor, and superscript T is the transpose sign.

3.1.1 Source terms

Due to fuel injection and chemical reactions in IC engines, there are source terms for the equations of mass, momentum, energy, kinetic energy, and kinetic energy dissipation.

Injection source term

Due to the complexity of fuel injection and lack of full understanding of the process, the injection source terms are usually obtained using droplet probability distribution function f. The exchange function $\dot{\rho}^s$, $\mathbf{O}^s$, $\dot{Q}^s$, and $\dot{W}^s$ are obtained by summing the rate of change of mass, momentum, and energy of all droplets at position $\mathbf{x}$ and time t:

$$\dot{\rho}^s = -\int f\rho_d 4\pi r^2 R d\mathbf{v}\ dr\ dT_d\ dy\ d\dot{y}, \tag{3.1.14}$$

$$\dot{\mathbf{O}}^s = -\int f\rho_d (4/3)\pi r^3 \mathbf{F}' + 4\pi r^2 R\mathbf{v}) d\mathbf{v}\ dr\ dT_d\ dy\ d\dot{y}, \tag{3.1.15}$$

$$\begin{aligned}\dot{Q}^s = &-\int f\rho_d \{4\pi r^2 R[\iota_l(T_d) + \frac{1}{2}(\mathbf{v}-\mathbf{u})^2] \\ &+ 4/3\pi r^3 [c_l \dot{T}_d + \mathbf{F}'\cdot(\mathbf{v}-\mathbf{u}-\mathbf{u}')]\} d\mathbf{v}\ dr\ dT_d\ dy\ d\dot{y},\end{aligned} \tag{3.1.16}$$

$$\dot{W}^s = -\int f\rho_d 4/3\pi r^3 \mathbf{F}'\cdot\mathbf{u}' d\mathbf{v}\ dr\ dT_d\ dy\ d\dot{y}, \tag{3.1.17}$$

where $\mathbf{F}' = \mathbf{F} - \mathbf{g}$.

Chemical reaction source terms

Consider elementary chemical reactions involving species χ_m:

$$\sum_{m=1}^{N_c} \nu'_{m,r}\chi_m \Leftrightarrow \sum_{m=1}^{N_c} \nu''_{m,r}\chi_m \qquad (r = 1, ..., N_r), \tag{3.1.18}$$

where $\nu'_{m,r}$ and $\nu''_{m,r}$ are stoichiometric coefficients of species m in reaction r, N_r is total number of the considered reactions.

The mass density source term for species m due to chemical reaction takes the form:

$$\dot{\rho}^c_m = W_m \dot{\omega}_m. \tag{3.1.19}$$

The chemical heat release source term are given by:

$$\dot{Q}^c = \sum_m \dot{\omega}_m (\Delta h^0_f)_m, \tag{3.1.20}$$

where $(\Delta h_f^0)_m$ is the heat of formation of species m at $T = 0$.

Production rate of species m, $\dot{\omega}_m$ in equation (3.1.19 and 3.1.20) is written as:

$$\dot{\omega}_m = \sum_{r=1}^{N_r} (\nu''_{m,r} - \nu'_{m,r})(k_{f,r} \prod_{m=1}^{N_c} [X_m]^{\nu'_{m,r}} - k_{b,r} \prod_{m=1}^{N_c} [X_m]^{\nu''_{m,r}}), \tag{3.1.21}$$

where X_m is the molar concentration of species m.

The forward and backward rate coefficients of reaction r, $k_{f,r}, k_{b,r}$, are calculated by Arrhenius law [30]:

$$k_{f,r} = A_r T^{\beta_r} exp(\frac{-E_r}{\mathcal{R}T}). \tag{3.1.22}$$

3.2 Solution of the governing equations

In the (11+N_c) governing equations from (3.1.1) to (3.1.12), there are (10+N_c) unknowns: ρ, $\mathbf{u} = (u, v, w)$, ι, k, ϵ, $\mathbf{J}$, p, T, $\rho_1, ..., \rho_{N_c}$. Because one of the mass equations is redundant due to the consistency equation, the system consists of (10+N_c) independent equations. With the source terms described in section 3.1.1, the equation system is closed. However, solving directly and simultaneously this system including the source terms is computationally intensive, since the system is very stiff, and there is a large number of involved chemical species. The most common way to avoid this difficulty is to reduce the number of involved species and to use a splitting scheme, in which each component of the equations in the system is resolved separately, then recoupled together. The chemical source terms and the physical processes have different eigenvalues. Both coupling the two different eigenvalues and reducing the number of involved species cause errors, especially in emissions prediction. Many authors have proposed different approaches to resolve this equation system and associated numerical difficulties. A literature review of proposed approaches developed by other authors is presented in chapter 4.

Due to the lack of an analytical solution for the problem, an accurate solution of the system is still being sought. A novel method named pre-integrated non-equilibrium combustion response mapping approach to solve this equation system is introduced in chapter 6. In the pre-integrated approach, a splitting scheme is used; diffusion, convection, and source terms are computed separately; then integrated together. However, the chemical source term is calculated in advance, decoupled from chemical eigenvalue, and integrated in physical timescale, then stored in a database file. The source term in the database file is introduced to the equation system when needed. Details of thermal dynamics, fluid dynamics, and chemical reaction modeling used in the pre-integrated approach are described in chapter 5.

Chapter 4

Review of numerical methods to solve the governing equations in IC engines

Operation of IC engines involves fuel atomization, thermal dynamics, fluid dynamics, and chemical reaction processes. Each of these processes is a very complex problem itself. Thus, simulating the operation of IC engines and predicting emissions are very difficult tasks for research scientists. To do this, many authors have developed various approaches to resolve the equation system introduced in chapter 3. These approaches to simulate reactive flow in IC engines are reviewed in this chapter.

At the lowest level of complexity are zero-dimensional models, in which the engine operation is modelled without accounting for the effects of engine geometry. The next level of modeling are multi-dimensional turbulence models that solve the Reynolds-averaged Navier-Stokes (RANS) equations for the time-mean field variables, and these values are used directly to resolve for the time-mean reaction rates. The third level is large eddy simulation (LES), where the large scales of the turbulent flow field are resolved explicitly, while the small scales are modelled. The highest level of modeling is direct numerical simulations (DNS), where the equation system is solved directly

on a fine grid and the instantaneous, small-scale structure of the flame is resolved.

4.1 Zero-dimensional models

In the zero-dimensional models, geometry of the cylinder chamber is not taken into account in the calculation, only scalar variables (fraction of fuel burnt, temperature, pressure, etc.) are computed as functions of time. This method was developed at different levels described in the following.

4.1.1 Empirical equation models

In the first attempt to model combustion in IC engines, empirical heat release models were employed by Heywood et al. [11], Hires et al. [12], and Wu et al. [13], in which time is the only independent variable. These combustion models make use of the three zones: 1) unburned gas, 2) burned gas, and 3) burned gas adjacent to the combustion chamber. The burned gas and unburned gas zones are separated by the flame front. Each zone, burned or unburned, is completely and instantaneously mixed (uniform in temperature, pressure, and composition). The combustion is calculated based on the propagation speed of the flame front. Heat transfer is predicted using the Woschni method [31]. The concentrations of carbon oxides and unburned hydrocarbon are calculated using equilibrium thermodynamics. The nitric oxide emissions are calculated using the extended Zeldovich mechanism [30]. The fraction of fuel burnt is obtained from an empirical formulation:

$$Y_1 = 1 - exp\{-c_1[(\theta - \theta_0)/\Delta\theta_{bn}]c_2 + 1\}, \tag{4.1.1}$$

where Y_1 is the mass fraction of fuel burnt at crank angle θ, θ_0 is the crank angle at the start of combustion, $\Delta\theta_{bn}$ is the duration of combustion, c_1 and c_2 are empirical

constants.

4.1.2 Single-zone models

The main part of the single-zone models is to use detailed chemical kinetics modeling programs to calculate combustion of air/fuel mixture. The engine cylinder is assumed to be a homogeneous volume (temperature, pressure, and composition are uniformly distributed over the considered volume) during the combustion process. Modeling starts from the beginning of ignition to the end of combustion. To calculate combustion of air/fuel mixture, many chemical kinetics modeling packages have been used, such as HCT [32] by Flowers et al. [33], and SENKIN [34] in the work of Ogink and Golovitchev [14]. The state of fluid in the cylinder chamber at the beginning of combustion is specified using different methods, such as the two-step scheme in the work of Ogink and Golovitchev [14], while Christensen et al. [35] used measured data from experiments. In the two-step scheme, AVL BOOST [36], a CFD code, was used to model the engine operation from the beginning of compression stroke to the start of ignition in the first step. The resulted data of this step were used to calculate air/fuel mixture combustion in the second step.

In the single-zone models heat transfer between the mixture and the cylinder walls is computed using the Woschni method [31]. The instantaneous total volume of the cylinder chamber is obtained from the piston-slide equation:

$$V_{total} = V_{clr} + \frac{\pi B^2}{4}(l_o + a - s), \tag{4.1.2}$$

where V_{clr} is the clearance volume, B is the bore diameter, l_o is the connecting rod length, and a is the crankshaft radius. The distance between the crankshaft axis and

the piston pin axis, s, is calculated from:

$$s = a\ cos(\theta) + (l_o^2 - a^2\ sin^2\theta)^{1/2}, \tag{4.1.3}$$

where θ is crank angle.

4.1.3 Multi-zone models

Multi-zone approach is an improved version of the two-step scheme of the single-zone method. In the multi-zone approach, operation of IC engines is modelled in two parts: physical and chemical. In the first part, a multi-dimensional CFD program is used to simulate the physical processes of the fluid in the cylinder chamber during compression stroke and up to the moment of ignition. During this phase, no chemical reaction is calculated. At the end of the first step, in-cylinder distributions of temperature, pressure, and composition of the mixture are specified. With the calculated temperature, pressure, and composition results of the first step, the cylinder chamber is divided into some typical zones: 1) constant volume zone representing crevices; 2) zone representing the thermal boundary layer; and 3) core zones. Each zone is assumed to be homogeneous and has different temperature and composition, but all the zones have the same pressure. There is no specified location of zones. The mass in each zone is conserved and there is no mixing, no diffusion, and no heat transfer between zones.

In the second part of the simulation, chemical reaction of air/fuel mixture in each zone is separately calculated from the start of ignition to the end of combustion stroke with volume as a specified function of crank angle. The total volume of the cylinder chamber varies as a function of crank angle using the piston-slide equation (4.1.2). The volume of each zone is computed based on the volume of the cylinder chamber

and the equation of state. This step is pure calculation of chemical reaction of air/fuel mixture plus change of volume due to motion of the piston, no fluid dynamic processes of the gas are computed.

Among multi-zone models, KIVA-3 [37] is widely used to model the physical processes in the first step (Aceves et al. [16, 38], Easley et al. [39], Shenghua et al. [40], and Flowers et al. [41]), while SENKIN, a subprogram in the CHEMKIN [34, 42, 1] package, is preferred for chemical kinetics calculations.

Comments

In the empirical equation approach, empirical equations are used to model the complex fluid dynamics and the combustion processes in IC engines. The effects of engine geometry on engine performance and emissions are ignored. This causes unacceptable errors in predicting emissions. Thus, this method is normally used only for parametric studies.

The single-zone models with the assumption that the cylinder chamber is a homogeneous volume, and using the two-step scheme, are simple and computationally effective. The advantage the single-zone approach is they can easily use detailed chemical kinetics to calculate combustion of air/fuel mixture. However, the assumption that the cylinder chamber is a homogeneous volume introduces errors in the simulation, because the gas composition and temperature in the combustion chamber are significantly different form location to location. The single-zone models overpredict peak pressure and NO_x, underpredict burning duration, and are unable to predict HC and CO [16].

The multi-zone approach reduces errors from the homogeneous assumption in the single-zone approach by dividing the cylinder chamber into zones. The number of

zones is a compromise between computer time and accuracy. This approach tries to simulate the real phenomenon in the combustion process by distributing different temperature and composition profiles in each zone. The disadvantage of this approach is that the zones are isolated from each other, there are no exchange processes modelled between these zones. The multi-zone models predict reasonably CO and HC but overpredict NO_x.

In the zero-dimensional approach, operation of IC engines is modelled without including the effects of engine geometry. This could lead to significant errors in predicted engine performance, and especially in emissions prediction.

4.2 Reynolds-averaged-Navier-Stokes equation approaches

Simulation of the operation of IC engines involves solving the Navier-Stokes equation system for air/fuel mixture in the engine cylinder. However, it is too expensive to resolve this equation system. Therefore, to save computer time an alternative equation system named Reynolds-averaged Navier-Stokes (RANS) equations was developed for mean values of the flow. Thus, the modeling task is to solve the RANS equations. The RANS equations are derived from the Navier-Stokes equations using time- and Farve-averaging. With the absence of the spray term, the RANS equations can be written as follows.

The conservation of total mass is:

$$\frac{\partial \overline{\rho}}{\partial t} + \nabla \cdot (\overline{\rho}\widetilde{\mathbf{u}}) = 0. \tag{4.2.1}$$

The conservation of species masses:

$$\frac{\partial(\overline{\rho}\widetilde{Y}_m)}{\partial t} + \nabla \cdot (\overline{\rho}\widetilde{\mathbf{u}}\widetilde{Y}_m) + \nabla \cdot (-\overline{\rho D_m \nabla Y_m} + \overline{\rho \mathbf{u}'' Y_m''}) = \overline{M_m \dot{\omega}_m}. \tag{4.2.2}$$

The equation of momentum conservation is of the form:

$$\frac{\partial(\overline{\rho}\widetilde{\mathbf{u}})}{\partial t} + \nabla \cdot (\overline{\rho}\widetilde{\mathbf{u}}\widetilde{\mathbf{u}}) + \nabla \cdot (\overline{\mathbf{\Pi}} + \overline{\rho \mathbf{u}''\mathbf{u}''}) = \overline{\rho}\mathbf{g}. \tag{4.2.3}$$

The equation of conservation of specific internal energy is written as:

$$\frac{\partial(\overline{\rho}\widetilde{\imath})}{\partial t} + \nabla \cdot (\overline{\rho}\widetilde{\mathbf{u}}\widetilde{\imath}) + \nabla \cdot (-\overline{\kappa \nabla T} + \overline{\rho \mathbf{u}'' \imath''}) = \overline{q}. \tag{4.2.4}$$

The equation of state is averaged as:

$$\overline{p} = \overline{\rho} R_0 \widetilde{T} / \overline{M}, \tag{4.2.5}$$

where $\overline{M}$ denotes the averaged mean molar mass of the mixture.

In the equations (4.2.1-4.2.5), Y_m is mass fraction of species m, the over-line and the over-tilde denote mean value of time- and Farve-averaging, prime ($'$) and double prime ($''$) are used for fluctuation of the time- and Farve-averaging, respectively; $\dot{\omega}_m$ and q are production rate of species m and heat release due to chemical reaction, respectively, and $\overline{\mathbf{\Pi}}$ is the stress tensor. The RANS equation system is closed if the Reynolds stresses $\overline{\rho \mathbf{u}'' G''}$ and source terms $\overline{\omega}_m$ and $\overline{q}$ are known.

The Reynolds stresses are normally modelled using a gradient-transport assumption which states that the Reynolds stress is proportional to the gradient of the mean value of the property,

$$\overline{\rho \mathbf{u}'' G''} = -\overline{\rho} \nu_T \nabla \widetilde{G}, \tag{4.2.6}$$

where ν_T is turbulent exchange coefficient, and G is an arbitrary variable.

Many models have been postulated for the turbulent exchange coefficient. Among these models, k-ϵ turbulence model is widely used [43, 44]. In the k-ϵ turbulence model, two differential equations for turbulent kinetic energy k and its dissipation rate ϵ are added into the RANS equation system. Modifications of the k-ϵ model

introduced by Hanjalic et al. [45], which include multiple-timescale effects and non-isotropic effects, are also used.

In IC engines the combustion process takes place in a turbulent environment, where all of the dependent variables fluctuate rapidly with time and position as a result of the turbulence, and chemical reaction is nonlinearly dependent on temperature. Because of these reasons, the most difficult task in resolving the RANS equations is to specify the chemical source terms $\overline{\dot{\omega}}_m$ and $\overline{q}$. Several turbulence combustion models are reported for predicting chemical reaction source terms to supply closure for the RANS equation system, including Eddy-Breakup-Model (EBM) [46], laminar flamelet models [47, 48, 49], assumed PDF method [50, 51], linear eddy model (LEM) [52, 53, 54], conditional moment closure (CMC) [55, 56, 57], and Monte Carlo PDF methods [58, 59, 60]. These models are outlined as follows.

4.2.1 Eddy-Break-up Models

Eddy-Break-up models (EBM) are empirical models first introduced by Spalding [61] for the case of fast chemistry. In this case, the reaction rate is governed by the rate of turbulent dissipation. The reaction zone is described as a mixture of unburned and burned regions. Similar to the decay of turbulent energy, a formulation by Spalding [62] describes the rate which governs the breakup of domain of unburned gas into smaller fragments. These fragments are in sufficient contact with already burned gases, thus are at sufficiently high temperature, and react. The combustion is assumed to occur at the small scales, where mixing occurs on a molecular level; the reaction rate is assumed to be proportional to the inverse of the turbulence timescale k/ϵ:

$$\overline{\dot{\omega}}_m = -\frac{\overline{\rho} C_{EBU}}{\overline{M}} \frac{\widetilde{\epsilon}}{\widetilde{k}} \sqrt{Y_m''^2}, \tag{4.2.7}$$

where C_{EBU} is a constant, and $\overline{Y_m''}$ is the variance of mass fraction of species m.

There are some modified versions of EBM [46, 63]. Magnussen and Hjertager [64] developed an Eddy dissipation concept (EDC) model, in which reaction is not allowed to occur unless both the fuel and oxidizer mix on the molecular level at sufficiently high temperatures. The main idea of EBM and its modifications is to replace the chemical timescale of an assumed one-step reaction by the turbulent timescale $t_{turb} = k/\epsilon$. Thereby the model eliminates the influence of chemical kinetics, representing the fast chemistry limit only.

4.2.2 Probability density function methods

In the probability density function (PDF) method, the mean chemical reaction rate is obtained using the statistical approach. If the PDF is known, the mean chemical reaction rate can be determined by integration. Bilger [50] proposed the mean reaction rate can be calculated from:

$$\overline{\dot{\omega}} = \int_0^1 ... \int_0^1 \int_0^\infty \int_0^\infty \dot{\omega}_m f(\rho, T, Y_1, ..., Y_{N_e-1}; \mathbf{x}) d\rho dT dY_1 ... dY_{N_e-1}, \qquad (4.2.8)$$

where f is PDF of reaction rate. Different methods have been applied to obtain the PDF f ranged from empirical construction of PDF to solving the PDF transport equation.

Assumed PDF methods

In the assumed PDF method, the chemistry is determined by one or more "progress variables" which are allowed to fluctuate; the PDF f is constructed using empirical knowledge about the shape. Several forms of PDF f have been used including beta functions (Rhodes et al. [65], Kolbe and Kollmann [66]), Gaussians, and clipped

Gaussians (Lockwood and Naguib [67]). Multidimensional PDF is also used to model the chemical reaction rate. Gutheil and Bockhorn [68] proposed that the multidimensional PDF can be computed from one-dimensional PDF with the assumptions that mixture fraction and reaction progress variables are statistically independent. Thus, the joint PDF is separable and the integration for each variable can be performed independently as:

$$f(\rho, T, Y_1, ..., Y_{N_s-1}) = f(\rho) \times f(T) \times f(Y_1) ... \times f(Y_{N_s-1}). \tag{4.2.9}$$

A "fast chemistry" assumption, where the instantaneous properties of the gas are in equilibrium and can be calculated from the mixture fraction, is usually applied in the assumed PDF. The disadvantage of the assumed PDF is that application to multiple-step chemistry is awkward because of the assumption of statistical independence for each additional reaction variable, and the significant increase in the required computational effort.

PDF transport equation models

In the PDF transport equation models, the PDF f is obtained by solving the PDF transport equation and usually formulated for one-point statistics; joint probabilities between the scalar field at multiple locations or for multiple times are not included. A transport equation for the time behavior of the PDF is derived from the conservation equations for the masses of species (Pope [69], O'Brien [51]). The PDF transport equation methods are capable of incorporating complex chemistry and accurately modeling the interactions of chemistry and turbulence. The PDF transport equation can be solved by conventional finite-difference and finite-volume techniques, but

Pope [69] argued that these methods are very computationally intensive for multidimensional problems because the memory requirements increase roughly exponentially with dimensionality. Pope [70] suggested that the PDF f can be computed by Monte Carlo methods using a large number of fluid particles to represent the statistics of the turbulent flow field. The memory requirements of Monte Carlo PDF methods depend only linearly on the dimensionality of the problem. The main advantage of these methods is the fact that the chemistry is treated exactly and no modeling of the reaction rates is required. The drawback of these methods is that the molecular transport still needs to be modelled. Approaches have been proposed for this requirement such as Curl's models by Curl [71] and Dopazo [72], interaction-by-exchange-with-the-mean (IEM) model by Mayeer and O'Brien [73] and Borghi [74]. Curl's and IEM models consider only the turbulence dissipation timescale, ignoring the detailed effects of flame structure. Monte Carlo PDF methods have been developed to different levels such as composition PDF (Dopazo [75], Pope [69]), velocity-composition PDF (Brewster et al. [76], Correa and Pope [77], and Haworth and Tahry [78]), and velocity-composition-dissipation PDF (Anand et al. [79], Pope and Chen [80]). The main drawback of the Monte Carlo PDF methods is that they suffer from a statistical error that decreases only slowly with the number of particles N_{pc} per cell: The error is proportional to $1/\sqrt{N_{pc}}$. Brewster et al. [76] have shown that these methods are computationally expensive compared to assumed PDF methods, and are only feasible for reduced chemistry mechanisms.

4.2.3 Laminar flamelet models

The laminar flamelet models are based on the assumption that a turbulent diffusion flame is an assembly of stretched laminar flamelets. Flamelets are thin reactive-diffusive layers embedded within a nonreacting turbulent flow field. Once ignition has taken place, chemistry accelerates as the temperature increases. When temperature reaches values that are in the vicinity of the closed-to-equilibrium branch, the reactions that determine fuel consumption become very fast. Since the chemical timescale of this reaction is short, chemistry is most active within a thin layer (inner layer). If this layer is thin compared to the size of a Kolmogorov eddy, it is embedded within the quasi-laminar flow field of such an eddy and the assumption of the laminar flamelet structure is justified. If, on contrary, turbulence is so intense that Kolmogorov eddies become smaller than the inner layer and can penetrate into it, they are able to destroy its structure. Under this condition, the entire flame is likely to extinguish. Flamelet equations were derived by Peters [81], in which the mixture fraction was an independent variable, and the scalar dissipation rate was used for the mixing process. The laminar flamelet models are relatively simple and can be used with complex chemistry, but they assume that the chemical reactions are all fast and that their length scales are smaller than the smallest (i.e. Kolmogorov) turbulence length scale. Since the reaction timescales (and the corresponding length scales) in IC engine combustion vary over as much as seven orders of magnitude [22], some reactions are clearly in the flamelet regime, some are in the distributed reaction regime, and some are in between [82, 83]. Therefore, the flamelet approach is not sufficiently general to treat all of the reactions of interest in IC engine combustion and their interactions with turbulence.

4.2.4 Linear Eddy Models

In 1988 Kerstein [84, 85] developed a linear-eddy model (LEM) for nonequilibrium chemical reaction rate. The LEM approach model presents the scalar field statistics to one dimension and resolves all length scales (from integral to Kolmogorov). The model treats the turbulent mixing as two concurrent processes: 1) turbulent stirring and 2) molecular diffusion. The non-local nature of the stirring process requires a stochastic simulation. First, the scalar field is represented by a one-dimensional array, each entry representing a fluid element. Then the turbulent stirring process is modelled by a stochastic process consisting of random, instantaneous rearrangements of the fluid elements. Each event involves spatial redistribution of the scalar field within a specified segment of the spatial domain. There are two parameters that govern each event: the eddy size and the location within one-dimensional domain. The eddy size is obtained randomly from a PDF of eddy sizes that is modelled using inertial range scaling. The location within the one-dimensional domain is chosen randomly from a uniform distribution. The molecular diffusion process is calculated by Fick's diffusion law. Both turbulent stirring and molecular diffusion processes are computed at the smallest scale of fluid-property variations on physical space, thus making this method computationally expensive. LEM remains in the early stages of development and is not yet considered a viable option for a comprehensive, three-dimensional combustion models.

4.2.5 Conditional moment closure methods

Conditional-moment-closure (CMC) has been independently developed by Klimenko [86] and Bilger [55]. In the CMC method, species mass fractions and enthalpy are

conditionally averaged over a fluctuating progress variable to account for the effects of turbulent fluctuations on the mean reaction rate. Bilger [87] suggested that the mixture fraction or reaction progress variable can be used as the conditioning variable. The method adopts the assumption that the fluctuations about the conditional mean are small, thus limiting the range of application to flames that are far from extinction. Smith et al. [57] pointed out that the shape of the PDF of the conditioning variable must be assumed in the CMC approach. Conditioning on both the mixture fraction and a reaction progress variable has been proposed by Swaminathan and Bilger [88] as a means of extending the range of application to near extinction, but the results of this approach are not yet available. CMC is a promising approach, particularly when the effects of detailed chemistry (e.g. full mechanisms) must be considered. The main advantage is that detailed chemistry can be accounted for at low computational cost; the computational workload associated with CMC is considerably less than PDF methods. However, it is not yet sufficiently generalized for practical application in IC engines.

4.3 Large eddy simulation methods

At the third level of complexity are large eddy simulation (LES) methods. LES has been developed during the past three decades, with significant progress (Germano et al. [89] and Pope [90]). In LES, the large energy containing motion caused by the large eddies is simulated directly by solving the instantaneous Navier-Stokes equations on a coarse mesh (as in a DNS). Ghosal and Moin [91] suggest that LES equations can be obtained by filtering the Navier-Stokes equations to remove the direct effect of small scale fluctuations. Modeling is applied to represent the smaller unsolved scales

(subgrid), which contain only a small fraction of the turbulent kinetic energy. This is consistent with scaling analysis by Kolmogorov [92], which states that the large eddies contain most of kinetic energy while the smaller scales are responsible for the dissipation of energy.

Several methods have been used to model the turbulent combustion in subgrid scales for LES. Rydén et al. [93] developed a subgrid combustion model based on the EDC method. Gao and OBrien [94], Cook and Riley [95] have used subgrid models based on PDF methods. A break through in subgrid model is the introduction of a method called dynamic modeling by Germano et al. [89]. In the dynamic subgrid-scale model, a test filter $\widehat{\Delta}$ is introduced in addition to the grid filter Δ. The dynamic model was extended by Moin et al. [96] to scalar transport to determine the subgrid scale turbulent Prandtl number. Because of advantage of LEM in resolving the fine scales where mixing and reaction take place, LES with sub-grid closure based on LEM is commonly used.

Recently Dahm et al. [97] proposed a local integral moment (LIM) model, which is a type of LES model, in that the large scales of the turbulent flow are computed explicitly. However, it uses a Lagrangian approach where the Navier-Stokes equations are transformed to a set of ordinary differential equations through a local parabolization around a time-evolving material surface on which the scalar gradients are concentrated. The parabolization is based on the observation that molecular mixing processes in turbulent flows are concentrated on universal, self-similar structures. The chemical species fields are obtained from the scalar field constructed from the integral moments on the time-evolving surface via a strained diffusion and reaction layer formulation. The method is economical and has produced accurate calculations

of complex flows with complex chemistry.

4.3.1 Reduced chemical reaction mechanism

Prediction of emissions of IC engines requires detailed chemical kinetics reaction of air/fuel mixture. Kong et al. [98] have proposed to couple directly chemical kinetics into fluid dynamics for emissions prediction. However, to integrate directly a detailed reaction mechanism into LES is impractical since chemical kinetics by itself is very computationally intensive. Thus, Kong et al. limit the reaction mechanism at a simple level. At the present time, use of chemical kinetics reaction is still at reduced reaction mechanisms. Although many authors have been trying to create proper reduced reaction mechanisms for emissions predictions (Cannon et al. [99], Griffiths [100], Li and Williams [101], and Glaude et al. [102]), use of a detailed chemical kinetics reaction mechanism to improve accuracy of emissions prediction is still in demand.

4.4 Direct Numerical Simulation method

The most obvious and straight-forward method to resolve a Navier-Stokes equation system is to compute the spatial-temporal evolution of the full range of time and length scales using direct numerical simulations (McMurtry and Queiroz [103], Rogallo and Moin [104]). DNS is highly accurate, and in some situations, can even predict errors in experimental measurements. The drawback of DNS is that it is very computationally intensive. Use of DNS is still strictly applicable only for fundamental physical phenomena in idealized flow within low Reynolds numbers. The application of DNS in high Reynolds number flows is limited since the grid resolution

requirement is proportional to Reynolds number: $Re^{9/4}$ (Fox [105]). The main role of DNS is a research tool to provide fundamental insight into turbulent flows and to help in developing improved statistical submodels, such as the LEM, for modeling the operation of the engine. The DNS is considered as a tool for the future; it is not currently applicable to the computation of IC engine processes.

4.5 Summary

The are several approaches applied to resolve the Navier-Stokes equation system for modeling operation of IC engines and predicting their emissions. They can be classified as four main groups: 1) the non-dimensional, 2) the Reynolds-averaged Navier-Stokes equations, 3) the large-eddy simulation, and 4) the direct numerical simulation. In the non-dimensional methods, the effects of engine geometry are not included in calculation. This could lead to errors in predicting engine performance, especially in formation of emissions.

In RANS equation approaches the simulation is based on a statistical averaging to solve only the mean flow. This implies that modeling concerns the whole spectrum of scales, which in turn makes the accuracy of RANS simulations dependent on the quality of the models used. Statistical averaging also extremely complicates addressing unsteady phenomena. The attractive feature of RANS modeling is that it is computationally effective, since only the mean flow is computed. However, this efficiency comes at a serious cost in terms of approximation of the physics since a single time and a single length scale are used to approximately represent all the turbulent scales. Thus, RANS turbulence models cannot resolve the dynamics of turbulence, which is highly unsteady, and also the effect of the large scales, which is highly geometry

dependent. Therefore, it has become apparent in many studies that RANS is not appropriate to simulate unsteady mixing process even in very simple configurations of IC engines.

LES is a compromise between RANS and DNS. In LES, the large, energy containing scales of motion are simulated numerically, while the small, unresolved subgrid scales and their interactions with the large scales are modelled. The large scales, which usually control the behavior and statistical properties of a turbulent flow, tend to be geometry and flow dependent, whereas the small scales tend to be more universal and consequently easier to model. LES computes resolved motion explicitly in a time- and space-accurate manner, and it requires relatively higher grid resolution when compared to RANS to obtain accurate results. This makes LES become more computationally expensive than RANS. Because it is less expensive than the detailed reaction mechanism, reduced reaction mechanisms are commonly used for emissions predictions with LES. However, the simple mechanism reduces the accuracy of predicted results, so there is still a requirement for using detailed chemical kinetics reaction for chemical processes in IC engines.

DNS is the most accurate method to calculate the complex processes in IC engines. However, it is too expensive so that at the present time, DNS is used as a calibrator for other calculating tools.

In order to resolve the equation system presented in chapter 3 with detailed chemical kinetics reaction mechanisms for engine modeling, the pre-integrated approach is developed. Because of its accurate and affordable features, LES is used in the pre-integrated approach to predict fluid dynamics performance. The alternative way avoid the chemical computational intensity of detailed chemical kinetics reaction while

preserving its accuracy is to pre-integrate reaction data in a database then retrieve results when needed. Details of this new approach are presented in chapter 6.

Chapter 5

Modeling codes

This chapter describes two modeling codes: KIVA-3V and SENKIN, used in the pre-integrated approach to predict emissions in IC engines. The overview, application, and calculating algorithm of KIVA-3V, including computational mesh, computations of diffusion and convection in gas-phase, droplet injection, and boundary conditions, are presented. Applications, calculating algorithm, input and output of SENKIN to calculate detailed chemical kinetics reaction are also described.

5.1 KIVA-3V

5.1.1 Applications of KIVA-3V

KIVA-3V is a CFD code developed by Amsden et al. [106] in Los Alamos Laboratory. The code has the ability to calculate flows in engine cylinders with arbitrarily shaped piston, cylinder head, and valves. It can also compute three-dimensional dynamics of evaporating fuel sprays interacting with flowing multi-component gases including the effects of turbulence and wall heat transfer. The KIVA-3V code was built in modular structure; the major parts of fluid dynamics calculation such as fuel injection, breakup, collision, and coalescence of droplets, chemical reactions are constructed in

modules. The activation of the modules is controlled using input parameters in an input file. This makes the code applicable to a wide variety of applications in fluid dynamics, with or without chemical reactions and sprays.

KIVA-3V uses arbitrarily shaped cells mesh and an arbitrary Lagrangian-Eulerian formulation to compute zones to follow the piston and valve motions. KIVA-3V is a LES program, in which the Navier-Stokes equations are solved for the large scales (cell mesh) whereas the turbulence of smaller scales is calculated using a subgrid scale model. The subgrid scale model uses a transport equation for turbulent kinetic energy and a law-of-the-wall treatment for turbulent boundary layers. In the spray dynamics model, a statistical representation is used to describe the spectrum of droplet sizes, the effects of evaporation, and collision and coalescence of the droplets. A partially implicit finite difference formulation and acoustic subcycling method are used to efficiently treat the acoustic terms for low Mach number flows. The chemistry was generalized to include both kinetic and equilibrium reactions. Chemical reactions are calculated using Arrhenius kinetics with an arbitrary number of reactions and by default includes 12 species (fuel, O_2, N_2, CO_2, H_2O, H, H_2, O, N, CO, NO) in the chemical reaction calculations.

5.1.2 Equation system and calculation strategy

Equation system

KIVA-3V solves the system of unsteady equations (3.1.1-3.1.12) of a turbulent, chemically reactive mixture of ideal-gases, and couples them to the equations for a single-component vaporizing fuel spray. To enhance computational efficiency in low Mach number flows, where the pressure is nearly uniform, a dimensionless quantity α is introduced in the conservation equation of momentum (3.1.4) and internal energy

Constant	Value	Constant	Value
c_{ϵ_1}	1.44	Pr_k	1.00
c_{ϵ_2}	1.92	Pr_ϵ	1.30
c_{ϵ_3}	-1.00	c_s	1.50

Table 5.1: Constants in transport equations of turbulent kinetic energy and its dissipation rate

(3.1.5). This dimensionless quantity (α) is used in conjunction with the Pressure Gradient Scaling (PGS) method developed by Ramshaw et al. [107]. With the introduction of α, the conservation equations of momentum and internal energy become:

$$\frac{\partial(\rho\mathbf{u})}{\partial t} + \nabla\cdot(\rho\mathbf{u}\mathbf{u}) = -\frac{1}{\alpha^2}\nabla p - A_0\nabla(2/3\rho k) + \nabla\cdot\bar{\bar{\sigma}} + \mathbf{O}^s + \rho\mathbf{g}, \tag{5.1.1}$$

$$\frac{\partial(\rho\iota)}{\partial t} + \nabla\cdot(\rho\mathbf{u}\iota) = -p\nabla\cdot\mathbf{u} + (1-A_0)\bar{\bar{\sigma}}:\nabla\mathbf{u} - \nabla\cdot\mathbf{J} + A_0\rho\epsilon + \dot{Q}^c + \dot{Q}^s. \tag{5.1.2}$$

In the case of $\alpha \equiv 1$, the PGS is deactivated. In equation (5.1.1), the quantity A_0 is zero in laminar calculations and unity when one of the turbulence models is used.

The effect of velocity dilation is added in the equations of turbulent kinetic energy (3.1.6) and its dissipation rate (3.1.7). Thus, these equations become:

$$\frac{\partial(\rho k)}{\partial t} + \nabla\cdot(\rho\mathbf{u}k) = -\frac{2}{3}\rho k\nabla\cdot\mathbf{u} + \bar{\bar{\sigma}}:\nabla\mathbf{u} + \nabla\cdot[(\frac{\mu}{Pr_k})\nabla k] - \rho\epsilon + \dot{W}^s, \tag{5.1.3}$$

$$\frac{\partial(\rho\epsilon)}{\partial t} + \nabla\cdot(\rho\mathbf{u}\epsilon) = -(\frac{2}{3}c_{\epsilon_1} - c_{\epsilon_3})\rho\epsilon\nabla\cdot\mathbf{u} + \nabla\cdot[(\frac{\mu}{Pr_\epsilon})\nabla\epsilon] + \frac{\epsilon}{k}[c_{\epsilon_1}\bar{\bar{\sigma}}:\nabla\mathbf{u} - c_{\epsilon_2}\rho\epsilon + c_s\dot{W}^s], \tag{5.1.4}$$

where $c_{\epsilon_1}, c_{\epsilon_2}, c_{\epsilon_3}, Pr_\epsilon$, and Pr_k are constants whose values are determined from experiments and theoretical considerations. The values of these constants are shown in table 5.1. In the state relation equations (3.1.11) and (3.1.12), the values of specific heat at constant pressure $c_{p,m}$ and specific enthalpy h_m of species m are taken from

the JANAF table [108]. The transport coefficients are computed as:

$$\begin{aligned} \mu &= (1.0 - A_0)\rho c_0 + \mu_{air} + A_0 c_\mu k^2/\epsilon \\ \lambda &= A_3 \mu \\ \kappa &= \frac{\mu c_p}{Pr} \\ D &= \frac{\mu}{\rho Sc} \\ \mu_{air} &= \frac{A_1 T^{3/2}}{T + A_2}, \end{aligned} \tag{5.1.5}$$

where the diffusivity c_0 is an input constant, c_μ is an empirical constant with a standard value of 0.09 [109], Pr, Sc are the Prandtl and Schmidt numbers, respectively, and A_1, A_2, A_3 are constants.

Gas-phase

In KIVA-3V, the gas-phase calculation procedure is based on the Arbitrary Lagrangian-Eulerian (ALE) finite volume method [110, 111]. The procedure used is to difference the governing equations in integral form, with the volume of a typical cell used as the control volume, and with divergence terms transformed to surface integrals using the divergence theorem [112]. Spatial differences are formed on a finite-difference mesh that subdivides the computational region into a number of small cells that are hexahedrons. The position of the vertices at the corner of the cells are arbitrarily specified functions of time, thereby allowing a Lagrangian, Eulerian, or mixed description. The arbitrary mesh can conform to curved boundaries and can move to follow changes in combustion chamber geometry.

The Cartesian components of the velocity vector are stored at cell vertices while the scalars are saved in the center of cells. The transient solution is marched-out in

a sequence of finite time increments called time steps. On each time step, the values of the dependent variables are calculated from those on the previous time step. Each time step is divided into two phases: a Lagrangian phase and a rezone phase. In the Lagrangian phase, the vertices move with the fluid velocity, and there is no convection across cell boundaries. In the rezone phase, the flow field is frozen, the vertices are moved to new mesh-pre-specified positions, and the flow field is re-mapped onto the new computational mesh. This re-mapping is accomplished by convecting material across the boundaries of the computational cells, which are regarded as moving relative to the flow field. Because the temporal difference scheme is largely implicit, the time steps used by KIVA-3V are calculated based on accuracy, not stability, criteria. Thus the equation system can be solved with considerably large time steps. This results in considerable saving of computational time. In the Lagrangian phase, implicit differencing is used for all the diffusion terms and the terms associated with pressure wave propagation. The coupled implicit equations are solved by a method similar to the SIMPLE algorithm [113], with individual equations being solved by the conjugate residual method [114].

Explicit methods are used to calculate convection in the rezone phase; but the convection calculation can be sub-cycled an arbitrary number of times, and thus the main computational time step is not restricted by the Courant stability condition of explicit methods [115]. The convection time step is a submultiple of the main computational time step and does satisfy the Courant condition. KIVA-3V uses two schemes for convection: partial donor cell differencing or a quasi-second-order upwind (QSOU). Based on the ideas of Van Leer [116], the QSOU scheme is monotone and approaches second-order accuracy when convecting smooth profiles. While more

accurate than partial donor cell differencing, QSOU is also more time-consuming.

Spray and droplet calculation

KIVA-3V calculates evaporating liquid sprays by a discrete particle technique [117], in which each computational particle represents a number of droplets of identical size, velocity, and temperature. Probability distributions govern the assignment of droplet properties at injection or the changes in droplet properties at downstream locations. Droplet properties are determined using a Monte Carlo sampling technique [69]. The distributions of droplet sizes, velocities, and temperatures are taken into account to calculate the mass, momentum, and energy exchange between the spray and the gas. The particles and fluid interact by exchanging mass, momentum, and energy. The momentum exchange is treated by implicit coupling procedures to avoid prohibitively small time steps. Accurate calculation of mass and energy exchange is ensured by automatic reductions in the time step when the exchange rates become large. Turbulence effects on the droplets are accounted for in one of two ways. When the time step is smaller than the droplet turbulence correlation time, a fluctuating component is added to the local mean gas velocity when calculating each particle's mass, momentum, and energy exchange with the gas [117]. When the time step exceeds the turbulence correlation time, turbulent changes in droplet position and velocity are chosen randomly from analytically derived probability distributions for these changes. If droplet Weber numbers [118] exceed unity, droplet breakup is computed using the Taylor Analogy Breakup (TAB) method [119]. The displacement of spray droplets in the fluid and thick spray effects on the exchange rates are neglected. The spray equation formulation [120] is used to calculate the complex droplet spray. In this formulation, a droplet probability distribution function (f) is solved, and in

KIVA-3V f has ten independent variables in addition to time. These variables are the three components of droplet position vector $\mathbf{x}$, three components of velocity vector $\mathbf{v}$, equilibrium radius r (the radius the droplet would have if it was spherical), temperature T (assumed to be uniform within the drop), distortion from sphericity y, and the time rate of change $\dot{y} = dy/dt$. KIVA-3V keeps track of the fundamental mode of oscillation corresponding to the lowest order spherical zonal harmonic with axis aligned with the relative velocity vector between the droplet and gas. The dimensionless quantity y is proportional to the displacement of the droplet surface from its equilibrium position divided by the droplet radius r. Droplets breakup if and only if $y > 1.0$ [119]. The droplet distribution function f is defined in the way that

$$f(\mathbf{x}, \mathbf{v}, r, T_d, y, \dot{y}, t) d\mathbf{v} dr dT_d dy d\dot{y}$$

is the probability number of droplets per unit volume at position $\mathbf{x}$ and time t with velocities in the interval $(\mathbf{v}, \mathbf{v} + d\mathbf{v})$, radii in the interval $(r, r + dr)$, temperatures in the interval $(T_d, T_d + dT_d)$, and displacement parameters in the interval $(y, y + dy)$ and $(\dot{y}, \dot{y} + d\dot{y})$. Two moments of f have important physical significance. The liquid volume fraction θ, given by:

$$\theta = \int f 4/3\pi r^3 \; d\mathbf{v} \; dr \; dT_d \; dy \; d\dot{y},$$

is assumed to be small compared to unity. The liquid macroscopic density ρ_l' is calculated as:

$$\rho_l' = \rho_d \theta,$$

where ρ_d is the liquid microscopic density, which is assumed constant. The time evolution of f is obtained by solving a form of the spray equation:

$$\frac{\partial f}{\partial t} + \nabla_{\mathbf{x}} \cdot (f_{\mathbf{v}}) + \nabla_{\mathbf{v}} \cdot (f\mathbf{F}) + \frac{\partial}{\partial r}(fR) + \frac{\partial}{\partial T_d}(f\dot{T}_d) + \frac{\partial}{\partial y}(f\dot{y}) + \frac{\partial}{\partial \dot{y}}(f\ddot{y}) = \dot{f}_{coll} + \dot{f}_{bu}. \quad (5.1.6)$$

Detail of the time rate change of droplet's velocity $\mathbf{F}$, droplet's radius R, droplet's temperature T_d, droplet's oscillation velocity $\dot{y}$, its change rate $\ddot{y}$, and the collision and breakup source terms $\dot{f}_{coll}$ and $\dot{f}_{bu}$ in KIVA-3V are presented in appendix A.

Boundary Conditions

In KIVA-3V, two kinds of boundary conditions are used: numerical boundary conditions, which are extra necessary conditions for implementing computational boundaries in fluid flow codes, and physical conditions. The physical boundaries conditions consist of inflow and outflow, rigid walls and periodic boundaries. There are, in turn, several types of rigid walls depending on velocity and temperature boundary conditions. The velocity boundary conditions on rigid walls can be free-slip, no-slip, or turbulent law-of-the-wall. Temperature boundary condition options are adiabatic walls and fixed temperature walls. Velocity boundary conditions on rigid walls are introduced either by imposing the value of the velocity on walls or the value of the wall stress $\bar{\sigma}_w = \bar{\sigma}.\mathbf{n}$, where $\mathbf{n}$ is the unit normal to the wall. On no-slip walls, the gas velocity is set equal to the wall velocity:

$$\mathbf{u} = w_{wall}\mathbf{k}, \tag{5.1.7}$$

where the wall is assumed to be moving with speed w_{wall} in the z-direction, and $\mathbf{k}$ is unit tangential to the wall. The wall stress is then determined implicitly through equation (5.1.1). On free-slip and turbulent law-of-the-wall boundaries the normal gas velocity is set equal to the normal wall velocity:

$$\mathbf{u} \cdot \mathbf{n} = w_{wall}\mathbf{k} \cdot \mathbf{n}, \tag{5.1.8}$$

and the two tangential components of $\bar{\sigma}_w$ explicitly specified. For free-slip walls the tangential components of $\bar{\sigma}_w$ is zero. For turbulent law-of-the-wall conditions the

tangential components are determined by matching to a logarithmic profile:

$$\frac{v}{u^*} = \begin{cases} 1/c_3\ ln(c_w\zeta^{7/8}) + c_4 & \zeta > Re \\ \zeta^{1/2} & \zeta < Re \end{cases}, \tag{5.1.9}$$

where u^* is the wall shear speed and $\zeta = \frac{\rho y v}{\mu_{air}(T)}$ is the Reynolds number based on the gas velocity relative to the wall, $v = |\mathbf{u} - w_{wall}\mathbf{k}|$. The gas relative velocity is evaluated a distance y_a from the wall. The wall shear stress is related to the tangential components of the wall stress by:

$$\bar{\boldsymbol{\sigma}}_w - (\bar{\boldsymbol{\sigma}}_w \cdot \mathbf{n})\mathbf{n} = \rho(u^*)^2\frac{\mathbf{v}}{v}, \tag{5.1.10}$$

where $\mathbf{v} = \mathbf{u} - w_{wall}\mathbf{k}$.

In equations (5.1.9) and (5.1.10) it is assumed that y_a is small enough to be in the logarithmic region or the laminar sublayer region of the turbulent boundary layer. The Reynolds number Re defines the boundary between these two regions. The constant c_3, c_4, c_w, and Re in equation (5.1.9) are related to the k-ϵ model constants by:

$$c_3 = \sqrt{c_\mu^{1/2}(c_{\epsilon_2} - c_{\epsilon_1})Pr_\epsilon}$$

and

$$c_4 = Re^{1/2}1/c_3\ ln(c_w Re^{7/8}). \tag{5.1.11}$$

For commonly accepted values of the k-ϵ, $c_3 = 0.4327$, $c_4 = 5.5$, c_w=0.15, and $Re = 114$.

Temperature boundary conditions on rigid walls are introduced by specifying either the wall temperature or the wall heat flux $J_w = \kappa\nabla T \cdot \mathbf{n}$. For adiabatic walls, J_w is set equal to zero. For fixed temperature walls that are also either free-slip or no-slip the wall temperature is prescribed; and J_w is determined implicity from equation (5.1.2). If the turbulent law-of-the-wall condition is used, J_w is determined from

the modified Reynolds analogy formula:

$$\frac{J_w}{\rho u^* c_p (T - T_w)} = \begin{cases} 1/(Pr_{la}\frac{v}{u^*}) & \zeta \leq Re \\ 1/\{Pr[\frac{v}{u^*} + (\frac{Pr_{la}}{Pr} - 1)Re^{1/2}]\} & \zeta > Re \end{cases}, \tag{5.1.12}$$

where T_w is the temperature of wall, Pr_{la} is the Prandtl number of the laminar fluid.

In addition to the wall heat loss, there is a source to the internal energy due to frictional heating. Frictional heating occurs whenever turbulent law-of-the-wall velocity conditions are used and has the form:

$$\begin{aligned} q_w &= \bar{\sigma}_w \cdot \mathbf{v} \\ &= \rho(u^*)^2 v, \end{aligned}$$

where q_w is the heating rate per unit area of wall.

Boundary conditions for the turbulent kinetic energy k and its dissipation rate ϵ are:

$$\nabla k \cdot \mathbf{n} = 0$$

and

$$\epsilon = c_{\mu_\epsilon} \frac{k^{3/2}}{y_a}, \tag{5.1.13}$$

where k and ϵ are evaluated a distance y_a

$$c_{\mu_\epsilon} [\frac{c_\mu}{Pr_\epsilon (c_{\epsilon_2} - c_{\epsilon_1})}]^{1/2}. \tag{5.1.14}$$

Boundary conditions for the spray equations are specified as following. When a spray droplet impinges on a rigid wall, its velocity is set equal to the wall velocity, and the Reynolds number of the spray droplet Re_d is set to zero. Heat transfer between the droplet and wall is not taken into account.

Chemical reaction

In KIVA-3V, chemical reaction is calculated directly using two types of reaction: slow reactions, which proceed kinetically, and fast reactions, which are assumed to be in equilibrium [121]. By default, up to 12 species (fuel, O_2, N_2, CO_2, H_2O, H, H_2, O, N, CO, NO) can be used. The number of chemical reactions involved are arbitrary. Although authors argue that the number of species and reactions can be extended even to a detailed chemical kinetics reaction mechanism, this can not be done at present time due to memory limitations and the difference between eigenvalues of fluid dynamic and chemical processes. Thus, with a simple reaction mechanism, KIVA-3V can not accurately predict emissions of IC engines. Some authors [122] have tried to use more complex reaction mechanisms, "reduced mechanism", which compromise the accuracy and computational intensity. However, use of a detailed chemical kinetics reaction mechanism to calculate combustion of air/fuel mixture is still desired for accurate emissions prediction.

5.1.3 Calculation algorithm

The calculation algorithm of KIVA-3V is illustrated in figure 5.1. At the beginning, KIVA-3V reads in inputs for the problem. The inputs consist of computational mesh of engine geometry, engine operation conditions, and valve shift profiles. The computational mesh of the engine geometry is prepared by a mesh generator (such as K3PREP subprogram in KIVA-3V package) and stored in ITAPE17 file. The engine operating conditions consist of information about fuel, engine rotational speed, temperature, pressure, and composition of the mixture inside the cylinder, at inlet pipe and exhaust manyfold, etc., are stored in ITAPE5 file. ITAPE18 file contains

all information about position of valves with respect to the position of crank angle.

The next step is to calculate the state of the fluid in the cylinder chamber, time step for next computational cycle, fuel injection, and collision; coalescence and breakup of droplets are computed if appropriate. Then heat transfer, wall stress, and chemical reaction are taken into account. After that, transport of fluid is calculated. The last step in the computational cycle is to compute new volumes due to motion of the piston and valves, and to update the new state of the mixture in the cylinder. More details of the calculation procedure of KIVA-3V are presented in appendix B.

5.1.4 Implementation of KIVA-3V in the pre-integrated approach

KIVA-3V has been used in many IC engine studies with complicated geometries and it is proven that KIVA-3V is a useful tool for IC performance modeling [123, 124, 125, 126]. However, due to the limitation of directly integrating chemical reactions into the fluid dynamics calculation (memory requirement and difference in eigenvalues), a detailed chemical kinetics reaction mechanism can not be directly used for emissions prediction. To overcome this drawback, in the pre-integrated approach, the advantageous ability to calculate fluid dynamics, fuel injection, motion of piston and valves, and heat transfer, is used to model the physical processes in the cylinder chamber. Combustion of air/fuel mixture is introduced into the system from a chemical reaction result database file created in advance using SENKIN subprogram in CHEMKIN-II package described in section 5.2. The generation of database and coupling technique are presented in chapter 6.

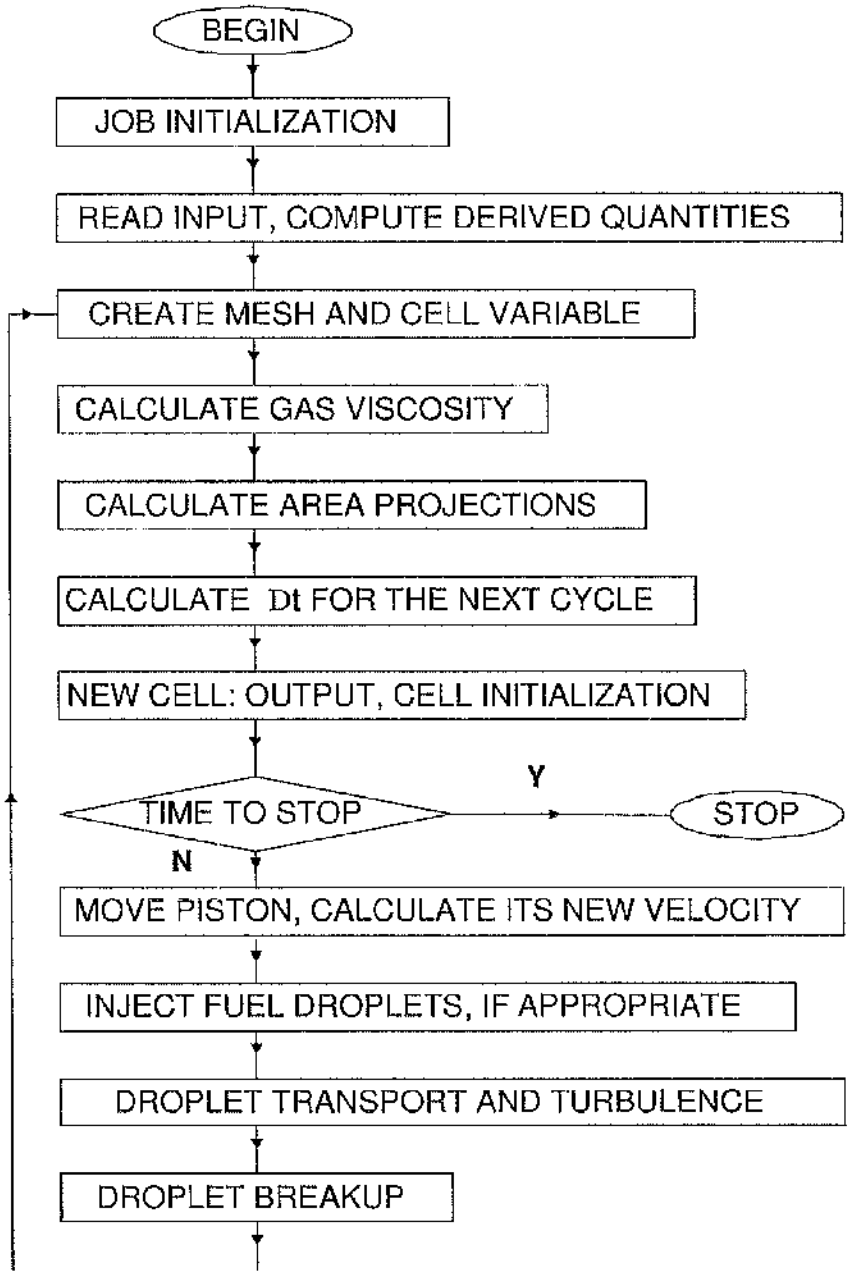

Figure 5.1: KIVA-3V calculation algorithm

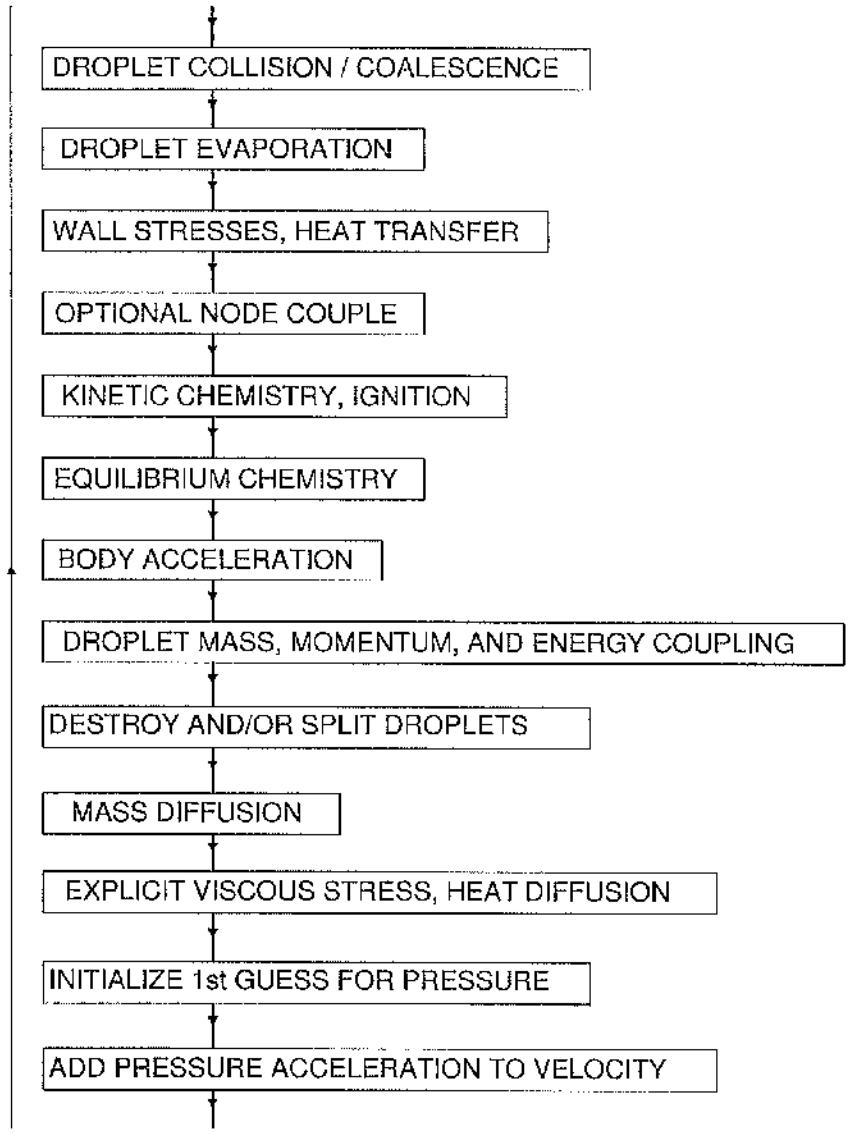

Figure 5.1: KIVA-3V calculation algorithm, continued

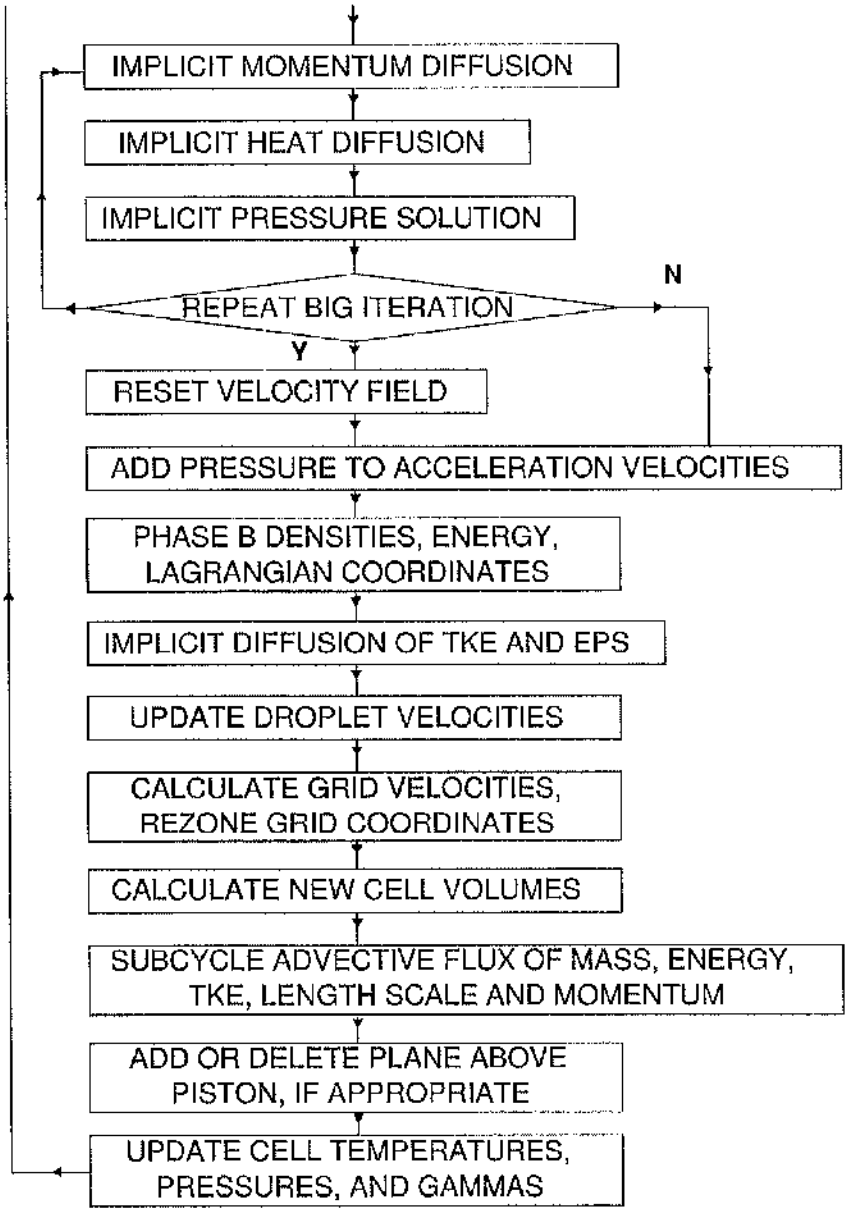

Figure 5.1: KIVA-3V calculation algorithm, continued

5.2 SENKIN

SENKIN is a Fortran subprogram written by Lutz et al. [127] in the CHEMKIN chemical kinetics calculation package developed by Kee et al. in Sandia National Laboratories [42, 34, 1]. SENKIN is a useful program to model chemical kinetics reaction of a combustible mixture, and has been validated by many authors on different kinds of fuels, from methane to diesel oil [128, 129].

5.2.1 Applications of SENKIN

SENKIN can be used to predict the time-dependent chemical kinetics behavior of a homogeneous gas mixture in a closed system. SENKIN can be used to solve the following six types of problems:

1) an adiabatic system with constant pressure,

2) an adiabatic system with constant volume,

3) an adiabatic system with the volume a specified function of time,

4) a system where the pressure and temperature are constant,

5) a system where the volume and temperature are constant, and

6) a system where the pressure and temperature are specified functions of time.

In addition to predicting the species and temperature histories, the program can also compute the first-order sensitivity coefficients with respect to the elementary reaction rate parameters. Sensitivity analysis is a formal procedure to determine quantitatively how the solution to a model depends on certain parameters in the model formulation. In SENKIN, the dependent parameters are the elementary reaction rate constants. Thus, without solving the problem repetitively with different values for the rate constants, the sensitivity analysis allows one to understand how the model will respond

to changes in the rate parameters. It also provides insight about how certain important reaction pathways are linked to the model's predictions. Compared to repetitive running of the model, the sensitivity analysis is significantly more efficient. This relative efficiency increases as the number of parameters increases, since the equations describing the sensitivity coefficients are linear, regardless of the nonlinearities in the model itself. Furthermore, when the model is solved by the implicit multi-step methods, solution of the sensitivity equations can take effective advantage of information that is already available from the previous solution of the model.

5.2.2 Calculating procedure

In SENKIN, chemical kinetics reaction of a mixture is modelled by solving the system of mass and energy conservation equations in a homogeneous, closed volume. No physical process, such as turbulence of fluid, is computed in SENKIN. Boundary conditions for the equation system, reaction mechanism, and thermodynamic properties of involved species are supplied by input files. Reaction results are recorded in output files for post-processing. The equation system, calculating algorithm, input files, and output files in SENKIN are described as follows.

Equations and calculation

The equation system in SENKIN consists of N_c equations of conservation of N_c species in the mixture plus the equation of conservation of energy. The equations of conservation of masses of species (3.1.19) are written in from of mass fractions as:

$$\frac{dY_m}{dt} = v\dot{w}_m W_m \qquad (m = 1, \ldots, N_c), \tag{5.2.1}$$

where Y_m is the mass fraction of species m, W_m is the molecular weight of species m, N_c is the total species in the system and v is the specific volume. In equation

(5.2.1) the production rate $\dot{w}_m$ of species m is obtained from equation (3.1.21) based on Arrhenius' relation (3.1.22).

The equation of conservation of internal energy for a closed system is:

$$de + pdv = 0, \tag{5.2.2}$$

where e is the specific energy and p is the pressure. In the case of constant volume, equation (5.2.2) is written in form:

$$c_v \frac{dT}{dt} + v \sum_{m=1}^{N_c} e_m \dot{w}_m W_m = 0, \tag{5.2.3}$$

where c_v is specific heat at constant volume, T is temperature, e_m is specific energy of species m. There are N_c+1 equations in this equation system, but only N_c equations are independent since the total mass in the considered volume is constant. Closure of the equation system is attained with specific heat, enthalpy, and entropy supplied from input files. The values of these parameters are calculated as functions of temperature using polynomial coefficients $(a_1 \div a_7)$ stored in a thermodynamic database as:

$$\frac{c_p}{R_0} = a_1 + a_2 T + a_3 T^2 + a_4 T^3 + a_5 T^4 \tag{5.2.4}$$

$$\frac{H^0}{R_0 T} = a_1 + \frac{a_2}{2} T + \frac{a_3}{3} T^2 + \frac{a_4}{4} T^3 + \frac{a_5}{5} T^4 + \frac{a_6}{T} \tag{5.2.5}$$

$$\frac{S^0}{R_0} = a_1 ln(T) + a_2 T + \frac{a_3}{2} T^2 + \frac{a_4}{3} T^3 + \frac{a_5}{4} T^4 + a_7 \tag{5.2.6}$$

The constants used in computing reaction rate in equation (3.1.21) are supplied from the reaction mechanism input file.

At high temperature and pressure, modeling chemical reaction of a mixture involves resolving a stiff system of ordinary differential equations (5.2.1 and 5.2.3), which means a system of equations with high eigenvalues. In SENKIN, this system is

solved implicitly using a Differential Algebraic Sensitivity Analysis Code (DASAC) written by Caracotsios and Stewart [130]. This code is based on the backwards differentiation formulas, and is a modification and extension of Petzold's differential/algebraic equation solver called DASSL [131]. DASAC handles the solution of the governing differential equations together with an efficient simultaneous computation of the first-order sensitivity coefficients.

The SENKIN calculation procedure is illustrated in figure 5.2. Prior to calculation of SENKIN, two input files a thermodynamic database and a reaction mechanism are integrated into a binary linking file by CKINTERP, a subprogram in the CHEMKIN package. Calculation starts by reading in boundary conditions of the problem from a text input file, reaction mechanisms and thermodynamic data from the binary linking file. With these boundary conditions, and reaction mechanisms from the linking file, the system of equations (5.2.1 and 5.2.3) is specified. The implicit equation system solver (DASAC) is called to compute the reaction solutions of the system. Reaction results are saved in binary and text output files in a certain interval specified in the boundary condition input file.

Input files

There are three input files used in SENKIN calculation: 1) boundary condition input file, 2) thermodynamic database file, and 3) reaction mechanism file. The thermodynamic database file contains thermodynamic properties of species involved in the reaction system. The reaction mechanism file consists of information of how these species react. The boundary condition input file supplies reaction condition and control parameters to write reaction results in output files. This input file consists of:
1) the initial temperature of the gas mixture,

2) the initial pressure of the gas mixture,

3) the composition of the mixture,

4) the auto ignition temperature of the mixture,

5) the initial time for a restart calculation,

6) the total reaction time,

7) the time interval for solution printouts to the text output file,

8) the absolute tolerance used by the differential equation solver as an indicator of the accuracy desired in the physical solution, and

9) the relative tolerance used by the differential equation solver as an indicator of the accuracy desired in the physical solution.

The thermodynamic database file provides the species name, its elemental makeup, and the temperature ranges over which the thermodynamic data are valid. This database file contains coefficients of polynomial fits to specific heat, enthalpy, and entropy in equations (5.2.4-5.2.6). For each species there are two polynomial fits, one for a low temperature range and one for higher temperatures. Each polynomial fit consists of seven coefficients for each temperature ranges ($a_1 \div a_7$); therefore, for each species, 14 coefficients are supplied in all.

The reaction mechanism file plays the most important role in SENKIN. It prescribes how the species react, computational time, and accuracy of the modeling. The reaction mechanisms describe the chemical kinetic reactions. This file contains a list of all of the reactions that involved in the simulation along with their Arrhenius rate coefficients A_r, β_r, E_r in equation (3.1.22).

For convenience, the thermodynamic database and the reaction mechanism are

integrated into a single binary linking file. The integration is implemented by CKINTERP. The linking file consists of all information of species, reaction mechanisms, Arrhenius coefficients of reaction rate, and coefficients of polynomial fits to calculate their thermodynamic properties. Therefore, at the beginning of SENKIN calculation, only the boundary condition input and linking file are read in by the program.

Output files

The calculated reaction results of SENKIN are written into two files: text and binary. The full solution is written to the binary solution file after each successful integration step. The binary file is intended for use in graphics post-processing and/or providing initial data for restart calculations.

The text output file is used to provide a record of the run; it includes a summary of the initial conditions and printouts of the partial solution at a selected time interval. Because this text output file is designed to keep track of the calculation process and used as a debug tool, reaction results are not stored in great detail to the file.

5.2.3 Use of SENKIN in the pre-integrated approach

Because of its advantage in chemical kinetics reaction calculation, in the pre-integrated approach SENKIN subprogram in CHEMKIN-II is used to compute kinetic reaction of air/fuel mixture in the combustion chamber. In our approach, the engine cylinder is divided into small cells using the finite-volume technique. The chemical process in the cylinder chamber is modelled with the assumption that each cell is a homogeneous, and reaction of air/fuel mixture in the cell occurs in a constant volume. Therefore, the case (2) in SENKIN is chosen to calculate the time-dependent chemical kinetics behavior of air/fuel mixture in each cell of the combustion chamber. In

this case, it is also assumed that reactions occur for a fixed mass of mixture that is reacting in an adiabatic system. However, the effects of volume changes, of diffusion of species between cells, and of heat transfer between cells are accounted for in the overall approach via linking the results of SENKIN described above with the KIVA3V computing procedure as described in chapter 6.

SENKIN is a useful program for chemical kinetics calculation. It gives accurate reaction results from detailed reaction mechanisms. However, the computational intensity and the different eigenvalues of program does not permit to couple it directly with fluid dynamics process in the IC engine modeling. It is necessary to modify SENKIN to use in the pre-integrated approach. Only one output file of SENKIN is used to store reaction information. The SENKIN code was modified to write all reaction results in detail into a result file. The results in this file in turn are fitted in polynomial functions of temperature, pressure, and species densities. The coefficients of these functions are stored in a database file with their corresponding reaction conditions. The binary file is omitted to save memory and computer time. Reaction results calculated in the chemical timescale of SENKIN are decoupled from the chemical timescale then re-integrated into the physical timescale.

SENKIN is executed many times to model reaction of air/fuel mixture at different temperatures, pressures, and compositions to generate the database. However, SENKIN is written for a single run. Therefore, it could require many repetitions of running the program. To avoid this, in the pre-integrated approach SENKIN is run in batch mode to create the reaction database files.

Since a detailed chemical reaction involves thousands of reactions and hundreds of species, it is impractical to take all species into account for the fluid dynamic

modelling. The sensitivity analysis ability of SENKIN is used to locate the species, which affect most the overall reaction results, and to represent the mixture in fluid dynamics computation.

Details about modifications to the SENKIN code, creation of the database file, and its use in the pre-integrated approach are presented in chapter 6.

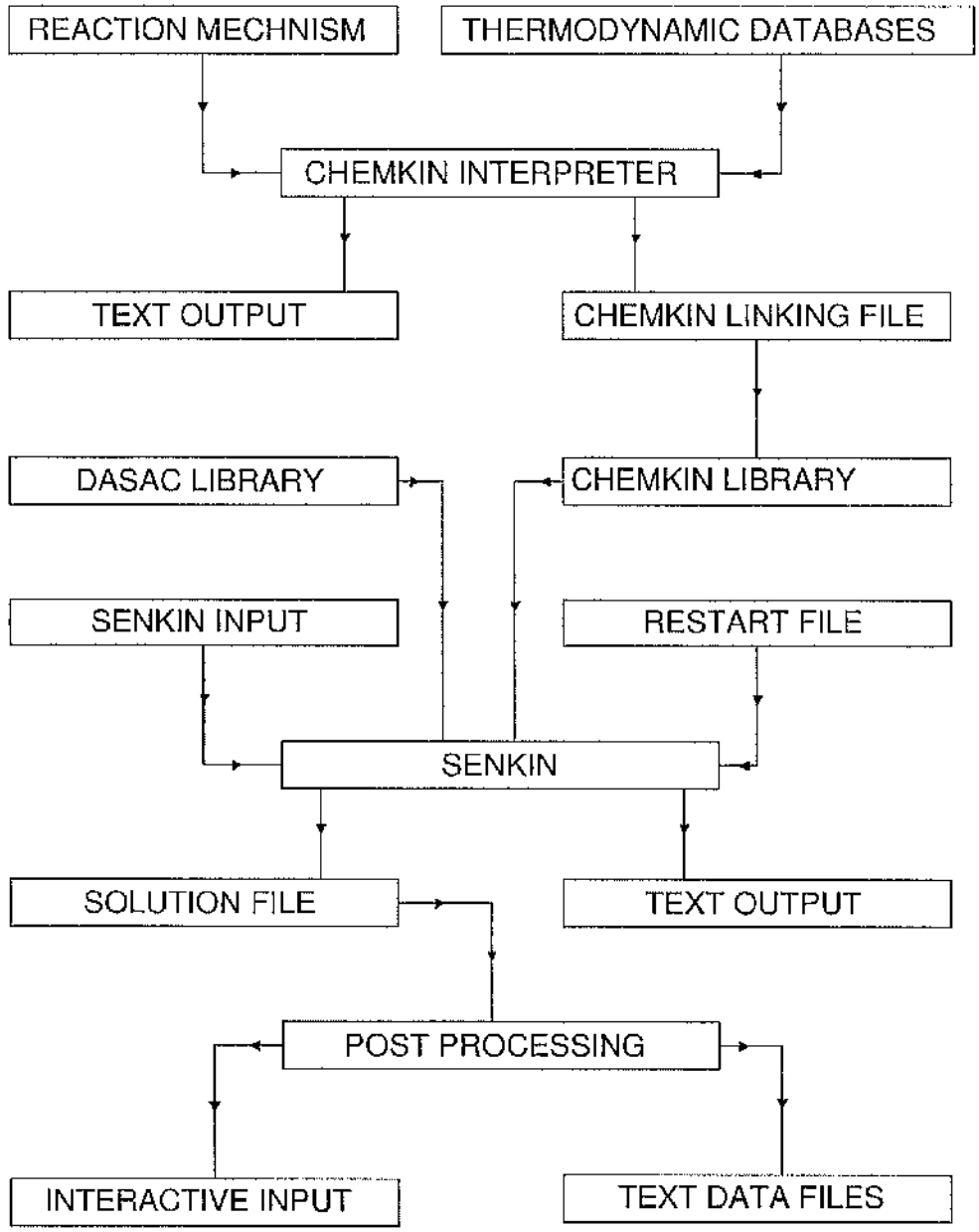

Figure 5.2: SENKIN calculation procedure

Chapter 6

Pre-integrated non-equilibrium combustion response mapping approach

This chapter describes the pre-integrated method to couple a multi-dimensional fluid dynamics modeling program with the detailed chemical kinetics reaction calculation of air/fuel mixture for emissions prediction. The method to create reaction database file including execution of SENKIN, the technique to decouple reaction results from chemical timescale then to integrate into physical eigenvalue, and to fit these results in polynomial functions are described. The method to retrieve chemical source terms from reaction database is also presented.

6.1 Description of the method

It is proven that chemical reactions can be accurately predicted using detailed chemical kinetics, and multi-dimensional modeling is a powerful tool for calculation of fluid dynamics in IC engines [17], [18]. Therefore, it is ideal to couple the advantages of the two methods for predicting emissions of IC engines. To do this, several researchers have tried to integrate detailed chemical reaction directly into multi-dimensional fluid

dynamics modeling [122]. However, this approach has a major drawback that is the high cost of computer time. This approach is only suitable for a simple engine geometry with some light fuels such as methane, with a small number of species and reactions. It is computationally intensive to calculate emissions for heavy fuel combustion which involves hundreds of species and thousands of reactions in a fine grid geometry. Another difficulty is the difference of eigenvalues of the chemical and physical processes, which causes errors when directly coupling the two processes.

The pre-integrated non-equilibrium combustion response mapping method was developed to avoid these difficulties. The idea of the approach is to use a detailed chemical kinetics modeling program to calculate in advance reaction of air/fuel mixture used in IC engines for a wide range of temperatures, pressures, and compositions. The results are saved in a database file. The physical processes in the engine cylinder are simulated using a multi-dimensional fluid dynamics modeling program. When the reaction results are required, instead of directly calculating combustion, chemical source terms are obtained from the reaction database. To apply this approach in predicting emissions, some basic requirements must be fulfilled. These requirements are:

1) results of the needed reaction must always be found in the database file,

2) reaction results must be retrieved fast from the reaction database file, and

3) those results are ready to use in the physical process simulation.

To satisfy the first requirement, the reaction database should be large enough to cover all possible reaction conditions in the application. The reaction database file must be well constructed for retrieval of results to meet the second demand. For the third requirement, the chemical reaction results must be stored in physical timescale.

In the pre-integrated approach, engine operation is modelled by resolving the equation system described in chapter 3 using a splitting scheme. Chemical reaction is not solved simultaneously with the physical processes, but is computed separately and appears in the equation system as source terms. However, instead of calculating in parallel with physical processes, the chemical reaction is computed in advance and results are stored in a database file. The chemical source term introduced into the equation system are taken from the reaction database file. Because of its advantage, LES is adopted to model fluid dynamics in the engine cylinder. In the pre-integrated approach, the combustion chamber is divided into small cells using the finite-volume technique. These cells are small enough for the homogeneous cell assumption. Chemical reaction is assumed fast compared to the movement of the piston and valves. Therefore, chemical source terms in each computing step are computed in homogeneous, constant volume condition.

Because of its advantages in chemical reaction prediction, SENKIN subprogram in the CHEMKIN-II package is used to calculate detailed chemical kinetic combustion of air/fuel mixtures in the pre-integrated approach. On the other hand, SENKIN reaction mechanisms and thermodynamic data of common fuels used in IC engines have been developed, carefully validated, and are available to use. Thus, using SENKIN would provide accurate results for predicting of air/fuel mixture combustion.

There are several CFD programs available for modeling fluid dynamics process in IC engines such as STAR-CD [132], HCT [32], AVL BOOST^{TM} [36], etc. Because of its ability to handle complex geometry and valve profile, KIVA-3V is chosen to model the fluid dynamics processes in IC engines in our approach.

The procedure to couple SENKIN and KIVA-3V in the pre-integrated approach

is illustrated in figure 6.1. Prior to the simulation of engine, SENKIN is used to calculate reaction of interest air/fuel mixture at different temperatures, pressures, and compositions. Sensitivity analysis is used to specify the most active species, which have the most influence on reaction results. The number of species represented the reaction behavior of the mixture were reduced using the equivalent N_2 adding technique, in which only concentrations of species of interest (CO, CO_2, NO, NO_2, etc.) are treated exactly, and the concentrations of the remaining species in the mixture are added into the concentration of nitrogen molecules (N_2). The reaction results are decoupled from the chemical timescale, then integrated in physical eigenvalues. The reaction results are saved in the results file. After calculation of all reaction conditions, reaction results in the result file are fitted into polynomial functions of temperature, pressure, and species densities. Coefficients of these polynomials are stored in reaction database in matrix form along with their corresponding reaction conditions. At the beginning of the simulation, geometry, engine operating condition, and valve shift profile are read in. KIVA-3V is used to calculate the state of the fluid in the cylinder chamber, heat transfer, motions of piston and valves, fuel injection, collision, coalescence, breakup, and evaporation of droplet if appropriate. Transportation of fluid is also computed. An interpolating subroutine is added in KIVA-3V to obtain chemical source terms from the reaction database. At the moment of ignition of the mixture, KIVA-3V sends a request, which contains reaction conditions and reaction time in the computational cell to the interpolating subroutine. The interpolating subroutine uses indices of these conditions to lookup reaction results in the reaction database and send them back to KIVA-3V. The new state of fluid, motions of piston and valves, and new volume of combustion chamber are calculated for a new

calculating cycle.

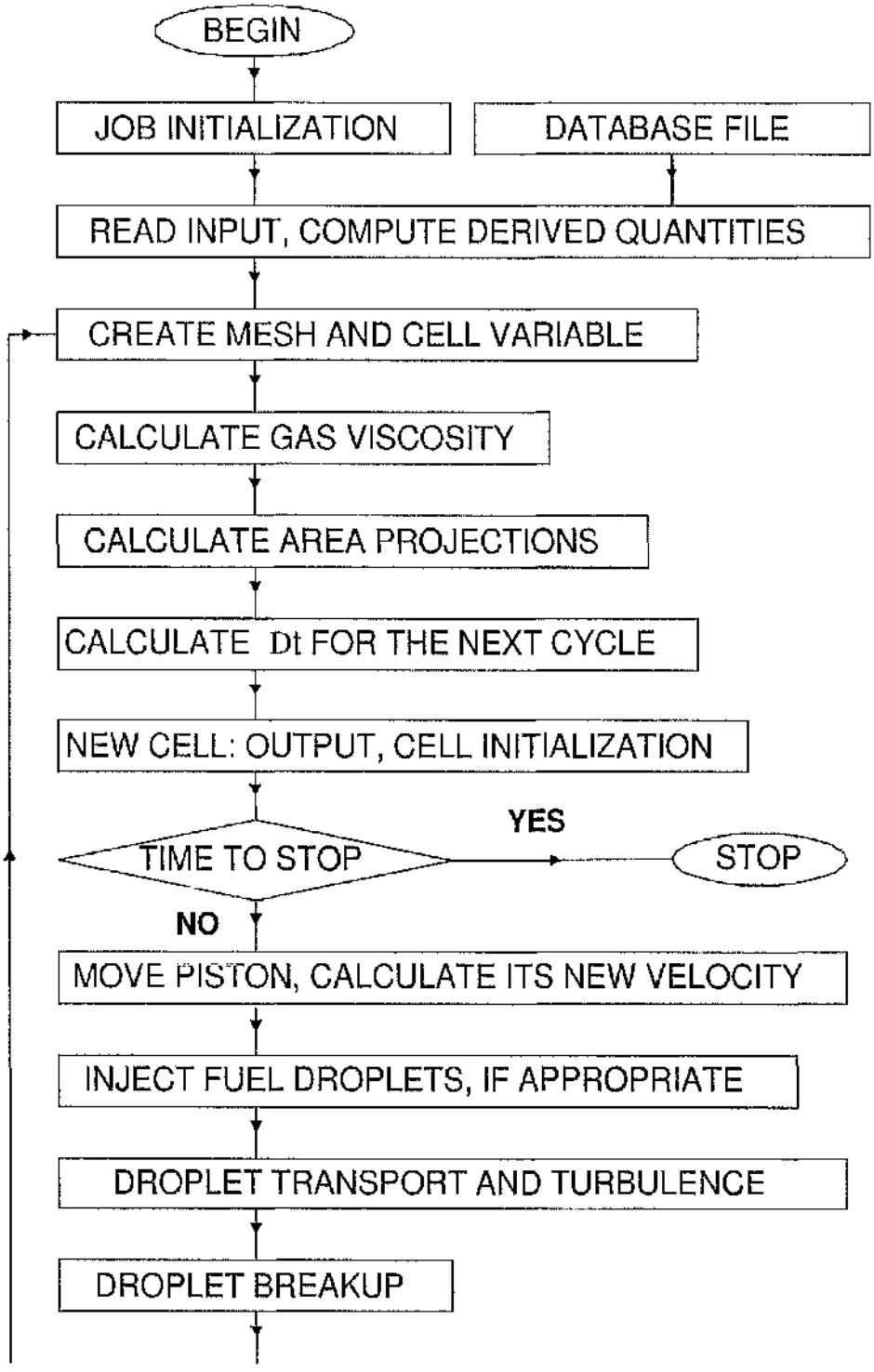

Figure 6.1: Pre-integrated non-equilibrium combustion response mapping algorithm

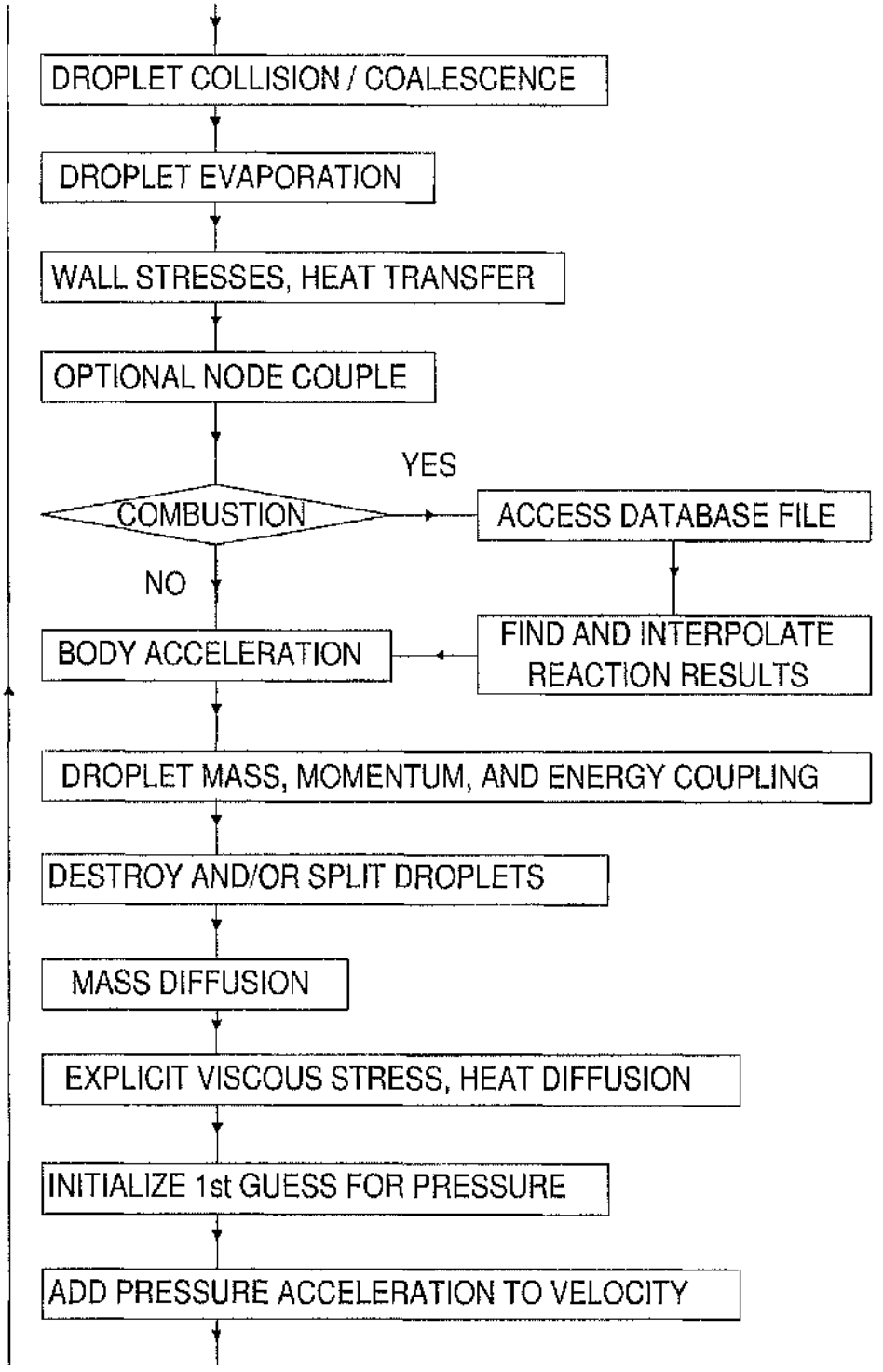

Figure 6.1: Pre-integrated non-equilibrium combustion response mapping algorithm, continued

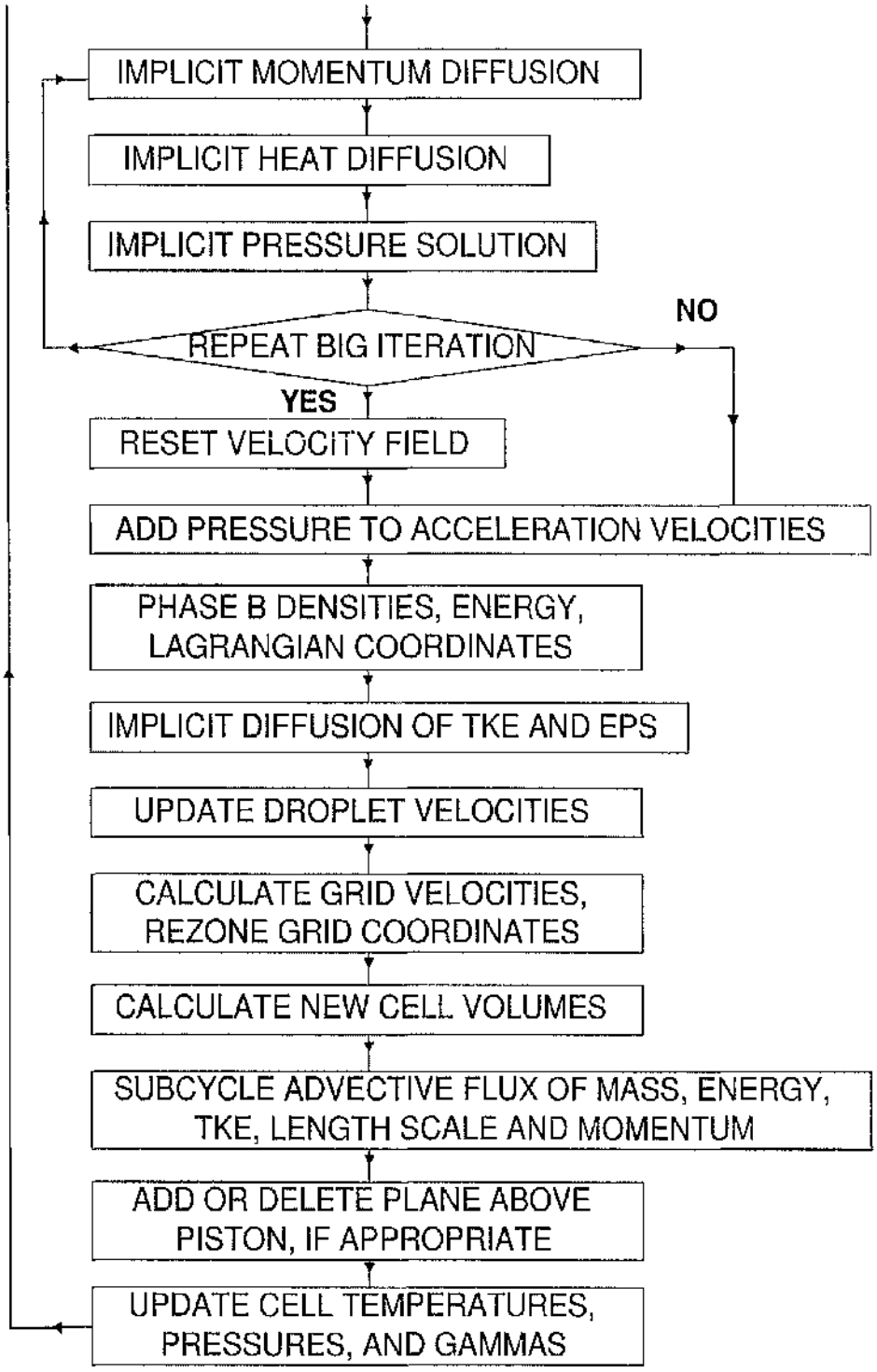

Figure 6.1: Pre-integrated non-equilibrium combustion response mapping algorithm, continued

6.2 Creation of reaction database file

6.2.1 Multi-execution for SENKIN

To satisfy that the chemical source terms are always found from the reaction database file, the database file must contain results of a wide range of reaction conditions. Thus, it is necessary to execute SENKIN to calculate reaction of air/fuel mixture at different temperatures, pressures, and compositions to create a sufficient database. It is very time consuming to run SENKIN manually for each case. To avoid this SENKIN is executed in batch mode. For each run, a different input file is supplied for SENKIN. There are two options for generating these input files. The first option is to create a new input file based on the previous one. In order to do this SENKIN needs to be modified to update automatically the input file with the information from the old input file. A new input file for the next run is created during the execution of the present running of SENKIN. The second option is to generate input files by a separate routine, so that all the input files are created prior to the execution of SENKIN. The first option is more compact and requires little space and memory compared to the second one. The advantage of the second option is that the input files are displayed explicitly, so it is much easier to check these input files before executing the program. The second one is chosen for executing SENKIN as it gives full control over the input parameters. The procedure is illustrated on the figure 6.2.

6.2.2 Chemical reaction results in physical timescale

Due to the difference in eigenvalues between chemical and physical precesses in IC engine, the reaction results calculated by SENKIN can not be used directly by KIVA-3V. In IC engine applications, during the combustion process, temperature and pressure

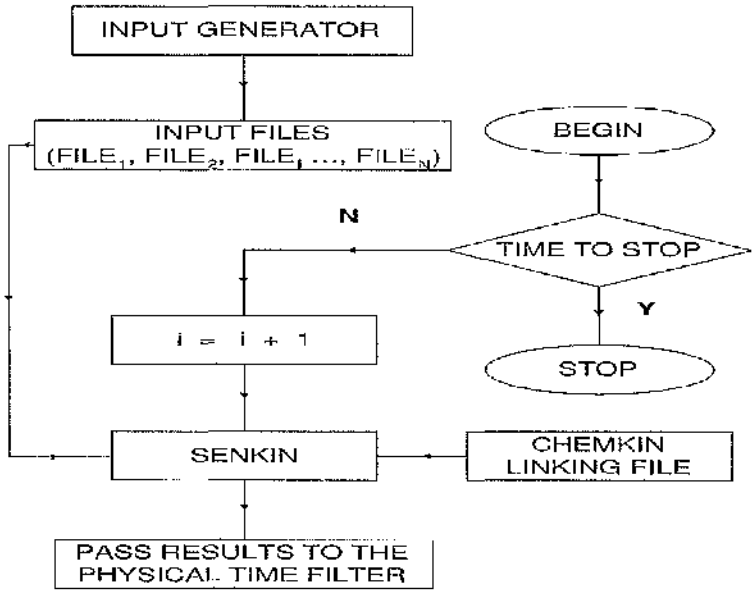

Figure 6.2: SENKIN execution algorithm

in the combustion chamber are very high, so that chemical reactions occur very fast with timescales of the order of $10^{-10} \div 10^{-6}$ second. The physical timescale of flow, transport, and turbulence is much longer (of the order of $10^{-5} \div 10^{-2}$ second). Because of this difference in eigenvalues coupling the fluid dynamics process directly with the chemical reaction results will cause calculation errors. In order to couple properly these two processes, it is necessary that they are matched in eigenvalue. If the chemical reaction is coupled to fluid dynamics using chemical timescale, the result is a very stiff equation system and solving such a system is very expensive. To avoid the stiff equation system the other approach is used, in which reaction results are saved in physical timescale. In SENKIN, the reaction results are saved with their absolute values after each interval specified by the input file. For convenience in the retrieval process, the reaction results are saved in form of production rate of species. All the

reaction results related to species concentration are normalized to the density of the mixture. Conversion of chemical reaction results to physical timescale is performed by a filtering technique. The filtering process is illustrated in the figure 6.3.

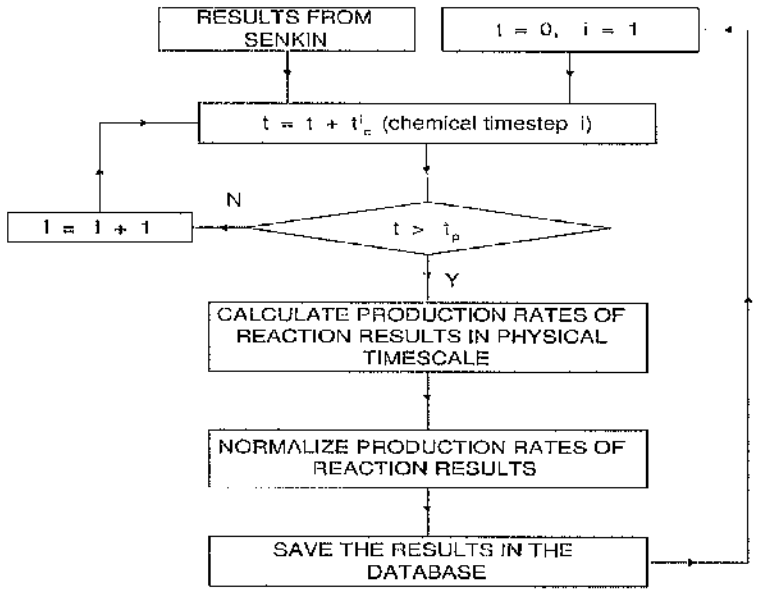

Figure 6.3: Physical timescale filtering algorithm

For an arbitrary reaction result G which has a value of G^0 at the beginning of a filtering cycle t_c^0, where subscript c denotes chemical and the superscript is step index. After one step of calculation, at the time t_c^1 SENKIN returns the result with value of G^1, and the duration of reaction is $\Delta t_c^1 = t_c^1 - t_c^0$. The filter compares Δt_c^1 to the physical timescale t_{ph}. If $\Delta t_c^1 \geq t_{ph}$ the production rate of G is calculated as:

$$(G^1 - G^0)/\Delta t_c^1$$

and this value is stored in the result file along with its reaction condition. If $\Delta t_c^1 < t_{ph}$ no result is stored in the result file. The computation process on SENKIN continues

until step t_c^n is reached at which $\Delta t_c^n \geq t_{ph}$ corresponding to the values G^n with $\Delta t_c^n = t_c^n - t_c^0$. At this moment production rate of G is stored as:

$$(G^n - G^0)/\Delta t_c^n$$

and a new filtering cycle starts. This procedure ensures all chemical reaction results are stored in the physical timescale t_{ph}, so that they are ready to use in the fluid dynamics process. However, the physical eigenvalue varies during the combustion process depending on the state of fluid. For simplicity, the physical time step is determined based on the temperature of the mixture in the cylinder chamber. The physical timescale is specified from the engine operation as follows. KIVA-3V is executed to model engine operation on a fine mesh, and the time steps of fluid dynamic calculations are recorded as a function of temperature. Based on this function, the value of t_{ph} is specified relatively to the reaction temperature of the mixture.

6.2.3 Creation of the reaction database file

After reactions of air/fuel mixture at discrete intervals of possible temperatures, pressures, and compositions in IC engines are modelled, the resultant file, which contains all results and their corresponding reaction conditions, is extremely large. To lookup a particular reaction result in this result file is computationally inefficient. To solve this problem, the reaction results are fitted in functions (i.e. in Fourier or polynomial form). In other words, the discrete reaction results are described as functions of temperature, pressure, and species densities, at which these reactions occur. The coefficients of these functions are stored in a database file along with their corresponding reaction conditions. In our approach the reaction results are represented by polynomial functions of normalized species densities, temperature and pressure. Since

the reaction result varies exponentially with the temperature and concentrations of species in the mixture, it is incorrect to use one polynomial function to describe this relation for the whole reaction conditions. Therefore, results and their reaction conditions are discretized into subregions, each subregion containing results for a small interval of normalized species densities, temperature and pressure. A two-dimensional illustration of the discretization is shown in figure 6.4. Suppose that the combustion

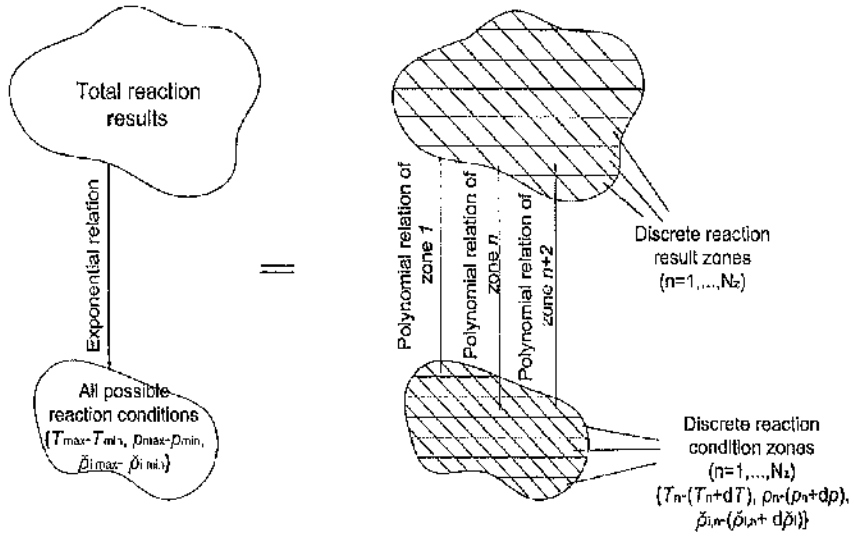

Figure 6.4: Two-dimensional sketch of relation between results and their reaction conditions

process in one IC engine involved reactions of N_c species with normalized densities from $(\breve{\rho}_m)_{min}$ to $(\breve{\rho}_m)_{max}$, temperature ranges from T_{min} to T_{max}, pressure ranges from p_{min} to p_{max}. The conditions and results of the reaction are represented by an assembly of N_z regions: the first region stores reaction results of mixtures that have

normalized densities of species, temperature and pressure in an interval of

$$\{[(\check{\rho}_1^1)_{min}, (\check{\rho}_1^1)_{min} + d\check{\rho}_1], [(\check{\rho}_2^1)_{min}, (\check{\rho}_2^1)_{min} + d\check{\rho}_2], ...,$$
$$[(\check{\rho}_{N_c}^1)_{min}, (\check{\rho}_{N_c}^1)_{min} + d\check{\rho}_{N_c}], [T_{min}^1, T_{min}^1 + dT], [p_{min}^1, p_{min}^1 + dp]\};$$

and second region stores reaction results of mixtures that have normalized densities of species, temperature and pressure in an interval of

$$\{[((\check{\rho}_1^2)_{min} + d\check{\rho}_1), ((\check{\rho}_1^2)_{min} + 2 \times d\check{\rho}_1)], [(\check{\rho}_2^2)_{min}, (\check{\rho}_2^2)_{min} + d\check{\rho}_2], ...,$$
$$[(\check{\rho}_{N_c}^2)_{min}, (\check{\rho}_{N_c}^2)_{min} + d\check{\rho}_{N_c}], [T_{min}^2, T_{min}^2 + dT], [p_{min}^2, p_{min}^2 + dp]\},$$

where the superscript denote subregions. The last region stores reaction results of mixtures that have normalized densities of species, temperature and pressure in an interval of

$$\{[(\check{\rho}_1^{(n_z)})_{min} + (n_z - 1) \times d\check{\rho}_1, (\check{\rho}_1^{(n_z)})_{min} + n_z \times d\check{\rho}_1], \tag{6.2.1}$$
$$[(\check{\rho}_2^{(n_z)})_{min} + (n_z - 1) \times d\check{\rho}_2, (\check{\rho}_2^{(n_z)})_{min} + n_z \times d\check{\rho}_2], ...,$$
$$[(\check{\rho}_{N_c}^{(n_z)})_{min} + (n_z - 1) \times d\check{\rho}_{N_c}, (\check{\rho}_{N_c}^{(n_z)})_{min} + n_z \times d\check{\rho}_{N_c}],$$
$$[T_{min}^{(n_z)} + (n_z - 1) \times dT, T_{min}^{(n_z)} + n_z \times dT], [p_{min}^{(n_z)} + (n_z - 1) \times dp, p_{min}^{(n_z)} + n_z \times dp]\},$$

where n_z is the number of intervals in each dimension. The number of discretized regions is $N_z = n_z^{N_c+2}$, in which each region has dimensions of $(d\check{\rho}_1,\ d\check{\rho}_2, ..., d\check{\rho}_{N_c},\ dT,\ dp)$, (where $d\check{\rho}_1 = [(\check{\rho}_1)_{max} - (\check{\rho}_1)_{min}]/n_z$, $dT = (T_{max} - T_{min})/n_z$, etc.).

Production rates of reaction results in each discretized subregion are presented as polynomial functions of corresponding temperature, pressure, and normalized species densities. Therefore, all the reaction results are presented by a series of polynomial functions, which are valid within their corresponding discretized reaction conditions.

There are (N_c+2) reaction results of interest in each region (production rates of N_c species, temperature, and pressure); and they are described by a set of (N_c+2) fitted polynomial functions. Each function has (N_c+3) coefficients a^i_m (described in equation (6.2.2), so that each subregion i is saved in the reaction database as a matrix (N_c+2, N_c+3) of coefficients $a^i_{m,G}$ of their presented functions and their reaction conditions. The normalized production rate of an arbitrary reaction result G (G can be species, temperature, or pressure) in a particular region i $\{(\check{\rho}^i_1,\ \check{\rho}^i_1 + d\check{\rho}^i_1),\ (\check{\rho}^i_2,\ \check{\rho}^i_2+d\check{\rho}^i_2),\ (\check{\rho}^i_3,\ \check{\rho}^i_3+d\check{\rho}^i_3),\ldots,(\check{\rho}^i_{N_c},\ \check{\rho}^i_{N_c}+d\check{\rho}^i_{N_c}),\ (T^i,\ T^i+dT),\ (p^i,\ p^i+dp^i)\}$ can be calculated from the fitted polynomial function:

$$\dot{\check{G}} = a^i_{0,G}+a^i_{1,G}\check{\rho}^i_1+a^i_{2,G}\check{\rho}^i_2+a^i_{3,G}\check{\rho}^i_3+a^i_{4,G}\check{\rho}^i_4+\cdots+a^i_{N_c,G}\check{\rho}^i_{N_c}+a^i_{(N_c+1),G}T^i+a^i_{(N_c+2),G}p^i, \tag{6.2.2}$$

where superscript i denotes region, $a_{m,G}(m=0,1,\ldots,(N_c+2))$ are coefficients of the fitted polynomial function of reaction result G corresponding to species m, $\check{\rho}_m(m=0,1,\ldots,N_c)$ are normalized densities of species m, N_c is the total number of species in the system, and T and p are temperature and pressure, respectively.

Calculation of coefficients $a^i_{m,G}$ for the production rate of reaction result G in a region i involves solving a system of (N_c+3) equations:

$$\dot{\check{G}}_j = a^i_{0,G}+a^i_{1,G}\check{\rho}^i_{1,j}+a^i_{2,G}\check{\rho}^i_{2,j}+\cdots+a^i_{N_c,G}\check{\rho}^i_{N_c,j}+a^i_{(N_c+1),G}T^i_j+a^i_{(N_c+2),G}p^i_j,$$
$$J=1,\ldots,(N_c+3), \tag{6.2.3}$$

where $\dot{\check{G}}_j$ is the normalized production rate of reaction result G corresponding to the reaction condition $\check{\rho}_{m,j}, T_j, p_j$ in the region i ($\check{\rho}^i_m < \check{\rho}^i_{m,j} \le \check{\rho}^i_m + d\check{\rho}^i_m,\ T^i < T^i_j \le T^i+dT^i,\ p^i < p^i_j \le p^i+dp^i$). This is a system of (N_c+3) equations for (N_c+3) unknown $(a^i_{m,G})$ where $\check{\rho}^i_{1,j}$, T^i_j and p^i_j are known values taken from the result file

created by SENKIN. In our approach, the system of (N_c+3) linear equations is solved using a Newton-Seidel iteration method [133, 134]. If the reaction conditions are subdivided into N_z regions, the reaction database consists of N_z coefficient matrices $\{(N_c+2),(N_c+3)\}$ for production rates of reaction results along with their conditions. To ease the result retrieval process, the beginning of the reaction database file contains information about where to find reaction results based on their indices of reaction conditions. This is a set of instructions specifying where the reaction results of the mixture were stored corresponding to their temperature, pressure, and composition.

Sensitivity analysis, adding technique, and uneven region distribution

To meet the second demand of the pre-integrated approach (fast retrieval of reaction results), the reaction database should be compact while containing results of all the possible reaction conditions in IC engines. The reaction database consists of N_z sets of matrices $\{(N_c+2),(N_c+3)\}$ as well as their reaction conditions. A detailed chemical kinetic reaction of air/fuel mixture involves a large number of species and reactions (i.e. in our sample calculation, detailed combustion of diesel oil modelled as $C_{12}H_{26}$ involves 821 species and 4491 reactions). To describe accurately the exponential relation between results and reaction conditions by a series of fitted polynomial functions, the reaction conditions and their results are discretized into thousands of subregions. Therefore, the reaction database for heavy fuel is very large ($N_z \times [N_c+2] \times [N_c+3]$ elements). On the other hand, to take all the species of a detailed reaction mechanism into the fitted polynomial functions leads to solving a system of hundreds of equations (6.2.3) for hundreds of unknowns (coefficients $a^i_{m,j}$ of their functions). Solving such a large system causes errors and is impractical for a conventional computer. Therefore, it is necessary to reduce the size of the reaction database. The are two promising

directions: to reduce the number of species presented in the matrix, and to reduce the number of regions N_z in the reaction database. Both approaches are used in our application.

In the first method, the total number of species N_c involving in reaction is reduced to N_c^* typical species. N_c^* depends on the number of the most active species and species of interest. The reaction behavior of the mixture of N_c species is represented by N_c^* species, which contains (N_c^*-1) species of interest and "equivalent nitrogen molecule" . Conservation of mass is satisfied by adding the densities of all the remaining species ($N_c - N_c^*$) in the "equivalent nitrogen molecule" density. This adding technique causes a change in the mixture structure, states of fluid, and consequently affects the reaction results. However, the dominance of N_2 in the mixture is large enough to minimize this effect. This effect is also limited since the results are stored in the reaction database by a function and taken out using the same function. In the pre-integrated method, sensitivity analysis is carried out in SENKIN calculations to find the most sensitive (active) species which have the largest influence on reaction rates. Then these species are used to represent the whole mixture. Use of this equivalent N_2 adding technique reduces the dimension of the matrix representing a region i to $\{(N_c^* + 2), (N_c^* + 3)\}$. However, omitting the effect of the remaining species on reaction leads to a small error. The advantages, disadvantages, and errors introduced by the equivalent N_2 adding technique are discussed in section 6.4.1.

Since the reaction results depend nonlinearly on reaction conditions (temperature, species concentration, etc.), one fitted polynomial function can not describe properly this relation. For this reason, the reaction result file is discretized into subregions. However, analysis of the kinetic reaction shows that some species are created only

in a narrow range of conditions, such as formation of NO_x mainly occurs at high temperature (thermal NO_x); at low temperature, the production rate of NO_x is very small. Thus, for this kind of reaction, the number of intervals in the reaction condition n_z can be reduced for the less sensitive parts while concentrating on the sensitive parts. For instance, temperatures in combustion processes of IC engines range from 800 K to 2800 K. In calculating the formation of NO_x, in the less sensitive region 800 K÷1100 K, the interval dT can be set at a value of $dT = 60$ K; but in the region of higher temperature sensitivity of 1100 K÷1500 K, the interval dT needs to be set at value of $dT = 30$ K. For higher temperature region dT needs to be even smaller (e.g. $dT = 10$ K for the range of 1500 K÷2800 K). In chemical reactions, production rates of some species do not depend much on other species. For example, the a large variation of nitrogen dioxide (NO_2) concentration does not affect much the formation of carbon monoxide (CO), while the presence of carbon atom C and oxygen atom O have a significant contribution to CO. Therefore, a reduction in the number of intervals in density of regions n_z for NO_2 range does not cause much error in the fitted function of CO, and the number of intervals in density n_z of NO can be smaller than that of oxygen atom and carbon atom. This uneven distribution in both n_z and interval $d\check{\rho}_m$, dT, dp in a region reduces significantly the total number of zones N_z.

6.3 Reaction result retrieval from the database

6.3.1 Interpolating process

After detailed chemical kinetics reactions of air/fuel mixture are calculated in a variety reaction conditions by SENKIN, the reaction results are normalized, discretized then represented by fitted polynomial functions. The coefficients of these fitted functions

are stored in the reaction database file in matrix form. In other words, all the possible reactions in IC engines are already saved in physical timescale in the database file. When a chemical source term of a particular reaction is needed, it can be obtained from the database file. The chemical source term retrieval process is illustrated in figure 6.5.

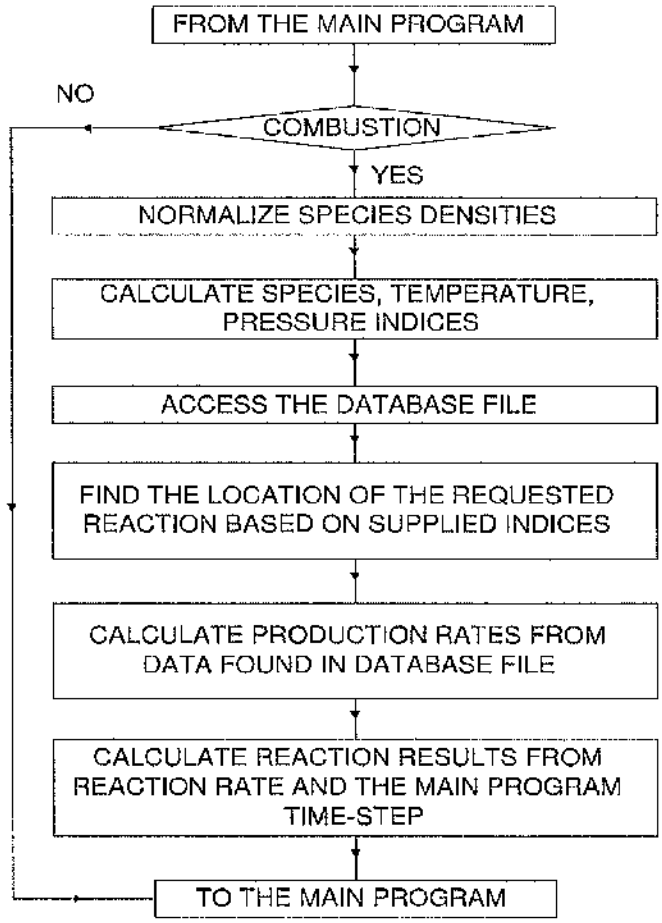

Figure 6.5: Reaction results interpolation algorithm

In the calculating algorithm, KIVA-3V calculates all the physical processes in the

cylinder chamber, and initial states of fluid (temperature, pressure, and composition of the mixture) in computational cells are computed. An interpolating subroutine is added in the KIVA-3V code to lookup chemical source terms from the reaction database. When computation of combustion is needed, instead of activating KIVA-3V subroutines (CHEM and CHEMEQ) to calculate the chemical reaction, the modified KIVA-3V issues a request to the interpolating subroutine. The request consists of information of needed reaction (species densities, temperature, and pressure of the mixture in the calculating cell along with reaction time). In the interpolating subroutine, species densities are normalized to the total density of the mixture, and indices of normalized species densities, temperature and pressure are calculated. Based on these indices and the instructions saved in the reaction database file, the interpolating subroutine locates the position of the reaction result in the database file (specifies where to find the coefficients for the fitted polynomial functions of the requested reaction). Once these coefficients are found, the normalized production rate of a requested chemical source term $\check{G}$ is obtained from equation (6.2.2). The normalized production rate is converted back to absolute value:

$$\dot{G} = \check{G} \times \rho \tag{6.3.1}$$

and the reaction result is:

$$G_2 = G_1 + \dot{G} \times \Delta t, \tag{6.3.2}$$

where ρ is the density of the mixture in the computing cell, Δt is requested reaction time, and G_1 is the value sent to the interpolating subroutine to request reaction results (initial condition for this reaction). The requested reaction time in turn depends on the calculating time step of the physical process, and computation of this time step is described in section 6.3.2.

6.3.2 Time step control

The time step for each calculating cycle in the pre-integrated approach, Δt, is taken from KIVA-3V. Because the Eulerian phase in KIVA-3V is computed explicitly, the convection time step must satisfy the Courant condition for stability. In rectangular mesh, this condition is:

$$\Delta t_{cr} \leq min(\frac{\Delta x}{|u - b_x|}, \frac{\Delta y}{|v - b_y|}, \frac{\Delta z}{|w - b_z|}), \tag{6.3.3}$$

where Δx, Δy, Δz are dimensions of the computational cell, and b_x, b_y, and b_z are the components of the grid velocity **b**. Constraint (6.3.3) limits the magnitude of the flux volume in any coordinate direction to a value less than the computational cell volume. For an arbitrary mesh, condition (6.3.3) is written as:

$$\Delta t_{cr}^{n} \leq \Delta t_{cr}^{n-1} min_{\alpha} \frac{V_{ijk}}{|\delta V_{\alpha}|}, \tag{6.3.4}$$

where V_{ijk} is volume of the computational cell (i, j, k), and δV_{α} are the flux volumes calculated for cell (i, j, k) using time step Δt_{cv}^{n-1}. In general for accuracy the time step Δt_{cr}^{n} is reduced by a factor l_{cv} with values of 0.2.

Since the Lagrangian phase in KIVA-3V is calculated implicitly, there is no stability restriction on Δt, but to ensure accuracy of the approach, Δt is constrained by several criteria.

The first accuracy condition on Δt is that:

$$|\frac{Du}{Dt}|\Delta t^2 < l_a \Delta x, \tag{6.3.5}$$

where l_a is positive real number (with value of about 0.5) and Δx is an average cell dimension.

The second criterion is the limitation of acceleration vertex velocities, Δt_a. The acceleration limit Δt_a is calculated as:

$$\Delta t_a^{n+1} = min_{(i,j,k)} \frac{l_a \, \Delta x_{i,j,k}}{|\mathbf{u}_{ijk}^{B} - \mathbf{u}_{ijk}^{n}|}, \tag{6.3.6}$$

where $\mathbf{u}$ is velocity and

$$\Delta \mathbf{x}_{ijk} = [(|\mathbf{x}_1 - \mathbf{x}_4|^2 |\mathbf{x}_2 - \mathbf{x}_3|^2 |\mathbf{x}_3 - \mathbf{x}_4|^2 |\mathbf{x}_2 - \mathbf{x}_1|^2 |\mathbf{x}_5 - \mathbf{x}_1|^2 |\mathbf{x}_8 - \mathbf{x}_4|^2)/6]^{\frac{1}{2}}. \tag{6.3.7}$$

In equation (6.3.7) $\mathbf{x}_i$ are position vectors of vertices of the computational cell.

The next accuracy condition on Δt is that:

$$|\lambda| \Delta t < l_{rd}, \tag{6.3.8}$$

where l_{rd} is of order unity and λ is an eigenvalue of the rate of strain tensor. This criterion limits the amount of cell distortion that can occur due to mesh movement in the Lagrangian phase. When cells become very distorted, the spatial accuracy of the difference approximations suffers. Constraint (6.3.8) limits the distance the upper and lower cell vertices can move relative to one another, divided by the cell height. Constraint (6.3.8) is enforced by calculating a time step Δt_{rd}. The limit for distortion of cells, Δt_{rd}, (used to ensure the spatial accuracy of the difference approximations) is the limit of the relative movement of upper and lower vertices of the cell divided by the cell height. Δt_{rd} is obtained as:

$$\Delta t_{rd}^{n+1} = min_{(i,j,k)} \frac{l_{rd}}{2\sqrt{a_{ijk}/3}}. \tag{6.3.9}$$

The fourth criterion is a limitation to couple accurately the flow field and source term due to chemical heat release, Δt_c. The energy released from the chemical reaction is kept lower than a small fraction of the internal energy of the cell. This is to limit the

maximum heat release due to chemical reaction, to ensure energy is released slowly from step to step. Δt_c is given by:

$$\Delta t_c = min_{ijk}\ l_c/[\frac{V^n_{ijk}(\dot{Q}^c)^n_{ijk}}{M^n_{ijk}\iota^n_{ijk}}], \tag{6.3.10}$$

where f_c is an input constant typically taken to be 0.1.

The fifth accuracy condition is the limitation of mass and energy exchange with the spray, Δt_s. This condition is to ensure the energy and mass exchanges between cell and spray do not exceed a small fraction of cell internal energy and of cell mass. The spray time step Δt_s is calculated from:

$$\Delta t_s = min_{ijk}\ \{l_c/[\frac{(\dot{\rho}^s)^n_{ijk}}{\rho^n_{ijk}}]\ , l_c/[\frac{V^n_{ijk}(\dot{Q}^s)^n_{ijk}}{M^n_{ijk}\iota^n_{ijk}}]\}. \tag{6.3.11}$$

The sixth criterion is a limitation for the growth of time step, Δt_{gr}. This is the maximum amount of time step can grow compared to the previous step. Δt_{gr} is given by:

$$\Delta t^{n+1}_{gr} = 1.02\Delta t^n_{gr}. \tag{6.3.12}$$

6.3.3 Existence and uniqueness

The existence and uniqueness of solution of the governing equation system introduced in chapter 3 has been analyzed elsewhere for the system used in KIVA-3V (for more detail see [135]). Therefore, in this work we concentrate on obtaining the chemical source terms from the reaction database, and their uniqueness.

A requested reaction result G is calculated by a fitted function, with its coefficients taken from the reaction database in a relevant matrix of subregion i. These coefficients in turn are computed from a system of (N_c+3) equations (6.2.2). This system is solved using $(N_c + 3)$ sets of reaction relations or points in the subregion i ($\dot{\bar{G}}$, $\bar{\rho}_m$, T, p).

However, there are more than $(N_c + 3)$ points in this subregion, say $(N_c + 3 + n_a)$, where n_a is an arbitrary positive number. Using different sets of points to calculate the coefficients $a^i_{m,G}$ will give slightly different results depending on the magnitude of the subregion. In our approach, all sets of points in the subregion are used to calculate the coefficients $a^i_{m,G}$ (in equation 6.2.3) and a spectrum of $a^i_{m,G}$ is created. Since the subregion is narrow, coefficients $a^i_{m,G}$ are concentrated, so that the average values of $a^i_{m,G}$ are used as the unique representative for their group. With the unique $a^i_{m,G}$, the chemical source term obtained from the reaction database is unique.

Because chemical reactions are calculated for all the possible ranges of reaction conditions in IC engines, the requested reaction results are always found in the reaction database. In exceptional cases, if the requested chemical source term can not be found, the interpolating subroutine reports to the main program to upgrade the reaction database file. Then SENKIN is used to calculate reaction results of these additional reaction conditions. To ensure the accuracy of the interpolating process, the results are bound within the subregion of interest. The values of the interpolated reaction results can not exceed the maximum or fall below the minimum values of the subregion. For instance, consider a subregion which contains reaction results of a mixture of methane and oxygen with mass fractions $40\% \div 42\%$ CH_4, and $60\% \div 58\%$ O_2, at 1200 K, and 2 bar. Within this subregion the maximum production rate of CO_2 is, say 0.0004 g/s. If a request for reaction results of methane/oxygen with reaction condition within this subregion is sent to the interpolating subroutine, even if the interpolated result for production rate of CO_2 exceeds 0.0004 g/s, the subroutine only returns the value of 0.0004 g/s. (In this case, the interpolated chemical source term is limited under the maximum value of the corresponding reaction result of this

subregion).

6.4 Effects of adding intermediate species into nitrogen

In the pre-integrated non-equilibrium combustion response mapping approach, detailed chemical kinetics reaction results are used to calculate combustion of air/fuel mixture. The detailed chemical reaction of the mixture involves many species (dozens of species in a light fuel like methane, hundreds of species in heavy fuel like diesel oil). Few species are chosen to represent the mixture (12 species in our specific calculation). This could affect the accuracy of the combustion prediction of both light and heavy fuels. The effects of this technique on combustion computation of each fuel are discussed in the following section.

6.4.1 Effect of equivalent N_2 adding technique on combustion of heavy fuel

When the equivalent N_2 adding technique is used in heavy fuel combustion, it increases the pressure and changes the structure of the mixture compared to the fully computed reaction rate. These influences are discussed here.

Increment of pressure

Since chemical reactions occur at molecular level and combustion starts with elementary reactions. Before combustion occurs in IC engines, fuel must be dissociated into smaller molecules. Dissociation of fuel is a multi-level process. In the first step fuel is decomposed into intermediate species. These species continue to dissociate in the following steps to become elementary species. For the case where the equivalent

N_2 adding technique causes the worst errors, we investigate combustion of a diesel engine fuelled with $C_{12}H_{26}$. Combustion of diesel oil consists of hundreds of intermediate species. At early stages of dissociation the molecular weight of the intermediate species is high compared to that of nitrogen N_2 (e.g. $C_{12}H_{26}$ may dissociate to $C_{12}H_{24}$ which is by about six times heavier than N_2). In fact during this stage the molecular weight of the intermediate species is closer to fuel than to N_2. Adding one molecule of $C_{12}H_{24}$ into N_2 has a similar effect to the introduction of 5 more molecules into the reaction system. This in turn creates overestimate of the increment of pressure. Suppose that the engine is operated at stoichiometric condition, and composition of air is 21% O_2, 78% N_2, and 1% other gasses. Addition of 6 times the correct number of molecules into N_2 increases total pressure about 4 percent due to the dominance of N_2 fraction in the mixture. The pressure shift due to the equivalent N_2 adding technique affects more heavier fuels like diesel oil. This effect is less severe with lighter fuels (but still heavier than N_2). The absolute increment of pressure is higher in the case of high compression ratio engines such as CI engines.

Accumulation of N_2

Another problem raised when adding all the less active species into N_2 is how to conserve total mass. One can argue that if we keep adding heavier intermediates into N_2, the structure of the combustible mixture is changed. Because of the dependence of reaction rates on the species concentration, the change of the mixture structure could lead to significant deviations from the real combustion process and causes errors in the computed formation of emissions. When all fuel has been already dissociated to heavy intermediates, but not to small species, one may see that there is no fuel to decompose and there is an abnormal fraction of N_2 (more than 78% because all

intermediate species have been added into N_2) in the mixture. Because there is no mechanism for N_2 to dissociate to species other than nitrogen atom (N), this could lead to a conclusion that all the intermediate species added in N_2 are not taken into consideration and the reaction could flame out due to lack of reactants. To keep the natural balance of mixture composition intermediates must be allowed to be extracted from N_2. The concentration of N_2 can roughly come back to its original value at the beginning of combustion. No intermediate species contributes to computed equivalent N_2 at the end of the reaction because all combustible elements are converted into products if the combustion is complete.

Effect of equivalent N_2 adding technique on reaction rates

The equivalent N_2 adding technique causes an increase of pressure and accumulation of N_2, changing reaction rates in the system. The increment of pressure is interpreted by the fluid dynamics calculation as there were more acting elements, and more collisions, and coalescence. However, in IC engines collision before combustion is a dominant process, thus accelerating dissociation of fuel. The accumulation of this unreal process results in computed combustion occurring sooner than reality. However, Warnatz et al. [22] and Thomas and William [136] show that the dissociation rate of unimolecular reaction is proportional to the logarithm of pressure within the pressure range at early stage of fuel decomposition in IC engines (under 20 bar).

There is a requirement to extract reactants from intermediates added in N_2. This can be seen as N_2 is "dissociated" to small intermediate reactants. In our approach, from the zero fuel moment described in section 6.4.1, even if there is no appearance of fuel in the mixture, combustion products are still created by the chemical reaction. Reactants are derived from artificial "decomposition" of N_2 until the concentration of

N_2 in the mixture comes back to its value at the beginning of reaction (about 78%). In other words, N_2 acts as an additive in the mixture. Its concentration increases to absorb intermediate species in early stages of fuel dissociation, and releases them later on for combustion. Our equivalent N_2 adding technique helps to treat the species of interest exactly at their real values, while appearance of other species is expressed through expansion and contraction of N_2 concentration. The equivalent N_2 adding technique does not introduce more error to the diffusion process since the fluid dynamics is calculated with the assumption of a single diffusive coefficient.

The change of the mixture composition also leads to variation of reaction rate. In a mixture, the overall reaction rate is much dependent on certain active species (Atkins [136]). In our approach, the most reactive species and species of interest are chosen to represent the mixture. Since they are the most active elements in the mixture, they can be used to describe the reaction behaviour of the mixture. In addition the upper and lower limits (maximum and minimum values of the production rates within the corresponding subregion) described in section 6.3 keep the reaction rates of the mixture within the accurate range.

6.4.2 Effect of equivalent N_2 adding technique on combustion of light fuel

The effects of the equivalent N_2 adding technique with light fuel combustion are less serious than those in the case of heavy fuel. The combustion of methane in a gas-fuelled Rover K4 engine (described in section 7.3.2) is discussed here. Since methane and intermediate species are lighter than N_2, the addition of intermediate species in N_2 slightly decreases pressure in the system. Because methane has low molecular weight, the dissociation process occurs very fast. With the dominance of N_2 in the

concentration the reduction of pressure is not high, and thus it does not significantly affect the combustion process. On the other hand, the species of interest which are taken into account are normally the direct products of methane decomposition. For these reasons it is safe to say that our equivalent N_2 adding technique does not seriously affect the combustion process of light fuels.

6.4.3 Advantages of equivalent N_2 adding technique over reduced reaction mechanism

The reduced chemical reaction mechanism is a compromise between chemical reaction accuracy and computational intensity. The reduced mechanism describes reaction of air/fuel mixture with simpler reactions and fewer species than the detailed chemical kinetics mechanism. The reduced mechanism also uses dozens of typical-most-active species to represent the mixture. Because of the limitation of the number of species taken into calculation, many intermediate species are omitted in the reduced mechanism (reaction of diesel oil involves hundreds of species in the detailed mechanism, but only dozens are used in the reduced one). The concentration of the omitted species are evenly added into the typical species. In the case of evenly adding, the addition of one $C_{12}H_{24}$ molecule into H_2 concentration causes an introduction of 83 more molecules into the system, resulting in 180% pressure increment. The advantage of our equivalent N_2 adding technique is very significant in heavy fuel cases such as diesel oil. In our approach, adding one intermediate $C_{12}H_{24}$ into the N_2 concentration causes 4% increment of pressure. Use of our equivalent N_2 adding technique permits the species of interest to be treated exactly, with the accuracy of detailed chemical kinetics reaction mechanism. On the other hand, the computational intensity is proportional to the exponent of the number of species in the system. Therefore, to keep

the accuracy of the chemical reaction, the reduced mechanism has to use more typical species than in our approach. This is another advantage of the equivalent N_2 adding technique.

6.5 Timescale conversion

Chemical reaction of air/fuel mixture in the combustion chamber of IC engines occurs at high temperature and pressure conditions. The timescale of chemical reactions is very short, while the timescale of fluid dynamics and motion of particles is much longer. Therefore, these two processes cannot be directly coupled. One physical time step includes many chemical time steps. The straight forward method to couple physical and chemical processes is to calculate all chemical reactions with their eigenvalue until the magnitude of reaction time approaches the value of the physical time step. Then the motion of fluid is computed. The two-step algorithm, first calculating physical phenomena, then wait for many chemical computations, then another jump for fluid dynamics is similar to the DNS idea, except that it is used for different eigenvalue processes. Thus, this algorithm is impractical for current computer abilities.

The pre-integrated method permits coupling the physical and chemical processes directly by decoupling the chemical eigenvalue and re-coupling into the physical eigenvalue. Instead of calculating fluid dynamics and waiting for many chemical time steps, the two processes are computed in parallel mode using the same eigenvalue. It is not too difficult to decouple the chemical reaction eigenvalue, but the decision to recreate the reaction result in physical eigenvalues may affect the accuracy of the interpolating process. The eigenvalue of turbulence processes lies within a range of $10^{-5} \div 10^{-2}$ depending on Reynolds number. If the re-coupled eigenvalue is too high, an inversion

phenomenon occurs. One chemical calculating step will see some physical step "past" it. This causes errors in the coupling process. On the other hand, if the re-coupled eigenvalue is low, one physical calculating process will "watch" some chemical steps pass through. This causes errors in the coupling process too. But the latter is the better option for accuracy. The reason is that chemical reactions are highly nonlinear compared to the fluid dynamics process, so that chemical reactions should be treated in small time steps to avoid linearization errors. The ideal option is to re-couple the chemical eigenvalue into the exact eigenvalue of the fluid dynamics process. However, Reynolds number in IC engines during the combustion process varies from location to location, and from crank angle to crank angle. This leads to variations of the fluid dynamics eigenvalue throughout the combustion process. Therefore, the re-coupling of eigenvalues should be a dependent variable of the fluid dynamic processes in the cylinder chamber. However, the detailed chemical kinetics calculation gives no information about the Reynolds number of the fluid inside the combustion chamber. It only supplies information about how fast and vigorous is the reaction depending on the reaction condition. Therefore, the re-coupled eigenvalue is determined using the reaction speed criteria. The value of the re-coupling timescale is inversely proportional to reaction speed. Reaction speed in turn depends on temperature and species concentrations. If the reaction occurs fast then the re-coupled timescale is small, and vice versa. Although using reaction rates as a representative for physical timescale in determining the re-coupled eigenvalue is not quite correct, there are reasons to support this approach. Combustion occurs locally at the molecular level. It can only occur vigorously if reactant and oxygen are mixed in a microscopic sense. It is safe to say that turbulence in the combustion chamber helps to improve the mixing quality

of reactant and oxygen. High mixing quality and high temperature in the combustion chamber increases reaction speed. Thus, turbulence has an effect on reaction rate. Using the reaction speed to indirectly represent the fluid dynamics timescale is acceptable. It is a good idea to run the engine modeling program (such as KIVA-3V) with its default chemical reaction routine to obtain the general range of re-coupled timescales. However, the physical eigenvalue of the fluid dynamics calculation in the combustion chamber depends on the resolution of the mesh of engine geometry. The higher the resolution of the mesh leads to smaller eigenvalue, and then the re-coupled eigenvalue must be smaller. Thus, one can conclude that using the database file (which is re-coupled using high eigenvalue) for a low resolution engine geometry mesh will cause errors. In other words, the accuracy of the solution is inversely proportional to mesh resolution. To avoid this effect, the re-coupled eigenvalue is specified to match the eigenvalue of the physical process for the finest intended mesh. (This depends on the computer ability and the required accuracy). In this case, the physical timescale increases with the dimension of the mesh and becomes larger than the re-coupled timescale. Thus, the database file can be used for coarser mesh with smaller error than when the re-couple timescale is larger than the physical timescale.

6.6 Summary

In the pre-integrated approach, chemical kinetics reaction of air/fuel mixture is calculated prior to engine modeling. The reaction results are converted from the chemical timescale to the physical timescale, discretized, normalized, then represented by fitted polynomial functions. The coefficients of the fitted functions are computed using a Newton-Seidel iteration method and stored in matrix form in a database file. Physical

processes in the cylinder chamber and temperature, pressure, and species densities of the mixture of the computational cells are calculated by KIVA-3V. When combustion occurs, the chemical source terms are obtained from the database file using an interpolating subroutine.

The approach avoids the direct calculation of chemical reactions while still obtains the high accuracy of the detailed reaction mechanism. This saves much memory and computer time for engine modeling, and improves the accuracy of emissions prediction.

The drawback of the approach is the creation of a reaction database file, which contains results of all possible reaction conditions in IC engines. This is very time consuming on a conventional computer. However, the reaction database file for a certain fuel needs to be created once, then it can be used for all the engines running on this kind of fuel.

The approach is validated by comparison with experiments on three types of engine: diesel, gasoline, and gas-fuelled engines. Details of experiments, sample computations for validation, and comparison between predicted results and experimental data are included in chapter 7. Results and discussions are presented in chapter 8. Recommendations for improving the accuracy of the approach are given in chapter 10.

Chapter 7

Experiments and sample calculations

This chapter reviews the measuring technique, and the experimental setups of three types of engine: CI diesel, gas-fuelled SI, and SI gasoline engine. The pre-integrated approach is applied to calculate emissions at certain operating conditions of these engines.

7.1 Review of measuring techniques in IC engines

Parallel to the requirement for the development of an engine emissions modeling method, there is a requirement for accurate experimental data to validate the calculated results from simulations. Experimental techniques are continuously improving. In IC engine applications, specially in modeling engine operation and emissions, the most important data for validation are in-cylinder temperature, pressure, and species concentration. This section presents techniques used to measure these data in IC engine.

7.1.1 In-cylinder temperature measurement

In-cylinder temperature plays an important role in the formation of emissions such as NO_x, CO, CO_2, etc. In addition, in-cylinder temperature determines autoignition characteristics, chemical reaction of air/fuel mixture, heat transfer to wall, and thermal stress of wall materials. There are several methods developed to measure in-cylinder temperature. They can be classified in three groups: 1) radiation thermometers, 2) velocity of sound method, and 3) spectroscopic techniques.

Radiation thermometers operate based on the detection of thermal radiation of gases in the cylinder. In 1932, Withrow and Rassveiler [137] developed the sodium-line reversal method, a particular application of the Null method. A calibrated tungsten lamp was used as the light source in their experiment on a gasoline engine, sodium was seeded in the cylinder chamber, and a spectroscope was used to detect radiation from the light source through the cylinder gas. The temperature of the light source was adjusted until the sodium lines in the spectroscope change from emission to absorption (from brighter than continuum spectra to darker). The temperature of the in-cylinder gas was specified as the temperature of the light source. In this experiment they found that temperature of gas in the vicinity of the spark plug was hundreds of degrees higher than that of the far end of the combustion chamber. In the sodium-line reversal method the temperature of the cylinder gas was measured at a particular crank angle. To measure temperature as a function of crank angle, Millar et al. [138] developed the emission-absorption method. In this method a chopper was placed between the light source and the engine cylinder. Radiation of the light source, of the gas in the cylinder (when the chopper obscured the light source to the cylinder chamber), and of the combination of the light source and gas were detected.

Temperature of the cylinder gas is calculated from Kirchhoff's law. Addition of sodium in the cylinder chamber in radiation thermometer causes interference with the combustion process. The radiation thermometers measure average temperature over the line-of-sight of the burned gas and can not be used to measure temperature of unburned gas. It is necessary to avoid excess radiation, such as chemiluminescence in electronic transformation. In the 1940s, Uyehara et al. [139] introduced the two-color method for temperature measurement in diesel engines. The two-color method is a particular application of the radiation thermometry. In this method, thermal radiation at two different wavelengths is detected, and the flame temperature is then determined from their ratio using Planck's equation. The two-color method has been developed to measure full-field temperature [140, 141]. In 1989 Kawamura et al. [142] extended the application of the two-color method to an SI engine by seeding the intake air with fine alumina particles. The radiation from burning of these particles was detected to measure the temperature of the flame.

In 1954 Livengood et al. [143] developed a velocity-of-sound method to measure temperature of gas in the cylinder chamber. The method is based on the dependence of velocity of sound on temperature. In their experiment a barium titanate ceramic crystal was mounted on a water-cooled rod, and it was excited by a 2.5 MHz oscillating circuit. The flight path of sound was 15 mm. The sound signal was detected and velocity of sound was calculated based on the measured flight time. Comparisons were made to measured results from radiation thermometers. A good agreement was obtained. Recently Bauer et al. [144] developed the velocity-of-sound method to measure temperature for both burnt and unburned gases. A pent-roof cylinder head engine fitted with two transducers was used in the experiment. Uncertainties due

to the flight time and gas composition were analyzed. They found that temperature measured using this method was close to the mass-average gas temperature. However, the sound signal was too weak in cases of high pressure and low temperature in the cylinder.

In 1980 Smith [145] used the Stokes-anti-Stokes method, a particular application of Spontaneous Raman Scattering (SRS), to measure temperature in an engine cylinder. The experiment was carried out on a transparent-cylinder head engine, and an Nd:YAG laser and spectrometer were used. The laser beam was focused onto small scattering volume. Stokes Raman signal at 607 ± 1 nm and anti-Stokes Raman signal at 474 ± 1 nm from the scattered light were detected by two photomultipliers. The measured results were calibrated using a radiation corrected thermocouple. Over 350 measurements had been made, and the precision of measurement was within 10 K. The experiment showed that the highest temperature in the combustion chamber was obtained at equivalence ratio of ϕ=0.9.

The Laser Rayleigh Scattering (LRS) method was used to measure two-dimensional temperature distributions in a transparent square piston methane-fuelled SI engine by Orth et al. [146] in 1994. In this experiment, a tunable KrF excimer laser was used, scattered light was imaged by a gated intensified charge coupled device (ICCD) at right angle. Light fluorescence was filtered using narrow bandpass filters. Calibration was made with an air/fuel mixture in a motored engine. Accurate temperature measurements were obtained, but the experimental procedure was too complex to eliminate the effects of background light from the cylinder wall and air-borne particles.

The first in-cylinder temperature measurement using coherent anti-Stokes Raman

scattering was made by Stenhouse et al. [147] in 1979. The measurement was carried out on a Ricardo E6 engine. The collinear scanned method was used with the pump beam created from an Nd:YAG laser and Stokes beam from a narrow dye laser. Because of the long ensemble-averaging time, the measured temperature was affected by unstable combustion during the measurement period.

To overcome the drawbacks of the scanning method and laser fluctuations, Marie and Cottereau [148] used broadband CARS with collinear scheme. They divided the coherent anti-Stokes Raman scattering (CARS) signal by the non-resonant CARS signal from a reference cell. Temperature was derived by fitting the complete CARS spectrum to the theoretical one. The accuracy of averaged temperature was within $\pm$ 50 K.

Temperature measurement using a dual-broadband rotational CARS was reported by Bood el at. [149] in 1997. They used one narrow-band laser beam and two broad-band laser beams. One of the red dye laser beam (Stokes beam) was superimposed on the green Nd:YAG laser beam (pump beam). The superimposed laser beams and the red beam were parallel, then focused onto a probe volume using an optical lens. In their experiment, the measured temperatures agreed well with the calculated ones.

Laser induced fluorescence (LIF) has also been used to measure in-cylinder temperature. A particular application of LIF is two-line fluorescence thermometry. In 1983 Gross and McKenzie [150] used two dye lasers sharing the same pumping laser to excite gas molecule. The relative population of two excited states was detected by two gated ICCD cameras. Temperature was calculated via the Boltzmann expression. They obtained a precision of 14 % on single-shot temperature distributions.

7.1.2 Species concentration measurement

Sampling and spectroscopic techniques are commonly used to measure species concentration in IC engines. Matsui et al. [151] employed a high-speed intermittent sampling technique to measure CO_2 concentration. In their experiment, in-cylinder gas was sampled by a needle-type sampling valve incorporated in the spark plug. The sample was diluted by helium and then fed to a CO_2 analyzer. The analyzer had a reduced measuring cell capacity to enhance fast response, thus allowing cycle resolved measurements of CO_2 concentration.

Aoyagi et al. [152] sampled NO and NO_2 from the combustion chamber of a direct injection (DI) diesel engine. A line conveying the sample from the valve, and the glass vessel were heated to 120 ^{0}C. Before collecting the sample, the sample lines and the glass vessel were evacuated, then the gas sample was filled in at a pressure of 1.2 bar. NO and NO_2 were measured by a chemiluminescence analyzer. Measurement of CO, CO_2 were made using gas chromatography. The gas sample was fed into an evacuated syringe, maintained at 200^{0}C, then driven out after the measurement.

In the experiments of Bäcker et al. [153], the sample gas from a DI diesel engine was diluted with nitrogen gas before CO, CO_2, and NO were measured using nondispersive infrared gas analyzer (NDIR) and a Flame inonization detector.

The first application of total cylinder dumping technique was reported by Voiculescu and Borman in 1978 [154]. Total in-cylinder concentration as a function of crank angle was obtained. The results represented NO concentrations spatially averaged over 75% of cylinder mass at a given crank angle. The experimental data showed that the NO histories had a rapid rise time of 17^0 to 25^0 crank angle (CA). The maximum in-cylinder NO concentration could exceed the exhaust concentrations by as much as

14%.

Using the same techniques as in-cylinder measurement, exhaust species concentrations were measured by many authors. Uludogan et al. [155] sampled exhaust gas from a surge exhaust tank, while in the experiment of Ball et al. [156, 157], gas samples were taken from the exhaust manifold.

Spectroscopic techniques were widely used for species concentration measurement. Lebel and Cottereau [158] used CARS to measure CO_2 concentration in an IC engine. Since it is expensive and complex, use of CARS was limited in single-point and single species measurement. In 1986, SRS was used by Sawerysyn et al. [159] to measure N_2, H_2O, CO, CO_2, O_2, and fuel. They used an Nd:YAG laser (532 nm) and a spatially resolved optical multi-channel detector to detect Raman scattering. But they concluded that it was not possible to obtain quantitative single-shot measurements because of the weak signals and the insensitive TV camera used in their experiment. To measure mole fraction of H_2O, CO_2, O_2, and fuel in a simple pancake type research engine, Miles and Dilligan [160] used an Nd:YAG laser (532 nm) and a back-illuminated charge coupled device (CCD) detector. Single-shot and cycle-resolved measurements were carried out. In their setup, the spectrograph entrance slit was oriented so that the slit was parallel to the laser beam. The light scattered from a portion of the laser beam was focused onto the entrance slit. In turn, the spectrograph formed multiple, spectrally dispersed images of the entrance slit onto the two-dimensional CCD array at the spectrograph exit. The vertical axis of the image on the CCD detector was a linear extension of the measurement along the incident laser beam. It imaged several millimeters along the laser beam. In the same image, the horizontal axis corresponded to wavelength, and it contained information

on the species concentration at a given spatial location.

In 1967, Newhall and Starkman [161] developed a spectroscopic system to measure transient NO concentration during the engine expansion process of a single-cylinder CFR engine using infrared radiation. The infrared radiation was detected by a monochromator and an infrared detector. The time-resolved output from the detector was recorded by an oscilloscope and averaged over 50-100 cycles. The NO concentration was inferred from its infrared radiation at 5.3 μm. Since emissions at 5.3 μm arises from both NO and CO_2 spectral bands, they derived NO concentration from measured emission intensity with CO_2 concentration calculated based on chemical equilibrium. Their results confirmed the theoretical prediction that nitric oxide is formed in approximate equilibrium quantities in the combustion process, and it was frozen at a level well above the equilibrium value during the early part of expansion stroke. But their time-resolved gave NO concentrations considerably in excess of equilibrium composition at the peak pressure and temperature, compared to predictions by their theoretical studies. Lavoie et al. [162] carried out an experiment on a single-cylinder, L-head CFR engine with a time-resolved spectroscopic technique based on measurement of emitted light intensities from the NO + O and CO + O recombination continua. In their setup, a number of small quartz windows allowed light emission measurements to be made at different positions along the flame path. The light emitted from a small volume of gas was detected by photomultiplier/interference filters pairs at 0.31 μm, 0.38μm, and 0.61 μm. Measurements made by Lavoie et al. [162] at two different windows, one closer to the spark plug than the other, showed that the NO concentration was higher near the spark plug. They also found that there was a negligible measured amount of NO produced at the flame front under

the engine operating condition tested. The measured values of NO concentrations exhibited non-equilibrium behavior and agreed rather well with computations using the extended Zeldovich mechanism.

7.1.3 In-cylinder pressure measurement

The most common method to measure in-cylinder pressure profile is using piezo-electric pressure transducers. Detail of experimental setup for this measurement is presented in section 7.2.

7.2 Experiments

To validate the pre-integrated non-equilibrium combustion response mapping approach for predicting operation and emissions of IC engines, the predicted results are compared to the experimental data. The experimental data were taken from other author's work in three types of engines: CI engine [155], methane-fuelled SI engine [156, 157], and gasoline SI engine [163]. We conducted additional measurements on Toledo 1500 gasoline engine and results obtained are compared with computations in section 8.

7.2.1 Compression ignition diesel engine

The experimental data for CI diesel engine are taken from the work of Uludogan et al. [155]. The test engine is an instrumented Caterpillar 3401 single-cylinder heavy-duty four-stroke diesel engine. The engine was fuelled with commercial diesel oil. The specifications of the engine are given in table 7.1. In the experiment the engine was operated at 2100 rev/min with power output of 54 kW. Fuel consumption was 0.1622 g/cycle.

The experimental setup is illustrated in figure 7.1. The cylinder pressure profile was measured using Kistler Model 6061-A piezoelectric transducer. The transducer was water cooled to reduce the effect of thermal shock on measuring pressure. The crankshaft was fitted with BEI optical shaft encoder. The signals from the pressure transducer and shaft encoder were sent to a PEI data acquisition system, where pressure was recorded as a function of crankshaft position.

To measure nitrogen oxides (NO/NO_x) emissions, a chemiluminescence analyzer (Thermo Environmental Instruments Inc., model 10S) was used. Horiba infrared gas analyzers were used to monitor carbon monoxide (CO) and carbon dioxide (CO_2) concentrations. An exhaust surge tank was used to regulate the pressure variation of the exhaust gas from the engine. The gaseous sample for emissions measurement was taken from the surge tank using a single probe. The probe was designed according to SAE J177 specifications. Since the infrared and chemiluminescence gas analyzer can be damaged by water vapor, the gas sample was dried before entering the system using an ice bath and a Drierite desiccant dryer. The ice bath also helps to cool down the sample gas and to freeze further the reaction of the burnt gas mixture. Gas also was driven through filters where large particulates were filtered out [164].

The fuel flow measurement were made by weighting a fuel tank at the beginning and the end of each testing period. The testing periods were approximately 15 minutes long. The scale used was a CCI, model TLEC-50 with 0.02 kg resolution. Temperature of inlet air and exhaust gas were measured by K type thermocouples. The engine intake air was metered using a metering orifice [165].

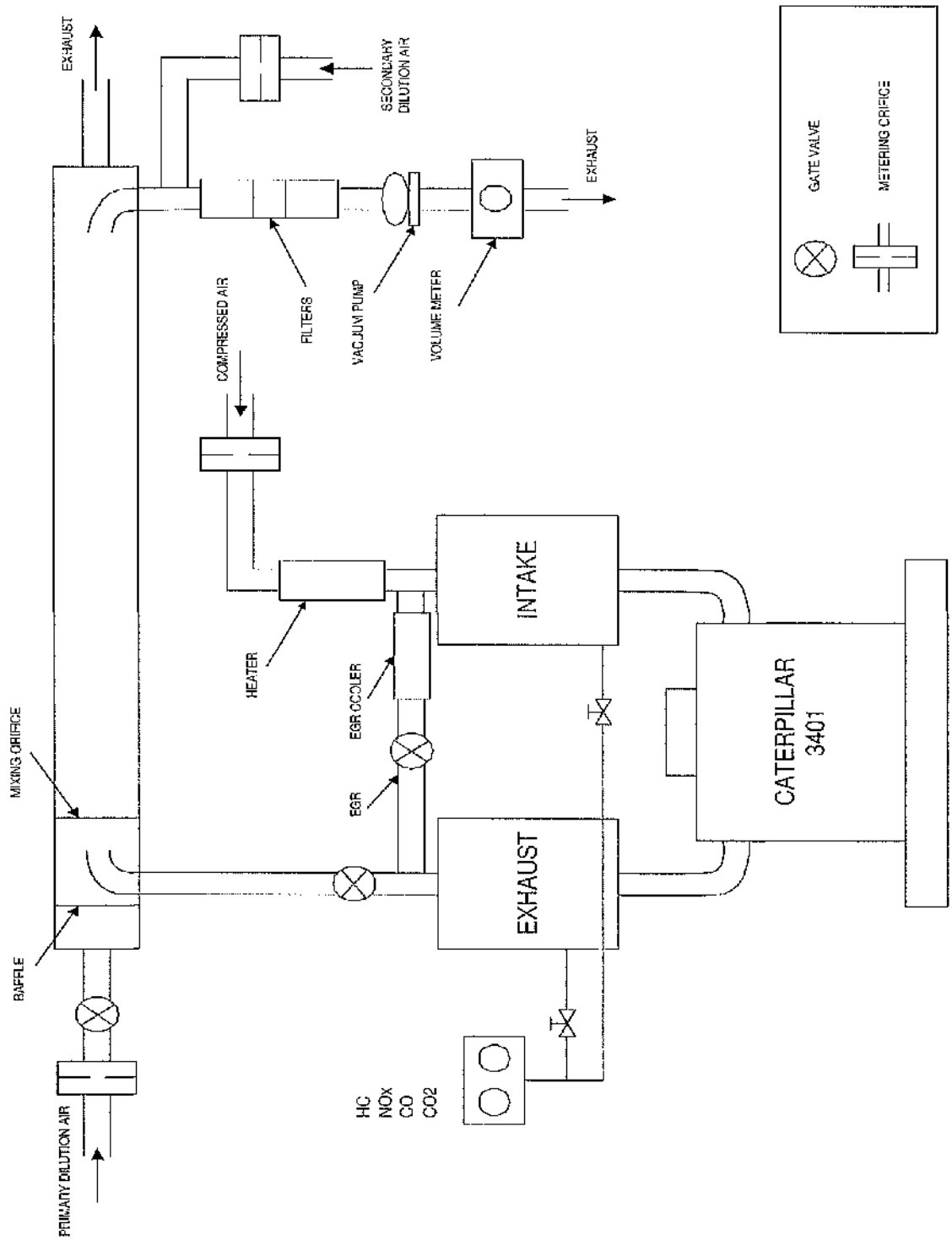

Figure 7.1: Caterpillar 3401 diesel engine experimental setup (from [155])

Bore	137.6 mm
Stroke	165.1 mm
Squish	4.58 mm
Connecting rod	261.62 mm
Compression ratio	15.1:1
Number of nozzle orifices	6
Volume displacement	2.44 l
Piston crown	Mexican hat
Cylinder head	flat
Fuel injection crank angle	349^0
Duration of injection pulse	21.5

Table 7.1: Specifications of the Caterpillar 3401 diesel engine

7.2.2 Spark ignition methane-fuelled engine

The experimental data for the gas-fuelled spark ignition engine were taken from the work of Ball et al. [156, 157]. The experiments were carried out on a Rover K4 four-stroke optical access engine. The engine was tested at speed of 1000 rev/min with equivalence ratio ϕ=1 and wide open throttle (WOT). The experimental setup is illustrated in figure 7.2. The specifications of the Rover K4 engine are presented in table 7.2. The cylinder was fitted with two pressure transducers, one piezoresistive and one piezoelectric. The piezoresistive transducer was mounted in the cylinder barrel. The piezoelectric transducer was fitted on the cylinder head. The data acquisition system records the cylinder pressure, crank flag, barrel pressure at each degree of crank angle interval.

A fast chemiluminescence detector (CLD)was used to measure NO exhaust emissions with response time of the order of a few milliseconds. The sampling system delivers the sample to the chemiluminescence chamber where it is mixed with a flow of ozonized air. The resulting chemiluminescence reaction produces photons in the 700-1500 nm wavelength range which are detected with a photomultiplier tube.

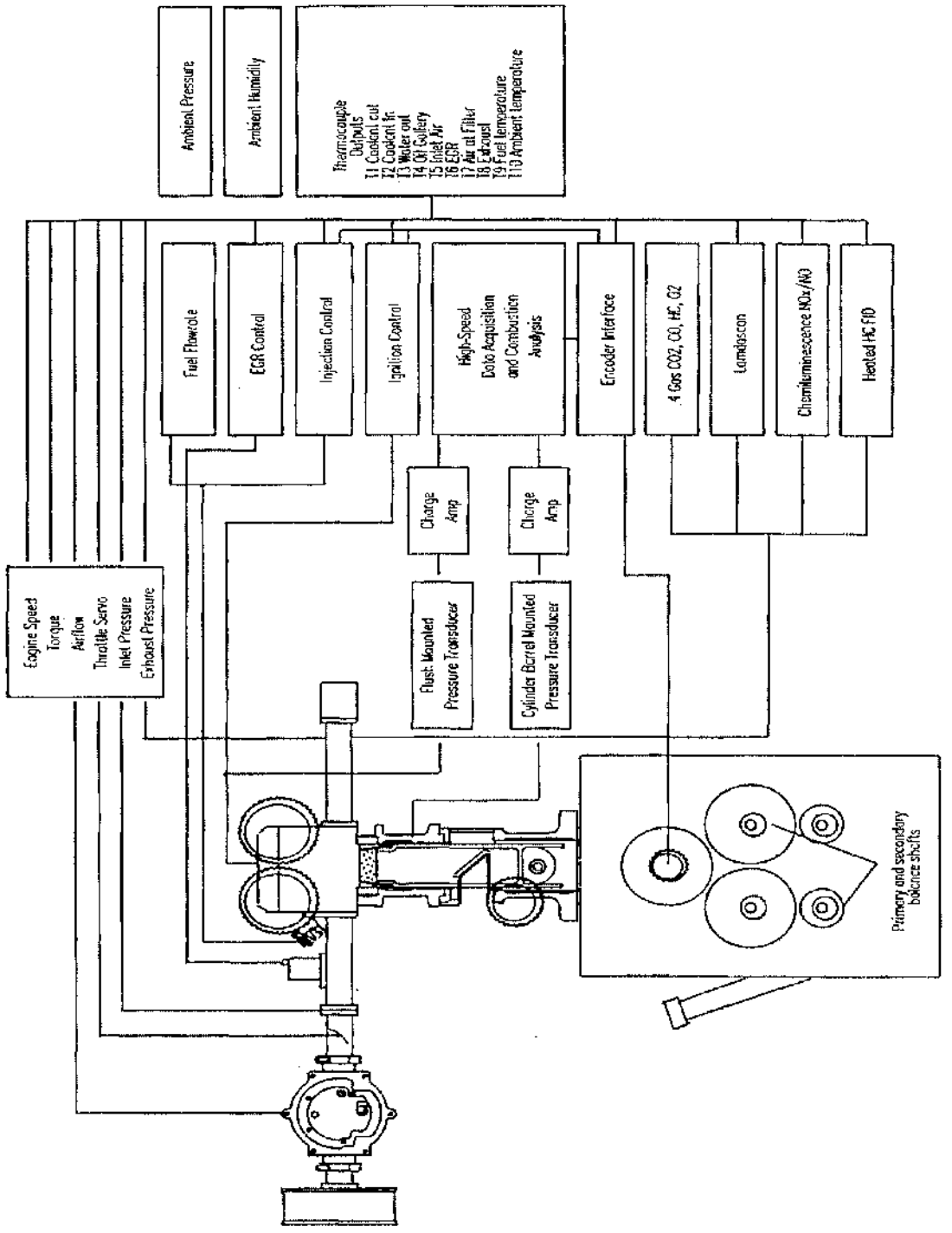

Figure 7.2: Rover K4 methane-fuelled engine experimental setup (from [156])

Main specifications	
Bore	80.0 mm
Stroke	89.0 mm
Squish	1.15 mm
Connecting rod	160.0 mm
Compression ratio	10:1
Number of valve	4
Cam timing	
IVO	-12^0 BTDC
IVC	52^0 ABDC
Peak lift inlet	8.8 mm at 70^0 BBDC
EVO	52^0 BBDC
EVC	12^0 ATDC
Peak lift exhaust	8.8 mm at 70^0 ABDC
Cylinder head	
Type	Rover K16 1.4 MPI
Pent angle	45^0
Inlet valve seat diameter	24.0 mm
Exhaust valve seat diameter	19.6 mm
Piston head	flat

Table 7.2: Specifications of the Rover K4 methane-fuelled engine

The gas reaction chamber of fast CLD was housed in a remote sampling head so that sampling may be performed close to the exhaust system. The probe for the fast CLD was inserted into the exhaust pipe at a point 50 mm from the exhaust port outlet, and exhaust pipe diameter is 40 mm. The light from the chamber was transferred to the photomultiplier by a fibre-optic bundle. The main control unit also housed power supply, electronics, ozone generator, and vacuum regulators. Because the CLD measures only NO, NO_2 in the sample was converted to NO prior to detection. Since NO typically accounts for more than 95 percent of NO_x in SI engine [19] the conversion process would not have a detrimental effect on the response time of the instrument. Calibration of the fast CLD was accomplished by flooding the sampling chamber with

nitrogen to set the zero. The chamber was then flooded with a span gas of known NO concentration (2390 ppm) to set the span.

7.2.3 Ricardo E6 CFR SI petrol gasoline engine

The experimental data for Ricardo E6 SI co-operative fuel research (CFR) SI gasoline engine were taken from the work of Sodré [163]. The specifications of the Ricardo E6 engine are presented in table 7.3. This experiment concentrates on emissions

Main specifications	
Bore	76.22 mm
Stroke	111.23 mm
Squish	15.589 mm
Connecting rod	241.30 mm
Compression ratio	variable (6.0÷8.8)
Cylinder head	flat
Piston head	flat
Cam timing	
IVO	-3^0 BTDC
IVC	88^0 ABDC
Peak lift inlet	8.4 mm at 45^0 BBDC
EVO	37^0 BBDC
EVC	5^0 ATDC
Peak lift exhaust	8.4 mm at 74^0 ABDC

Table 7.3: Specifications of the Ricardo E6 CFR gasoline engine

measurement, so that no pressure data was recorded. The gas samples were taken from the exhaust pipe, in the location close to the port. The gaseous emissions measuring apparatus were similar to those used in the methane-fuelled SI engine and CI diesel tests described in section 7.2.2 and 7.2.1. The concentrations of carbon monoxide (CO) and carbon dioxide (CO_2) in the exhaust were measured with non-dispersive infrared equipment. Oxides of nitrogen (NO_x) were measured using a chemiluminescence analyzer.

The engine was run using commercial gasoline. The maximum tested speed of the engine was 2200 rpm at WOT; air/fuel mass ratio varied from 12.0 to 20.0, corresponding to equivalence ratio from ϕ=0.755 to ϕ=1.258.

7.2.4 Toledo 1500 SI gasoline engine

Experiments were carried out on a Toledo 1500 four-stroke SI gasoline engine. The engine is fitted with an HD hydraulic dynamometer, shown in figure 7.3. The specifications of the engine are presented in table 7.4.

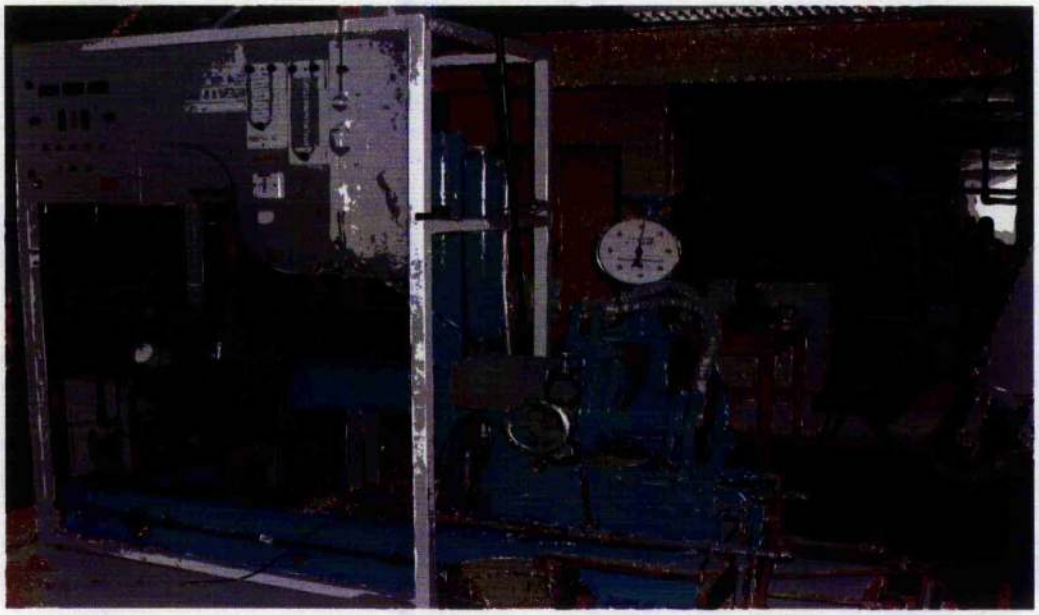

Figure 7.3: Toledo 1500 gasoline engine and dynamometer

In this experiment the averaged air flow rate was measured using an air box with an orifice plate. The design of the air box follows BS 1042 (1964); the box has volume of 0.2 m^3, the orifice diameter is 0.05 m, and a 0.07 m diameter pipe is used to connect the air box with the inlet manifold. The sketch of the air flow rate measurement setup is shown in figure 7.4.

Main specifications	
Bore	73.66 mm
Stroke	87.38 mm
Squish	10.00 mm
Connecting rod	241.30 mm
Compression ratio	9:1
Cylinder head	flat
Piston head	flat
Cam timing	
IVO	-6^0 BTDC
IVC	87^0 ABDC
Peak lift inlet	8.1 mm at 44^0 BBDC
EVO	35^0 BBDC
EVC	6^0 ATDC
Peak lift exhaust	8.1 mm at 76^0 ABDC

Table 7.4: Specifications of the Toledo 1500 SI gasoline engine

The averaged fuel consumption was measured using the Burette method. This method relies on recording the time taken for the engine to consume a certain volume of fuel. The sketch of the fuel consumption measurement setup is shown in figure 7.5. The consumption of the fuel for a calibrated volume in the burette was timed using a stopwatch by observing the level of the fuel menicus descending past two spacers.

The in-cylinder pressure was measured using a piezoelectric pressure transducer (Kistler 6061B) with measuring range from 0 to 250 bars. The piezoelectric pressure transducer is mounted on the cylinder head in the squish region with a passes of 4 mm in diameter. To reduce the effect of thermal shock on measured pressure, the transducer is water cooled. Water is branched from the engine cooling system and led through the cooling chamber of the pressure transducer. The weak signals (25pC$\sim$1 bar) from the transducer were transferred in a shield cable and amplified using a Kistler charge amplifier (5041E type) before being fed to a personal computer (PC).

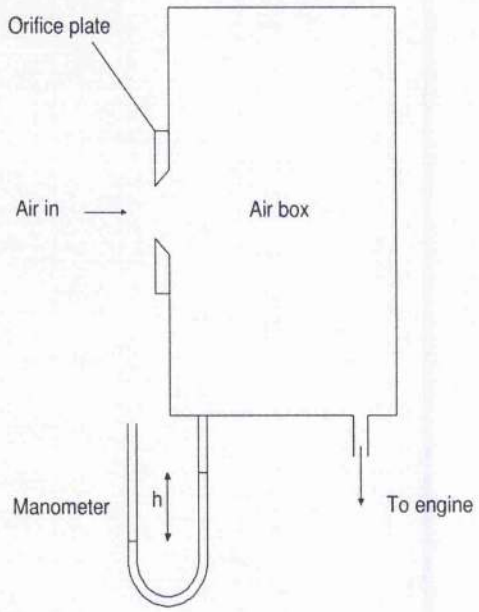

Figure 7.4: Setup for air flow rate measurement

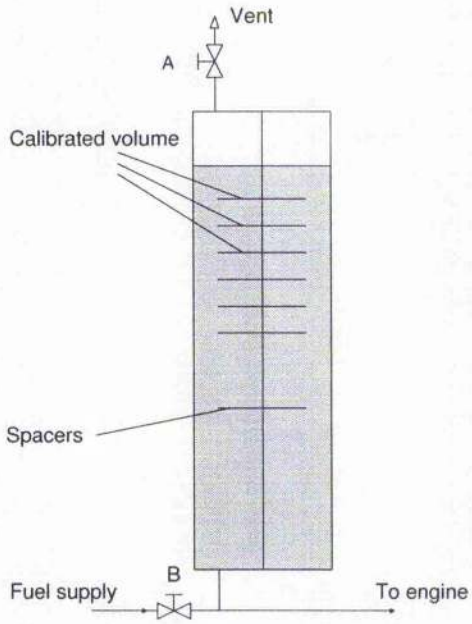

Figure 7.5: Setup for fuel consumption measurement

The setup for pressure measurement is illustrated in figure 7.6. TDC of the piston was detected using an infrared shaft encoder system fitted on the crankshaft.

CO_2, CO, and NO concentrations were measured using the sampling technique. The experimental setup for emissions measurement is illustrated in figure 7.7. The exhaust gas was sampled from a point 60 mm from the exhaust manifold outlet. The exhaust manifold diameter is 50 mm. The exhaust gas was pumped through the measuring system using a vacuum pump. In the filtration system water vapor and particulates larger than 1 μm were filtered. The exhaust gas was pumped to the sample cell of the nondispersive infrared gas analyzer, where CO, CO_2, and unburned hydrocarbon were measured, then the sample gas was led through NO_x and O_2 electrochemical sensors, and driven out. In the sampling system, filters also act as pressure regulators for the exhaust gas. The pressure pulsation of the gas sample

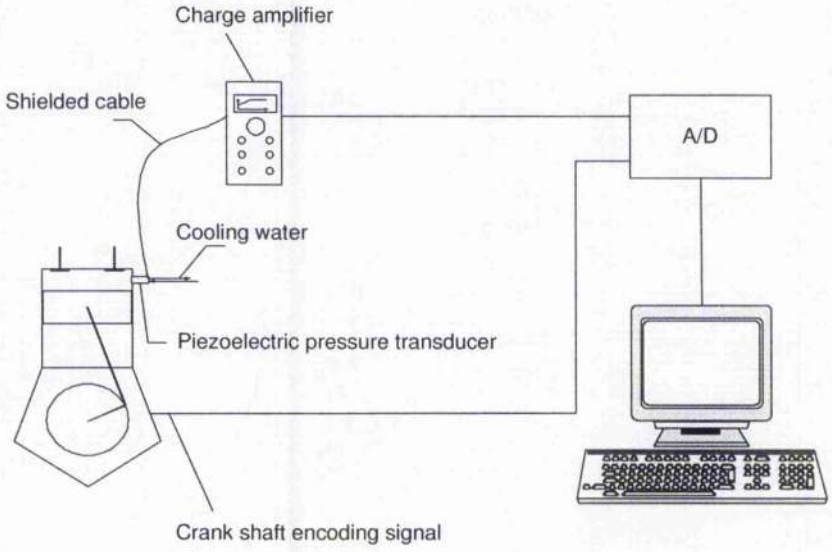

Figure 7.6: Pressure measurement setup

in the measuring cell was smoothed due to the expansion of gas in the filter volumes.

The Toledo 1500 engine was operated in three modes:

Mode A: the engine was tested at constant throttle (1/2 WOT), ignition timing was adjusted from θ=-30^0 BTDC to θ=10^0 ATDC, and dynamometer was controlled to keep engine speed constant at 1800 rpm;

Mode B: the engine was tested at maximum load of the dynamometer, ignition timing θ=-30^0 BTDC, and engine speed varying from 1500 rpm to 3500 rpm;

Mode C: the engine was tested at 2/3 WOT, ignition timing at θ=-30^0 BTDC, and the dynamometer was adjusted to vary engine speed from 1500 rpm to 3500 rpm.

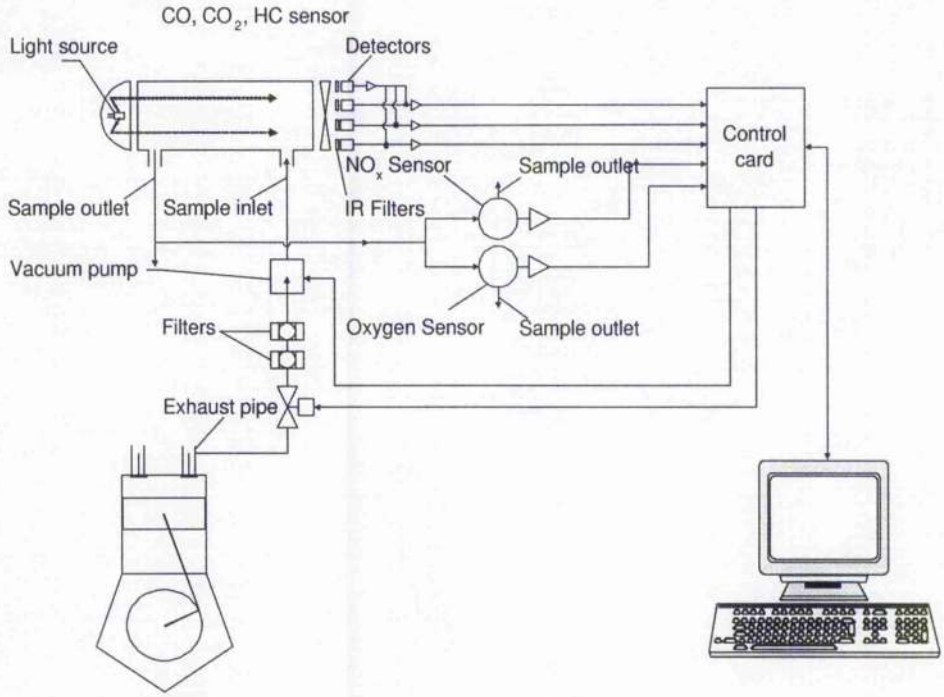

Figure 7.7: Experimental setup for emissions measurement in the Toledo 1500 gasoline engine

7.3 Sample calculations

Since this study concentrates on the emissions prediction, predicted CO, CO_2 and NO_x as well as in cylinder pressure profile were compared to the data obtained from experiments. It could be better if the in cylinder temperature profiles were measured and compared to the calculated results to enhance validation. However, temperature in the cylinder varies from location to location, and the temperature fluctuation is too fast compared to the response time of conventional temperature apparatus such as thermocouple. Because of lack of fast response temperature measuring equipment, the comparison of temperature profiles was omitted. The computational meshes for all four modeling cases were created by K3PREP, a mesh generator in the KIVA-3V package. KIVA-3V code was modified to write graphic output in TECPLOT format for post processing. In four cases the reaction database files were created by running in parallel two Dell PCs (2.4 GHz CPU). SENKIN was used to calculate reaction of air/fuel mixture with equivalence ratio from 0.2 to 5.0 in increments of 0.05; the initial temperatures of reactions was from 700 K to 1800 K with steps of 20 K. Initial pressures of reactions varied from 10 bar to 140 bar with interval of 1 bar. The engine simulations were carried out on a Dell Power Edge 2600 (2 x 2.4 GHz CPU) server.

7.3.1 Modeling of Caterpillar 3401 CI diesel engine

The pre-integrated approach is applied to model operation and emissions of the Caterpillar 3401 CI diesel engine. Because of the symmetry of the combustion chamber, the computational mesh was created for 60 degrees to save computer time. The computational mesh consists of 22000 cells, partly illustrated in figure 7.8.

In this calculating sample, $C_{12}H_{26}$ was used to simulate reaction of diesel oil. The

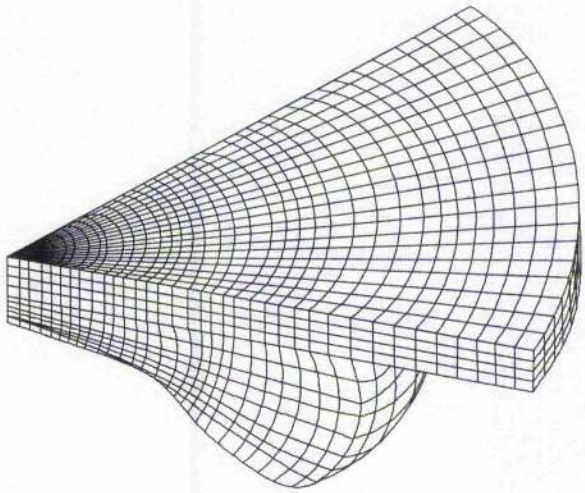

Figure 7.8: Modeling mesh for the Caterpillar 3401 diesel engine

detailed chemical kinetics reaction mechanism was supplied by Glaude [166] with inclusion of NO_x reaction mechanism of Sandia National Laboratories. The reaction mechanism consists of 821 species and 4491 reactions. Generation of the database file for diesel fuel took 29 days. The simulation parameters are described in table 7.5. It took 11.8 hours to finish this modeling work.

7.3.2 Modeling of Rover K4 methane-fuelled SI engine

The Rover K4 engine was modelled using a mesh of 80,000 cells in three dimensions. The computational geometry is illustrated in figure 7.9. The engine was modelled at two ignition crank angles: case 1, θ_{ign}=-15^0 BTDC and case 2, θ_{ign}=-30^0 BTDC. The engine modeling parameters are presented in table 7.6. The reaction database file was created with reaction mechanism of Sandia National Laboratories. The reaction mechanism consists of 33 species and 100 reactions. The reaction database files were

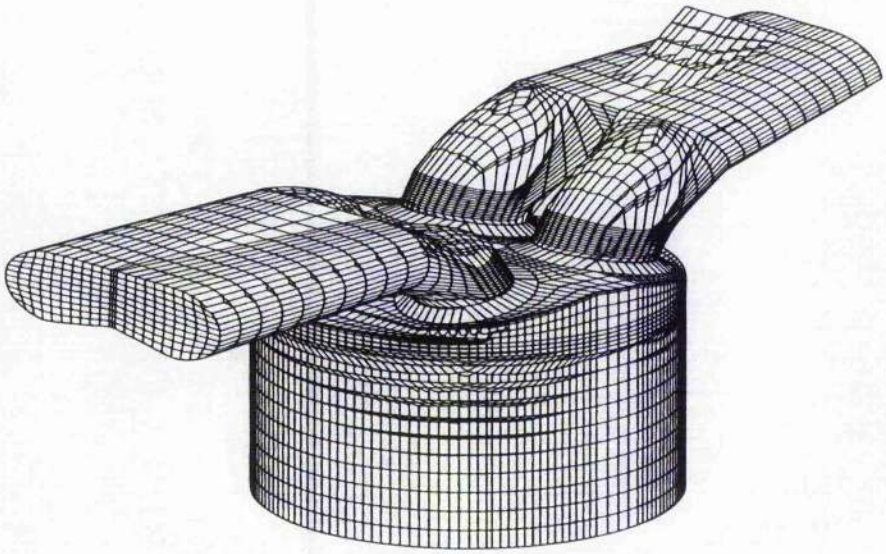

Figure 7.9: Modeling mesh for Rover K4 engine

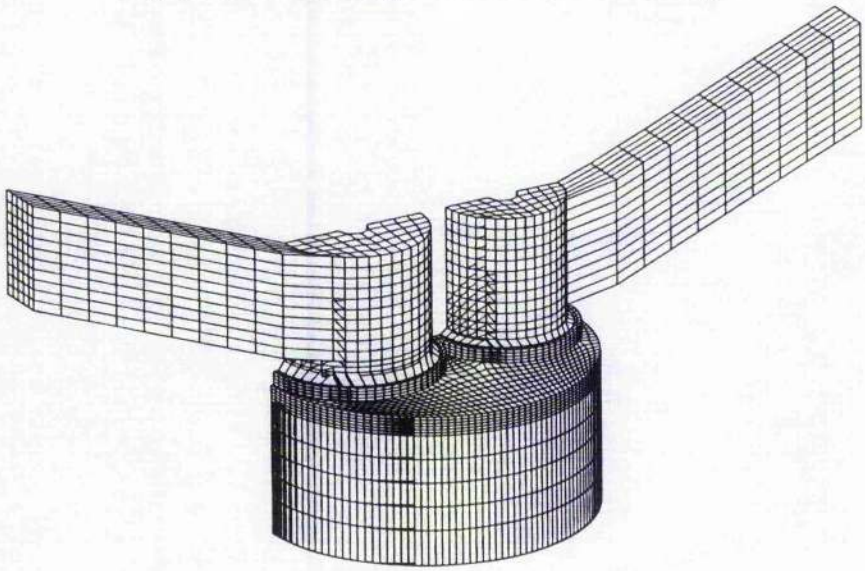

Figure 7.10: Illustration of the modeling mesh for the Ricardo E6 CFR and Toledo 1500 SI gasoline engines

Rotational speed	1600 rev/min
Fuel	$C_{12}H_{26}$
Cylinder wall temperature	525 K
Cylinder head temperature	525 K
Piston face temperature	525 K
Volume displacement	2.44 l
Inlet air pressure	184 kPa
Inlet air temperature	310 K
Exhaust gas pressure	200 kPa
Exhaust gas temperature	580 K
Injection pressure	90 MPa
Fuel injected per cycle	0.1622 g/cycle
Injection crank angle	349^0
Duration of injection pulse	21.5
Number of spray particle	9000

Table 7.5: Simulation parameters for the Caterpillar 3401 diesel engine

Rotational speed	1000 rev/min
Fuel	CH_4
Cylinder wall temperature	540 K
Cylinder head temperature	540 K
Piston face temperature	540 K
Inlet air pressure	104 kPa
Inlet air temperature	320 K
Exhaust gas pressure	150 kPa
Exhaust gas temperature	610 K

Table 7.6: Simulation parameters for the Rover K4 methane-fuelled engine

created by running in parallel two Dell PCs (2.4 GHz CPU). SENKIN was used to calculate reaction of air/fuel mixture with equivalence ratio from 0.2 to 5.0 in increments of 0.05; the initial temperatures of reactions was from 700 K to 1800 K with steps of 20 K. Initial pressures of reactions varied from 10 bar to 140 bar with interval of 1 bar. The engine simulations were carried out on a Dell Power Edge 2600 (2 x 2.4 GHz CPU) server. Since the number of species and reactions involved are small, the creation of the database file took only 3.5 hours to finish. Computing time for each simulation was 16 hours.

7.3.3 Ricardo E6 CFR SI gasoline engine

In modeling operations of the Ricardo E6 CFR SI gasoline engine, a mixture of 90 % iso-octane (C_8H_{18}) and 10% n-heptane (C_7H_{16}) was used to model the reaction of gasoline (this mixture is equivalent to gasoline which has octane number of 90). The reaction mechanism consists of 716 species and 2541 reactions. The reaction database files were created by running in parallel two Dell PCs (2.4 GHz CPU). SENKIN was used to calculate reaction of air/fuel mixture with equivalence ratio from 0.2 to 5.0 in increments of 0.05; the initial temperatures of reactions was from 700 K to 1800 K with steps of 20 K. Initial pressures of reactions varied from 10 bar to 140 bar with interval of 1 bar. Creation of the database file took 12 days.

Simulation of the Ricardo E6 CFR engine was carried out on a mesh of 68,000 cells on a Dell Power Edge 2600 (2 x 2.4 GHz CPU) server. Computational geometry was created for haft the engine cylinder due to its symmetry. The mesh is illustrated in figure 7.10. The engine was simulated for operating speeds from 1200 rpm to 2200 rpm with interval of 100 rpm. Ignition timing varied from θ=-8^0 BTDC to θ=-40^0 BTDC, and air/fuel ratio from 12 to 20 (corresponding to the equivalence ratio from ϕ=1.34 to ϕ=0.75). The modeling conditions are described in table 7.7. It took 12.2 hours to model each operating condition of this engine.

Rotational speed	2200 rpm
Ignition timing	-30^0 BTDC
Fuel	C_8H_{18} and C_7H_{16}
Cylinder wall temperature	590 K
Cylinder head temperature	590 K
Piston face temperature	590 K
Inlet air pressure	103 kPa
Inlet air temperature	330 K
Exhaust gas pressure	135 kPa
Exhaust gas temperature	560 K

Table 7.7: Simulation parameters for the Ricardo E6 CFR gasoline engine

7.3.4 Toledo 1500 SI gasoline engine

Simulation for Toledo 1500 gasoline engine operations was carried out on a mesh of 68,000 cells on a Dell Power Edge 2600 (2 x 2.4 GHz CPU) server. The combustion of gasoline was modelled using the reaction database file similar to that used in modeling the Ricardo E6 CFR SI in section 7.3.3. Computational geometry was created for haft engine cylinder due to its symmetry. The illustration of the computational mesh is presented in figure 7.10. The modeling conditions are described in table 7.8. It took 11.6 hours to model each operating condition of this engine.

Rotational speed	1500 rpm to 3500 rpm
Ignition timing	-30^0 BTDC to 10^0 ATDC
Fuel	C_8H_{18} and C_7H_{16}
Cylinder wall temperature	580 K
Cylinder head temperature	580 K
Piston face temperature	580 K
Inlet air pressure	103 kPa
Inlet air temperature	320 K
Exhaust gas pressure	135 kPa
Exhaust gas temperature	550 K

Table 7.8: Simulation parameters of the Toledo 1500 gasoline engine

Chapter 8

Results and discussions

Modeling results and comparisons between experimental data and predicted results are presented in this chapter. The results discussed are cylinder pressure and emissions of CO, CO_2, and NO_x.

8.1 Caterpillar 3401 diesel engine

The calculated pressure profile in the Caterpillar 3401 diesel engine is presented in figure 8.1. The increase rate of the cylinder pressure was nearly stable in early stage of fuel injection from crank angle θ=349^0 to θ=354^0. This reasonably agrees with the predicted in-cylinder fuel profile shown in figure 8.2. During this period the injected fuel starts dissociating, and the fuel mass in the cylinder is the result of competition between the injection and decomposition rates. In this early stage the formation of the small, light intermediates is limited, and it does not affect much the increase in the rate of pressure. After this period, the change rate of pressure increases due to the start of combustion. At crank angle of θ=354^0 the predicted pressure profile slightly diverges from the measured one. After the early dissociating stage, due to the overpredicted pressure, the dissociation rate of high molecular weight intermediates

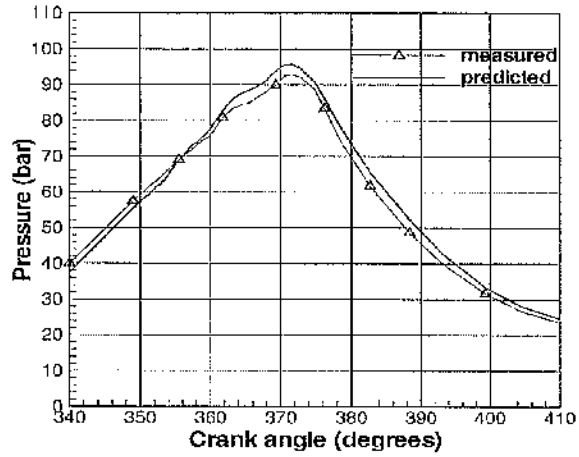

Figure 8.1: In-cylinder pressure history (bar) of the Caterpillar 3401 diesel engine (1600 rpm, injection from θ=349^0 to θ=354^0)

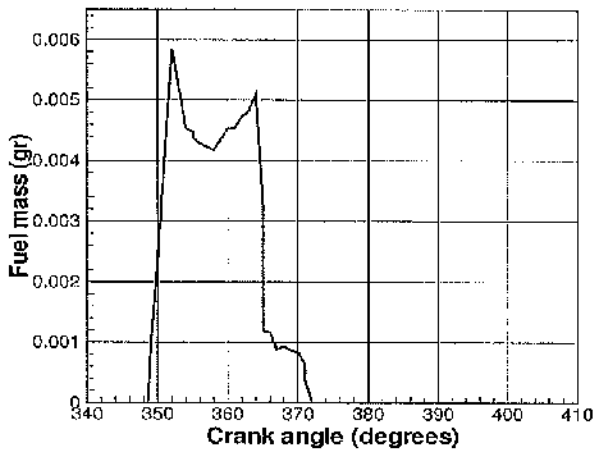

Figure 8.2: In-cylinder fuel history (grams) of the Caterpillar 3401 diesel engine (1600 rpm, injection from θ=349^0 to θ=354^0)

into small species is increased through third-body reactions. This makes the predicted composition of the mixture and pressure return closer to the measured values. At this moment fuel has been already decomposed into lighter species and the error caused by the equivalent N_2 adding technique is counterbalanced. So the predicted pressure has not been affected much by the equivalent N_2 adding technique in which early heavy intermediates were "translated" as N_2. This explains why the predicted pressure profile agrees very well with the measured data. The two pressure profiles are parallel and very close to each other after crank angle $\theta = 357^0$ in figure 8.1.

After crank angle $\theta = 357^0$, the increase in the rate of pressure is slightly reduced. Despite the additional fuel injected, as fuel burns the overall fuel mass in the cylinder is reduced. The increase in temperature in the cylinder causes faster dissociation of fuel. However, after the piston passes top dead center (TDC) by a few degrees, the mass of injected fuel increases again. The decrease in the rate of the pressure increase after TDC despite the fuel mass injected in the combustion chamber may be explained by the nature of IC engines. When the piston reaches towards TDC, although the increment of pressure reduces the travel distance of the droplets injected, the space within the combustion chamber is small, and fuel impinges onto the cylinder walls and piston face. In our model, on the piston and cylinder wall surface, the fuel impinging is not taken into consideration. Therefore, the fuel mass temporarily decreases, and the increase in the rate of pressure reduces. After crank angle θ=363^0 a large amount of fuel has been dissociated into lighter species and is ready to react. Combustion is vigorous, a rapid increase in temperature occurs, and all injected fuel is burned immediately. The increase in temperature causes a rapid increase in nitrogen monoxide from θ=365^0 to θ=375^0 (figure 8.3). As the piston travels down, pressure

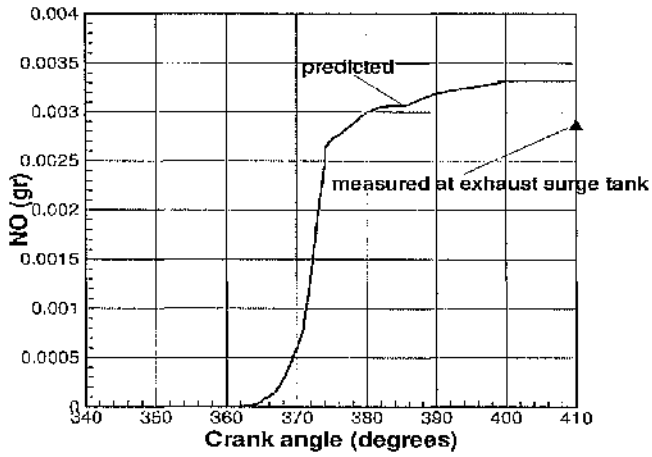

Figure 8.3: In-cylinder NO history (grams) of the Caterpillar 3401 diesel engine (1600 rpm, injection from θ=349^0 to θ=354^0)

and temperature decrease and the production rate of NO reduces significantly. The concentration of NO remains nearly stable to the end of the engine stroke. The in-cylinder distribution of pressure is shown in figure 8.4. The in-cylinder distribution of temperature is shown in figure 8.5. The in-cylinder distributions of CO_2 and CO are presented in figures 8.6 and 8.7, respectively. The in-cylinder distribution of NO in figure 8.8 indicates that high concentration of NO is found in the high temperature regions. This agrees with the thermal route of NO formation mechanism.

It can be seen from figure 8.1 that the calculated pressure profile agrees well with the measured data. The difference between the predicted and measured pressure lies within a range of 93% to 106%. From crank angle of θ=340^0 to θ=355^0 the predicted pressure is lower than the measured one. There is a pressure shift at θ=355^0, after which the calculated pressure increases faster than the experimental data. The

predicted pressure profile intersects, and from then on lies above the experimental profile. The pressure shift could be a result of adding the heavy fuel intermediates into equivalent nitrogen molecular concentration, thus misinterpreting molecules of heavy intermediate species as additional nitrogen molecules. More details of this equivalent N_2 adding technique are discussed in section 6.4.1. The model predicts the crank angle at which peak pressure at θ=371.0^0 while the measured one occurs at θ=372.5^0. Due to the lack of detailed experiment data for in-cylinder NO, the comparison is made with the data obtained from exhaust surge tank. The comparison shows that the model predicts a reasonable result for NO, 14% overpredicted.

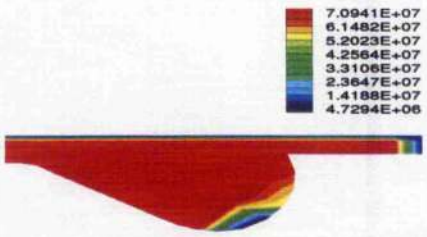

(a) $\theta = 358^0$

(b) $\theta = 362^0$

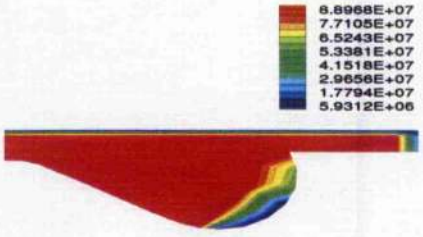

(c) $\theta = 366^0$

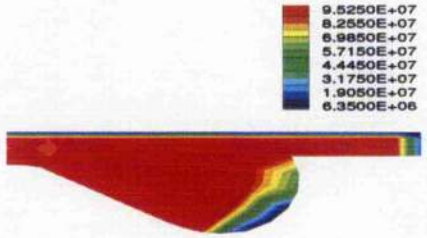

(d) $\theta = 368^0$

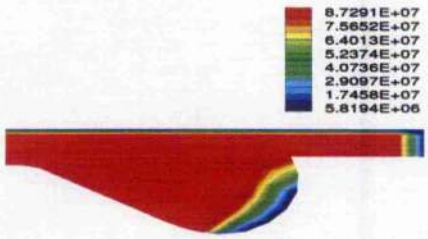

(e) $\theta = 371^0$

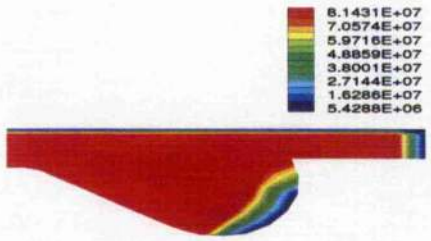

(f) $\theta = 373^0$

Figure 8.4: Predicted in-cylinder pressure distribution (dynes/cm^2) of the Caterpillar 3401 diesel engine (1600 rpm, injection from θ=349^0 to θ=354^0)

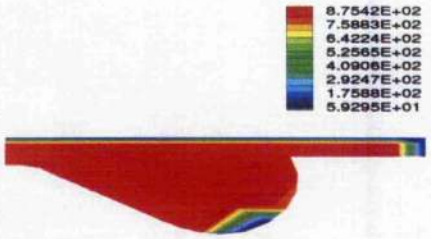

(a) $\theta = 358^0$

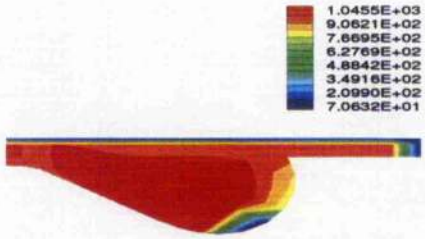

(b) $\theta = 362^0$

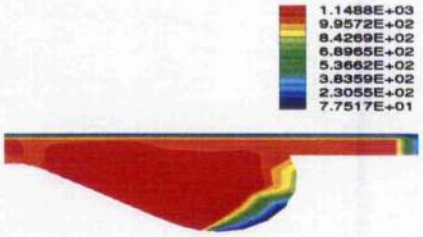

(c) $\theta = 366^0$

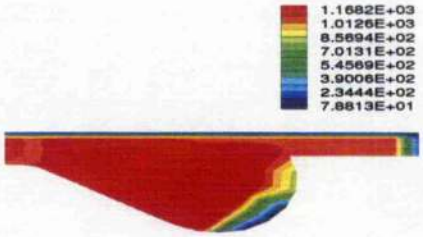

(d) $\theta = 368^0$

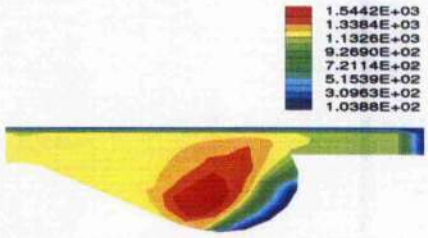

(e) $\theta = 371^0$

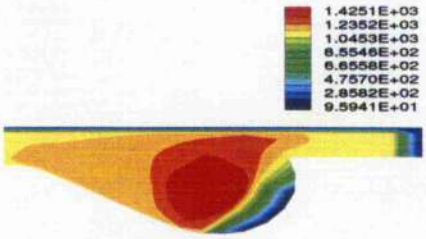

(f) $\theta = 373^0$

Figure 8.5: Predicted in-cylinder temperature distribution (K) of the Caterpillar 3401 diesel engine (1600 rpm, injection from θ=349^0 to θ=354^0)

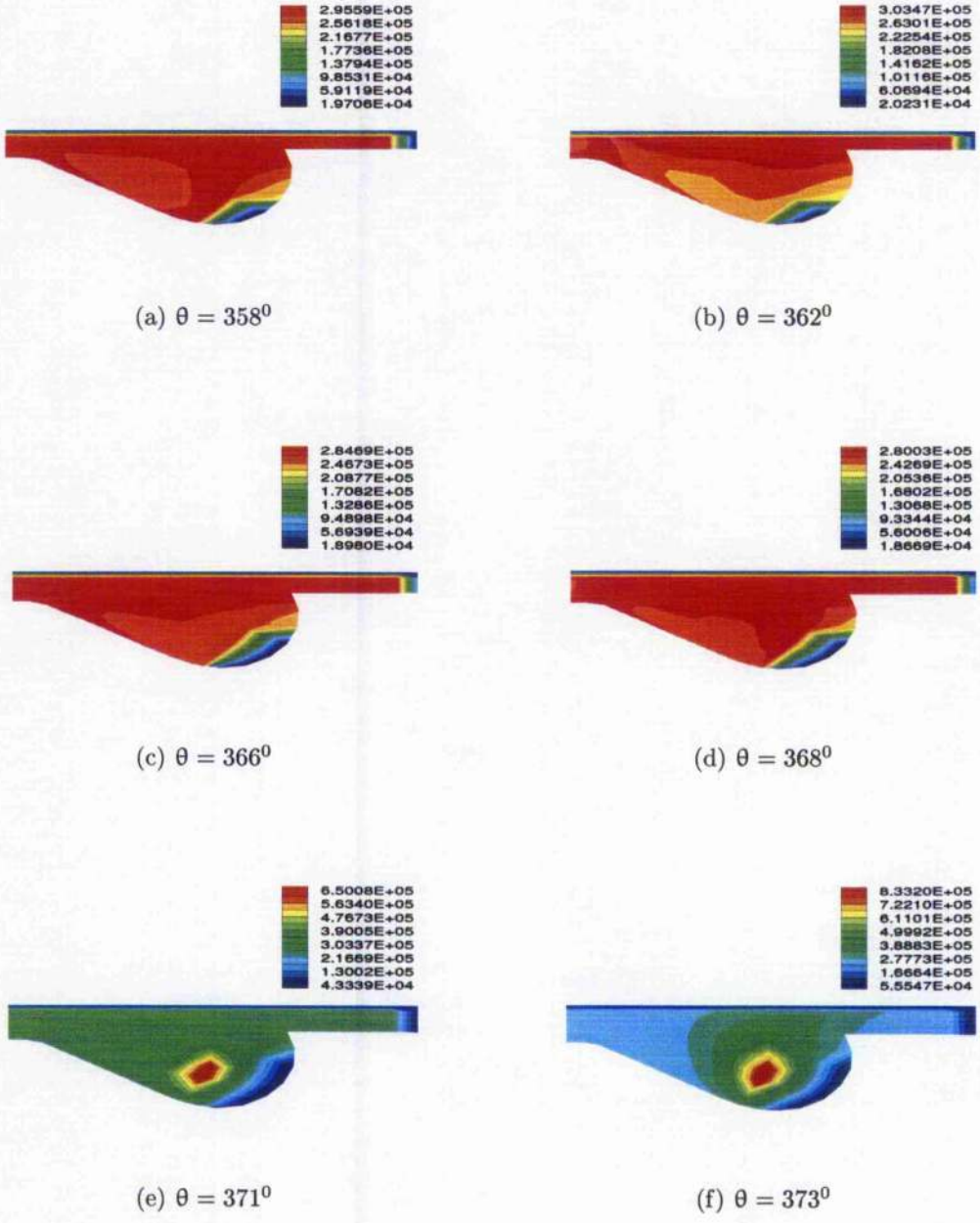

(a) $\theta = 358^0$

(b) $\theta = 362^0$

(c) $\theta = 366^0$

(d) $\theta = 368^0$

(e) $\theta = 371^0$

(f) $\theta = 373^0$

Figure 8.6: Predicted in-cylinder CO_2 distribution (gr/m^3) of the Caterpillar 3401 diesel engine (1600 rpm, injection from θ=349^0 to θ=354^0)

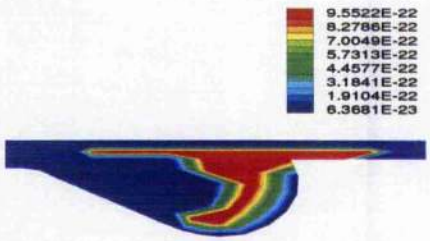

(a) $\theta = 358^0$

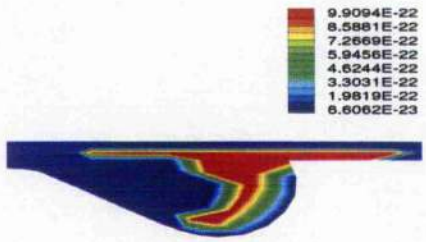

(b) $\theta = 362^0$

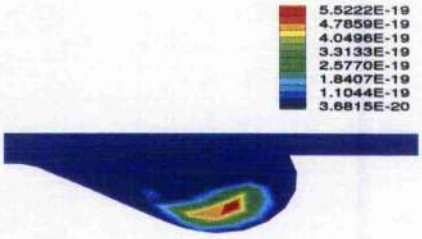

(c) $\theta = 366^0$

(d) $\theta = 368^0$

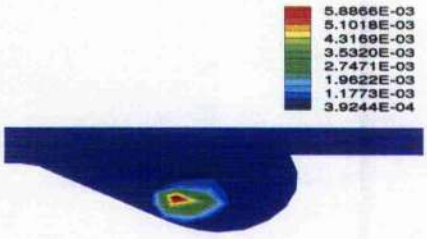

(e) $\theta = 371^0$

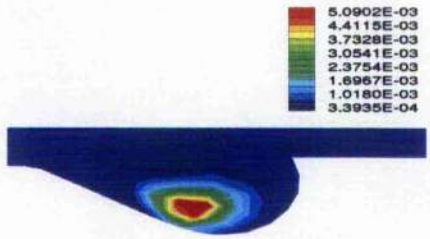

(f) $\theta = 373^0$

Figure 8.7: Predicted in-cylinder CO distribution (gr/m^3) of the Caterpillar 3401 diesel engine (1600 rpm, injection from θ=349^0 to θ=354^0)

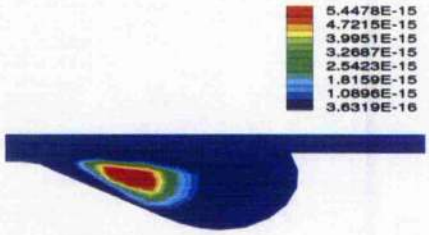

(a) $\theta = 358^0$

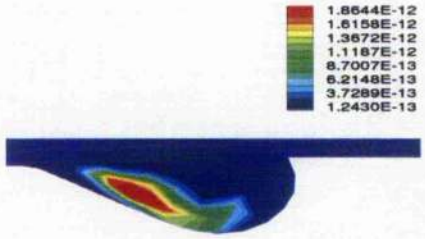

(b) $\theta = 362^0$

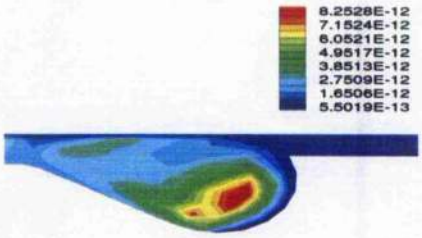

(c) $\theta = 366^0$

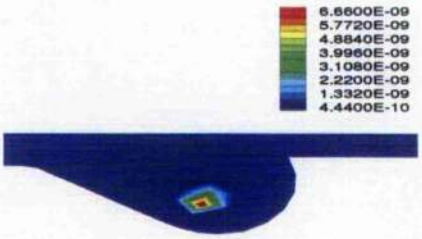

(d) $\theta = 368^0$

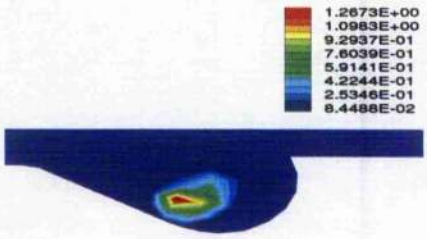

(e) $\theta = 371^0$

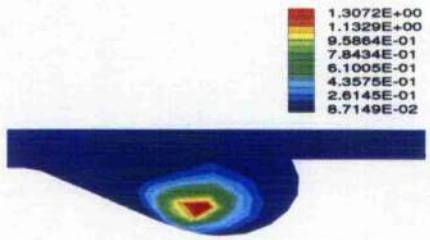

(f) $\theta = 373^0$

Figure 8.8: Predicted in-cylinder NO distribution (gr/m^3) of the Caterpillar 3401 diesel engine (1600 rpm, injection from θ=349^0 to θ=354^0)

8.2 Rover K4 methane-fuelled SI engine

The predicted pressure profiles of the Rover K4 methane-fuelled SI engine for ignition at θ=-30^0 BTDC and θ=-15^0 BTDC are illustrated in figures 8.9 and 8.10, respectively. In case 1, the model predicts well the peak pressure, 0.5 % lower than the experimental data, but the calculated peak occurs at θ=379^0, 1 degree earlier than the measured one.

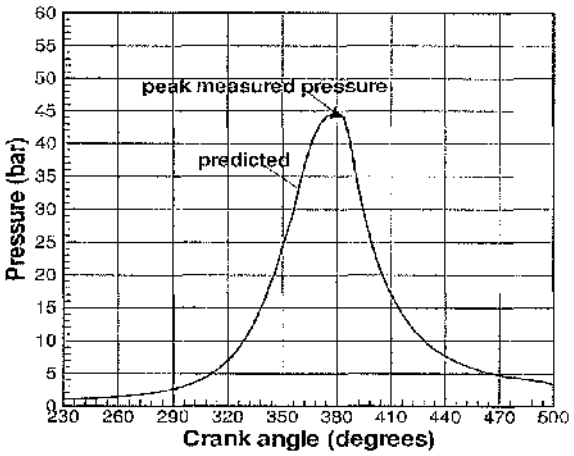

Figure 8.9: In-cylinder pressure history (bar) of the Rover K4 engine (1000 rpm, ignition at -30^0 BTDC)

In case 2 the pre-integrated approach predicts peak pressure at θ=379^0, 2 degrees earlier and 10 % lower than the measured one. The non-smooth pressure profile in case 2 is caused by the late ignition. It takes some time for air/fuel mixture to react and for the flame front to propagate through the combustion chamber. The combustion process becomes vigorous after this delay time. When the piston approaches TDC, the reduction of combustion chamber volume causes pressure increase, then a decrease

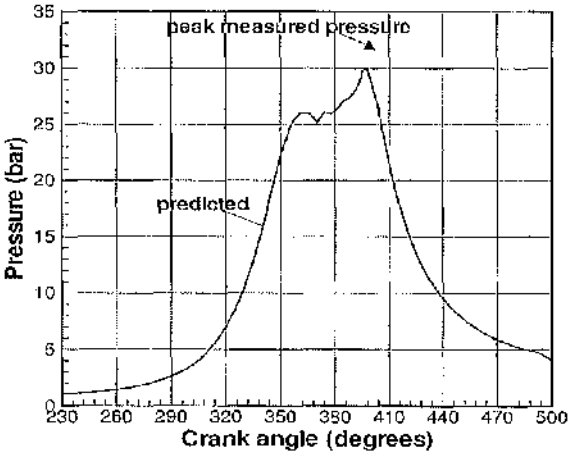

Figure 8.10: In-cylinder pressure history (bar) of the Rover K4 engine (1000 rpm, ignition at -15^0 BTDC)

of pressure is observed when the piston travels down. In the late-ignition case fast combustion occurs after the piston has passed TDC, therefore, even the volume of the combustion chamber is decreased, the in-cylinder pressure increases again. The peak pressure in case 2 is also lower than that of case 1.

The predicted and measured NO_x emissions for ignition at θ=-30^0 BTDC and θ=-15^0 BTDC are illustrated in figure 8.11. NO_x emissions are predicted rather well in both cases. The predicted results are both higher than the measured data (22 % in case 1 and 12 % in case 2). NO_x emissions are higher for ignition at θ=-30^0 BTDC than at θ=-15^0 BTDC. In comparing these two cases more vigorous combustion occurs in case 1 than case 2 when the piston is just around TDC, resulting in high temperature and pressure, which leads to increase of the NO_x production rate. In case 2 the calculated NO_x is closer than the measured one corresponding to the

lower predicted pressure and temperature when compared to case 2.

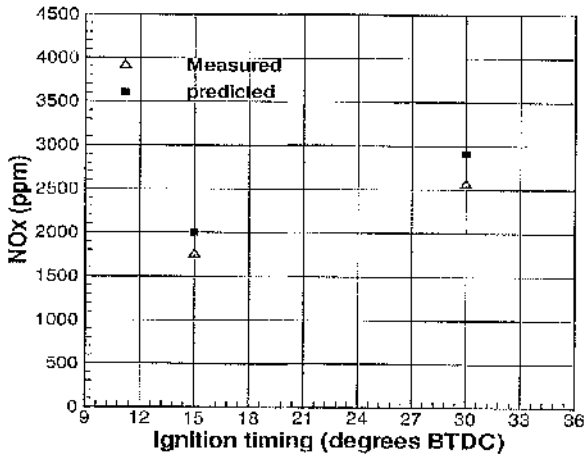

Figure 8.11: Exhaust NO_x variation with ignition timing of the Rover K4 engine ($\phi = 1$)

The calculated in-cylinder pressure, temperature, CO_2, CO, and NO_x distributions in the Rover K4 methane-fuelled SI engine (1000 rpm, ignition at θ=-30^0 BTDC) are illustrated in figures 8.12, 8.13, 8.16, 8.14, and 8.15, respectively. It can be infered from the in-cylinder temperature distribution in figure 8.13 that the combustion process starts from the location of the spark plug and rapidly propagates throughout the combustion chamber. The propagation of high temperature flame front corresponds with high NO_x concentration regions (figure 8.16). A similar phenomenon is found for CO_2 concentrations in figure 8.14. It can be seen from figure 8.15 that high concentration of CO appears mainly at low temperature regions. The calculated in-cylinder pressure, temperature, CO_2, CO, and NO_x distributions in the Rover K4 methane-fuelled SI engine (1000 rpm, ignition at θ=-15^0 BTDC) are illustrated in

figures 8.17, 8.18, 8.19, 8.20, and 8.21, respectively.

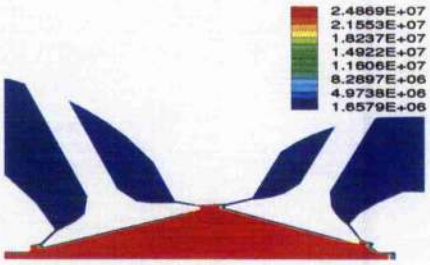

(a) $\theta = 350^0$

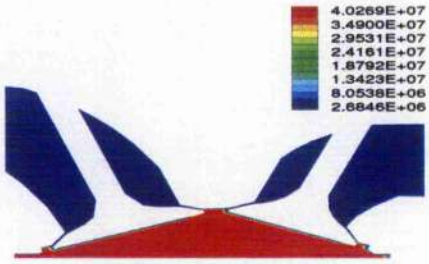

(b) $\theta = 362^0$

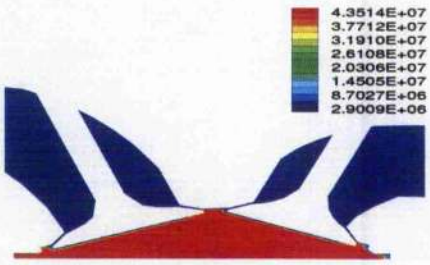

(c) $\theta = 366^0$

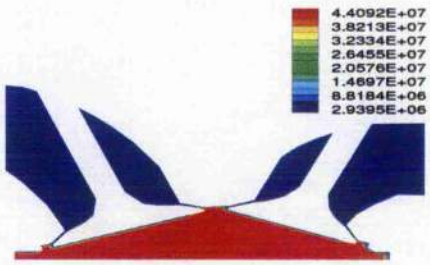

(d) $\theta = 370^0$

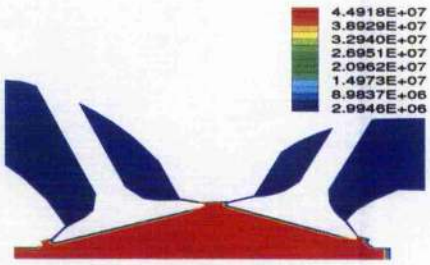

(e) $\theta = 376^0$

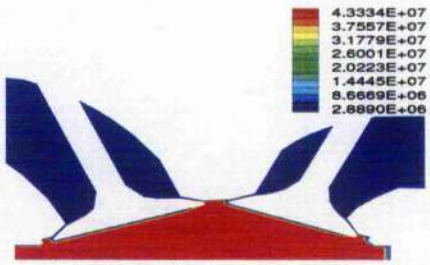

(f) $\theta = 380^0$

Figure 8.12: In-cylinder pressure distribution (dynes/cm^2) of the Rover K4 engine (1000 rpm, ignition at -30^0 BTDC)

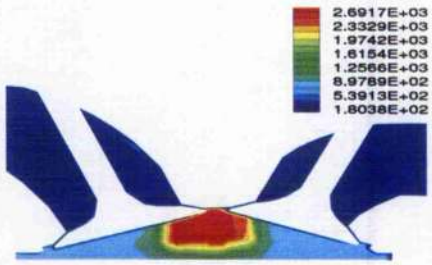

(a) $\theta = 350^0$

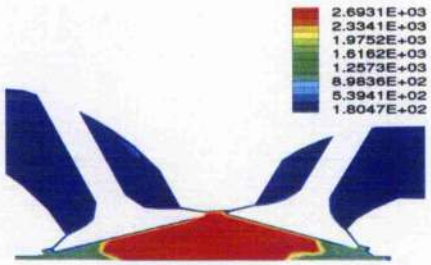

(b) $\theta = 362^0$

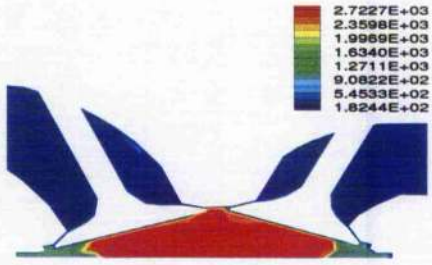

(c) $\theta = 366^0$

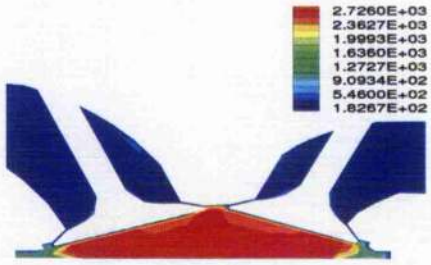

(d) $\theta = 370^0$

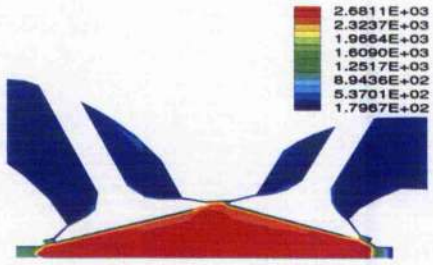

(e) $\theta = 376^0$

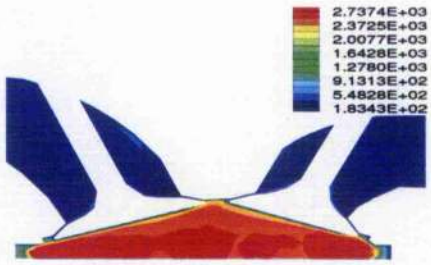

(f) $\theta = 380^0$

Figure 8.13: In-cylinder temperature distribution (K) of the Rover K4 engine (1000 rpm, ignition at -30^0 BTDC)

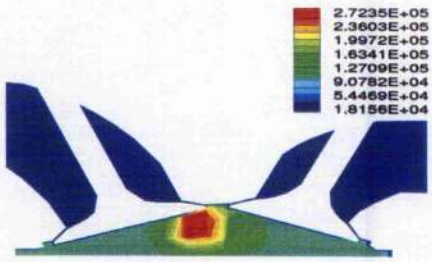

(a) $\theta = 350^0$

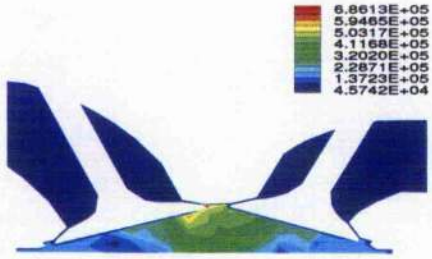

(b) $\theta = 362^0$

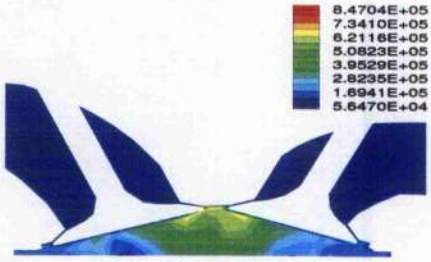

(c) $\theta = 366^0$

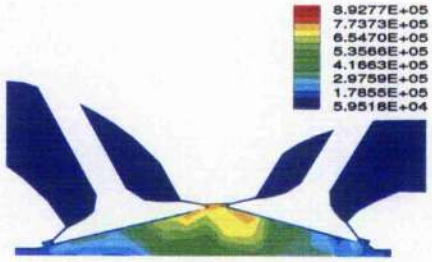

(d) $\theta = 370^0$

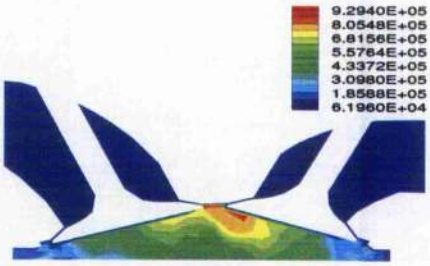

(e) $\theta = 376^0$

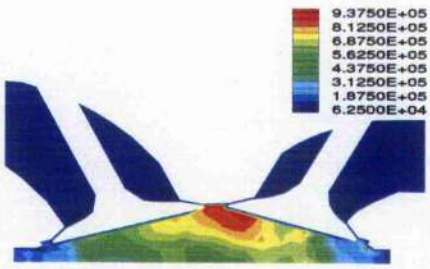

(f) $\theta = 380^0$

Figure 8.14: In-cylinder CO_2 distribution (gr/m^3) of the Rover K4 engine (1000 rpm, ignition at -30^0 BTDC)

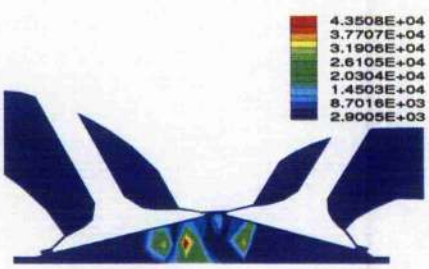

(a) $\theta = 350^0$

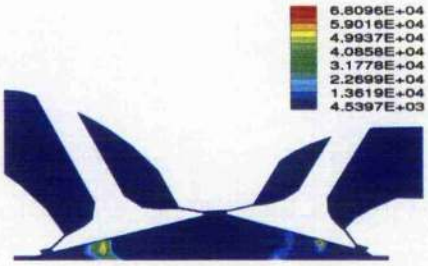

(b) $\theta = 362^0$

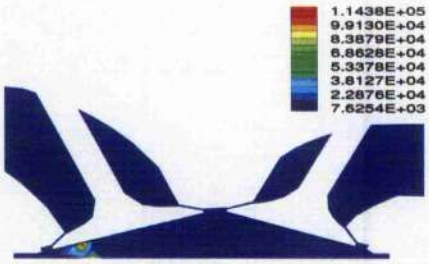

(c) $\theta = 366^0$

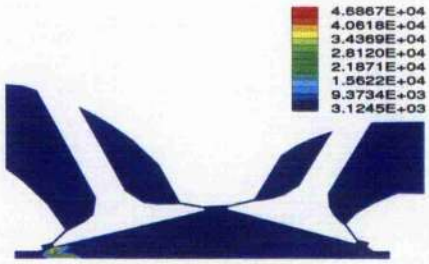

(d) $\theta = 370^0$

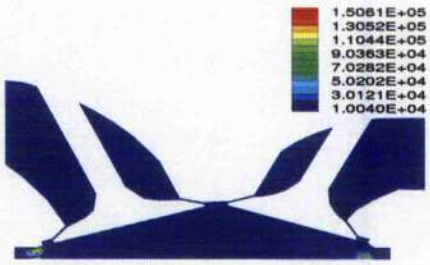

(e) $\theta = 376^0$

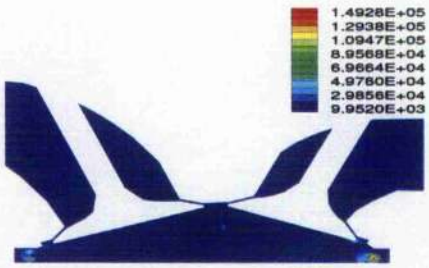

(f) $\theta = 380^0$

Figure 8.15: In-cylinder CO distribution (gr/m^3) of the Rover K4 engine (1000 rpm, ignition at -30^0 BTDC)

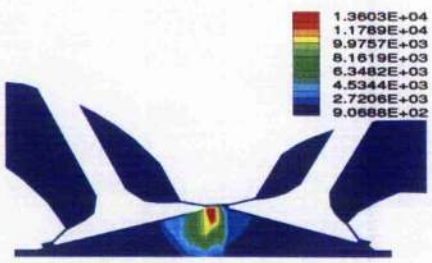

(a) $\theta = 350^0$

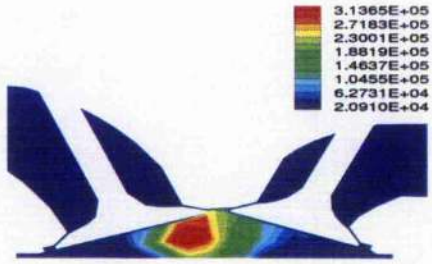

(b) $\theta = 362^0$

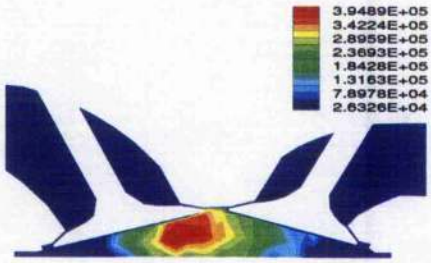

(c) $\theta = 366^0$

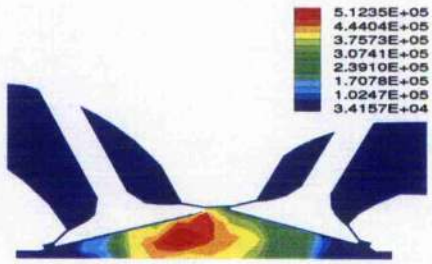

(d) $\theta = 370^0$

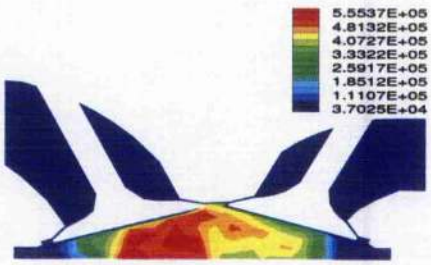

(e) $\theta = 376^0$

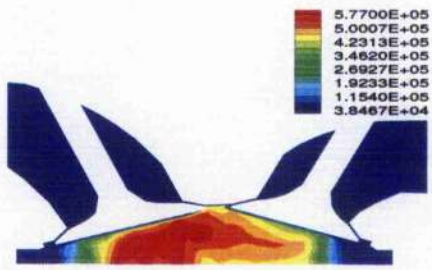

(f) $\theta = 380^0$

Figure 8.16: In-cylinder NO_x distribution (gr/m^3) of the Rover K4 engine (1000 rpm, ignition at -30^0 BTDC)

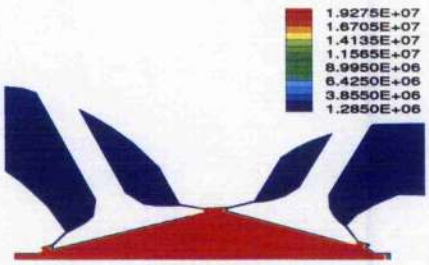

(a) $\theta = 350^0$

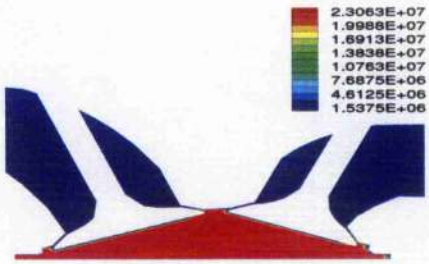

(b) $\theta = 365^0$

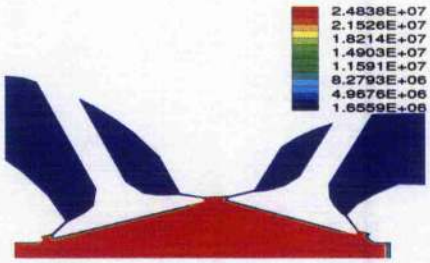

(c) $\theta = 380^0$

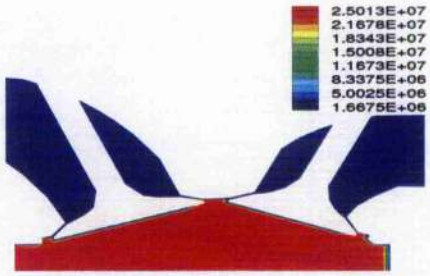

(d) $\theta = 388^0$

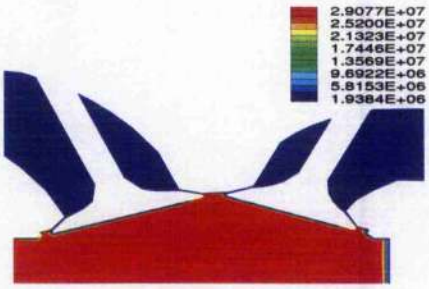

(e) $\theta = 399^0$

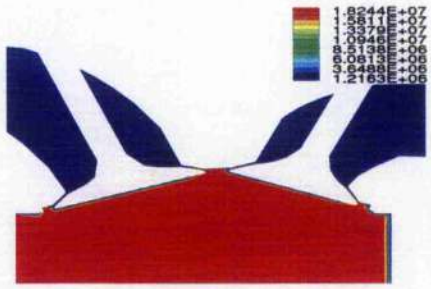

(f) $\theta = 410^0$

Figure 8.17: In-cylinder pressure distribution (dynes/cm^2) of the Rover K4 engine (1000 rpm, ignition at -15^0 BTDC)

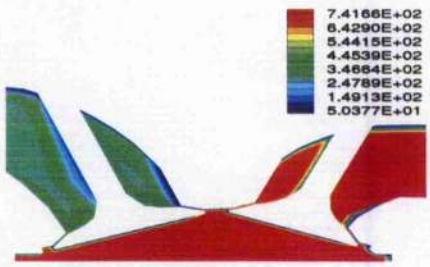

(a) $\theta = 350^0$

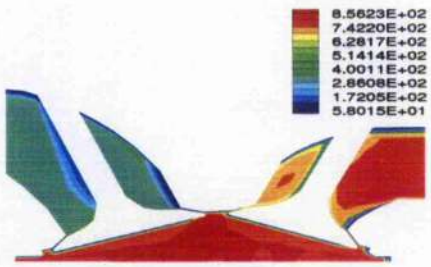

(b) $\theta = 365^0$

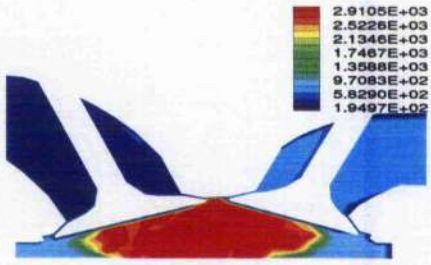

(c) $\theta = 380^0$

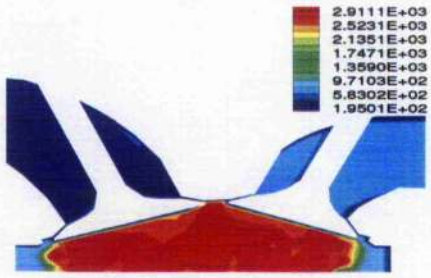

(d) $\theta = 388^0$

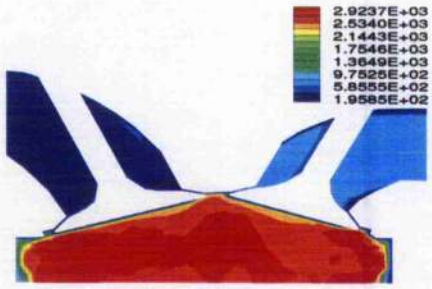

(e) $\theta = 399^0$

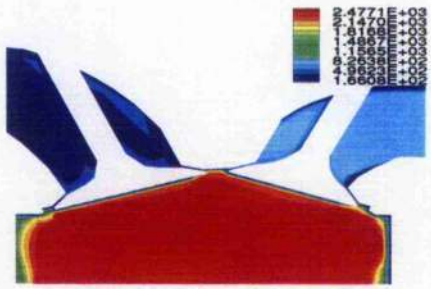

(f) $\theta = 410^0$

Figure 8.18: In-cylinder temperature distribution (K) of the Rover K4 engine (1000 rpm, ignition at -15^0 BTDC)

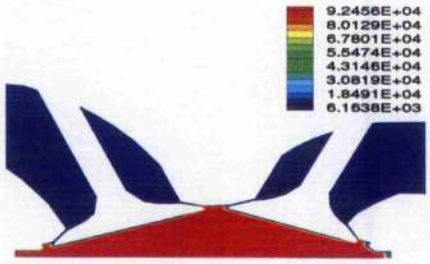

(a) $\theta = 350^0$

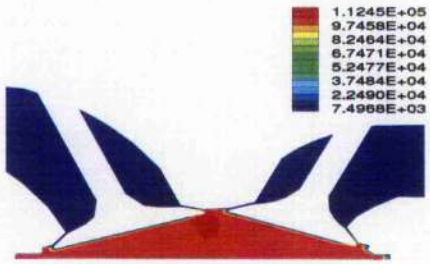

(b) $\theta = 365^0$

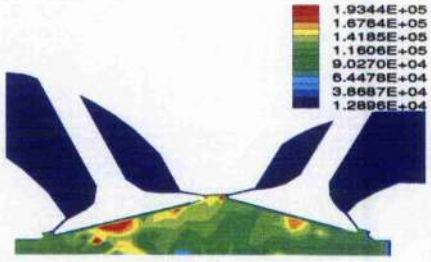

(c) $\theta = 380^0$

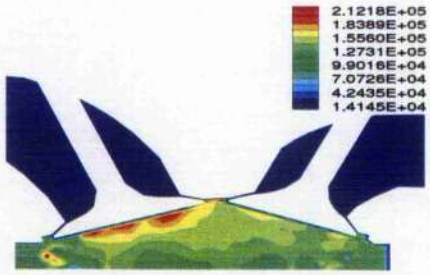

(d) $\theta = 388^0$

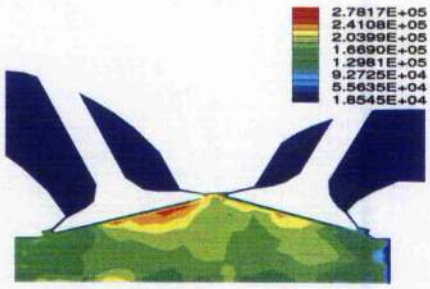

(e) $\theta = 399^0$

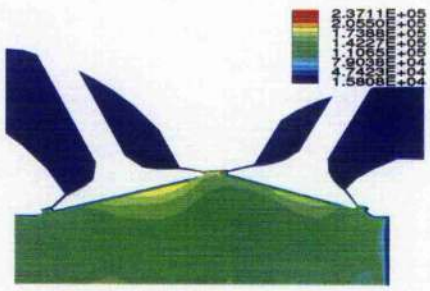

(f) $\theta = 410^0$

Figure 8.19: In-cylinder CO_2 distribution (gr/m^3) of the Rover K4 engine (1000 rpm, ignition at -15^0 BTDC)

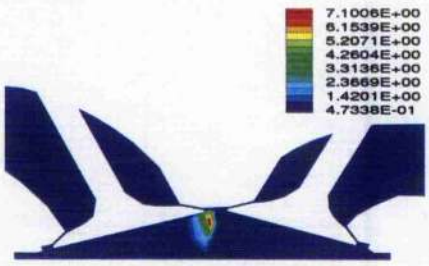

(a) $\theta = 350^0$

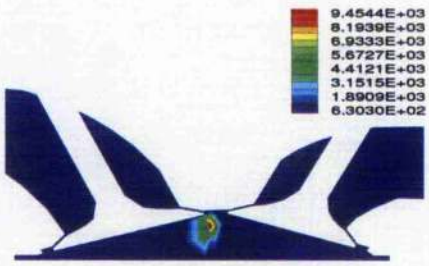

(b) $\theta = 365^0$

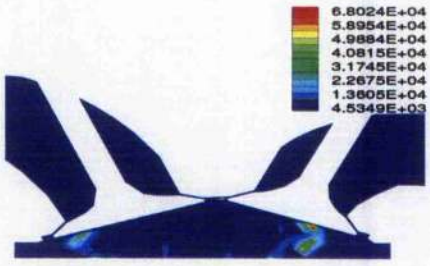

(c) $\theta = 380^0$

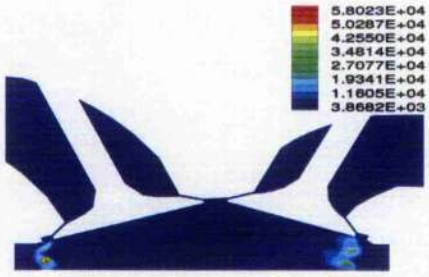

(d) $\theta = 388^0$

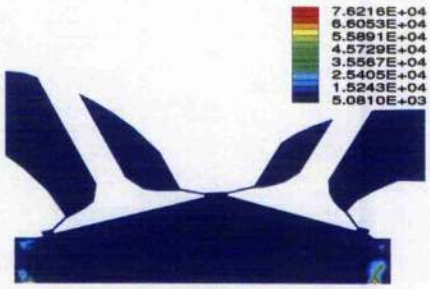

(e) $\theta = 399^0$

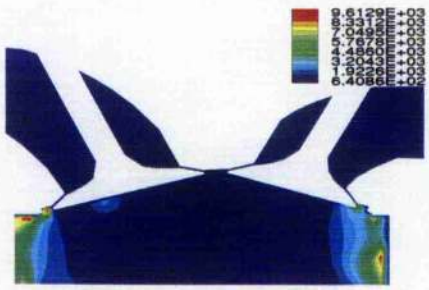

(f) $\theta = 410^0$

Figure 8.20: In-cylinder CO distribution (gr/m^3) of the Rover K4 engine (1000 rpm, ignition at -15^0 BTDC)

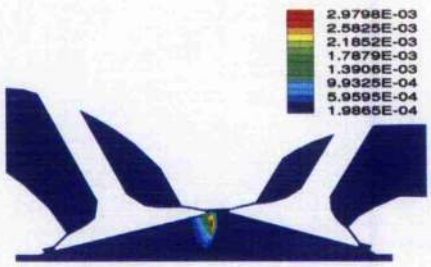

(a) $\theta = 350^0$

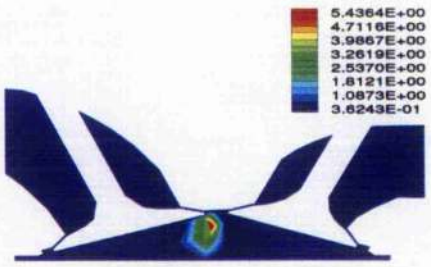

(b) $\theta = 365^0$

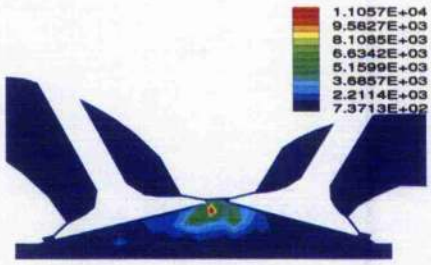

(c) $\theta = 380^0$

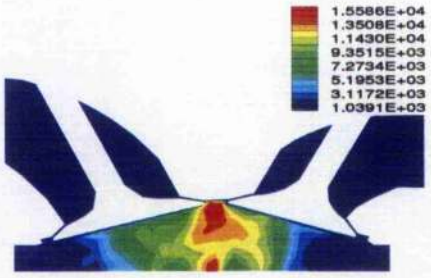

(d) $\theta = 388^0$

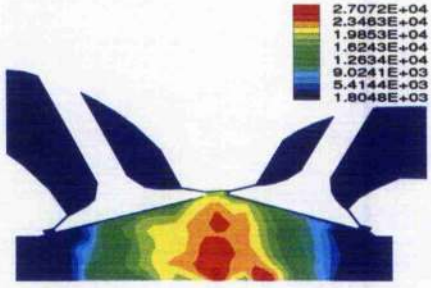

(e) $\theta = 399^0$

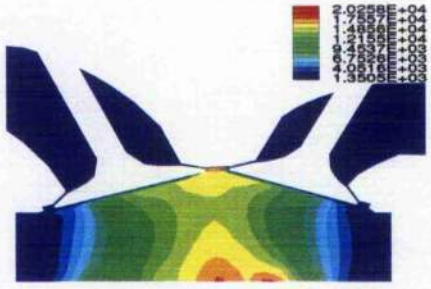

(f) $\theta = 410^0$

Figure 8.21: In-cylinder NO_x distribution (gr/m^3) of the Rover K4 engine (1000 rpm, ignition at -15^0 BTDC)

8.3 Gasoline SI engines

8.3.1 Ricardo E6 CFR SI petrol engine

The variations of CO and CO_2 of the Ricardo E6 CFR SI gasoline engine with air/fuel ratio are shown in figure 8.22. It can be seen in figure 8.22 that in the low range of air/fuel ratio from 12 to 16 (co-responding to the equivalence ratio from ϕ=1.34 to ϕ=0.94) the concentration of CO_2 increases and concentration of CO decreases with increasing values of air/fuel ratio. This agrees with analysis that at a low air/fuel ratio, insufficient oxygen for complete reaction of carbon, therefore more carbon monoxide is found in this condition. With increase of air/fuel ratio, more oxygen is available for combustion so that the concentration of CO is decreased along with appearance of more CO_2. The concentration of CO_2 obtains a peak value at air /fuel ratio of 16 (ϕ=0.94), then the concentration of CO_2 decreases at even higher values of air/fuel ratio because there is more unused oxygen in the mixture. A similar trend was found

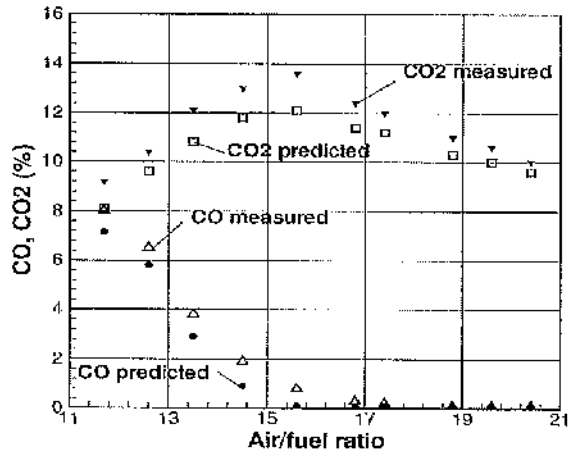

Figure 8.22: Exhaust CO, CO_2 variation with A/F of the Ricardo E6 CFR SI gasoline engine (ignition at -28^0 BTDC, 1500 rpm)

in the case of NO_x emissions. At low values of air/fuel ratio the concentration of NO_x increases with air/fuel ratio, then a peak value of NO_x concentration is observed at air/fuel ratio of 16 (ϕ=0.94), then NO_x reduces at higher values of air/fuel ratio. The explanation is that at air/fuel ratio of 16 (ϕ=0.94), the amount of oxygen is just

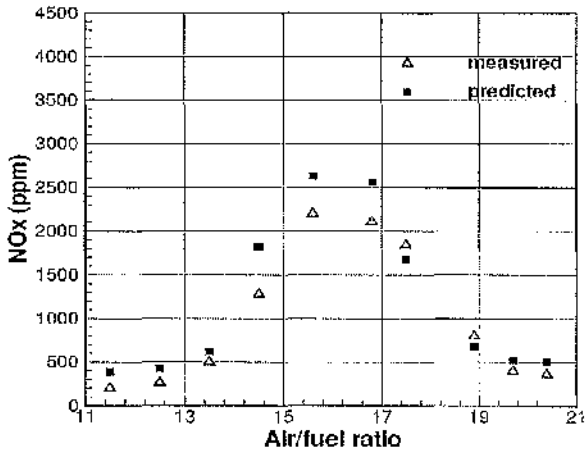

Figure 8.23: Exhaust NO_x variation with A/F of the Ricardo E6 CFR SI gasoline engine (ignition at -28^0 BTDC, 1500 rpm)

enough for reaction and it is the most efficient condition for combustion. Therefore, the temperature is maximized leading to high production rate of NO_x. The reason for the reduction of NO_x when air/fuel ratio exceeds 16 is that the extra oxygen in the mixture absorbs some of the energy of the reaction and leads a to decrease in temperature, which in turn reduces the formation rate of NO_x. It is observed that NO_x concentration increases almost linearly with ignition timing in figure 8.24. This behavior can be explained in a similarly manner to the case for methane-fuelled engine in section 8.2.

In modeling of the Ricardo E6 CFR SI gasoline engine the pre-integrated approach

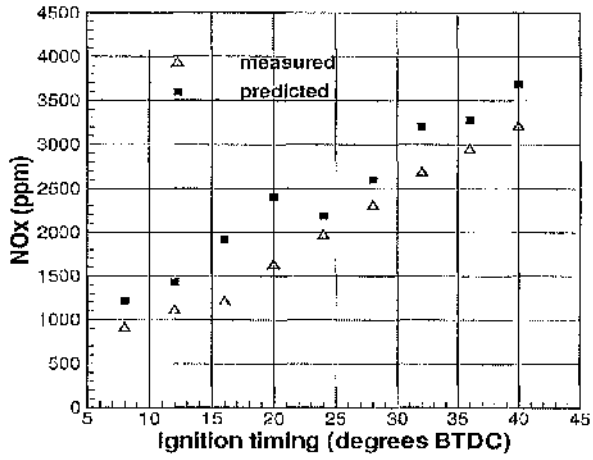

Figure 8.24: Exhaust NO_x variation with ignition timing of the Ricardo E6 CFR SI gasoline engine (Λ/F=16.4, 1500 rpm)

over predicts both CO_2 and NO_x in all cases, while the CO concentration is under predicted. The differences between calculated results and experimental data lie within 6% to 18%. This error could be introduced during the interpolating process of reaction results as well as by the use of the equivalent N_2 adding technique.

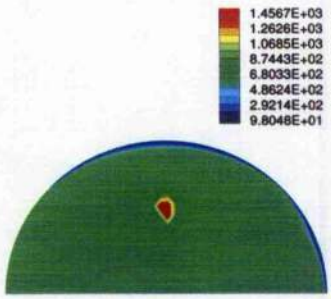

(a) $\theta = 332^0$

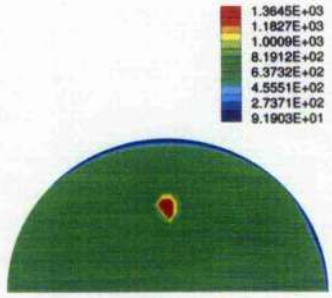

(b) $\theta = 342^0$

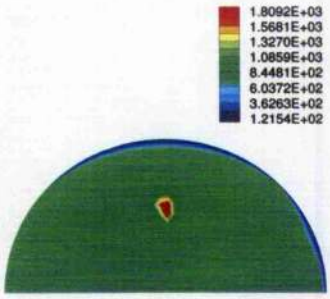

(c) $\theta = 350^0$

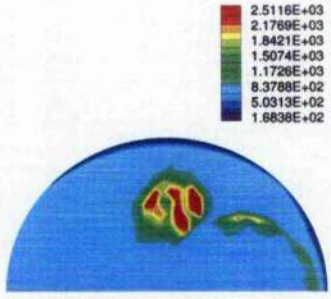

(d) $\theta = 360^0$

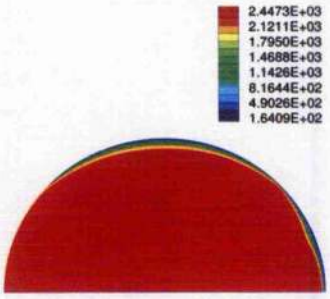

(e) $\theta = 370^0$

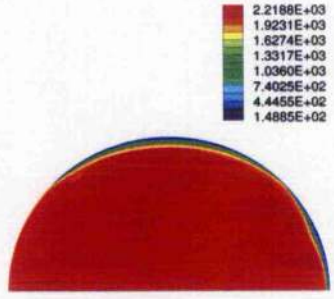

(f) $\theta = 380^0$

Figure 8.25: In-cylinder temperature distribution (K) of the Ricardo E6 CFR gasoline engine (1500 rpm, ignition at θ=-36^0 BTDC, WOT)

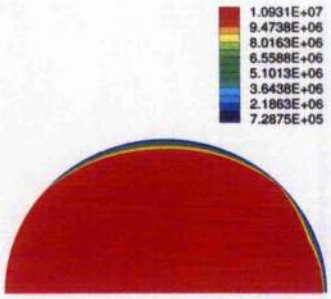

(a) $\theta = 332^0$

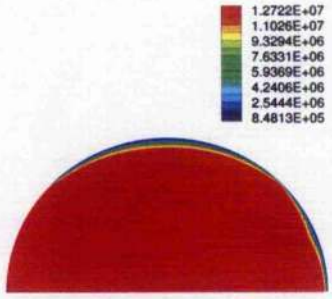

(b) $\theta = 342^0$

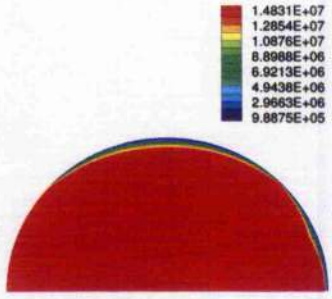

(c) $\theta = 350^0$

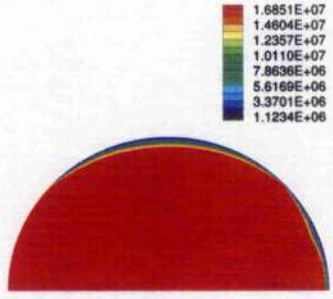

(d) $\theta = 360^0$

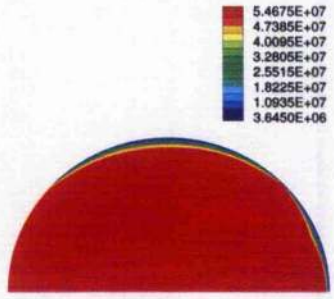

(e) $\theta = 370^0$

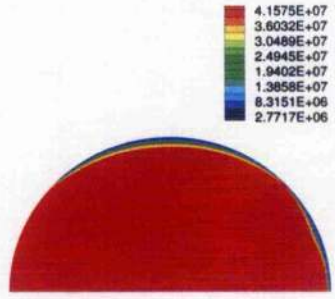

(f) $\theta = 380^0$

Figure 8.26: In-cylinder pressure distribution (dynes/cm^2) of the Ricardo E6 CFR gasoline engine (1500 rpm, ignition at θ=-36^0 BTDC, WOT)

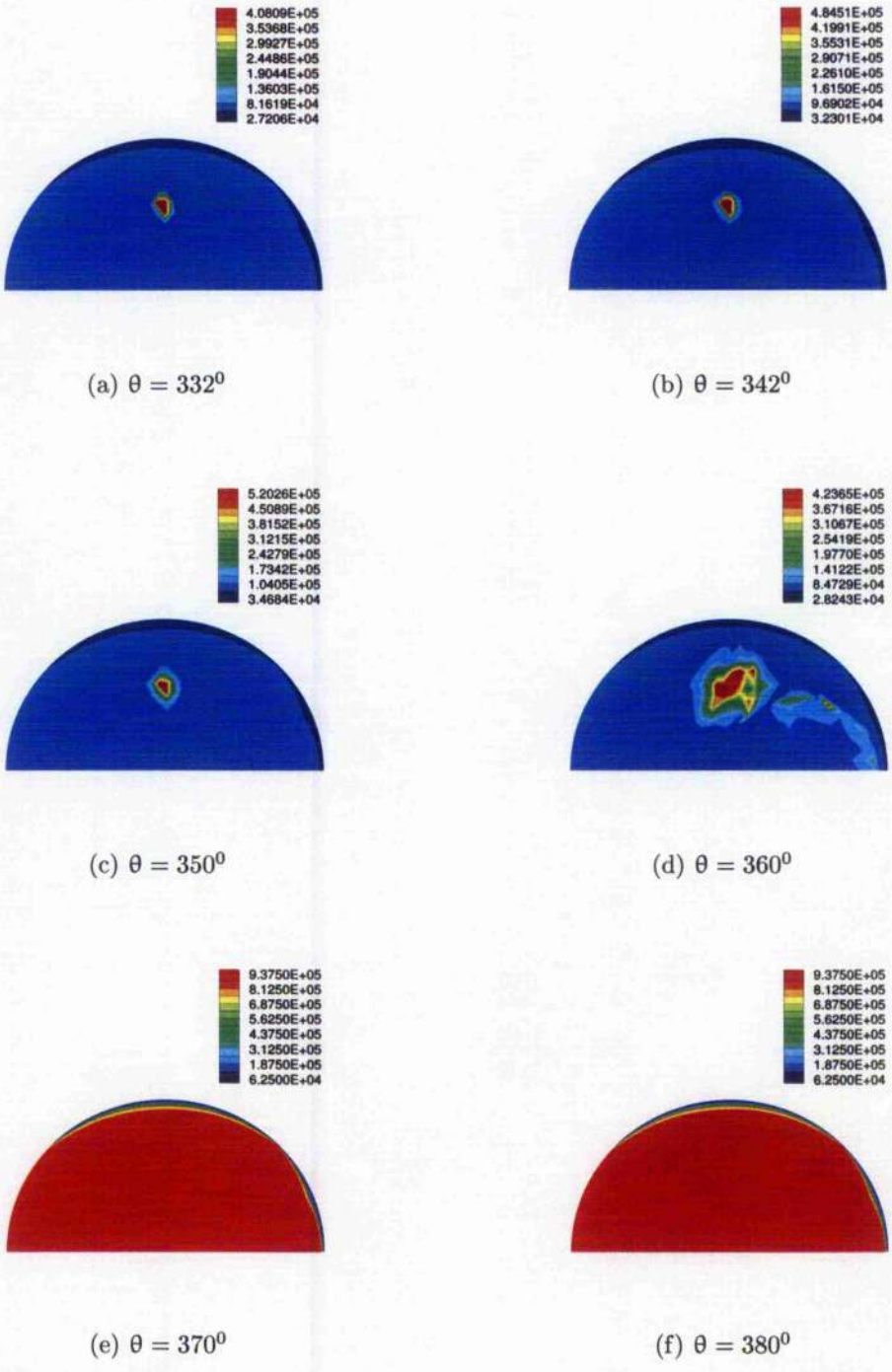

(a) $\theta = 332^0$

(b) $\theta = 342^0$

(c) $\theta = 350^0$

(d) $\theta = 360^0$

(e) $\theta = 370^0$

(f) $\theta = 380^0$

Figure 8.27: In-cylinder CO_2 distribution (gr/m^3) of the Ricardo E6 CFR gasoline engine (1500 rpm, ignition at θ=-36^0 BTDC, WOT)

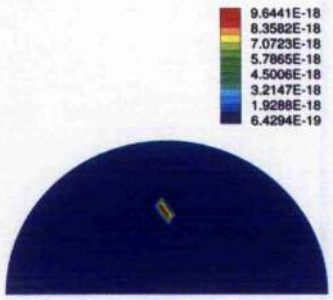

(a) $\theta = 332^0$

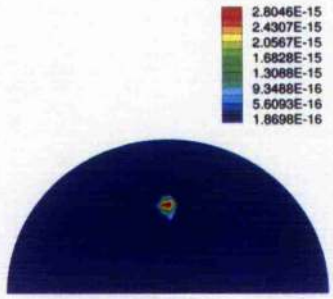

(b) $\theta = 342^0$

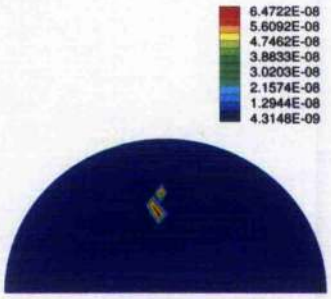

(c) $\theta = 350^0$

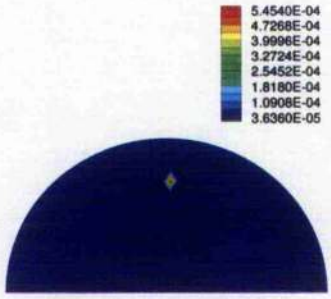

(d) $\theta = 360^0$

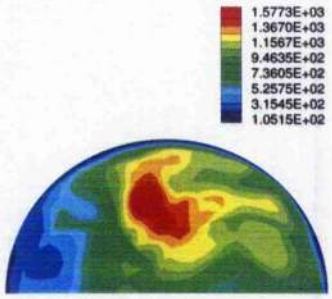

(e) $\theta = 370^0$

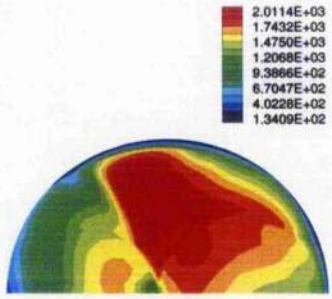

(f) $\theta = 380^0$

Figure 8.28: In-cylinder CO distribution (gr/m^3) of the Ricardo E6 CFR gasoline engine (1500 rpm, ignition at θ=-36^0 BTDC, WOT)

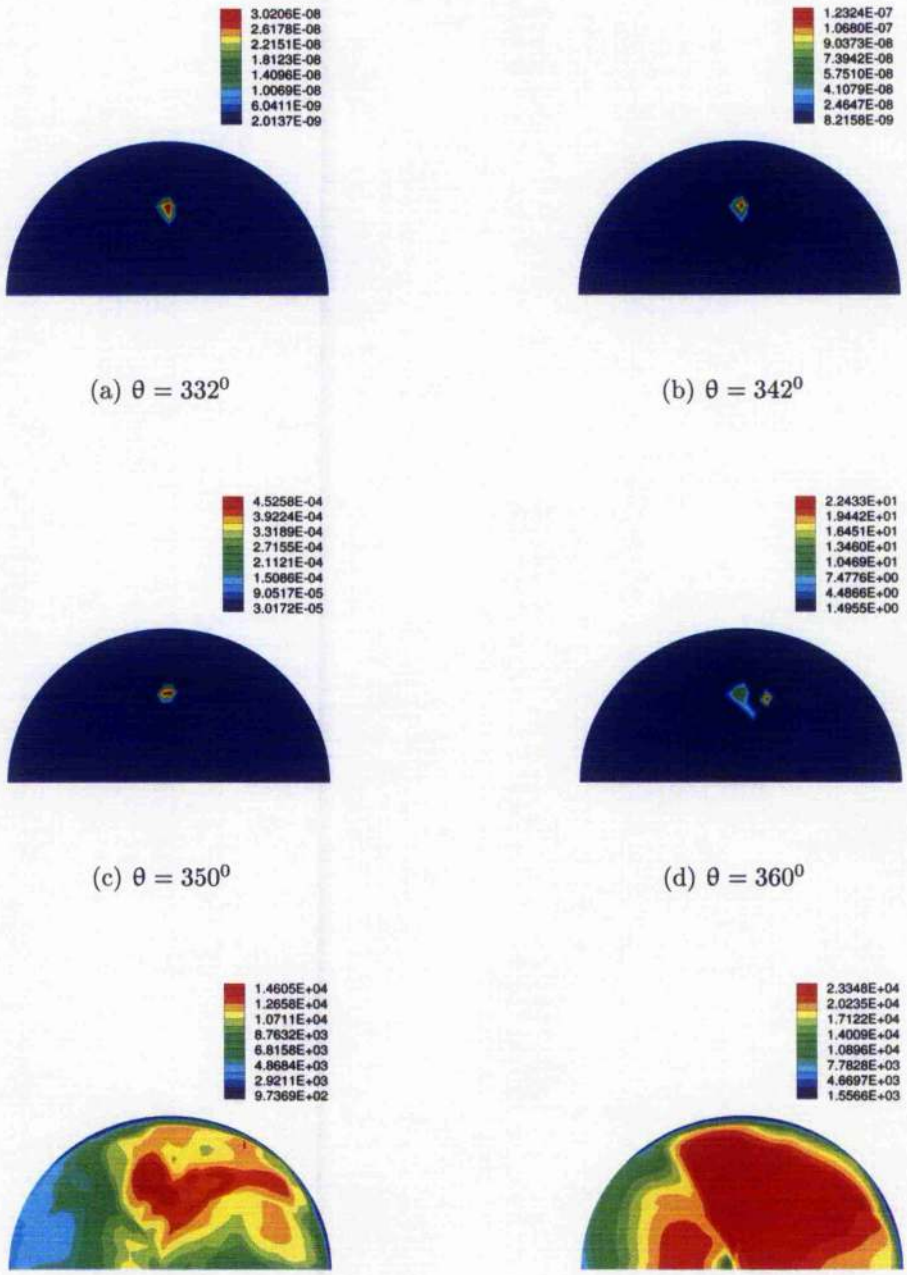

(a) $\theta = 332^0$ (b) $\theta = 342^0$

(c) $\theta = 350^0$ (d) $\theta = 360^0$

(e) $\theta = 370^0$ (f) $\theta = 380^0$

Figure 8.29: In-cylinder NO_x distribution (gr/m^3) of the Ricardo E6 CFR gasoline engine (1500 rpm, ignition at θ=-36^0 BTDC, WOT)

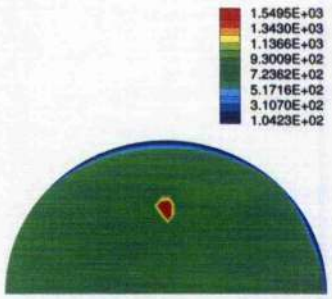

(a) $\theta = 339^0$

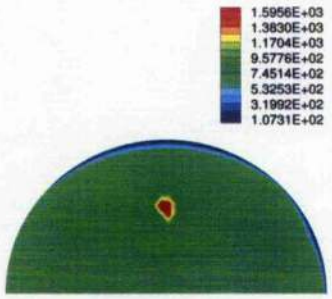

(b) $\theta = 350^0$

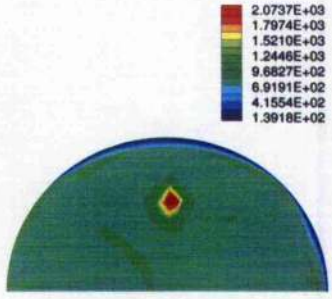

(c) $\theta = 360^0$

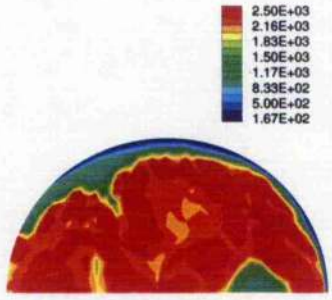

(d) $\theta = 370^0$

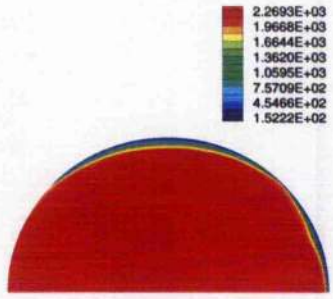

(e) $\theta = 380^0$

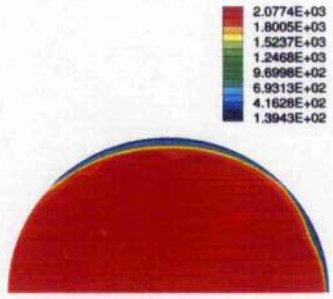

(f) $\theta = 390^0$

Figure 8.30: In-cylinder temperature distribution (K) of the Ricardo E6 CFR gasoline engine (1500 rpm, ignition at θ=-24^0 BTDC, WOT)

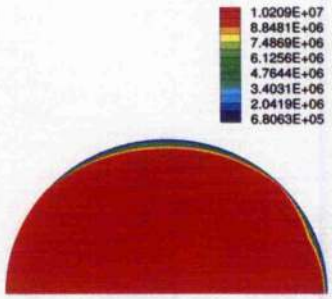

(a) $\theta = 339^0$

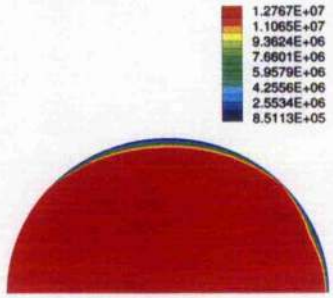

(b) $\theta = 350^0$

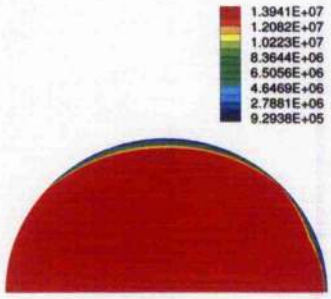

(c) $\theta = 360^0$

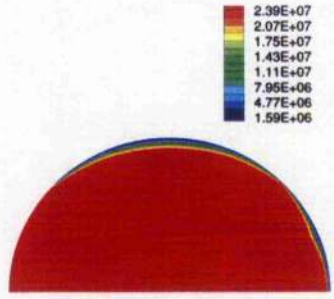

(d) $\theta = 370^0$

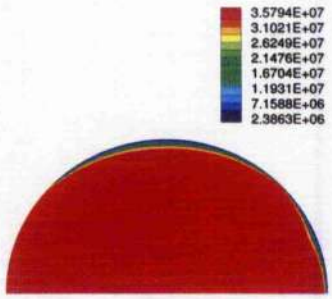

(e) $\theta = 380^0$

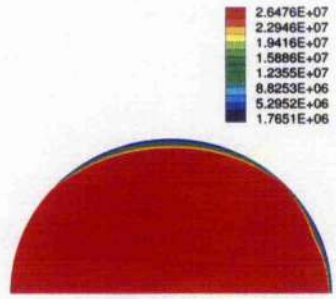

(f) $\theta = 390^0$

Figure 8.31: In-cylinder pressure distribution (dynes/cm^2) of the Ricardo E6 CFR gasoline engine (1500 rpm, ignition at θ=-24^0 BTDC, WOT)

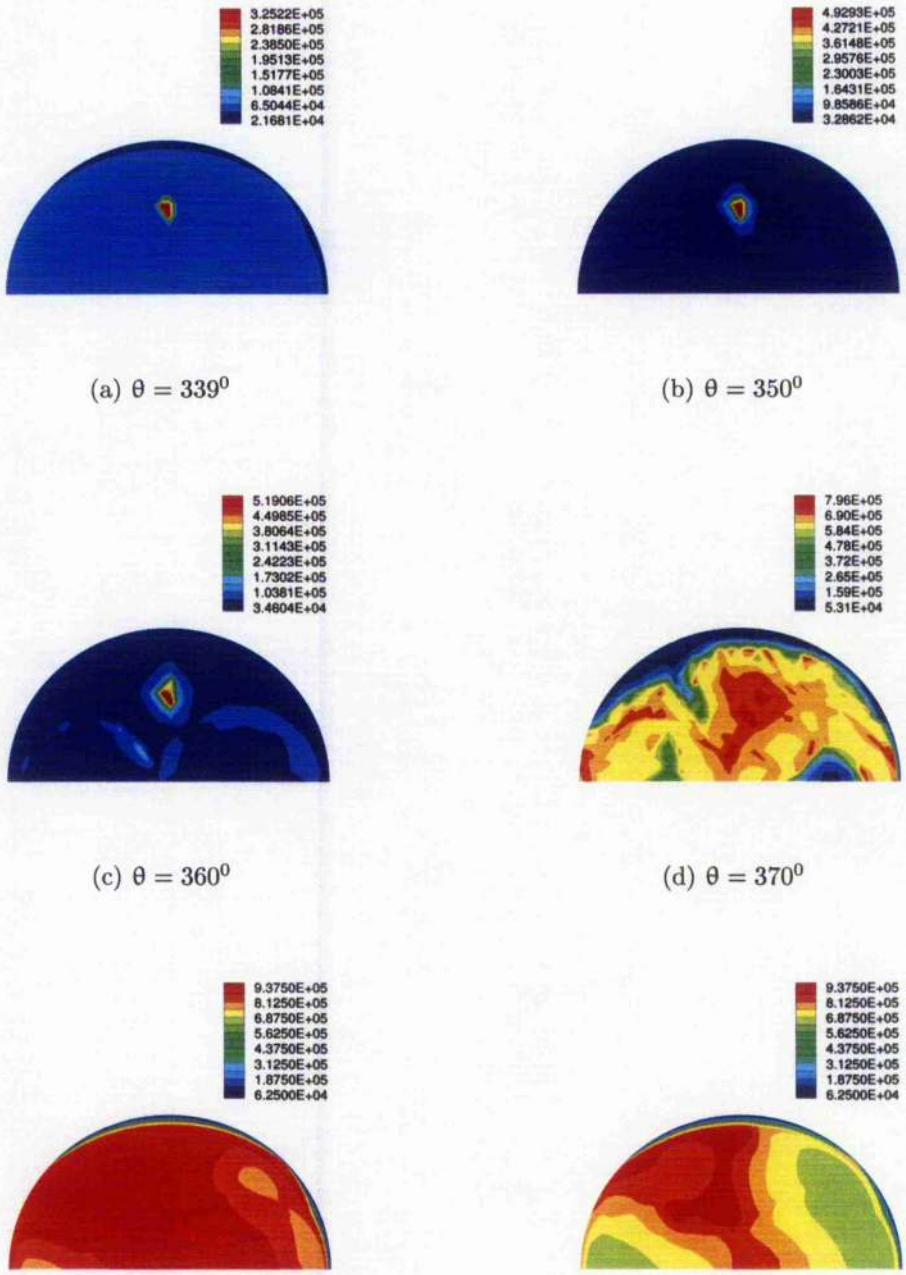

(a) $\theta = 339^0$

(b) $\theta = 350^0$

(c) $\theta = 360^0$

(d) $\theta = 370^0$

(e) $\theta = 380^0$

(f) $\theta = 390^0$

Figure 8.32: In-cylinder CO_2 distribution (gr/m^3) of the Ricardo E6 CFR gasoline engine (1500 rpm, ignition at θ=-24^0 BTDC, WOT)

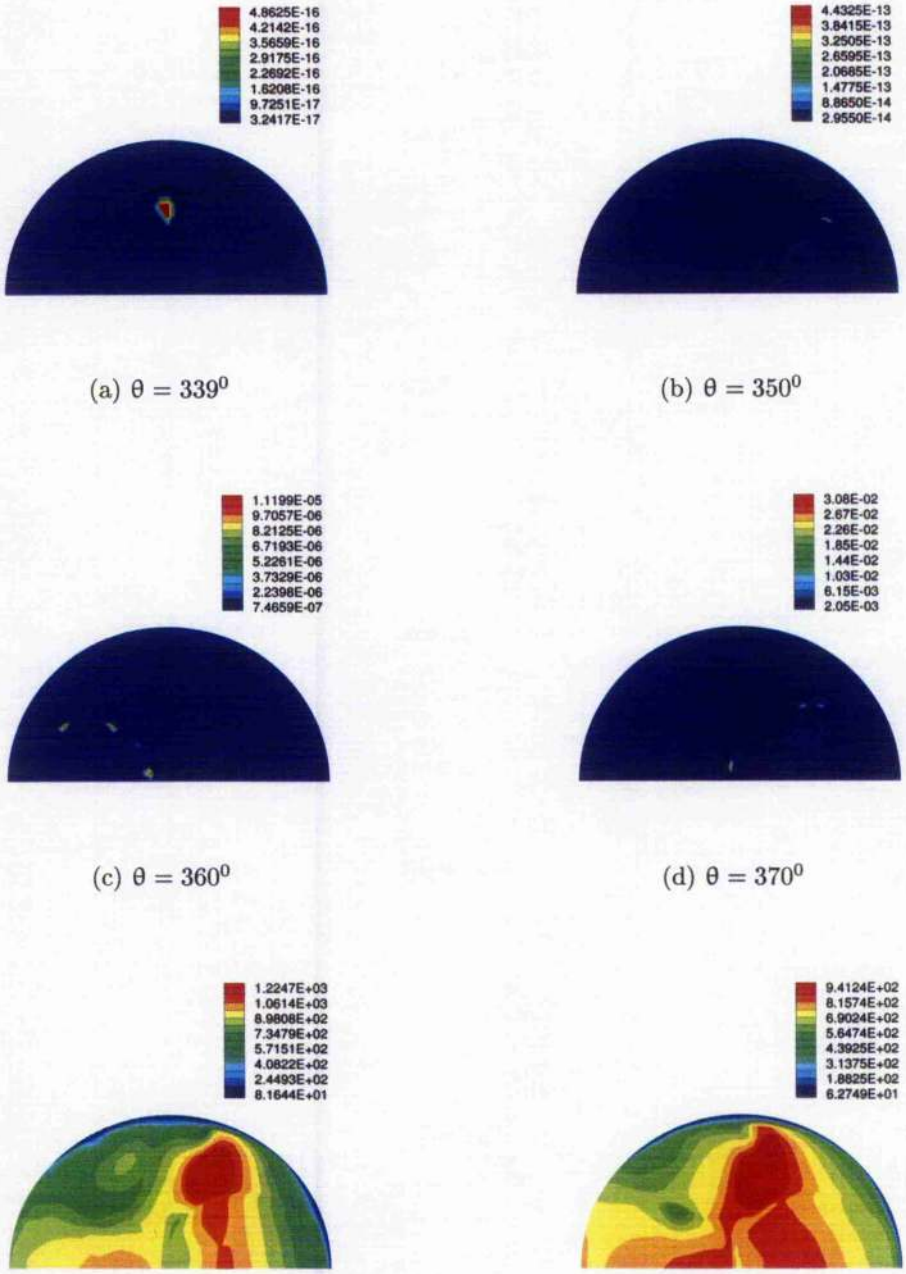

(a) $\theta = 339^0$

(b) $\theta = 350^0$

(c) $\theta = 360^0$

(d) $\theta = 370^0$

(e) $\theta = 380^0$

(f) $\theta = 390^0$

Figure 8.33: In-cylinder CO distribution (gr/m^3) of the Ricardo E6 CFR gasoline engine (1500 rpm, ignition at θ=-24^0 BTDC, WOT)

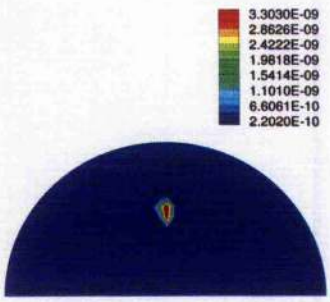

(a) $\theta = 339^0$

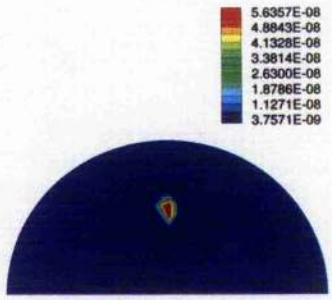

(b) $\theta = 350^0$

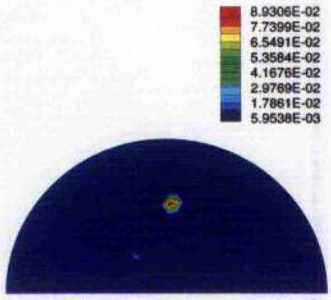

(c) $\theta = 360^0$

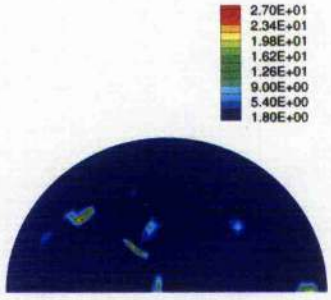

(d) $\theta = 370^0$

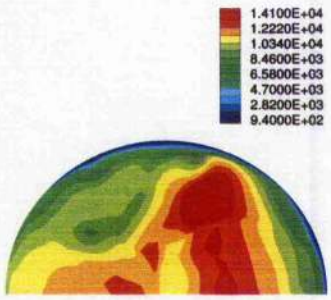

(e) $\theta = 380^0$

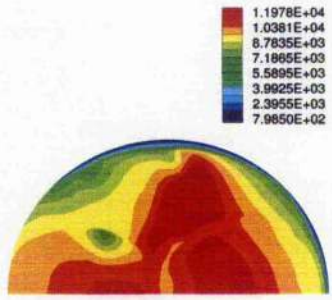

(f) $\theta = 390^0$

Figure 8.34: In-cylinder NO distribution (gr/m^3) of the Ricardo E6 CFR gasoline engine (1500 rpm, ignition at θ=-24^0 BTDC, WOT)

8.3.2 Toledo 1500 SI gasoline engine

The predicted and measured in-cylinder pressures of Toledo 1500 SI engine (operating at 2000 rpm, 2/3 WOT) are illustrated in figure 8.35. It can be seen that the maximum predicted pressure is about 8% higher than the maximum measured value. Before θ=342^0 the predicted pressure is lower than the measures one. Overprediction of the pressure occurs from θ=342^0 to θ=388^0, then the pressure is underpredicted. The model predicts the maximum pressure at θ=375^0, while the measured peak pressure occurs at θ=378^0. The explanation for the difference between predicted and measured pressure is similar to that of in Caterpillar 3401 diesel engine in section 8.1.

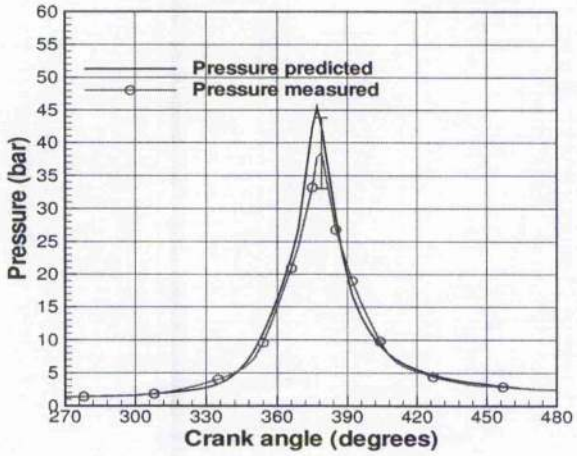

Figure 8.35: In-cylinder pressure of the Toledo 1500 SI engine (2/3 WOT, ignition at -30^0 BTDC, 2000 rpm)

The effects of ignition timing on NO, CO_2, and CO concentrations of the Toledo 1500 SI engine operating in mode A (1800 rpm, 1/2 WOT) are illustrated in figures 8.36, 8.37, and 8.38, respectively. It is observed in figure 8.36 that NO concentration

decreases monotonically with retarding of ignition timing from the ignition point θ=-30^0 BTDC. In figure 8.37 CO_2 concentration increases with retarding ignition, a peak value is observed when ignition occurs at θ=-20^0 BTDC, then CO_2 concentration reduces at retarding ignition timing. It can be seen in figure 8.38 that the variation of CO concentration with the changing of ignition timing is similar to that of CO_2. The effects of ignition timing on emissions are explained as follows.

When the piston approaches TDC, the spark plug discharges to ignite the air/fuel mixture in the cylinder chamber. It takes about 0.0004 second (about 5^0 crank angle (CA) at engine speed of 1800 rpm) to transfer energy from the spark plug to the unburned mixture in the cylinder. After the development of the flame front, it takes about an additional 20^0 CA for the flame front to reach the cylinder wall and another 10^0 CA for completion of air/fuel burning. In the case of advanced ignition timing (ignition at -30^0 BTDC) the flame front develops and propagates through the combustion chamber when the piston is close to TDC. Most of the chemical energy of fuel is converted into thermal energy in the combustion chamber resulting in maximized temperature and pressure in the cylinder, and in high production rate of NO from thermal and prompt routes. When ignition timing occurs closer to TDC complete combustion of air/fuel mixture occurs further into the expansion stroke. Therefore the chemical energy of fuel is released in a larger volume. This leads to reduction of the in-cylinder maximum temperature and pressure, which in turn reduces the production rate of NO.

In figures 8.36 and 8.37, when ignition timing retards from θ=-30^0 BTDC to θ=-20^0 BTDC, the concentration of NO reduces, while the concentration of CO_2 increases. This is explained as follows. When ignition timing is retarded at constant

throttle, load is lowered to keep engine speed constant, which leads to reduction of the residual gas in the cylinder. On the other hand, the unburned mixture in the cylinder is compressed to higher pressure before being ignited (compared to the more advanced ignition cases), which results in high temperature of the mixture. Low residual gas and high unburned mixture temperature lead to faster development and propagation of the flame front, the combustion of the mixture is more complete, and more CO_2 is created. However, the combustion process finishes when the piston has passed TDC, so that the maximum in-cylinder temperature and pressure are lower than those in the cases of more advanced ignition, leading to lower NO production rate. This phenomenon occurs until ignition timing retards to θ=-20^0 BTDC, where a peak value of CO_2 is observed. If ignition timing continues to retard, the combustion precess occurs in the expansion stroke. Therefore the in-cylinder maximum temperature and pressure decrease, and monotonic reductions of CO_2 and NO are observed. The variation of CO concentration as a function of ignition timing in figure 8.38 can be explained in a similar manner to that of CO_2 concentration.

The in-cylinder pressure profiles as engine was operated in mode B (maximum load of dynamometer, ignition at θ=-30^0 BTDC) are shown in figures 8.39, 8.40, and 8.41. Results for CO_2, CO, and NO emissions are shown in figures 8.42, 8.43, and 8.44, respectively. Increase of engine speed causes the point of complete air/fuel combustion to move further into the expansion stroke. The reduction of the combustion rate due to increase the residual gas when the engine is operated at high load may contribute to the low maximum temperature. The reductions of the in-cylinder maximum temperature and pressure continue until engine speed reaches 2200 rpm. At this speed a minimum NO concentration is observed. As engine speed continues to

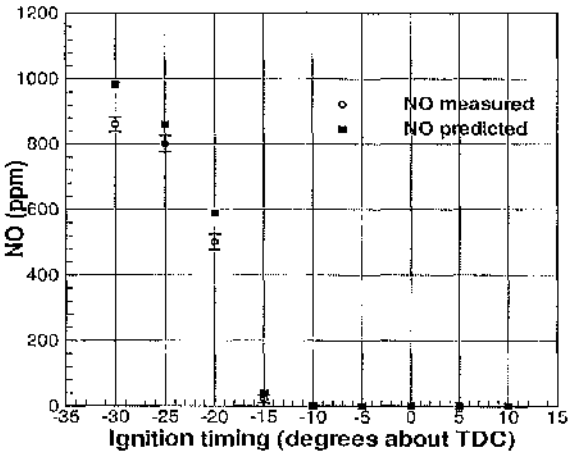

Figure 8.36: Exhaust NO variation with ignition timing of the Toledo 1500 SI engine (1/2 WOT, 1800 rpm)

increase, the energy added to the in-cylinder gas is larger than the energy taken away by exhaust, cooling water, and radiation. The dominance of the supplied energy in the competition between lost energy and added energy causes rise in the temperature of the in-cylinder mixture, which in turn accelerates the combustion rate. The combustion is more complete, the concentration of CO_2 increases (figure 8.42), and a higher maximum temperature and pressure in the combustion chamber are observed. NO concentration gradually increases with engine speed from 2200 rpm.

In figure 8.44 NO concentration increases with increasing engine speed from 1500 rpm to 2000 rpm, and a maximum peak value is seen at the engine speed of 2000 rpm; after that NO concentration gradually decreases with increasing engine speed. A minimum peak value of NO concentration is observed at the speed of 2200 rpm. Above the speed of 2200 rpm there is a monotonic increase of NO concentration with increasing speed.

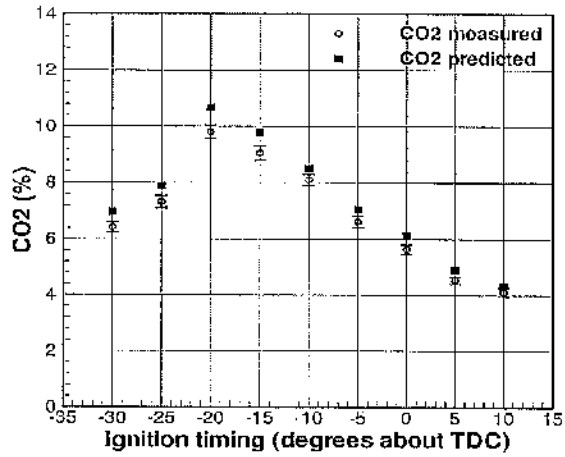

Figure 8.37: Exhaust CO_2 variation with ignition timing of the Toledo 1500 SI engine (1/2 WOT, 1800 rpm)

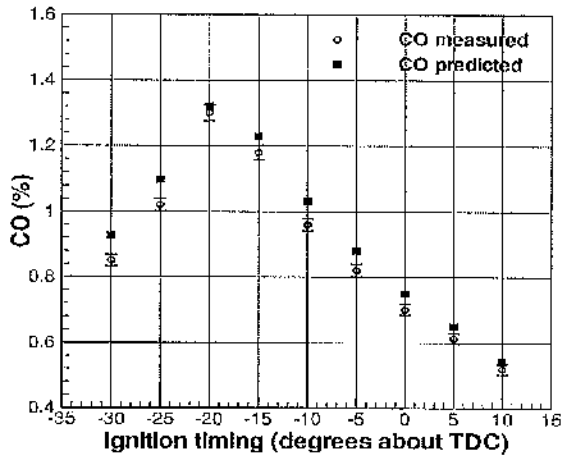

Figure 8.38: Exhaust CO variation with ignition timing of the Toledo 1500 SI engine (1/2 WOT, 1800 rpm)

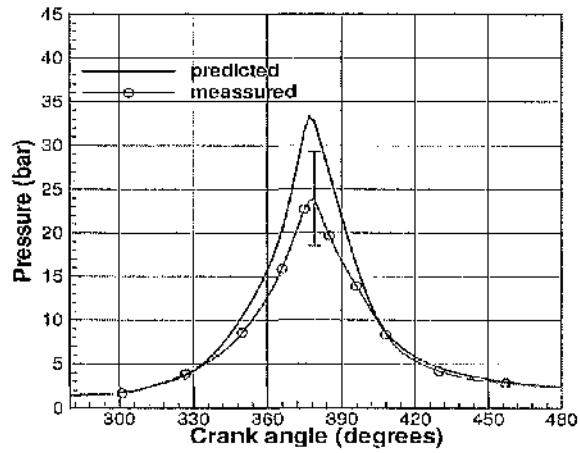

Figure 8.39: In-cylinder pressure of the Toledo 1500 SI engine (1/2 WOT, ignition at -30^0 BTDC, 1800 rpm)

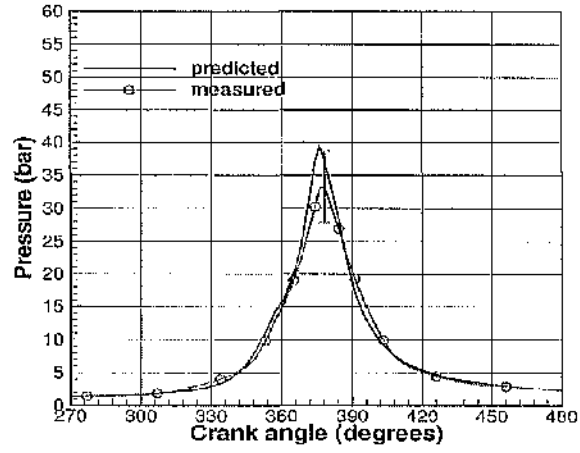

Figure 8.40: In-cylinder pressure of the Toledo 1500 SI engine (5/8 WOT, ignition at -30^0 BTDC, 1900 rpm)

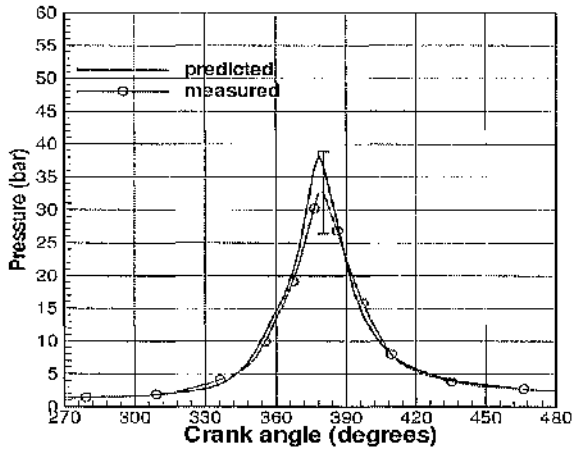

Figure 8.41: In-cylinder pressure of the Toledo 1500 SI engine (2/3 WOT, ignition at -30^0 BTDC, 2300 rpm)

The variation of NO concentration with engine speed is the result of the combination of many factors. The energy supplied to the engine per unit of time increases with increasing engine speed increases. Because the flow rate of cooling water is constant, the energy taken away by cooling water is proportional to the difference of temperature between cylinder liner and cooling water. The combination of these parameters leads to increase of the in-cylinder temperature. The residual gas influences the in-cylinder temperature in two aspects. On one hand, the residual gas dilutes the air/fuel mixture leading to reduction of the combustion rate (reducing the development and propagation rates of the flame front). On the other hand, more residual gas in the cylinder increases the temperature of the unburned mixture, resulting in high combustion rate. When the engine is operated at high load and speed, the residual gas is high. At the maximum load the overall effect of the above parameters causes the maximum temperature and pressure in the combustion chamber to increase with

increasing engine speed from 1500 rpm to 2000 rpm. Within this range of speeds more CO_2 is created as seen in figure 8.42. High in-cylinder temperature and pressure also results in high NO production rate.

The variations of CO_2, CO, and NO concentrations as engine was operated in mode C (2/3 WOT, ignition at θ=-30^0 BTDC) are illustrated in figures 8.45, 8.46, and 8.47. Similar variation trends of CO_2, CO, and NO concentrations to those in the mode B are observed. However, in mode C the increase of engine speed is associated with the lowering of load. From the speed of 1500 rpm, the residual gas in the cylinder reduces and engine revolution increases with lower load. The increase of engine speed relatively moves the ignition point towards TDC at constant ignition timing. The combustion process moves further into the expansion stroke. The combustion of the air/fuel mixture still completes close to TDC when the engine speed increases to 1900 rpm. On the other hand, the fuel consumption increases with increasing engine speed, while the cooling water flow rate is constant, leading to an increase of the in-cylinder temperature, which in turn accelerate the combustion rate. CO_2 concentration is seen increasing from the speed of 1500 rpm to 1900 rpm. NO concentration is also observed increasing with engine speed within this range, and a maximum peak of NO concentration occurs at the speed of 1900 rpm.

From the speed of 1900 rpm CO_2 and NO concentrations decrease with increase of engine speed, and minimum peaks of CO_2 and NO concentrations occur at the speed of 2200 rpm. This is explained as follows. The late ignition leads to reduction of the in-cylinder maximum temperature. On the other hand, the combined effect of reduction of the residual gas and the increase in fuel consumption leads to increase of the in-cylinder maximum temperature. However, in these cases the effect of the

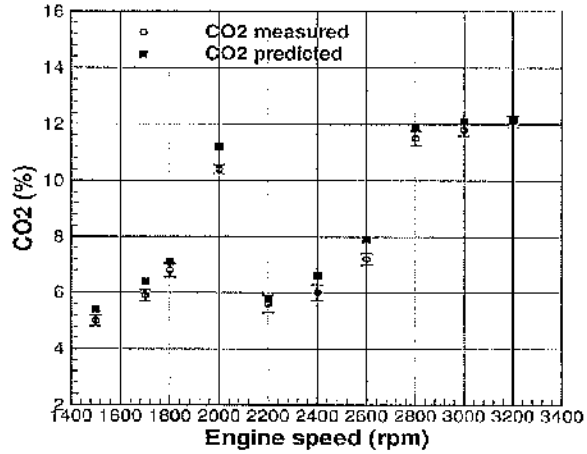

Figure 8.42: Exhaust CO_2 variation with speed of the Toledo 1500 SI engine (maximum load of dynamometer, ignition at θ=-30^0 BTDC)

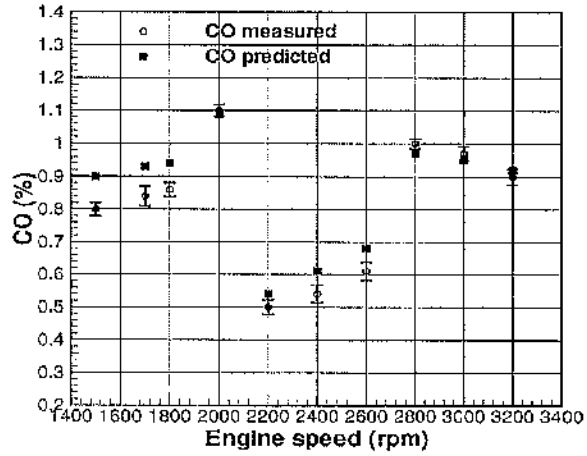

Figure 8.43: Exhaust CO variation with speed of the Toledo 1500 SI engine (maximum load of dynamometer, ignition at θ=-30^0 BTDC)

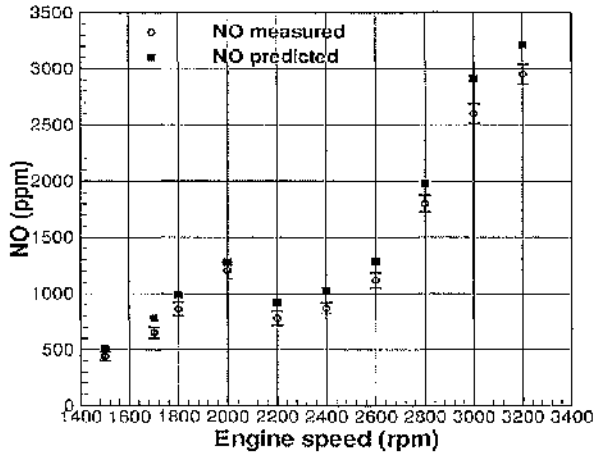

Figure 8.44: Exhaust NO variation with speed of the Toledo 1500 SI engine (maximum load of dynamometer, ignition at θ=-30^0 BTDC)

late ignition on temperature is greater than that of the residual gas and the fuel consumption. The overall effect is that the combustion of the unburned mixture moves further towards the expansion stroke, leading to decrease of the in-cylinder maximum temperature and pressure. Therefore the production rates of CO_2 and NO reduce.

For speeds above 1900 rpm the added energy from the fuel is larger than the energy taken away by the exhaust, cooling water, and radiation. More vigorous combustion occurs at high temperature, and the production rates of CO_2 and NO monotonically increase with engine speed.

The in-cylinder distributions of temperature, pressure, CO_2, CO, and NO of the Toledo 1500 SI gasoline engine operating at 1800 rpm and 1/2 WOT, 1900 rpm and 5/8 WOT, 2000 rpm and 2/3 WOT, and 2300 rpm and 3/4 WOT are illustrated in figures 8.48, 8.49, 8.50, 8.51, 8.52, 8.53, 8.54, 8.55, 8.56, 8.57, 8.58, 8.59, 8.60, 8.61,

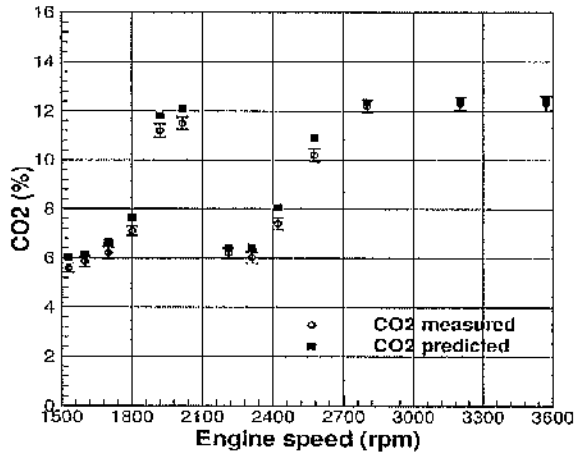

Figure 8.45: Exhaust CO_2 variation with speed of the Toledo 1500 SI engine (2/3 WOT, ignition at θ=-30^0 BTDC)

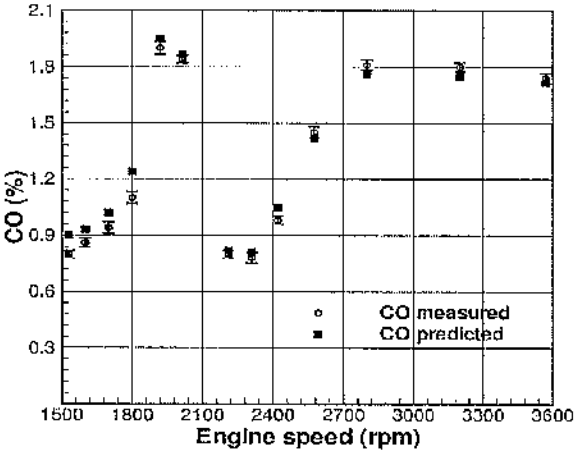

Figure 8.46: Exhaust CO variation with speed of the Toledo 1500 SI engine (2/3 WOT, ignition at θ=-30^0 BTDC)

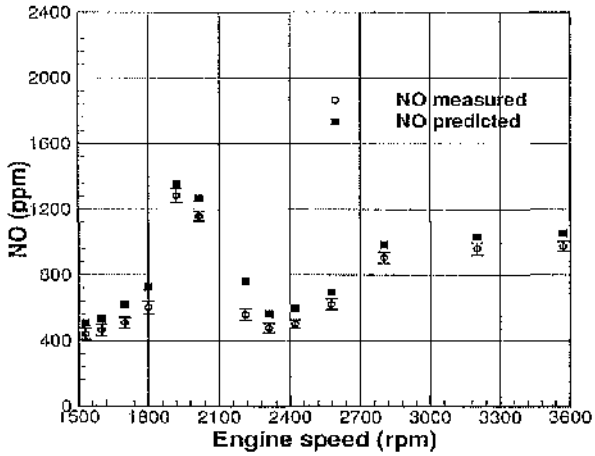

Figure 8.47: Exhaust NO variation with speed of the Toledo 1500 SI engine (2/3 WOT, ignition at θ=-30^0 BTDC)

8.62, 8.63, 8.64, 8.65, 8.66, and 8.67.

In modeling of the Toledo 1500 SI gasoline engine the pre-integrated approach slightly overpredicts both CO_2 and NO_x in all cases while CO concentration is slightly underpredicted. The differences between calculated results and experimental data lie within 6 to 18 %. This error could be introduced during the interpolating process reaction results as well as the use of the equivalent N_2 adding technique.

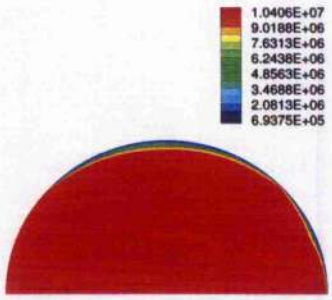

(a) $\theta = 342^0$

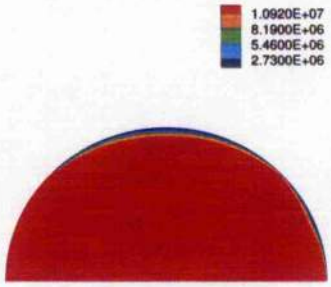

(b) $\theta = 350^0$

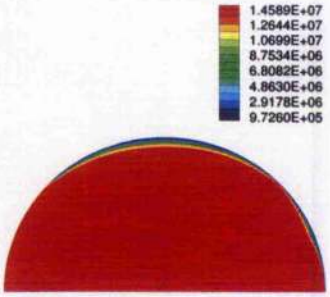

(c) $\theta = 360^0$

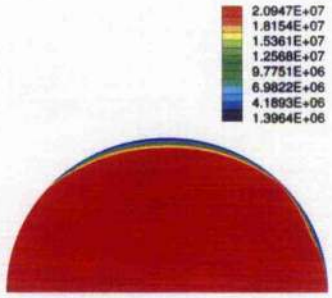

(d) $\theta = 370^0$

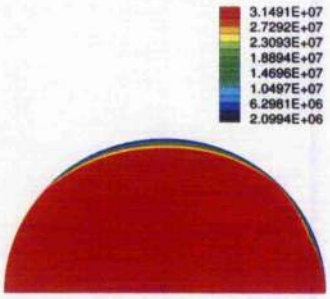

(e) $\theta = 380^0$

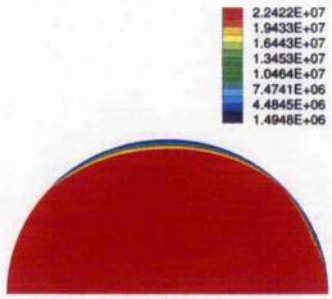

(f) $\theta = 390^0$

Figure 8.48: In-cylinder pressure distribution (dynes/cm^2) of the Toledo 1500 SI engine (1/2 WOT, ignition at -30^0 BTDC; 1800 rev/min)

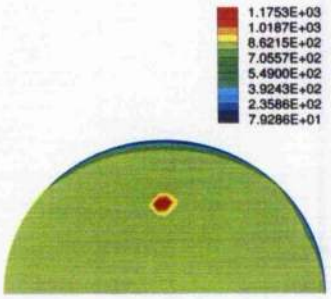

(a) $\theta = 342^0$

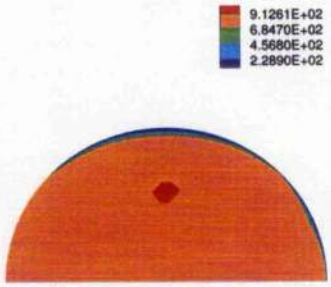

(b) $\theta = 350^0$

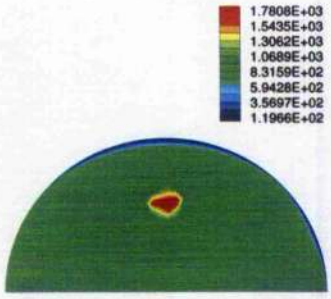

(c) $\theta = 360^0$

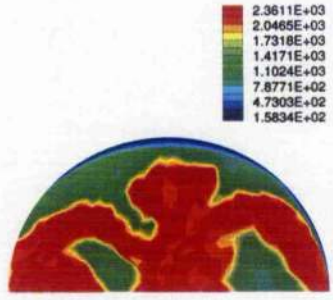

(d) $\theta = 370^0$

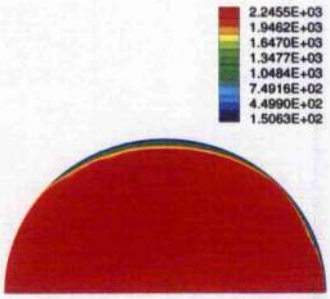

(e) $\theta = 380^0$

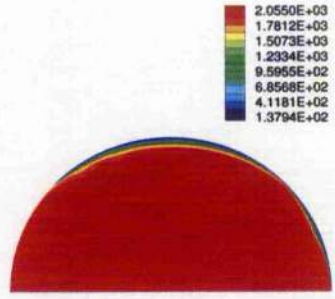

(f) $\theta = 390^0$

Figure 8.49: In-cylinder temperature distribution (K) of the Toledo 1500 SI engine (1/2 WOT, ignition at -30^0 BTDC; 1800 rev/min)

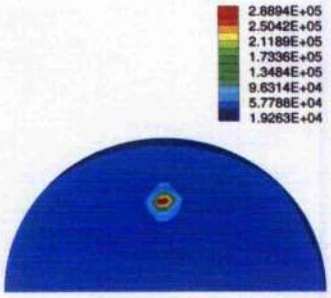

(a) $\theta = 342^0$

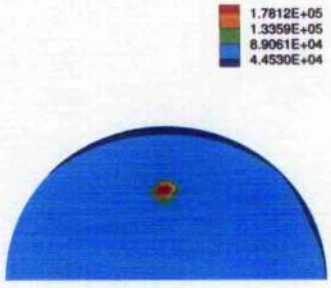

(b) $\theta = 350^0$

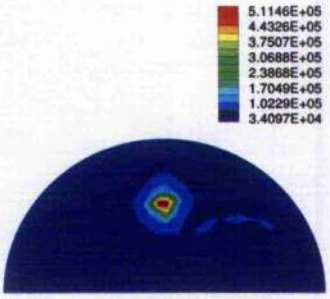

(c) $\theta = 360^0$

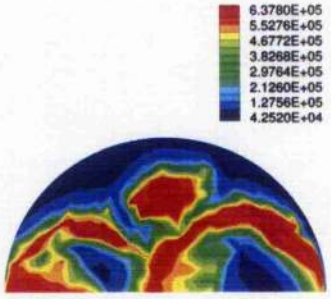

(d) $\theta = 370^0$

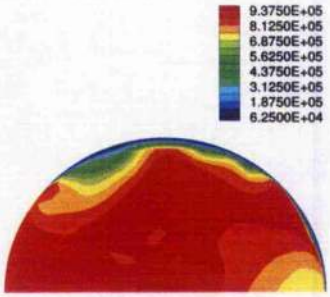

(e) $\theta = 380^0$

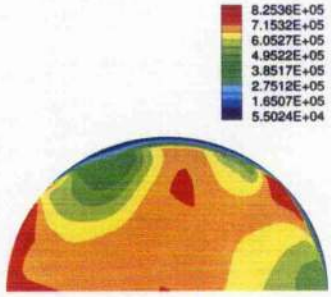

(f) $\theta = 390^0$

Figure 8.50: In-cylinder CO_2 distribution (gr/cm^3) of the Toledo 1500 SI engine (1/2 WOT, ignition at -30^0 BTDC; 1800 rev/min)

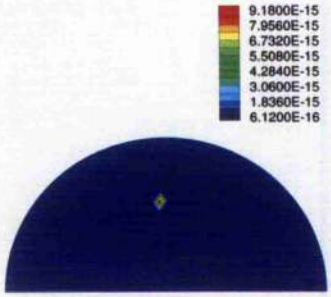

(a) $\theta = 342^0$

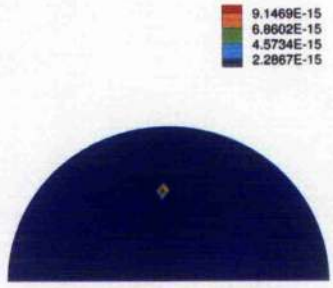

(b) $\theta = 350^0$

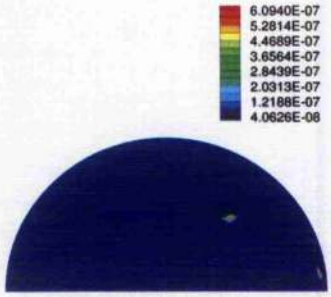

(c) $\theta = 360^0$

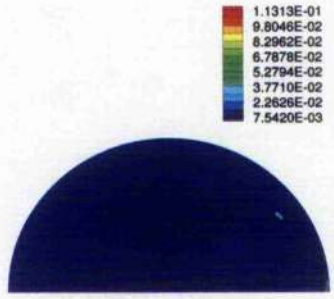

(d) $\theta = 370^0$

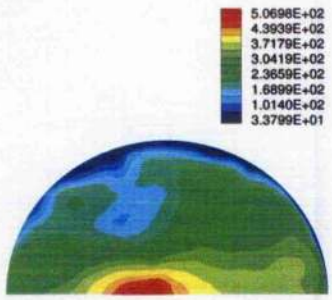

(e) $\theta = 380^0$

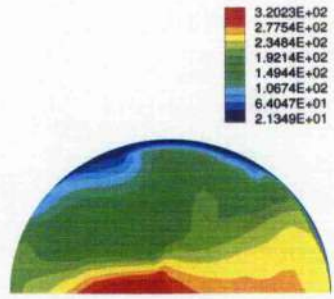

(f) $\theta = 390^0$

Figure 8.51: In-cylinder CO distribution (gr/cm^3) of the Toledo 1500 SI engine (1/2 WOT, ignition at -30^0 BTDC; 1800 rev/min)

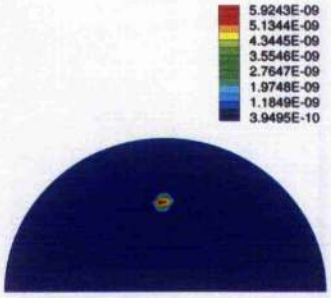

(a) $\theta = 342^0$

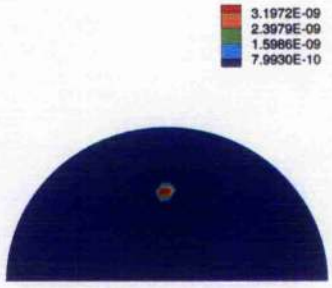

(b) $\theta = 350^0$

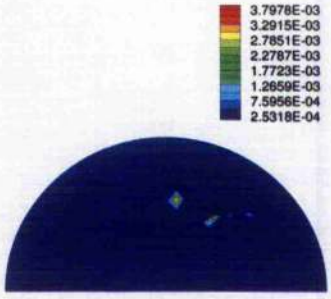

(c) $\theta = 360^0$

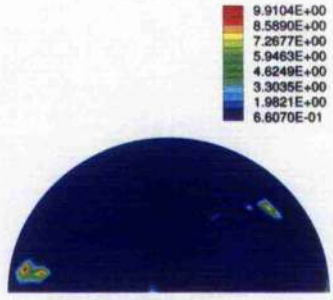

(d) $\theta = 370^0$

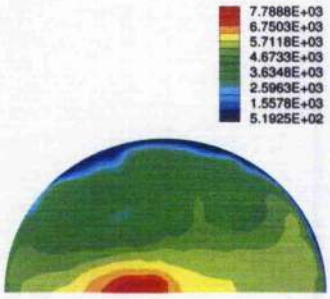

(e) $\theta = 380^0$

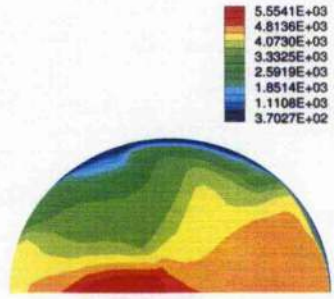

(f) $\theta = 390^0$

Figure 8.52: In-cylinder NO distribution (gr/cm^3) of the Toledo 1500 SI engine (1/2 WOT, ignition at -30^0 BTDC; 1800 rev/min)

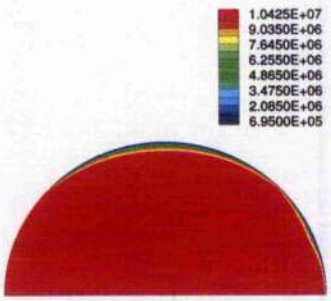

(a) $\theta = 342^0$

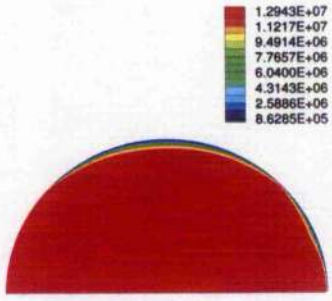

(b) $\theta = 350^0$

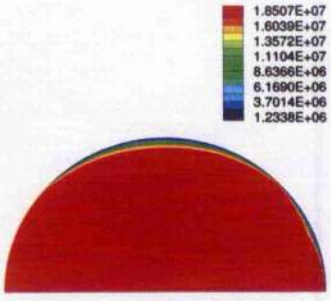

(c) $\theta = 360^0$

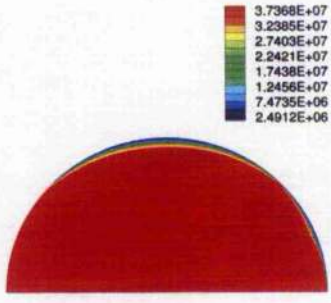

(d) $\theta = 370^0$

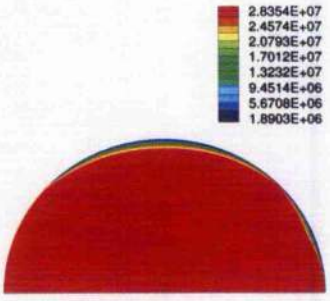

(e) $\theta = 380^0$

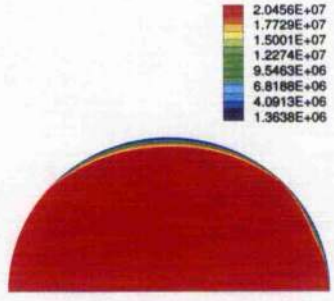

(f) $\theta = 390^0$

Figure 8.53: In-cylinder pressure distribution (dynes/cm^2) of the Toledo 1500 SI engine (5/8 WOT, ignition at -30^0 BTDC; 1900 rev/min)

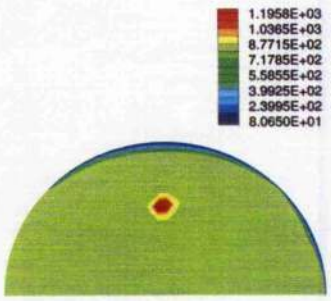

(a) $\theta = 342^0$

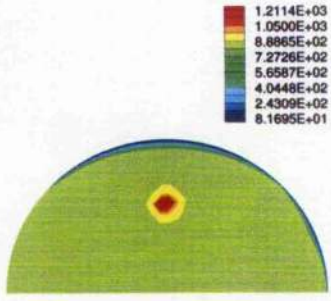

(b) $\theta = 350^0$

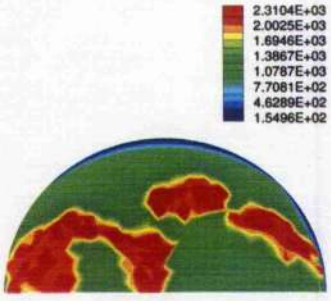

(c) $\theta = 360^0$

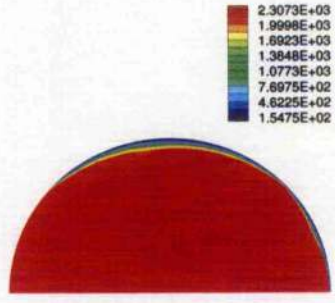

(d) $\theta = 370^0$

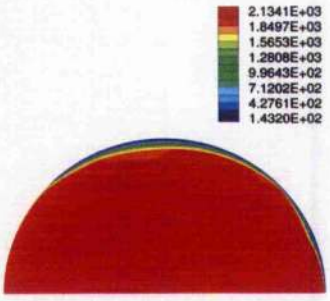

(e) $\theta = 380^0$

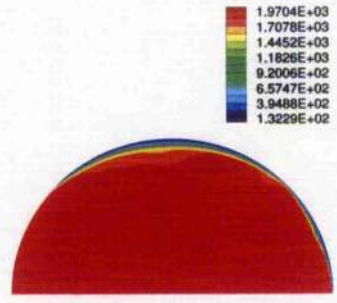

(f) $\theta = 390^0$

Figure 8.54: In-cylinder temperature distribution (K) of the Toledo 1500 SI engine (5/8 WOT, ignition at -30^0 BTDC; 1900 rev/min)

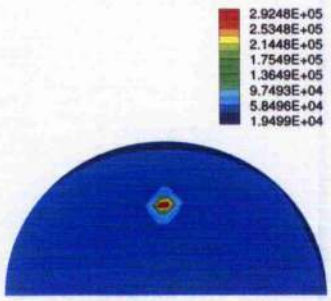

(a) $\theta = 342^0$

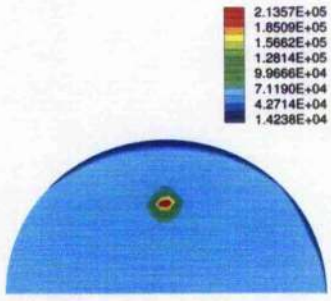

(b) $\theta = 350^0$

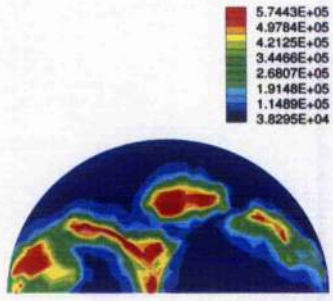

(c) $\theta = 360^0$

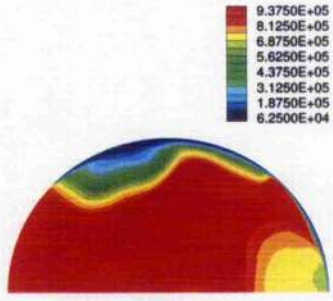

(d) $\theta = 370^0$

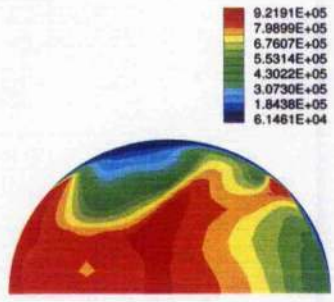

(e) $\theta = 380^0$

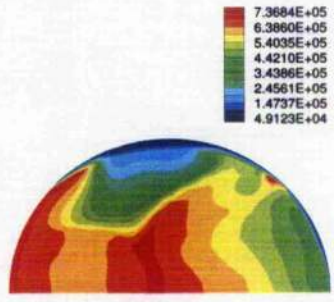

(f) $\theta = 390^0$

Figure 8.55: In-cylinder CO_2 distribution (gr/cm^3) of the Toledo 1500 SI engine (5/8 WOT, ignition at -30^0 BTDC; 1900 rev/min)

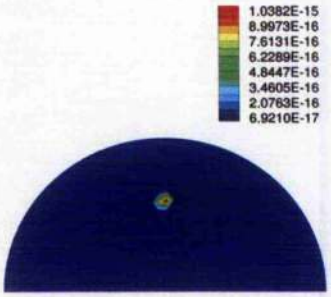

(a) $\theta = 342^0$

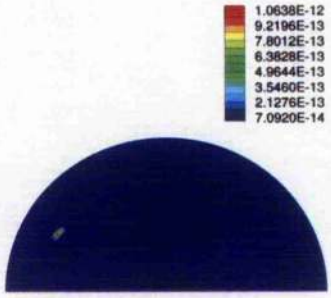

(b) $\theta = 350^0$

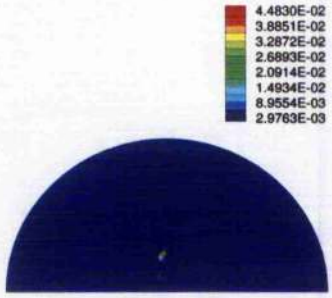

(c) $\theta = 360^0$

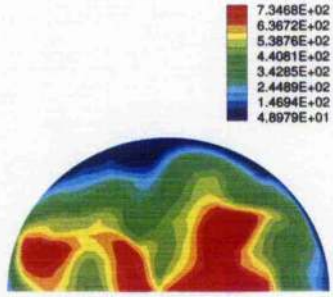

(d) $\theta = 370^0$

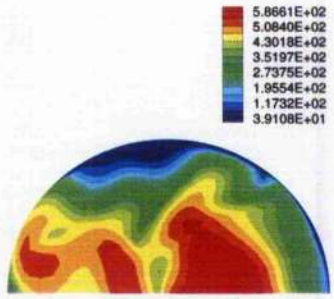

(e) $\theta = 380^0$

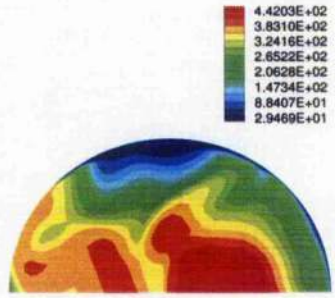

(f) $\theta = 390^0$

Figure 8.56: In-cylinder CO distribution (gr/cm^3) of the Toledo 1500 SI engine (5/8 WOT, ignition at -30^0 BTDC; 1900 rev/min)

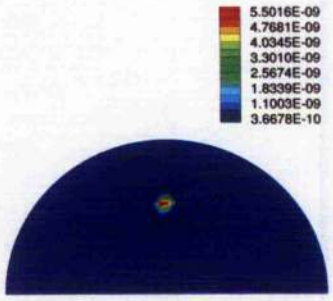

(a) $\theta = 342^0$

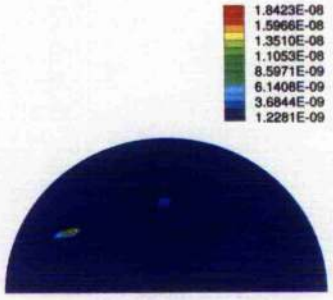

(b) $\theta = 350^0$

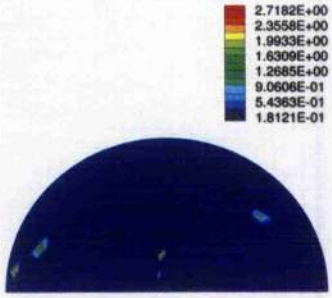

(c) $\theta = 360^0$

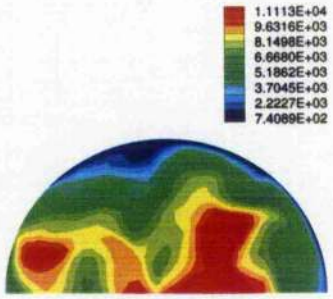

(d) $\theta = 370^0$

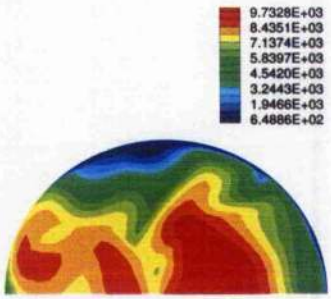

(e) $\theta = 380^0$

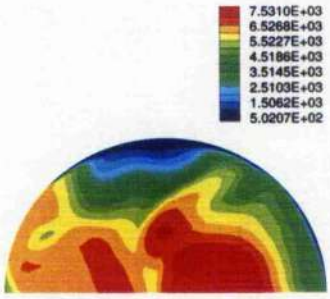

(f) $\theta = 390^0$

Figure 8.57: In-cylinder NO distribution (gr/cm^3) of the Toledo 1500 SI engine (5/8 WOT, ignition at -30^0 BTDC; 1900 rev/min)

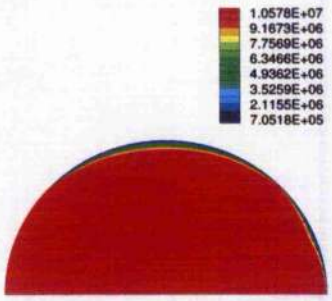

(a) $\theta = 342^0$

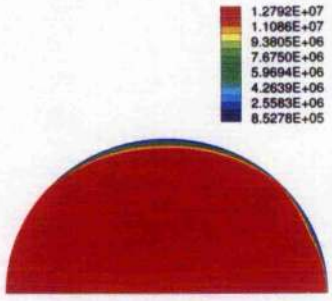

(b) $\theta = 350^0$

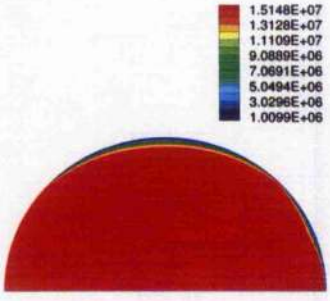

(c) $\theta = 360^0$

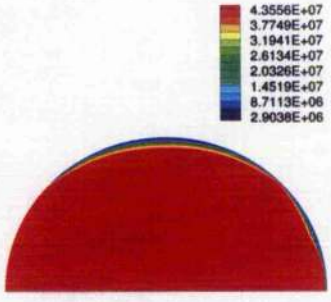

(d) $\theta = 370^0$

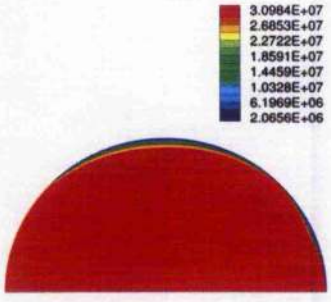

(e) $\theta = 380^0$

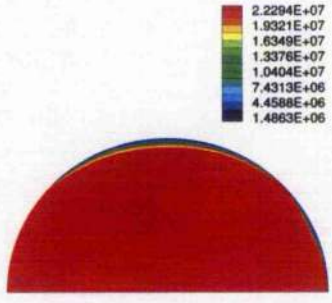

(f) $\theta = 390^0$

Figure 8.58: In-cylinder pressure distribution (dynes/cm^2) of the Toledo 1500 SI engine (2/3 WOT, ignition at -30^0 BTDC; 2000 rev/min)

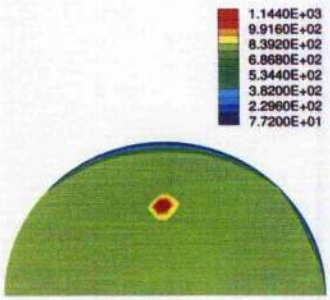

(a) $\theta = 342^0$

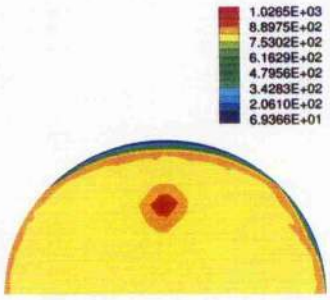

(b) $\theta = 350^0$

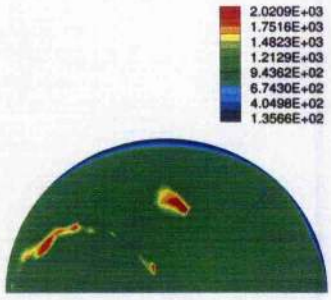

(c) $\theta = 360^0$

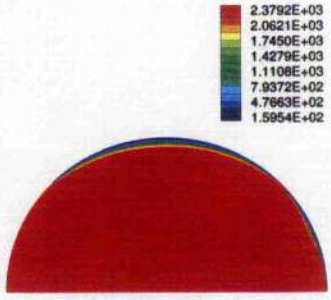

(d) $\theta = 370^0$

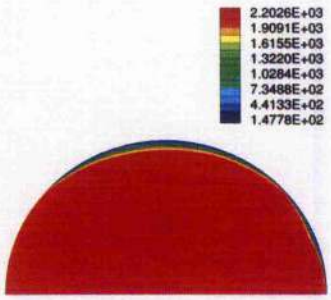

(e) $\theta = 380^0$

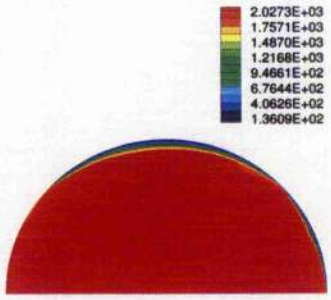

(f) $\theta = 390^0$

Figure 8.59: In-cylinder temperature distribution (K) of the Toledo 1500 SI engine (2/3 WOT, ignition at -30^0 BTDC; 2000 rev/min)

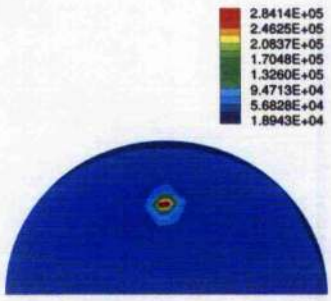

(a) $\theta = 342^0$

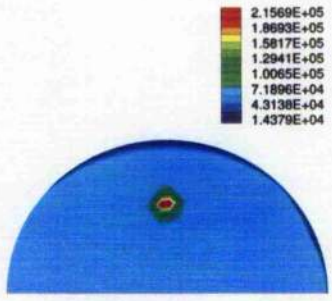

(b) $\theta = 350^0$

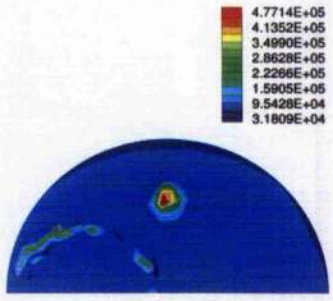

(c) $\theta = 360^0$

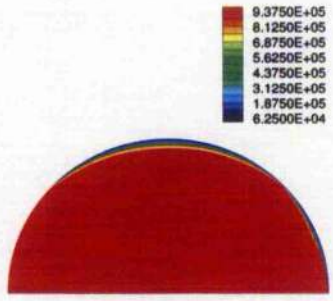

(d) $\theta = 370^0$

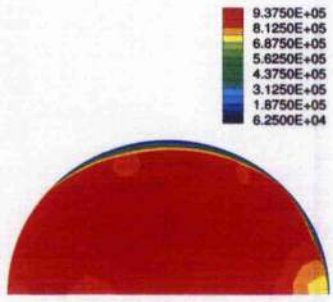

(e) $\theta = 380^0$

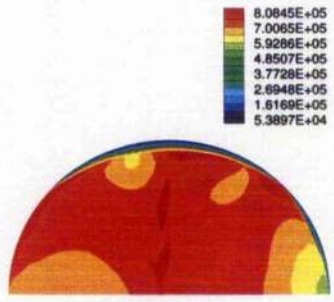

(f) $\theta = 390^0$

Figure 8.60: In-cylinder CO_2 distribution (gr/cm^3) of the Toledo 1500 SI engine (2/3 WOT, ignition at -30^0 BTDC; 2000 rev/min)

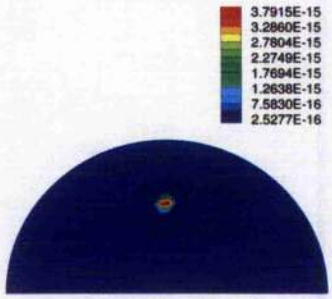

(a) $\theta = 342^0$

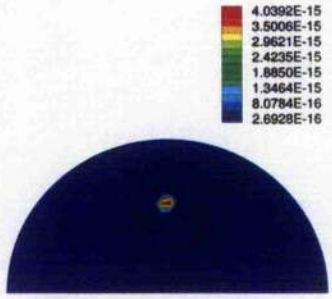

(b) $\theta = 350^0$

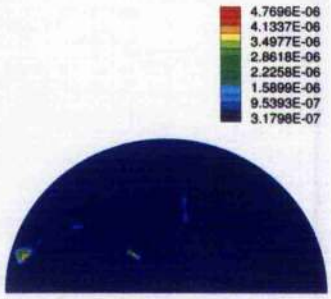

(c) $\theta = 360^0$

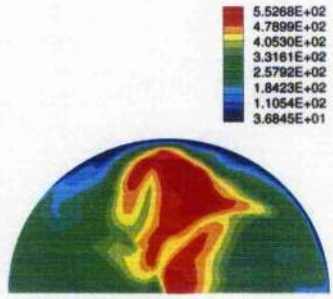

(d) $\theta = 370^0$

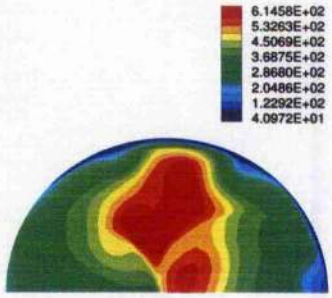

(e) $\theta = 380^0$

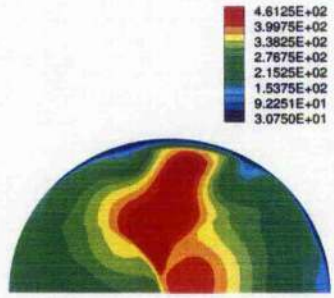

(f) $\theta = 390^0$

Figure 8.61: In-cylinder CO distribution (gr/cm^3) of the Toledo 1500 SI engine (2/3 WOT, ignition at -30^0 BTDC; 2000 rev/min)

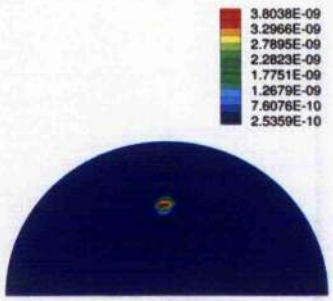

(a) $\theta = 342^0$

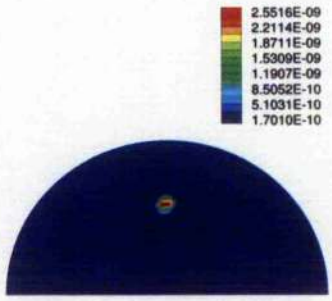

(b) $\theta = 350^0$

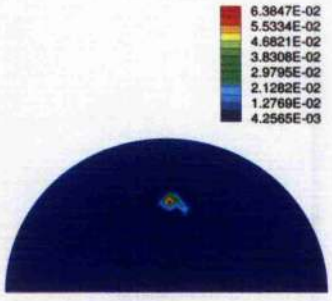

(c) $\theta = 360^0$

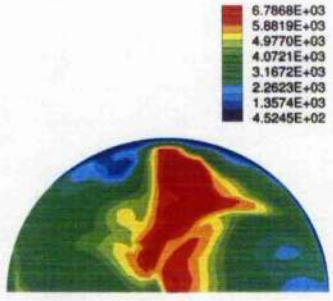

(d) $\theta = 370^0$

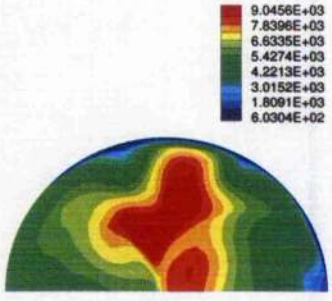

(e) $\theta = 380^0$

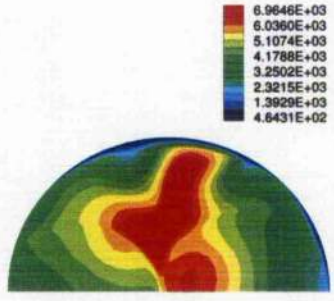

(f) $\theta = 390^0$

Figure 8.62: In-cylinder NO distribution (gr/cm^3) of the Toledo 1500 SI engine (2/3 WOT, ignition at -30^0 BTDC; 2000 rev/min)

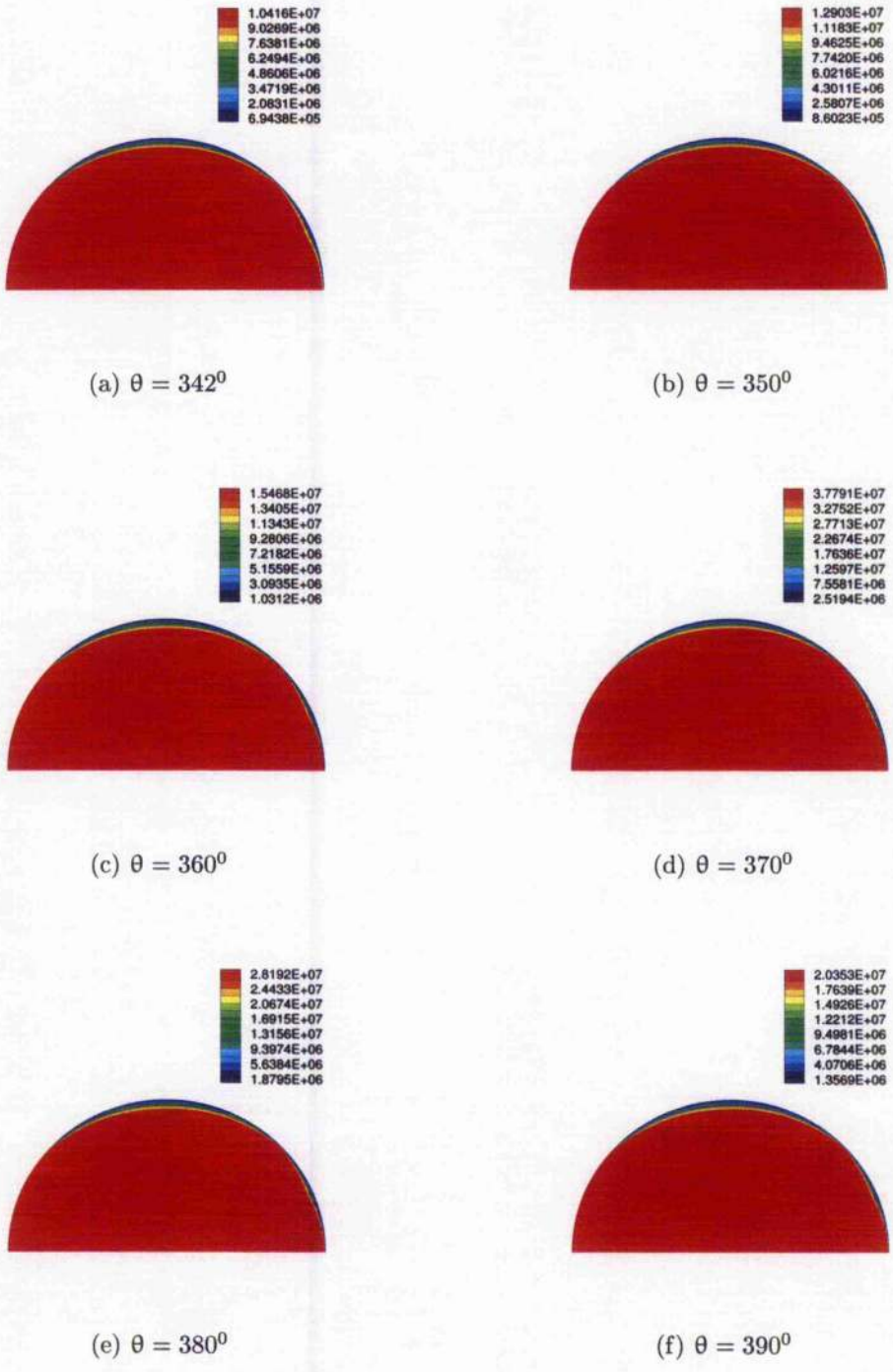

(a) $\theta = 342^0$

(b) $\theta = 350^0$

(c) $\theta = 360^0$

(d) $\theta = 370^0$

(e) $\theta = 380^0$

(f) $\theta = 390^0$

Figure 8.63: In-cylinder pressure distribution (dynes/cm^2) of the Toledo 1500 SI engine (2/3 WOT, ignition at -30^0 BTDC; 2000 rev/min)

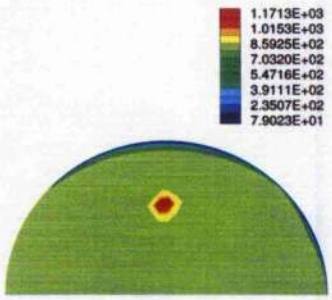

(a) $\theta = 342^0$

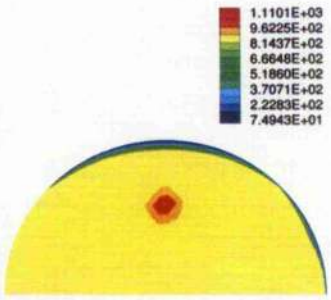

(b) $\theta = 350^0$

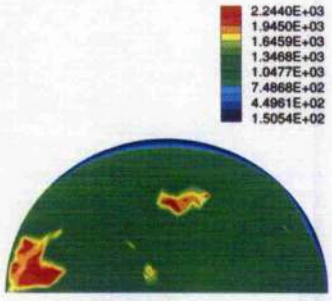

(c) $\theta = 360^0$

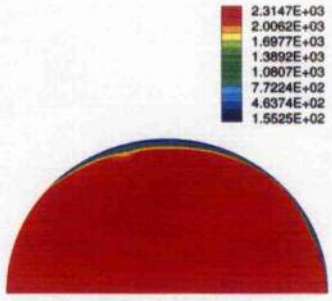

(d) $\theta = 370^0$

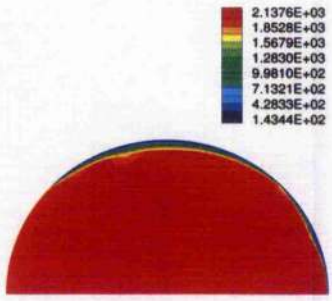

(e) $\theta = 380^0$

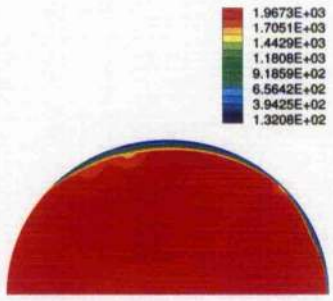

(f) $\theta = 390^0$

Figure 8.64: In-cylinder temperature (K) distribution of the Toledo 1500 SI engine (2/3 WOT, ignition at -30^0 BTDC; 2300 rev/min)

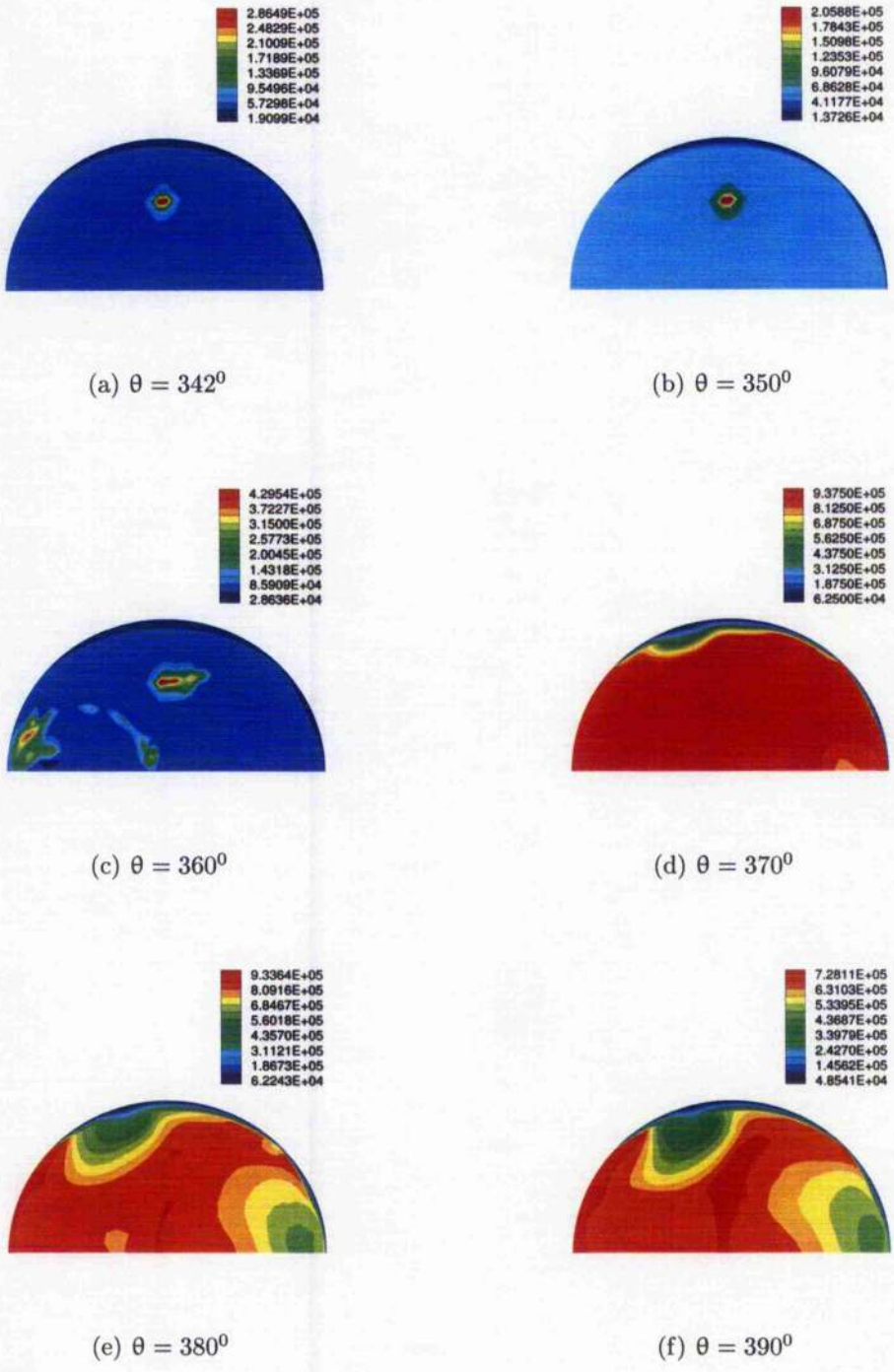

(a) $\theta = 342^0$

(b) $\theta = 350^0$

(c) $\theta = 360^0$

(d) $\theta = 370^0$

(e) $\theta = 380^0$

(f) $\theta = 390^0$

Figure 8.65: In-cylinder CO_2 distribution (gr/cm^3) of the Toledo 1500 SI engine (2/3 WOT, ignition at -30^0 BTDC; 2300 rev/min)

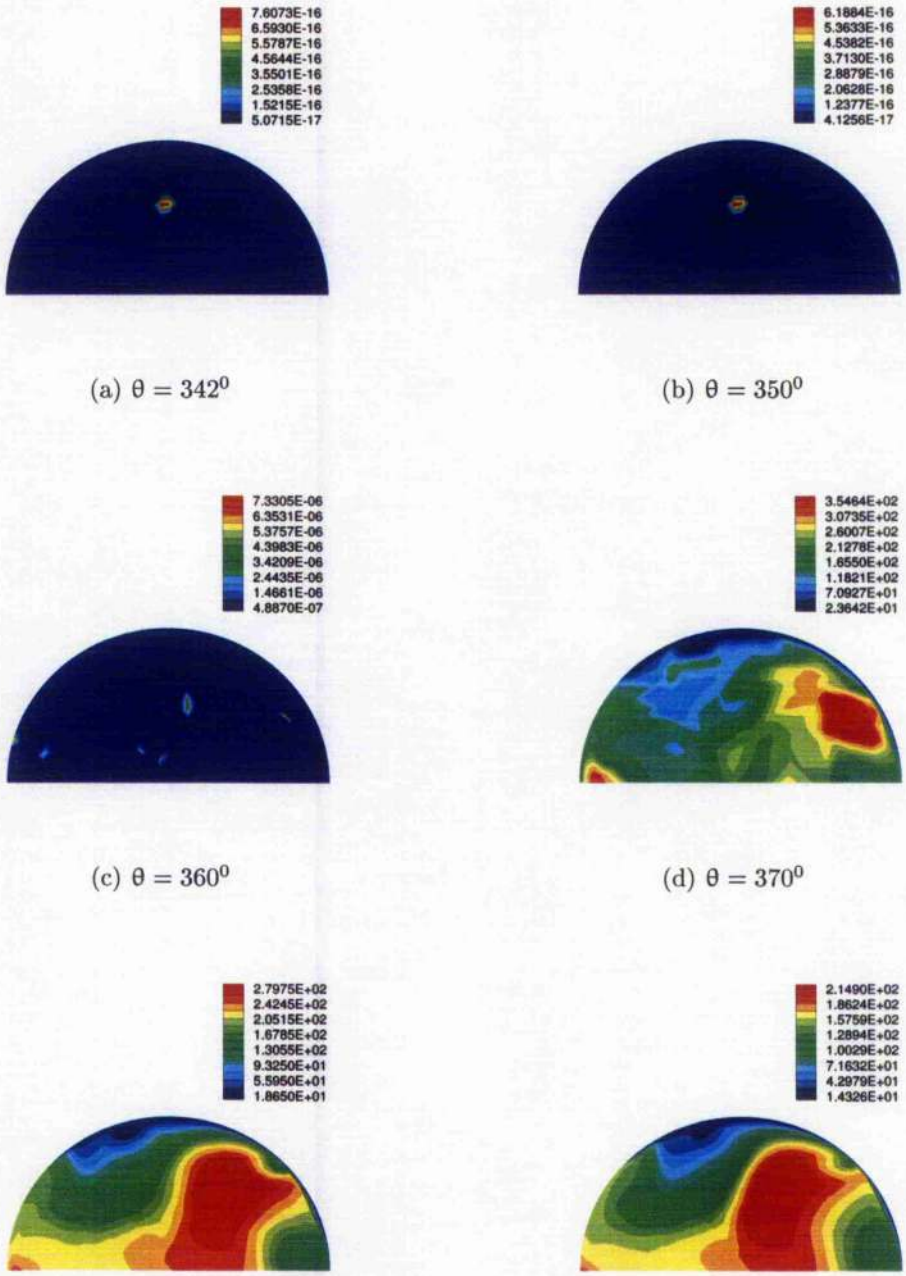

(a) $\theta = 342^0$ (b) $\theta = 350^0$

(c) $\theta = 360^0$ (d) $\theta = 370^0$

(e) $\theta = 380^0$ (f) $\theta = 390^0$

Figure 8.66: In-cylinder CO distribution (gr/cm^3) of the Toledo 1500 SI engine (2/3 WOT, ignition at -30^0 BTDC; 2300 rev/min)

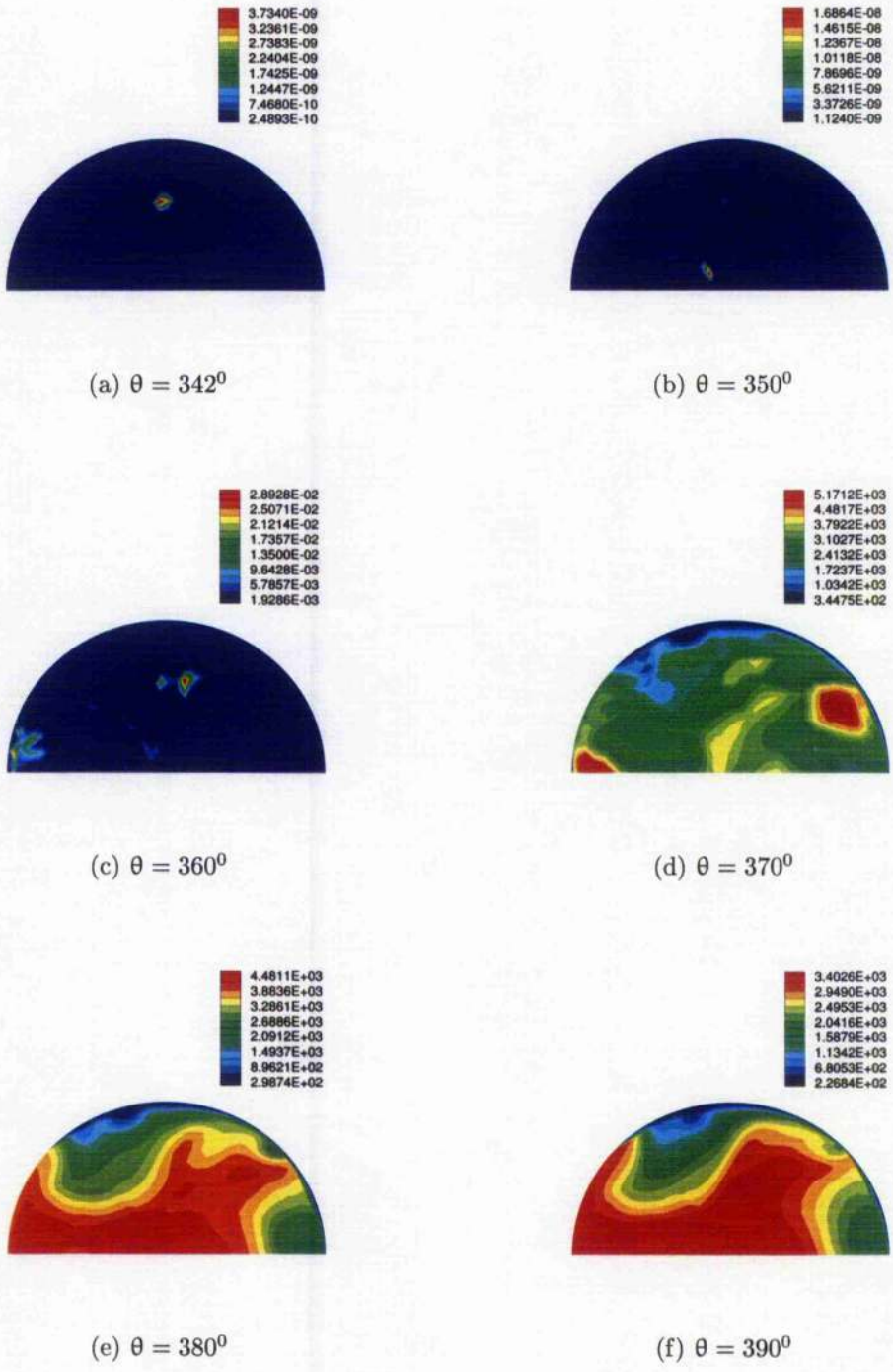

(a) $\theta = 342^0$

(b) $\theta = 350^0$

(c) $\theta = 360^0$

(d) $\theta = 370^0$

(e) $\theta = 380^0$

(f) $\theta = 390^0$

Figure 8.67: In-cylinder NO distribution (gr/cm^3) of the Toledo 1500 SI engine (2/3 WOT, ignition at -30^0 BTDC; 2300 rev/min)

Chapter 9

Conclusions

There is an urgent demand to reduce emissions of IC engines due to their serious effects on human health and the environment. Parts of the effort is modeling the engine operation and predicting emissions in order to produce better designs, environmentally friendly engines. Many approaches have been proposed to predict emissions from IC engines. These approaches can be classified in four main groups: 1) non-dimensional, 2) Reynolds-averaged Navier-Stokes equations, 3) large-eddy simulation, and 4) direct numerical simulation. Each of them has its own advantages and disadvantages.

Among these approaches the non-dimensional simulation is the simplest, thus, it is the computationally cheapest. However, the method computes the engine operation and emissions without considering the effect of engine geometry. This leads to errors in predicting engine performance and formation of emissions. Therefore, this method is not used in our application.

In the RANS equation approach simulations are based on a statistical averaging to solve only the mean flow. All the scales of the flow are modelled. Therefore the accuracy of the method is strongly dependent upon the quality of the models used. The attraction of the RANS equation approach is its computational efficiency, since

only the mean flow is computed. The averaged calculation of the RANS equation approach is not chosen to solve the combustion process cylinder due to large errors introducing during calculation of high Reynolds number fluids.

DNS is a straight forward method in which all the turbulent scales are solved. DNS is highly accurate but very computationally intensive, therefore its application is still limited to low Reynolds numbers. It is not possible to use DNS for IC engine applications at present time.

In computational fluid dynamics, LES lies in the middle range, between RANS and DNS. It greatly reduces the computational time but still reasonably keeps the accuracy of DNS. The solution from LES is much more accurate than that of RANS, since in LES large scale eddies are calculated exactly, only eddies, which are smaller than the dimension of the computational cell, are modelled. Because of its advantages, LES is used to calculate fluid dynamics process in the pre-integrated approach.

Modeling operation of IC engines and prediction emissions requires coupling the non-equilibrium chemical reaction of air/fuel mixture with the fluid dynamics process. Correct and appropriate use of detailed chemical kinetics reaction mechanisms can predict accurately the formation of emissions. Because computational time grows exponentially with the number of involved species and reactions, at present time researchers prefer using reduced chemical reaction mechanisms, in which the number of involved species and reactions is limited. A novel and effective approach is developed in this study, which avoids the computationally intensive drawback, while keeping the accuracy of the detailed reaction kinetics mechanism. The approach is called "Pre-integrated non-equilibrium combustion response mapping". In this approach, detailed chemical kinetics reactions of air/fuel mixture are pre-calculated in discrete

intervals corresponding to all possible reaction conditions in the engine. The most active species and species of interest are treated exactly. The remaining reaction results are then rearranged using the equivalent N_2 adding technique, in which all concentrations of intermediate species are added in the nitrogen molecular concentration. The results are decoupled from the chemical timescale and re-coupled into the engine physical timescale, while the timescale is also limited by the intensity of species production rates. After that, the results are converted into a database file. The database file is an assembly of fitted polynomial relations between the reaction conditions and results. Whenever a chemical reaction result is required during the calculating procedure, instead of computing the chemistry directly (as other researchers did with reduced reaction mechanisms), reaction results are obtained from the database file through an interpolating process.

The pre-integrated approach has been applied to calculate performance and compared with published emissions results of three major types of engine: 1) CI engine using diesel fuel, 2) SI gasoline engine, and 3) SI engine fuelled by methane. The pre-integrated approach is also validated using experimental data obtained from Toledo 1500 SI gasoline engine. The predicted emissions agree well with experimental data. The approach can be assessed as following.

Computational efficiency

1) With the pre-integrated approach for calculating chemical results computer time is reduced significantly compared to using reduced reaction mechanisms and/or direct detailed chemical kinetics.

2) The memory requirement is reduced since the number of species treated is lower than in the case of reduced mechanisms and/or direct detailed chemical kinetics,

because there is no requirement to calculate directly thousands of species reactions.

3) The method is robust. The chemical reaction can be obtained at any possible reaction conditions in IC engines.

4) The method is very flexible since it can be applied for all types of fuels. Once a database file of a certain fuel is created, it can be used for many kinds of engines using this fuel.

Computational accuracy

Comparison has been made for in-cylinder pressure, temperature, CO_2, CO, and NO_x concentrations. The predicted results of the pre-integrated approach agree reasonably with the experimental data. The differences between computed results and measured data lie within 6 % to 24 %.

Limitation of the approach

Although the pre-integrated approach has distinct advantages in emissions predictions, it still has some limitations. These limitations mostly arise from the equivalent N_2 adding technique, and from discretizing chemical reaction results, which are exponentially dependent on temperature and species concentrations into the database file using polynomial relations. The equivalent N_2 adding technique artificially introduces or takes away less active molecules into or from the system, and causes a pressure shift in early stage of fuel dissociation. Some recommendations to reduce this error are presented in chapter 10.

Contributions of this study

In this work a new approach is introduced to solve the difficulties in coupling chemical kinetics with turbulent fluid dynamics processes for predicting emissions in IC engines.

This approach is an efficient tool to eliminate the problem caused by the difference in the eigenvalues of the two processes. It helps IC modeling research to obtain more accurate results in both engine performance and emissions, while reducing the computational effort.

Concluding remarks

The assessment of this novel method concludes that the pre-integrated non-equilibrium combustion mapping approach is a reliable and efficient tool to predicting emissions in IC engines. The approach can be used for a wide range of engines, and different types of fuels with high accuracy and robustness.

Chapter 10

Recommendations

The pre-integrated non-equilibrium combustion response mapping approach for predicting engine emissions has advantages over both reduced and detailed chemical reaction mechanisms. It treats the species of interest temporally and spatially exactly, while reducing the total number of species taken into account. The pre-integrated method is more accurate and faster than the reduced reaction mechanism approach. This novel approach significantly reduces computational intensity, while keeping reasonable accuracy of the detailed chemical kinetics mechanism. Use of the equivalent N_2 adding techniques and polynomial fitting of the database file in this approach causes some errors. Although these errors do not affect seriously the overall accuracy of the approach, the method could be improved to reduce these errors.

Because the approach treats species exactly, all intermediate species during the dissociating process are added in to nitrogen molecule N_2 using the equivalent N_2 adding technique. For heavy fuel, in the early stage of the decomposition process, heavy intermediate species are interpreted as N_2, equivalent to the introduction of additional N_2 molecules into the system. Although later on in the calculation process these species are extracted from the equivalent N_2, without affecting the reaction

rate, it still causes a small shift in pressure of the air/fuel mixture in the cylinder in the early fuel decomposition stage and drive the predicted pressure profile away from the measured data. It is recommended that instead of adding all the intermediate species in N_2, a numerical sensor should be used to detect heavy intermediates. If their molecular weights are closed to N_2, then we add their concentration in equivalent N_2. In contrast, if their molecular weights are closer to the fuel, then we can add them back to the fuel. The numerical sensor would be based on molecular weight, but the sensitivity level (this is the minimum value of molecular weight at which the molecular concentration is added in equivalent N_2) must be treated carefully. If the sensitivity level is set too high, then the dissociation of fuel will be halted, since all intermediates resulting from fuel decomposition would be added back to fuel. If the sensitivity level is set at the N_2 molecular weight, then the process would be reduced to our present equivalent N_2 adding technique is obtained.

In our approach the detailed chemical kinetics reaction results of fuel/air mixture are represented by an assembly of discrete regions of results. The exponential relationship between the reaction results and reaction conditions namely temperature and species concentration is replaced by polynomials in the database file. The transformation of reaction results into the database file causes errors. These errors are curbed by reducing the interval of highly nonlinear variables (such as temperature) in the reaction conditions region. Increment of the resolution of the reaction region increases computer cost, even if an uneven resolution technique is used (in which the highly nonlinearity regions are represented by higher resolution whereas other regions are described with lower resolution). It is believed that the accuracy of transformation process will increase if the polynomial relation is replaced by more accurate forms

such as Fourier transforms. The Fourier transform may produce as accurate results as when using polynomial relation with increased resolution for the reaction condition region.

Appendix A

Droplet collision and breakup source terms

In KIVA-3 the collision source term ($\dot{f}_{coll}$) in the spray equation (5.1.6) is calculated by:

$$\begin{aligned}\dot{f}_{coll} &= \frac{1}{2}\int\int f(\mathbf{x},\mathbf{v}_1,r_1,T_{d_1},y_1,\dot{y}_1,t)\ f(\mathbf{x},\mathbf{v}_2,r_2,T_{d_2},y_2,\dot{y}_2,t)\pi(r_1+r_2)^2|\mathbf{v}_1-\mathbf{v}_2| \\ &\quad \{\sigma(\mathbf{v},r,T_d,y,\dot{y},\mathbf{v}_1,r_1,T_{d_1},y_1,\dot{y}_1,\mathbf{v}_2,r_2,T_{d_2},y,\dot{y}_2) \\ &\quad -\delta(\mathbf{v}-\mathbf{v}_1)\delta(r-r_1)\delta(T_d-T_{d_1})\delta(y-y_1)\delta(\dot{y}-\dot{y}_1)\} \\ &\quad -\delta(\mathbf{v}-\mathbf{v}_2)\delta(r-r_2)\delta(T_d-T_{d_2})\delta(y-y_2)\delta(\dot{y}\quad \dot{y}_2) \\ &\quad d\mathbf{v}_1\ dr_1\ dT_{d_1}\ dy_1\ d\dot{y}_1\ d\mathbf{v}_2\ dr_2\ dT_{d_2}\ dy_2\ d\dot{y}_2. \end{aligned} \tag{A.0.1}$$

The collision transition probability function σ is defined so that $\sigma d\mathbf{v}drdT_d dydy$ is the probable number of drops with properties in the implied intervals that result from a collision between a droplet with subscript 1 properties and one with subscript 2 properties. Two types of collisions are accounted for. If the collision impact parameter b is less than a critical value b_{cri}, then the droplets coalesce. If b exceeds b_{cri}, then the droplets maintain their sizes and temperatures but undergo velocity changes. The

critical impact parameter b_{cri} is given by:

$$\begin{aligned} b_{cri}^2 &= (r_1+r_2)^2 min(1.0, 2.4f(\gamma)/We_l) \\ f(\gamma) &= \gamma^3 - 2.4\gamma^2 + 2.7\gamma \\ \gamma &= r_2/r_1 \\ We_l &= \rho_d|\mathbf{v}_1 - \mathbf{v}_2|r_1/\alpha(\overline{T}_d), \end{aligned}$$

and

$$\overline{T}_d = \frac{r_1^3 T_{d_1} + r_2^3 T_{d_2}}{r_1^3 + r_1^3}. \tag{A.0.2}$$

The quantity α is the liquid surface-tension coefficient, which is assumed to vary linearly between reference value α_0 at reference temperature T_0, and zero at the fuel species critical temperature T_{cri}. The precise form for collision transition probability function σ is:

$$\begin{aligned} \sigma \quad - \quad & \frac{b_{cri}^2}{(r_1+r_2)^2}\delta[r - (r_1^3+r_2^3)^{\frac{1}{3}}]\delta[\mathbf{v} - \frac{r_1^3\mathbf{v}_1 + r_2^3\mathbf{v}_2}{r_1^3+r_2^3}] \\ & \delta[T_d - \frac{r_1^3 T_{d_1} + r_2^3 T_{d_2}}{r_1^3 + r_2^3}]\delta(y-y_2)\delta(\dot{y}-\dot{y}_2) \\ & + \frac{2}{(r_1+r_2)^2}\int_{b_{cri}}^{r_1+r_2} [\delta(r-r_1)\delta(\mathbf{v}-\mathbf{v}_1')\delta(T_d - T_{d_1})\delta(y-y_1)\delta(\dot{y}-\dot{y}_1) \\ & \delta(r-r_1)\delta(\mathbf{v}-\mathbf{v}_1')\delta(T_d - T_{d_2})\delta(y-y_2)\delta(\dot{y}-\dot{y}_2)]b\ db, \end{aligned} \tag{A.0.3}$$

where

$$\mathbf{v}_1' = \frac{r_1^3\mathbf{v}_1 + r_2^3\mathbf{v}_2 + r_2^3(\mathbf{v}_1 - \mathbf{v}_2)\frac{b-b_{cri}}{r_1+r_2-b_{cri}}}{r_1^3+r_2^3},$$

and

$$\mathbf{v}_2' = \frac{r_1^3\mathbf{v}_1 + r_2^3\mathbf{v}_2 + r_1^3(\mathbf{v}_2 - \mathbf{v}_1)\frac{b-b_{cri}}{r_1+r_2-b_{cri}}}{r_1^3+r_2^3}.$$

The breakup source term $\dot{f}_{bu}$ is given by equation:

$$\dot{f}_{bu} = \int f(\mathbf{x}, \mathbf{v}_1, r_1, T_{d_1}, 1, \dot{y}_1, t)\ \dot{y}_1 B(\mathbf{v}, r, T_d, y, \dot{y}, \mathbf{v}_1, r_1, T_{d_1}, \dot{y}_1, \mathbf{x}, t) d\mathbf{v}_1 dr_1 dT_{d_1} d\dot{y}_1. \tag{A.0.4}$$

The breakup transition probability function B is defined so that $B d\mathbf{v} dr dT_d dy d\dot{y}$ is the probable number of droplets with properties in the implied interval that are produced by the breakup of a droplet with subscript 1 properties. The meaning of the equation (A.0.4) is: when a droplet's distortion y exceeds unity, it breaks up into a distribution of smaller drops given by B. The total source f is obtained by multiplying the local flux of droplets through the surface $y \equiv 1$ by B, and integrating over the entire surface $y \equiv 1$. After breakup the droplet radii is assumed to follow a χ-square distribution:

$$g(r) = \frac{1}{\bar{r}} e^{-r/\bar{r}} \tag{A.0.5}$$

where the Sauter mean radius r_{32} is given by:

$$r_{32} = 3\bar{r} = \frac{r_1}{\frac{7}{3} + \frac{1}{8}\frac{\rho_d r_1^3}{\alpha(T_{d_1})}\dot{y}_1^2}. \tag{A.0.6}$$

The product droplet velocities also differ from that of the parent droplet by a velocity with magnitude w and with direction randomly distributed in a plane normal to the relative velocity vector between the parent drop and gas. The quantity w is given by:

$$w = \frac{1}{2} r_1 \dot{y}_1. \tag{A.0.7}$$

The precise form for B is:

$$B = g(r)\delta(T_d - T_{d_1})\delta(y)\delta(\dot{y})\frac{1}{2\pi}\int \delta[\mathbf{v} - (\mathbf{v}_1 + w\mathbf{n}]d\mathbf{n}, \tag{A.0.8}$$

where the integral is over normal directions to the relative velocity vector [119].

The droplet acceleration F has contributions due to aerodynamic drag and gravitational force calculated from:

$$\mathbf{F} = \frac{3}{8}\frac{\rho}{\rho_d}\frac{|\mathbf{u}+\mathbf{u}'-\mathbf{v}|}{r}(\mathbf{u}+\mathbf{u}'-\mathbf{v})C_D + \mathbf{g}. \tag{A.0.9}$$

The drag coefficient C_D is given by:

$$C_D = \begin{array}{ll} \frac{24}{Re_d}(1+1/6\ Re_d^{2/3}) & Re_d < 1000 \\ 0.424 & Re_d > 1000 \end{array}, \tag{A.0.10}$$

where

$$Re_d = \frac{2\rho|\mathbf{u}+\mathbf{u}'-\mathbf{v}|r}{\mu_{air}(\hat{T})},$$

$$\hat{T} = \frac{T+2T_d}{3},$$

and μ_{air} is given by equation (5.1.2). The gas turbulence velocity $\mathbf{u}'$ is added to the local mean gas velocity when calculating a droplet's drag and vaporization rate. It is assumed that each component $\mathbf{u}'$ follows a Gaussian distribution with mean square deviation $2/3\ k$:

$$\mathrm{G}(\mathbf{u}') = (4/3\ \pi\ k)^{-3/2} exp\{-3|\mathbf{u}'|^2/4k\}. \tag{A.0.11}$$

The value of $\mathbf{u}'$ is chosen once every turbulence correlation time t_{turb}, and is otherwise held constant. The droplet correlation time is given by:

$$t_{turb} = min(\frac{k}{\epsilon}, c_{ps}\frac{k^{3/2}}{\epsilon}\frac{1}{|\mathbf{u}+\mathbf{u}'-\mathbf{v}|}), \tag{A.0.12}$$

where c_{ps} is an empirical constant with value 0.16432. Thus t_{turb} is the minimum of an eddy breakup time and a time for the droplet to traverse an eddy.

The rate of droplet radius change R is given by the Frossling correlation [167]:

$$R = -\frac{(\rho D)_{air}(\hat{T})}{2\rho_d r}\frac{Y_1^* - Y_1}{1 - Y_1^*}Sh_d, \tag{A.0.13}$$

where Sh_d is the Sherwood number for mass transfer, Y_1^* is the fuel vapor mass fraction at the droplet's surface, $Y_1 = \rho_1/\rho$, and $(\rho D)_{air}(\hat{T})$ is the fuel vapor diffusivity in air. The Sherwood number is given by:

$$Sh_d = (2.0 + 0.6\ Re_d^{\frac{1}{2}} Sc_d^{\frac{1}{3}})\frac{ln(1 + c_d)}{c_d}, \tag{A.0.14}$$

where $Sc_d = \frac{\mu_{air}(\hat{T})}{\rho D_{air}(\hat{T})}$ and $c_d = \frac{Y_1^* - Y_1}{1 - Y_1^*}$. The surface mass fraction Y_1^* is obtained from:

$$Y_1^*(T_d) = \frac{W_1}{W_1 + W_0(\frac{p}{p_v(T_d)} - 1)}, \tag{A.0.15}$$

where W_0 is the local average molecular weight of all species exclusive of fuel vapor and $p_v(T_d)$ is the equilibrium fuel vapor pressure at temperature T_d. The equation (A.0.15) is obtained with the assumption that the droplet temperature is uniform and that the partial pressure of fuel vapor at the droplet's surface equals the equilibrium vapor pressure. The vapor diffusivity in air is computed using the empirical correlation:

$$(\rho D)_{air}(T) = c_1 T^{c_2},$$

where c_1 and c_2 are constants.

The rate of droplet temperature change is determined by the energy balance equation:

$$\rho_d \frac{4}{3}\pi r^3 c_l \dot{T}_d - \rho_d 4\pi r^2 R L(T_d) = 4\pi r^2 Q_d, \tag{A.0.16}$$

where c_l the liquid specific heat, $L(T_d)$ is the latent heat of vaporization, and Q_d is the rate of heat conduction to the droplet surface per unit area. Equation (A.0.11) is a statement that the energy conducted to the droplet either heats up the droplet

or supplies heat for vaporization. The heat conduction rate Q_d is given by the Ranz-Marshall correlation [167]:

$$Q_d = \frac{\kappa_{air}(\hat{T})(T - T_d)}{2r} Nu_d, \tag{A.0.17}$$

where

$$\begin{aligned} Nu_d &= (2.0 + 0.6 Re_d^{\frac{1}{2}} Pr_d^{\frac{1}{3}}) \frac{ln(1 + c_d)}{c_d}, \\ Pr_d &= \frac{\mu_{air}(\hat{T}) c_p(\hat{T})}{\kappa_{air}(\hat{T})}, \\ \kappa_{air}(\hat{T}) &= \frac{c_1 \hat{T}^{3/2}}{\hat{T} + c_2}, \end{aligned}$$

c_p is the local specific heat at constant pressure and at temperature $\hat{T} = (T + 2T_d)/3$, and c_1 and c_2 are constants.

Consistent with the approximation that the liquid density is constant the internal energy ι_l of liquid is assumed to be a function of temperature alone. Thus, the liquid enthalpy will have a small pressure dependence,

$$h_l(T_d, p) = \iota_l(T_d) + p/\rho_d. \tag{A.0.18}$$

The latent heat of vaporization is calculated form equation:

$$L(T_d) = h_1(T_d) - h_l(T_d, p_v(T_d)) = \iota_1(T_d) + RT_d/W_1 - \iota_l(T_d) - p_v(T_d)/\rho_d. \tag{A.0.19}$$

The equation for the acceleration of the droplet distortion parameter is:

$$\ddot{y} = \frac{2}{3}\frac{\rho}{\rho_d}\frac{(\mathbf{u} + \mathbf{u}' - \mathbf{v})^2}{r^2} - \frac{8\alpha(T_d)}{\rho_d r^3} y - \frac{5\mu_l(T_d)}{\rho_d r^2}\dot{y}, \tag{A.0.20}$$

where $\mu_l(T_d)$ is the viscosity of the liquid. Equation (A.0.20), which is based on the analogy between an oscillating droplet and a spring-mass system, is the equation of a

forced damped harmonic oscillator. The external force is supplied by the gas aerodynamic forces on the droplet. The restoring force is supplied by surface tension forces. Damping is supplied by liquid viscosity.

Appendix B

Calculating technique for KIVA-3V equation system

In KIVA-3V calculation of a cycle is performed in three phases. Phases A and B together constitute a Lagrangian calculations in which computational cells move with the fluid. Phase A is calculations of collision and oscillation breakup terms of spray droplet, and of mass and energy source terms due to the chemistry and spray. Phase B calculates in a coupled, implicit fashion the acoustic mode terms (namely the pressure gradient in the momentum equation and velocity dilatation terms in the mass and energy equations), the spray momentum source term, and the terms due to diffusion of mass, momentum, and energy. Phase B also calculates the remaining source terms in the turbulence equations. In Phase C, the flow field is frozen and rezoned or re-mapped onto a new computational mesh.

The spatial differencing is based on the Arbitrary Lagrangian Eulerian (ALE) finite volume method. The cylinder chamber is subdivided into a number of small cells. In the general case, the cells are asymmetrical; a typical cell is shown in figure B.1. The cells are indexed by integers (i, j, k). For convenience in differencing the momentum equations auxiliary momentum cells are defined. A momentum cell (i, j, k) is centered

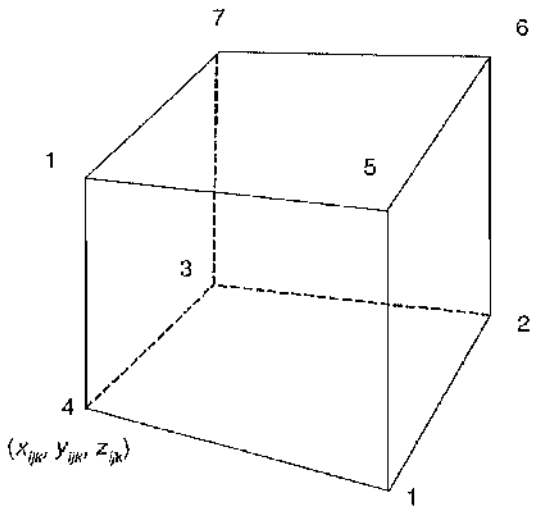

Figure B.1: Finite-difference cell

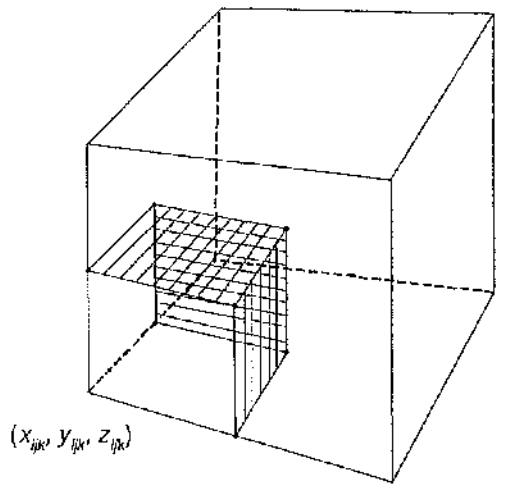

Figure B.2: Momentum cell

about vertex (i, j, k). In contrast to regular cells, which have six faces, momentum cells have twenty-four faces, each of which is comparable in size to one-fourth of a regular cell face. Three of these twenty-four faces lie within each of the eight regular cells which share common volume with the momentum cells. The momentum cell is illustrated in figure B.2. The points of intersection of the momentum cell faces with the regular cell edges are defined as the midpoints of the regular cell edges. The points of intersection of the momentum cell edges with the regular cell faces are then defined implicitly by the requirement that the regular cell face be partitioned into four subfaces of equal area by the momentum cell faces. The corners of the momentum cells are then implicitly defined by the requirement that the overlap volume between a regular cell and a momentum cell centered at one of its corners be one-eighth of the regular cell volume. In general, the momentum cell corners do not coincide with the cell centers.

Accelerations of the cell-face velocities due to pressure gradients are calculated by

constructing momentum control volumes centered about the cell faces. Like the momentum cells the cell-face control volumes have twenty-four faces. In figures B.1 and B.2, the cell-face control volume for the left face of cell (i, j, k) is composed of those portions of the momentum cells of vertices 3, 4, 7, and 8 that lie in regular cells (i, j, k) and $(i-1, j, k)$.

In the finite-difference approximations, velocities are located at the vertices, so that

$$\mathbf{u}_{ijk} = \mathbf{u}(x_{ijk}, y_{ijk}, z_{ijk}). \tag{B.0.1}$$

Thermodynamic quantities are located at cell centers:

$$Q_{ijk} = Q(x^c_{ijk}, y^c_{ijk}, z^c_{ijk}), \tag{B.0.2}$$

where Q is function of p, T, ι, ρ_i or ρ_{in}, as well as k and ϵ. Quantities needed at points where they are not fundamentally located are obtained by averaging neighboring values.

Volume integrals of gradient or divergence terms are converted into surface area integrals using the divergence theorem. In turn surface area integrals are performed under the assumption that the integrands are uniform within cells or on cell faces. Thus area integrals over surfaces of cells become sums over cell faces:

$$\int G \cdot d\mathbf{A} \rightarrow \sum_{\alpha} G_\alpha \cdot \mathbf{A}_\alpha, \tag{B.0.3}$$

where G is an arbitrary variable.

Phase A

In phase the spray dynamics equations are solved using a Stochastic Particle Technique. The continuous probability distribution function of droplet f is approximated

by a discrete distribution f':

$$f' = \sum_{pc=1}^{NP} N_{pc}\delta(\mathbf{x} - \mathbf{x}_{pc})\delta(\mathbf{v} - \mathbf{v}_{pc})\delta(r - r_{pc})\delta(T_d - T_{d_{pc}})\delta(y - y_{pc})\delta(\dot{y} - \dot{y}_{pc}). \quad \text{(B.0.4)}$$

In discrete particle methods, each particle pc is composed of a number of droplets N_{pc} having equal location $\mathbf{x}_{pc}$, velocity $\mathbf{v}_{pc}$, size r_{pc}, temperature $T_{d_{pc}}$, and oscillation parameters y_{pc} and $\dot{y}_{pc}$. Particle and droplet trajectories coincide, and the particles exchange mass, momentum, and energy with the gas in the computational cells in which they are located.

Phase B

In phase B values of the flow field variables are found by solving implicitly the equation system without convection terms using SIMPLE method [113] in two steps. In step 1 a predicted value of the Phase B pressure p^{B} is selected. In step 2, the values of the diffusion terms obtained in step 1 are frozen and the corrected pressure field is solved using equations that difference pressure terms implicitly. Step 2 simultaneously solves the cell-face velocity equations, the volume change equations, and a linearized form of the equation of state. Following step 2, the predicted and corrected pressures are compared. If they agree to within a specified convergence tolerance, the equations have been solved, and the calculation proceeds to Phase C. If the difference between the pressure fields exceeds the convergence tolerance, the corrected pressure field becomes the new predicted pressure field and the process is repeated.

The predicted pressure p^{p}_{ijk} is first initialized by linear extrapolation using the phase B pressures from the previous two cycles:

$$p^{p}_{ijk} = (p^{\mathrm{B}}_{ijk})^{n-1} + \frac{\Delta t^n}{\Delta t^{n-1}}[(p^{\mathrm{B}}_{ijk})^{n-1} - (p^{\mathrm{B}}_{ijk})^{n-2}], \quad \text{(B.0.5)}$$

where superscript p denotes predicted, superscript B is phase B, and superscript n is step index. The predicted temperature field is obtained from:

$$T^{\mathrm{B}}_{ijk} = \{T^{t}_{ijk} + \frac{p^{n}_{ijk} + p^{p}_{ijk}}{2(c_v)^{t}_{ijk}} \frac{V^{n}_{ijk}}{M^{\mathrm{B}}_{ijk}} + \frac{\Delta t}{M^{\mathrm{B}}_{ijk}(c_v)^{t}_{ijk}} [\sum_{\alpha} \kappa^{n}_{\alpha} \nabla [\Phi_{dif} T^{p} + (1 - \Phi_{dif}) \tilde{T}]_{\alpha} \cdot \mathbf{A}^{n}_{\alpha} + (1 - A_0)[\Phi_D \bar{\sigma}(\mathbf{u}^{p}) : \nabla \mathbf{u}^{p} + (1 - \Phi_D) \bar{\sigma}(\mathbf{u}^{n}) : \nabla \mathbf{u}^{n}]_{ijk}]\} / \{1.0 + \frac{p^{n}_{ijk} + p^{n}_{ijk}}{2(c_v)^{t}_{ijk} p^{p}_{ijk}} R_0 [\sum_{m} \frac{(Y_m)^{\mathrm{B}}_{ijk}}{W_m}]\}, \tag{B.0.6}$$

where subscript α denotes regular cell face, Φ_{dif} is the implicitness parameter for the diffusion term, and Y_m is mass fraction of species m.

After solving for the predicted temperatures, the predicted cell volumes V^{p}_{ijk} are found using:

$$V^{p}_{ijk} = \frac{M^{\mathrm{B}}_{ijk}}{p^{p}_{ijk}} R_0 [\sum_{m} \frac{(Y_m)^{\mathrm{B}}_{ijk}}{W_m}] T^{p}_{ijk}. \tag{B.0.7}$$

Finally, the corrected pressure field p^{c}_{ijk} is calculated from equation:

$$\begin{aligned} [(M^{s})^{\mathrm{B}}_{\alpha} + S^{s}_{\alpha}] \frac{(uA)^{\mathrm{B}}_{\alpha} - (uA)^{t}_{\alpha}}{\Delta t} &= -\sum_{\gamma} \{[\Phi_p p^{c} + (1 - \Phi_p) p^{n}] / (\alpha^{n})^{2} \\ &+ A_0 \frac{2}{3} \rho^{\mathrm{A}} k^{\mathrm{A}}\}_{\gamma} (\mathbf{\Lambda}'')^{n}_{\gamma} \cdot \mathbf{A}_{\alpha} \\ &+ \frac{\mathbf{A}^{t}_{\alpha} - \mathbf{A}^{n}_{\alpha}}{\Delta t} \cdot \frac{\mathbf{u}^{n}_{a} + \mathbf{u}^{n}_{b} + \mathbf{u}^{n}_{c} + \mathbf{u}^{n}_{d}}{4} [(M^{s})^{\mathrm{B}}_{\alpha} + S^{s}_{\alpha}], \end{aligned} \tag{B.0.8}$$

where double prime denote cell-face control volume, Φ_p is the implicitness parameter for the pressure gradient term, superscript A is used for phase A, subscript γ refers to the faces of the cell-face control volume, a, b, c, and d are labels of the vertices that form the four corners of the cell face α, and S^{s}_{α} is added mass due to spray droplets in the cell-faces of control volume α.

The corrected volume V^c_{ijk} is:

$$V^c_{ijk} = V^p_{ijk}\frac{1}{Y^t_{ijk}} R_0 \frac{V^p_{ijk}}{p^p_{ijk}}(p^c_{ijk} - p^p_{ijk}), \tag{B.0.9}$$

where

$$\frac{1}{Y^t_{ijk}} = \frac{2(c_v)^t_{ijk} + R_0[\sum_m \frac{(Y_m)^B_{ijk}}{W_m}](1 - \frac{V^n_{ijk}}{V^p_{ijk}})}{2(c_v)^t_{ijk} + \frac{p^n_{ijk}+p^p_{ijk}}{p^p_{ijk}} R_0[\sum_m \frac{(Y_m)^B_{ijk}}{W_m}]} \tag{B.0.10}$$

The predicted and corrected pressure field are then compared to see if convergence has been attained. If convergence has not been obtained, then the-corrected pressure field becomes the new predicted pressure field, and step 1 is repeated.

If convergence has been obtained, then p^B_{ijk} is equal to p^c_{ijk}. The vertex positions of phase B are given by:

$$\mathbf{x}^B_{ijk} = \mathbf{x}^n_{ijk} + \mathbf{u}^B_{ijk}\Delta t. \tag{B.0.11}$$

Phase C

Phase C is the rezone phase, in which the convective transport associated with moving the mesh relative to the fluid is calculated. This is accomplished in a subcycled, explicit calculation using a time step Δt_c that is an integral submultiple of the main computational time step Δt. The Δt_c must satisfy the Courant condition $u_r \Delta t_c/\Delta x < 1$, where u_r is the fluid velocity relative to the grid velocity, (but there is no upper bound on the number of subcycles).

The transport of cell centered quantities is computed using a volume δV_α that is swept out by regular cell face α each convective subcycle, as it moves from its Lagrangian position (defined by the corner positions $\mathbf{x}^B_{ijk}$) to its final position (defined by the user specified $\mathbf{x}^{n+1}_{ijk}$). δV_α is associated with both the face and the regular cell under consideration, so that δV_α is positive if the volume of the cell is increased by moving

face α from the Lagrangian to its final position. δV_α are evaluated in terms of the cell-face velocities and the old and new grid positions:

$$\delta V_\alpha = \delta V_\alpha^G \Delta t_c / \Delta t - (uA)_\alpha^B \Delta t_c. \tag{B.0.12}$$

In equation (B.0.12), δV_α^G is the volume swept out by cell face α when the four vertices defining the face are moved from their old-time positions x_{ijk}^n to their new-time positions x_{ijk}^{n+1}. δV_α^G are positive if the volume of the cell (i,j,k) is increased by the grid motion. δV_α must satisfy equation:

$$V_{ijk}^{\mathrm{B}} + NS \sum_\alpha \delta V_\alpha = V_{ijk}^{n+1} \tag{B.0.13}$$

where $NS = \Delta t / \Delta t_c$ is the number of convective subcycles.

The species densities $(\rho_m)_{ijk}^v$ after v convective subcycles are given by:

$$(\rho_m)_{ijk}^v V_{ijk}^v = (\rho_m)_{ijk}^{v-1} V_{ijk}^{n+1} + \sum_\alpha (\rho_m)_{ijk}^{v-1} \delta V_\alpha, \tag{B.0.14}$$

where the summation is over the number of the faces of the cell (i,j,k). The species densities are initialized at the beginning of phase C by their phase B values:

$$(\rho_m)_{ijk}^0 = (\rho_m)_{ijk}^{\mathrm{B}}, \tag{B.0.15}$$

And the subcycle volume V_{ijk}^v are given by:

$$V_{ijk}^v = [v V_{ijk}^{n+1} (NS - v) V_{ijk}^{\mathrm{B}}] / NS, \tag{B.0.16}$$

where V_{ijk}^{n+1} is the cell volume based on the final coordinates. The cell densities $(\rho_m)_\alpha^v$ are evaluated by the quasi-second-order upwind scheme. The total density after v convective subcycles is given by:

$$\rho_{ijk}^v = \sum_m (\rho_m)_{ijk}^v. \tag{B.0.17}$$

The specific internal energy ι^v_{ijk} after v convective subcycles is determined from:

$$\rho^v_{ijk} V^v_{ijk} \iota^v_{ijk} = \rho^{v-1}_{ijk} V^{v-1}_{ijk} \iota^{v-1}_{ijk} + \sum_\alpha (\rho\iota)^{v-1}_\alpha \delta V_\alpha \tag{B.0.18}$$

where the cell face energy densities $(\rho\iota)^v_\alpha$ are evaluated by second-order-upwind differencing.

The formula for updating turbulence quantity g^v_{ijk} in the subcycle is:

$$\rho^v_{ijk} V^v_{ijk} g^v_{ijk} = \rho^{v-1}_{ijk} V^{v-1}_{ijk} g^{v-1}_{ijk} + \sum_\alpha (\rho g)^{v-1}_\alpha \delta V_\alpha \tag{B.0.19}$$

where $g = k$ or $g = k^{3/2}/\epsilon = L$. In phase C, turbulence length scale L is convected rather than ϵ because ϵ generally has steeper gradients, and therefore large numerical errors arise when convecting ϵ. The cell face quantities $(\rho g)^v_\alpha$ are evaluated by second-order-upwind differencing.

After completion of all convective subcycles, the final values of cell-centered quantities are set equal to their values after NS subcycles. The final value of temperature is computed by inverting equation (3.1.10) using final values of internal energy and mass densities. The final pressure is given by:

$$p^{n+1}_{ijk} = R_0 T^{n+1}_{ijk} \sum_m (\rho_m)^{n+1}_{ijk} / W_m. \tag{B.0.20}$$

Convective transport of momentum on subcycle v is calculated in terms of the mass increments across momentum cell faces, which are related to the mass increments across regular cell faces. The mass increments across regular cell face α of a particular momentum cell are defined by:

$$(\delta M'_\alpha)^{v-1} = \frac{1}{8}(p^{v-1}_o \delta V_o - p^{v-1}_i \delta V_i) \tag{B.0.21}$$

where o and i are the regular cell faces on either side of the momentum cell face α. The vertex masses are calculated as:

$$(M')^{v}_{ijk} = (M')^{v-1}_{ijk} + \sum_{\alpha} (\delta M'_{\alpha})^{v-1}, \tag{B.0.22}$$

where the summation extends over all faces of momentum cell (i, j, k).

Before calculating convection of momentum the mass increments $\delta M'_{\alpha}$ corresponding to the twenty four faces of momentum cell (i, j, k) are added in groups to obtain mass fluxes δM^{c}_{β} through the six composite faces β of the momentum cell. Each composite face is formed from the four cell faces α that touch a common regular cell edge that emanates from vertex (i, j, k). The momentum convection is then computed by:

$$(M')^{v}_{ijk}\mathbf{u}^{v}_{ijk} = (M')^{v-1}_{ijk}\mathbf{u}^{v-1}_{ijk} + \sum_{\beta} (\delta M^{c}_{\beta})^{v-1}\mathbf{u}^{v-1}_{\beta}, \tag{B.0.23}$$

where the velocities $\mathbf{u}^{v-1}_{\beta}$ are evaluated by the quasi-second-order upwind scheme.

References

[1] Kee, R. J., Rupley, F. M., and Miller, J. A. CHEMKIN-II: A Fortran Chemical Kinetics Package for the Analysis of Gas-Phase Chemical Kinetics. Technical Report SAND89-8009, Sandia National Laboratories, Livermore, CA, USA, 1980.

[2] Amsden, A. A. KIVA-3V: A Block-Structured KIVA Program for Engines with Vertical or Canted Valves. Technical Report LA-13313-MS, UC-1412, Los Alamos National Laboratory, Los Alamos, 1997.

[3] Vesley, D. *Human health and the environment: A turn-of-the-Century perspective.* Kluwer Academic, London, 1999. ISBN 0-7923-8616-7.

[4] Roberts, T. M., Darrall, M. N., and Lane, P. Effects of Gaseous Air Pollutants on Agriculture and Forestry in the UK. *Advance Applied Biology*, 9:1–142, 1983.

[5] Grennfelt, P., and Hultberg, H. Effects of Nitrogen Deposition on the acidification of Terrestrial and Aquatic Ecosystems. *Water Air and Soil Pollution*, 30:945–963, 1986.

[6] Blank, L. W., and Roberts, T. M. Ecological effects of nitrogen oxides and hydrocarbons on central European forests. In *Vehicle emissions and their impact on European air quality*, pages 17–30. Mechanical Engineering Publications limited, London, 1987. ISBN 0 85298 632 7.

[7] Oeschger, H. CO_2 and the green-house effect: present assessment and perspectives. *Symposium on Environmental change and human health*, pages 2–22, Ciba foundation, Netherlands, 1992.

[8] European Conference of Ministers of Transport. *Vehicle emission reductions.* Organisation for Economic Co-Operation and Development, Paris, 2001. ISBN 9282113639.

[9] International Energy Agency, www.iea.org.

[10] Plint, M. A., and Martyr, A. J. *Engine testing: Theory and Practice.* Butterworth-Heinemann, Oxford, 1998. ISBN 0750640219.

[11] Heywood, J. B., Higgins, J. M., Watts, P. A., and Tabaczynski, R. J. Development and use of a cycle simulation to predict SI engine efficiency and NO_x emissions. SAE Paper 790291, 1979.

[12] Hires, S. D., Ekchian, A., Heywood, J. B., Tabaczynski, R. J., and Wall, J. C. Performance and NO_x emissions modeling of a jet ignition prechamber stratified charge engine. SAE Paper 760161, 1976.

[13] Wu, K. C., Hochgreb, S., and Norris, M. G. Chemical kinetic modeling of exhaust hydrocarbon oxidation. *Combustion and Flame*, 100:193–201, 1995.

[14] Ogink, R., and Golovitchev, V. Gasoline HCCI modelling: Computer program combining detailed chemistry and gas exchange process. SAE Paper 01FL-532, 2001.

[15] Ogink, R., and Golovitchev, V. Gasoline HCCI modeling: an engine cycle simulation code with a multi-zone combustion model. SAE Paper 2002-01-1745, 2002.

[16] Aceves, S. M., Flower, D. L., Westbrook, C. K., Smith, J. R., Pitz, W., Dibble, R. W., Christensen, M., and Johansson, B. A Multi-zone model for prediction of HCCI combustion and emissions. SAE Paper 2000-01-0327, 2000.

[17] Senecal, P. K., Xin, J., and Reitz, R. D. Predictions of residual gas fraction in IC engines. SAE Paper 962052, 1996.

[18] Uludogan, A., Foster, D. E., and Reitz, R. D. Modeling the effect of engine speed on the combustion process and emissions in a DI Diesel engine. SAE Paper 962056, 1996.

[19] Heywood, J. B. *Internal Combustion Engine Fundamentals.* McGraw-Hill, New York, 1988. ISBN 0-07-028637-X.

[20] Stone, R. *Introduction to Internal Combustion Engines.* Macmillan, London, 2nd edition, 1992. ISBN 0-33-55083-8.

[21] Zeldovich, Y. The oxidation of nitrogen in combustion and explosions. *Acta Physicochimica USSR*, 21(4):577–628, 1947.

[22] Warnatz, J., Mass, U., and Dibble, R. W. *Combustion.* Springer-Verlag, New York, 3rd edition, 2000. ISBN 3-540-677518.

[23] Fenimore, C. P. Studies of fuel-nitrogen in rich flame gases. *Proceedings of the Combustion Institute*, 17:661–669, 1979.

[24] Glassman, I. *Combustion.* Academic Press, London, 3rd edition, 1997. ISBN 0122858522.

[25] Hill, S. C., and Smoot, L. D. Modeling of nitrogen oxides formation and destruction in combustion systems. *Progress in Energy Combustion Science*, 26:417–458, 2000.

[26] Burgess, A. R., and Langley, C. J. The chemical structure of premixed fuel-rich methane flames: the effects of hydrocarbon species in the secondary reaction zone. *Proceedings of the Royal Society*, A 433:1–21, 1991.

[27] Malte, P. C., and Prantt, D. T. Measurement of atomic oxygen and nitrogen oxides in jet-stirred combustion. *Proceedings of the Combustion Institute*, 15:1061, 1974.

[28] Toof, J. L. A model for the prediction of thermal, prompt and fuel NO_x emissions from combustion turbines. *ASME Journal of Engineering for Gas Turbines and Power*, 108:340–347, 1986.

[29] Khan, I. M., Greeves, G., and Wang, C. H. T. Factors affecting smoke and gaseous emissions from direct injection engines and a method of calculation. SAE Paper 730169, 1973.

[30] Fine, L. W. *Chemistry*. Williams and Wilkins, Baltimore, 2nd edition, 1978. ISBN 0-683-03210-0.

[31] Woschni, G. A universally applicable equation for the instantaneous heat transfer coefficient in the internal combustion engine. SAE Paper 670931, 1967.

[32] Lund, C. M. HCT-A General Computer Program for Calculating Time-Dependent Phenomena Involving One-Dimensional Hydrodynamics, Transport, and Detailed Chemical Kinetics. Technical Report UCRL-52504, Lawrence Livermore National Laboratory, Livermore, 1978.

[33] Flowers, D., Aceves, S., Westbrook, C. K., Smith, R., and Dibble, R. Detailed chemical kinetic simulation of natural gas HCCI combustion: Gas composition effects and investigation of control strategies. *ASME Journal of Engineering for Gas Turbines and Power*, 123:433–439, 2001.

[34] Kee, R. J. Chemkin-III A Fortran chemical kinetics package for the analysis of gas-phase chemical and plasma kinetics. Technical Report SAND96-8216, Sandia National Laboratories, Livermore, CA, USA, 1996.

[35] Christensen, M., Johansson, B., Amnjus, P., and Mauss, F. Supercharged homogeneous charge compression ignition. SAE Paper 980787, 1998.

[36] AVL BOOST^{TM} User's Guide version 3.3, AVL LIST GmbH. 2000.

[37] Amsden, A. A. KIVA-3: A KIVA Program with Block-Structured Mesh for Complex Geometries. Technical Report LA-12503-MS, Los Alamos National Laboratory, Los Alamos, 1993.

[38] Aceves, S. M., Martinez-Frias, J., Flowers, D. L., Smith, J. R., Dibble, R. W., Wright, J. F. and Hessel, R. P. A decoupled model of detailed fluid mechanics followed by detailed chemical kinetics for prediction of iso-octane HCCI combustion. SAE Paper 2001-01-3612, 2001.

[39] Easley, W. L., Agarwal, A., and Lavoie, G. A. Modeling of HCCI combustion and emissions using detailed chemistry. SAE Paper 2001-01-1029, 2001.

[40] Shenghua, L., Hwang, J. W., Park, J. K., Kim, M. H., and Chea, J. O. Multizone model for DI Diesel engine combustion and emissions. SAE Paper 1999-01-2926, 1999.

[41] Flowers, D., Aceves, S., Smith, R., Torres, J., Girard, J., and Dibble, R. W. HCCI in a CFR engine: Experiments and detailed kinetic modeling. SAE Paper 2000-01-0328, 2000.

[42] Kee, R. J., Miller, J. A., and Jefferson, T. H. CHEMKIN: A General-Purpose, Problem-Independent, Transportable, Fortran Chemical Kinetics Code Package. Technical Report SAND80-8003, Sandia National Laboratories, Livermore, CA, USA, 1980.

[43] Launder, B. E., and Spalding, B. *Mathematical Models of Turbulence.* Academic Press, New York, 1972. ISBN 0-12-438050-6.

[44] Jones, W. P., and Whitelaw, J. H. Calculation methods for reacting turbulent flows: A review. *Combustion and Flame*, 48:1–26, 1982.

[45] Hanjalic, K., Launder, B. E., and Schiestel, R. Multipletime-scale concepts in turbulent transport modeling. In Bradbury, L. J. S, Durst, F., Launder, B. E., Schmidt, F. W., and Whitelaw, J. H., editor, *Turbulent Shear Flows*, volume 2, pages 36–49. Springer-Verlag, New York, 1980. ISBN 0387100679.

[46] Chan, L. K., Sarofim, A. F., and Beér, J. M. Kinetics of NO-Carbon reaction at fluidized bed combustor conditions. *Combustion and Flame*, 52:37–45, 1983.

[47] Peters, N. Laminar flamelet concepts in turbulent combustion. *Twenty-first Symposium (International) on Combustion*, pages 1231–1250, The Combustion Institute, Pittsburgh, 1986.

[48] Cook, A. W., Riley, J. J., and George, K. A laminar flamelet approach to subgrid-scale chemistry in turbulent flows. *Combustion and Flame*, 109:332 341, 1997.

[49] Benim, A. C., and Syed, K. J. Laminar flamelet modelling of turbulent premixed combustion. *Applied Mathematical Modelling*, 22(2):113–136, 1998.

[50] Bilger, R. W. Turbulent Flows with Nonpremixed Reactants. In Libby, P. A., and Williams, F. A., editor, *Topics in Applied Physics: Turbulent Reacting Flows*, pages 65–113. Springer-Verlag, New York, 1980. ISBN 3-540-10192-6.

[51] O'Brien, E. E. The Probability Density Function (pdf) Approach to Reacting Turbulent Flows. In Libby, P. A., and Williams, F. A., editor, *Topics in Applied Physics: Turbulent Reacting Flows*, pages 185–218. Springer-Verlag, New York, 1980. ISBN 3-540-10192-6.

[52] Kerstein, A. R. Linear-Eddy modelling of turbulent transport. II: Application to shear layer mixing. *Combustion and Flame*, 75:397–413, 1989.

[53] Zimberg, M. J., Frankel, S. H., Gore, J. P., and Sivathanu, Y. R. A Study of Coupled Turbulent Mixing, Soot Chemistry, and Radiation Effects Using the Linear Eddy Model. *Combustion and Flame*, 113:454–469, 1998.

[54] McMurtry, P. A., Menon, S., and Kerstein, A. R. Linear eddy modeling of turbulent combustion. *Energy and Fuels*, 7:817–826, 1993.

[55] Bilger, R. W. Conditional moment closure for turbulent reaction flow. *The Physics of Fluids A*, 5(2):436–444, 1993.

[56] Bushe, W. K., and Steiner, H. Conditional moment closure for large-eddy simulation of nonpremixed turbulent reaction flows. *The Physics of Fluids A*, 11(7):1896–1906, 1999.

[57] Smith, N. S. A., Bilger, R. W., and Chen, J-Y. Modelling of nonpremixed hydrogen jet flames using conditional moment closure method. *Twenty-fourth Symposium (International) on Combustion*, pages 263–269, The Combustion Institute, Pittsburgh, 1992.

[58] Anand, M. S, and Pope, S. B. Calculations of premixed turbulent flames by PDF methods. *Combustion and Flame*, 67:127–142, 1987.

[59] Hulek, T., and Lindstedt, R. P. Computations of steady-state and transient premixed turbulent flames using PDF methods. *Combustion and Flame*, 104:481–504, 1996.

[60] Pope, S. B. Monte Carlo method for the PDF equations of turbulent reactive flow. *Combustion Science and Technology*, 25:159–174, 1981.

[61] Spalding, D. B. Mixing and chemical reaction in steady confined turbulent flames. *Thirteenth Symposium (International) on Combustion*, pages 649–657, The Combustion Institute, Pittsburgh, 1971.

[62] Spalding, D. B. Development of the eddy-breakup model of turbulent combustion. *Sixteenth Symposium (International) on Combustion*, pages 1657–1663, The Combustion Institute, Pittsburgh, 1976.

[63] Hjertager, L. K., Osenbroch, J., Hjertager, B. H., and Solberg, T. Validation of the Eddy Dissipation Concept for fast chemical reactions in turbulent flows. In *VII Chemical Reaction Engineering Conference*, Quebec City, Canada, August 2000.

[64] Magnussen, B. F., and Hjertager, B. H. On mathematical modeling of turbulent combustion with special emphasis on soot formation and combustion. *Sixteenth Symposium (International) on Combustion*, pages 719–729, The Combustion Institute, Pittsburgh, 1976.

[65] Rhodes, R. P., Harsha, P. T., and Peters, C. E. Turbulent kinetic energy analyses of hydrogen-air diffusion flames. *Chemical Reaction Engineering*, 1(4):443–470, 1974.

[66] Kolbe, W., and Kollmann, W. Prediction of turbulent diffusion flames with a four-equation turbulence model. *Acta Astronautica*, 7:91–104, 1980.

[67] Lockwood, F. C., and Naguib, A. S. The prediction of the fluctuations in the properties of free, round-jet, turbulent, diffusion flames. *Combustion and Flame*, 24:109–124, 1975.

[68] Gutheil, E., and Bockhorn, H. The Effect of Multi Dimensional PDF's on the Turbulent Reaction Rate in Turbulent Reactive Flows at Moderate Damköhler Numbers. *PhysicoChemical Hydrodynamics*, 9:525–535, 1987.

[69] Pope, S. B. PDF methods for turbulent reacting flows. *Progress in Energy Combustion Science*, 11:119 192, 1985.

[70] Pope, S. B. Monte Carlo method for the PDF equations of turbulent reactive flow. *Combustion Science and Technology*, 25:159 174, 1981.

[71] Curl, R. L. Dispersed phase mixing: I Theory and effects in single reactors. *American Institute of Chemical Engineers*, 9:175–181, 1963.

[72] Dopazo, C. Relaxation of initial probability density functions in the turbulent convection of scalar fields. *The Physics of Fluids*, 22(1):20–30, 1979.

[73] Mayeer, R. E., and O'Brien, E. E. . The joint PDF of a scalar and its gradient as a point in a turbulent fluid. *Combustion Science and Technology*, 26:123–134, 1981.

[74] Borghi, R. Turbulent combustion modelling. *Progress in Energy Combustion Science*, 14:245–292, 1985.

[75] Dopazo, C. Recent developments in pdf methods. In Libby, P. A., editor, *Turbulent Shear Flows*, pages 375–474. Academic Press, London, 1994. ISBN 0387100679.

[76] Brewster, B. S., Cannon, S. M., Farmer, J. R., and Meng, F. Modeling of lean premixed combustion in stationary gas turbines. *Progress in Energy Combustion Science*, 25:353–385, 1999.

[77] Correa, S. M., and Pope, S. B. Comparison of a Monte Carlo PDF/finite-volume mean flow model with bluff-body Ramandata. *Twenty-fourth Symposium (International) on Combustion*, pages 279–285, The Combustion Institute, Pittsburgh, 1992.

[78] Haworth, D. C., and El Tahry, S. H. Probability density function approach for multidimensional turbulent flow calculations with application to in-cylinder flows in reciprocating engines. *AIAA Journal*, 29(2):208 218, 1991.

[79] Anand, M. S., and Pope, S. B. PDF calculations for swirl combustors. AIAA Paper 93-0106, 1993.

[80] Pope, S. B., and Chen, Y. L. The velocity-dissipation propagation density function model for turbulent flows. *The Physics of Fluids A*, 2(8):1437–1449, 1990.

[81] Peters, N. Laminar diffusion flamelet models in non-premixed turbulent combustion. *Progress in Energy Combustion Science*, 10:319–339, 1984.

[82] Pope, S. B. Computation of turbulent combustion: Progress and challenges. *Proceedings of the Combustion Institute*, 23:591–612, 1991.

[83] Libby, P. A., and Williams, F. A. *Turbulent reacting flows.* Academic Press, New York, 1994. ISBN 0-12-447945-6.

[84] Kerstein, A. R. Fractal dimension of turbulent premixed flames. *Combustion Science and Technology*, 60:441–445, 1988.

[85] Kerstein, A. R. Linear-eddy model of turbulent transport and mixing. *Combustion Science and Technology*, 60:391–421, 1988.

[86] Klimenko, A. Y. Multicomponent diffusion of various admixtures in turbulent flow. *Fluid Dynamics*, 25:327–334, 1990.

[87] Bilger, R. W. Conditional moment closure modelling and advanced laser measurement. In Takeno, T., editor, *Sixth Toyota conference: Turbulence and Molecular Processes in combustion*, pages 267–285. Elsevier, Amsterdam, 1992. ISBN: 0444897577.

[88] Swaminathan, N., and Bilger, R. W. Assessment of combustion submodels for turbulent nonpremixed hydrocarbon flames. *Combustion and Flame*, 116:519 - 545, 1999.

[89] Germano, M., Piomelli, U., Moin, P., and Cabot, W. H. A dynamic subgrid-scale eddy viscosity model. *The Physics of Fluids A*, 3(7):1760 1765, 1991.

[90] Pope, S. B. *Turbulent flows*. Cambridge University Press, Cambridge, 2000. ISBN: 0521598869.

[91] Ghosal, S., and Moin, P. The Basic Equations for the Large Eddy Simulation of Turbulent Flows in Complex Geometry. *Journal of Computational Physics*, 118:24–37, 1995.

[92] Kolmogorov, A. N. The Local Structure of Turbulence in Incompressible Viscous Fluid for Very Large Reynolds Number. *Proceedings of the Royal Society*, A 434:9–13, 1991.

[93] Rydén, R., Eriksson, L., and Olovsson, S. Large eddy simulation of bluff body stabilised turbulent premixed flames. *International Gas Turbine and Aeroengine Congress and exposition*, ASME Paper 93-GT-157, 1993.

[94] Gao, F., and O'Brien, E. E. A large-eddy simulation scheme for turbulent reacting flows. *The Physics of Fluids A*, 5(6):1282–1284, 1993.

[95] Cook, A. W., and Riley, J. J. A subgrid model for equilibrium chemistry in turbulent flows. *The Physics of Fluids A*, 6(8):2868–2870, 1994.

[96] Moin, P., Squires, K., Cabot, W., and Lee, S. A dynamic subgrid-scale model for compressible turbulence and scalar transport. *The Physics of Fluids A*, 3(11):2746–2757, 1991.

[97] Dahm, W. J. A., Tryggvason, G., Frederiksen, R. D., and Stock, M. J. Local integral moment (LIM) simulations. In Baukal, C., Gershtein, V., and Li, X., editor, *Computational Fluid Dynamics in Industrial Combustion*, pages 161–208. Williams and Wilkins, Baltimore, 2000. ISBN 0849320003.

[98] Kong, S. C., Marriott, C. D., Reitz, R. D., and Christensen, M. Modeling and experiments of HCCI engine combustion using detailed chemical kinetics with multidimensional CFD. SAE Paper 2001-01-1026, 2001.

[99] Cannon, S. M., Brewster, B. S., and Smoot, L. D. Stochastic modeling of CO and NO in premixed methane combustion. *Combustion and Flame*, 113:135–146, 1998.

[100] Griffiths, J. F. Reduced kinetic models and their application to practical combustion systems. *Progress in Energy Combustion Science*, 21:25–107, 1995.

[101] Li, C. S., and Williams, F. A. Reaction mechanism for methane ignition. *ASME Journal of Engineering for Gas Turbine and Power*, 124:471–480, 2002.

[102] Glaude, P. A., Warth, V., Fournet, R., Battin, L. F., Scacchi, G., and Côme, G. M. Modelling of the oxidation of n-octane and n-decane using an automatic generation of mechanisms. *International journal of Chemical Kinetics*, 30:949–959, 1998.

[103] McMurtry, P. A., and Queiroz, M. Turbulent Reacting Flows. In Smoot, L.D., editor, *Fundamentals of Coal Combustion*, pages 511–566. Elsevier, Amsterdam, 1993. ISBN 0444896430.

[104] Rogallo, R. S., and Moin, P. Numerical Simulation of Turbulent Flows. *Annual review of Fluid Mechanics*, 16:99–137, 1984.

[105] Fox, R. O. *Computational model for turbulent reacting flows.* University Press, Cambridge, 2003. ISBN 0-521-65049-6.

[106] Amsden, A. A., O'Rourke, P. J., and Butler, T. D. KIVA-II: A computer program for Chemically Reactive Flow with Sprays. Technical Report LA-11560-MS, Los Alamos National Laboratory, Los Alamos, 1989.

[107] Ramshaw, J. D., O'Rourke, P. J., and Stein, L. R. Pressure gradient scaling method for fluid flow with nearly uniform pressure. *Journal of Computational Physics*, 58:361–376, 1985.

[108] Chase, M. W. (Editor). *NIST-JANAF Thermochemical Tables (Journal of Physical and Chemical Reference Data)*. Springer-Verlag, New York, February 2000. ISBN 1563968312.

[109] Schlichting, H. *Boundary-Layer Theory*. McGraw-Hill, New York, 6th edition, 1968. LCCN 67-29199 55329.

[110] Hirt, C. W., Amsden, A. A., and Cook, J. L. An arbitrary Lagrangian-Eulerian computing method for all flow speeds. *Journal of Computational Physics*, 14:227–253, 1974.

[111] Pracht, W. E. Calculating three-dimensional fluid flows at all speeds with Eulerian-Lagrangian computing mesh. *Journal of Computational Physics*, 17:132–159, 1975.

[112] Kreyszig, E. *Advanced Engineering Mathematics*. Jonh Wiley and Sons, New York, 2nd edition, 1967. LCCCN 66-28748.

[113] Vuika, C., Saghirb, A., and Boerstoelb, G. P. The Krylov accelerated SIMPLE(R) method for flow problems in industrial furnaces. *International Journal of Numerical Methods in Fluids*, 33:1027–1040, 2000.

[114] Pavarino, L. F. Preconditioned conjugate residual methods for mixed spectral discretizations of elasticity and Stokes problems. *Computer Methods in Applied Mechanics and Engineering*, 146(1-2):19–30, 1997.

[115] Roache, P. J. *Computational Fluid Dynamics.* Hermosa Publishers, Albuquerque, New Mexico, 2003. ISBN 0913478091.

[116] Leer, B. V. Towards the ultimate conservative difference scheme. V. A second-order sequel to Godunov's method. *Journal of Computational Physics*, 32:101–136, 1979.

[117] Dukowicz, J. K. A particle-fluid numerical model for liquid sprays. *Journal of Computational Physics*, 35:229–253, 1980.

[118] Wallis, G. B. *One-dimensional two-phase flow.* McGraw-Hill Book Company, London, 1969. LCCN 75-7517067942.

[119] O'Rourke, P. J., and Amsden, A. A. The TAB method for numerical calculation of spray droplet breakup. SAE Technical Paper 872089, 1987.

[120] Williams, F. A. Spray combustion and atomization. *The Physics of Fluids*, 1(6):541–545, 1958.

[121] Ramshaw, J. D. Partial chemical equilibrium in fluid dynamics. *The Physics of Fluids*, 23(4):675–680, 1980.

[122] Gustavsson, J., and Golovitchev, V. I. Spray Combustion Simulation Based on Detailed Chemistry Approach for Diesel Fuel Surrogate Model. SAE Paper 2003-0137, 2003.

[123] Reitz, R. D., and Diwakar, R. Structure of high-pressure fuel sprays. SAE Technical Paper 870598, 1987.

[124] Diwakar, R. Three-dimensional modeling of the in-cylinder gas exchange processes in a uniflow-scavenged two-stroke engine. SAE Technical Paper 870596, 1987.

[125] Grasso, F., Wey, M. J., Bracco, F. V., and Abraham, J. Three dimensional computations of flows in a stratified charge rotary engine. SAE Technical Paper 870409, 1987.

[126] O'Rourke, P. J., and Amsden, A. A. Three-dimensional numerical simulations of the UPS-292 stratified charge engine. SAE Technical Paper 870597, 1987.

[127] Lutz, A. E., Kee, R. J., and Miller, J. A. SENKIN: a Fortran program for predicting homogenous gas phase chemical kinetics with sensitivity analysis. Technical Report SAND87-8248, Sandia National Laboratories, Livermore, CA, USA, 1988.

[128] Schwer, D. A., Tolsma, J. E., Green, W. H., JR., and Barton, P. I. On upgrading the numerics in combustion chemistry codes. *Combustion and Flame*, 128:270–291, 2002.

[129] Bendtsen, A. B., Glarborg, P., and Johansen, K. D. Visualization methods in analysis of detailed chemical kinetics modelling. *Computers and Chemistry*, 25(2):161–170, 2001.

[130] Caracotsios, M. and Stewart, W. E. Sensitivity analysis of initial value problems including ODES and algebraic equations,. *Computers and Chemical Engineering*, 9(4):359–365, 1985.

[131] Petzold, L. R. A description of DASSL: a differential/algebraic system solver. Technical Report SAND82-8637, Sandia National Laboratories, Livermore, CA, USA, 1982.

[132] CDadapco Group. Instruction manual of STAR-CD version 3.15A, Computational Dynamics Limited, 2002.

[133] William, T. V., Saul, A. T., William, H. P., and Brian, P., F. *Numerical Recipes*. Cambrige University Press, 1st edition, 1985. ISBN 0-521-31330-9.

[134] Etter, D. M. *Structured Fortran 77 for Engineers and Scientists.* Benjamin/Cummings, Sydney, 1st edition, 1987. ISBN 0-8053-2495-X.

[135] Doering C. R. and Gibbon J. D. *Applied Analysis of the Navier-Stokes Equations.* Cambridge University Press, Cambridge, 1995. ISBN 052144568X.

[136] Baer, T., and Hase, W. L. *Unimolecular Reaction Dynamics: Theory and Experiments (International Series of Monographs on Chemistry).* Oxford University Press, Oxford, 1996. ISBN 0195074947.

[137] Rassveiler, G. M., and Withrow, L. Emissions spectra of engine flames. *Industrial and Engineering Chemistry,* 24:528–538, 1932.

[138] Millar, G. M., Winans, J. G., and Uyehara, O. A. A fast, electro-optical, hot-gas pyrometer. *Journal of the Optical Society of America,* 43:609–617, 1953.

[139] Uyehara, O. A., Myer, P. S., Watson, K. M., and Wilson, L. A. Diesel combustion temperatures-The influence of operating variables. *Transaction of ASME,* 69:465–477, 1947.

[140] Miyamoto, N., Ogawa, H., Arima, T., and Miyakawa, K. Improvement of temperature combustion and emissions with addition of various oxygenated agents to diesel fuels. SAE Paper 962115, 1996.

[141] Kobayashi, S., Sakai, T., Nakahira, T., Komori, M., and Tsujimura, K. Measurement of flame temperature distribution in DI engine with high pressure fuel injection. SAE Paper 920692, 1992.

[142] Kawamura, K., Saito, A., Yaegashi, T., and Iwashita, Y. Measurement of flame temperature distribution in engines using a two-colour high speed shutter TV camera system. SAE Paper 890320, 1989.

[143] Livengood, J. C., Rona, T. P., and Baruch, J. J. Ultrasonic temperature measurement in internal combustion engnine chamber. *The Journal of the Acoustical Society of America*, 26(5):924–930, 1953.

[144] Bauer, W., Tam, C., Heywood, J. B., and Ziegler, C. Fast gas temperature measurement by velocity of sound for IC engine applications. SAE Paper 972829, 1997.

[145] Smith, J. R. Temperature and density measurement in an engine by pulsed Raman spectroscopy. SAE Paper 800137, 1980.

[146] Orth, A., Sick, V., Wolfrum, J., Maly, R.R., and Zahn, M. Simutaneous 2D single-shot imaging of OH concentrations and temperature fields in an SI engine simulator. *Proceedings of Combustion Institute*, 25:143–150, 1994.

[147] Stenhouse, I. A., Williams, D. R., Cole, J. B., an Swords, M. D. CARS measurements in an internal combustion engine. *Applied Optics*, 18(22):3819–3825, 1979.

[148] Marie, J., and Cottereau, M. Single-shot temperature measurements by CARS in an IC engine for normal and knocking conditions. SAE Paper 870458, 1987.

[149] Bood, J., Bengtsson, P-E., Mauss, F., Burgdorf, K., and Denbratt, I. Knock in Spark-ignition Engines: End-gas temperature measurements using rotational CARS and detailed kinetic calculations of the autoignition process. SAE Paper 971669, 1997.

[150] Gross, K. P., and McKenzie, R. L. Single-pulse gas thermometry at low temperatures using two-photon Laser-induced fluorescence in NO-N_2 mixtures. *Optics Letters*, 8(7):368–370, 1983.

[151] Matsui, K., Tanaka, T., and Ohigashi, S. Measurement of local mixture strength at spark gap of SI engines. SAE Paper 790483, 1979.

[152] Aoyagi, Y., Kamimoto, T., and Matsuoka, S. A gas sampling study on the formation processes of soot and NO in a DI diesel engine. SAE Paper 800254, 1980.

[153] Bäcker, H., Hild, O., and Lepperhoff, G. Investigation on particle size distribution in the cylinder of a passenger car DI diesel engine using a fast gas sampling valve. SAE Paper 970875, 1997.

[154] Voiculescu, I. A., and Borman, G. L. An experimental study of diesel engine cylinder-averaged NO_x histories. SAE Paper 780228, 1978.

[155] Uludogan, A., Xin, J., and Reitz, R. D. Exploring the use of multiple injectors and split injection to reduce DI Diesel engine emissions. SAE Paper 962058, 1996.

[156] Ball, J. K., Stone, C. R., and Collings, N. Cycle-by-cycle modelling of NO formation and comparison with experimental data. *Proceedings of IMechE*, 213(D):175–190, 1999.

[157] Ball, J. K., Raine, R. R., and Stone, C. R. Combustion analysis and cycle-by-cycle variations in spark ignition engine combustion Part 2: A new parameter for completeness of combustion and its use in modelling cycle-by-cycle variations in combustion. *Proceedings of IMechE*, 212(D):507–524, 1998.

[158] Lebel, M., and Cottereau, J. M. Study of the effect of the residual gas fraction on combustion in a SI enigne using simultaneous CARS measurements of temperature and CO_2 concentration. SAE Paper 922388, 1992.

[159] Sawerysyn, J. P., Sochet, L., Desene, D., Crunell-Cras, M., Grase, F., and Bridoux, M. A study of spatial distribution of molecular species in an engine by

pulsed multi-channel Raman spectroscopy. *Twenty-first Symposium (International) on Combustion*, pages 491–496, The Combustion Institute, Pittsburgh, 1986.

[160] Miles, P., and Dilligan, M. Quantitative in-cylinder fluid composition measurements using broadband spontaneous Raman scattering. SAE Paper 960828, 1996.

[161] Newhall, H. K., and Starkman, E. S. Direct spectroscopic determination of nitric oxide in reciprocating engine cylinders. SAE Paper 670122, 1967.

[162] Lavoie, G., Heywood , J. B., and Keck, J. C. Experimental and theoretical study of nitric oxide formation in internal combustion engines. *Combustion Science and Technology*, 1:313 326, 1970.

[163] Sodré, J. R. Modelling NO_x emissions from spark-ignition engines. *Proceedings of IMechE*, 214(D):929–934, 2000.

[164] Nehmer, D. A., and Reitz, R. D. Measurement of the effect of injection rate and split injections on Diesel engine soot and NO_x emissions. SAE Paper 940668, 1994.

[165] Montgomery, D. T., Chan, M., Chang, C. T., Farrell, P. V., and Reitz, R. D. Effect of injector nozzle hole size and number on spray characteristics and the performance of a heavy duty D. I. Diesel engine. SAE Paper 962002, 1996.

[166] Glaude, P. A. Departement de Chimie Physique des Reactions, Universite de Nancy, Personal communication, December 2002.

[167] Faeth, G. M. Current status of droplet and liquid combustion. *Progress in Energy Combustion Science*, 3:191–224, 1977.